



**UNIVERSITÀ DEGLI STUDI DI CATANIA**

**IN CONVENZIONE CON**



**UNIVERSITÀ DEGLI STUDI DI PALERMO**

---

**DOTTORATO DI RICERCA IN**

**SCIENZA DEI MATERIALI E NANOTECNOLOGIE - XXXII CICLO**

---

*FRANCESCA MONFORTE*

**PLASMA SYNTHESIS OF Si NANOPARTICLES AND THEIR FUNCTIONALIZATION WITH  
METAL ORGANIC FRAMEWORKS AS ANODE MATERIALS FOR LITHIUM ION BATTERIES**

TUTOR: PROF. G.G. CONDORELLI

DOTT. A. LA MAGNA

SUPERVISOR: DOTT. G. MANNINO

COORDINATORE: PROF.SSA M. G. GRIMALDI

---

**TESI PER IL CONSEGUIMENTO DEL DOTTORATO DI RICERCA**

*“Ad Angela”*

# Contents

INTRODUCTION.....	5
1 Anode Materials for Rechargeable Lithium Ion Battery.....	8
1.1 Alloy Anode: Silicon “quasi” ideal anode.....	11
1.1.1 Limits of Silicon Anode.....	13
1.1.2 Solution: Si-based nanomaterials.....	16
1.1.3 Doped Si Nanostructures.....	19
1.2 Metal Organic Frameworks for Lithium Ion Battery.....	20
1.2.1 MOF Films: Synthetic Methods.....	23
1.2.2 Zeolitic Imidazolate Frameworks (ZIF-8).....	25
1.2.3 Materials of Institute Lavoisier (MIL).....	27
REFERENCES.....	31
2 Direct Growth from Solution of ZIF-8 Films.....	46
2.1 Synthesis of ZIF-8 films on Si-based surfaces.....	47
2.1.1 Experimental Section.....	49
2.1.2 Results and Discussions.....	51
2.2 Doping of ZIF-8/Quartz films with Iodine and TCNQ.....	65
2.2.1 Iodine Doping of ZIF-8/Quartz films.....	67
2.2.2 TCNQ Doping of ZIF-8/Quartz films.....	71
2.2.3 Electrical Characterization.....	74
2.3 Synthesis of ZIF-8 films on Copper foil.....	75
2.3.1 Doping of Cu/ZIF-8 films with Lithium acetate.....	78
2.3.2 Electrochemical Characterization of ZIF-8/Cu electrode.....	79
REFERENCES.....	86

3	Direct Growth from Solution of Fe-Based MIL-Frameworks .....	91
3.1	Synthesis of Fe-MIL-frameworks on Si Surface .....	92
3.1.1	Synthesis strategy to control MIL morphology and film coating .....	93
3.1.2	GAA and free-additive synthetic strategies to achieve Fe-Based MIL films .....	94
3.1.3	4-VBA synthetic strategy to achieve Fe-based MIL-88 film .....	102
3.2	Synthesis of MIL-based composites on Copper foils .....	107
3.2.1	Growth of Iron Oxy-Hydroxide MIL composite .....	108
3.2.2	Iron Oxy-hydroxide MIL composite: <i>Structural and chemical characterization</i> .....	109
3.2.3	Iron Oxy-hydroxide MIL composite: <i>Electrochemical characterization</i> .....	115
	REFERENCES .....	119
4	Octahedral Silicon Nanoparticles: an <i>Innovative</i> Negative Electrode Material in Lithium Cells 126	
4.1	Chemical Vapour Deposition: ICP-CVD system. ....	128
4.1.1	Formation Mechanism of Si-NPs and structural characterization by TEM analysis .	132
4.2	Electrodes Preparation and their assembly in LiBs .....	135
4.2.1	Electrochemical Li loading of intrinsic Si-NPs .....	137
4.2.2	LiBs Anode based on doped Si-NPs .....	144
4.3	Functionalization of octahedral Si-NPs with ZIF-8 .....	149
4.3.1	XPS analysis of octahedral Si-NPs .....	149
4.3.2	Si-NPs functionalization with ZIF-8 .....	151
	REFERENCES .....	156
	CONCLUSIONS .....	160
	ACKNOWLEDGMENTS .....	163

# INTRODUCTION

Technological innovations are imperative for a sustainable development, for controlling the climate change and for reducing the fossil fuel use. Renewable energy source (RES), like solar, wind, geothermal and hydropower, are naturally originated, are clean and increasingly competitive energy. They allow to reduce the carbon emission limiting the environmental pollution, and to guarantee health security and cost-competitive with fossil fuels. Noteworthy progresses have been reached in the sustainable energy field through the development of innovative photovoltaic cells, photothermal receivers and wind turbines. However, sustainable technologies are closely correlated to the capability of electrical energy storage (EES) needed to accumulate the generated electricity especially for intermittent sources like photovoltaics. Highly efficient, reliable and secure EES devices are needed to optimize the large-scale RES use. Secondary battery and supercapacitors result promising EES systems as able to store electrical energy through chemical reactions and electrostatic fields, respectively. They are leading supply power source for portable electronic market, as laptops, mobile phone and medical microelectronic devices. In contrast, several drawbacks must be overcome to implement their application in electrical vehicles field. In this regard, rechargeable lithium ion batteries play a key role respect to supercapacitors because they are able to guarantee high energy density resulting well-suited for long-term energy storage and provide a gradual voltage loss with a near-constant voltage output until spent whereas, the voltage output of capacitors declines linearly with the charge. However, it is necessary to increase the power density, the cycle stability life reducing charging time of lithium ion battery in order to reduce costs and to guarantee high-capacity devices. The development of low-cost, ultra-lightweight and high-power density lithium ion battery would be a remarkable breakthrough in modern electrochemistry. Thin film lithium batteries represent an advanced solid-state EES architecture consisting of solid electrolyte and active layers electrode deposited on specific substrate leading to multilayers cells. Indeed, they are suitable to integration and miniaturization and to the realization of microdevices enabling further cost reduction. Solid-state lithium ion battery guarantees also higher average operating voltage (3.4 V), higher energy density for both electrodes (460 Wh / Kg), longer cycle life (up to 10 years, compared to 2) than conventional lithium ion battery and wide working temperature range (-20 -60 °C). By modulating the size of the electrode materials, their morphology and

composition it is possible to tune physical-chemical properties and to optimize the battery performance. Electrode surface modification represents a crucial issue because allow to achieve coating with functional featuring in order to guarantee more versatility and flexibility. Thanks to the intrinsic security of solid-state battery, the cycling performance of anode are limited by oxidative degradation and lithium dendrites growth on its surface.

Therefore, it would be needed to develop innovative hybrid materials for secondary Li batteries in order to enable the implementation of high capacity negative electrodes in next generation energy storage devices. Among all the possible proposed materials, silicon acts as “quasi-ideal” anode in terms of theoretical capacity, closely to one of lithium metallic, and for the intrinsic low discharge voltage. In addition, thanks to its low toxicity and its abundance in earth’s crust, silicon guarantees high safety and low production costs. However, the large volume change due to insertion/extraction of lithium ion represents a practical limit of any silicon anode.

The aim of this thesis is the development of new materials for lithium ions battery, using few hundred nanometres in size and octahedrally shaped Silicon nanoparticles (Si-NPs) as active anode materials. Si-NPs intrinsic or doped, were synthesized by plasma assisted chemical vapor deposition. In order to obtain hybrid core-shell systems, Metal Organic Frameworks (MOFs) films were firstly grown on Silicon-based and Copper surfaces to optimize heterogenous nucleation and were assembled on octahedral Si-NPs then. The combination of the carbon porous framework of MOF with the electronic properties of the Si nanoparticles, allow to reduce the capacity fade due to the irreversible reactions and, therefore, enhance the electrochemical characteristics of the battery.

In summary, the Ph.D. thesis is organized as follows:

1. ***Anode materials for Rechargeable Lithium Ion Battery:*** it includes an introduction to lithium ion battery technology focusing on intercalation materials proposed as anode in literature until Silicon use. The advantages of Silicon nanostructures as active materials but their limits and the possible technological solutions will be described. In addition, the insertion of dopants, like phosphorous and boron, into Si lattice, will be introduce as a new and promising strategy suitable to improve silicon conductive and to preserve anode integration. A short outlook regarding the structural featuring and chemical-physical property of Metal Organic Frameworks will be discussed with particular focus on Zeolitic Imidazolate (ZIF-8) and Carboxylate-based

(Materials of Institute Lavoisier, MIL) frameworks topology. The importance of MOF films design will be highlight in order to strengthen their integration in thin film lithium ion battery.

2. ***Direct Growth from solution of ZIF-8 films:*** it is structured in two parts concerning the synthesis of ZIF-8 films through direct growth from solution on Si and Cu surfaces respectively. A combined approach based on experimental data and theoretical model is reported to explain the growth mechanism of ZIF-8 on Si-based substrates (Si, a-Si, quartz and SiO<sub>2</sub>) by analysing the role of the solvent and the surface chemistry. For the films ZIF-8/Quartz is described the post-doping with iodine (I<sub>2</sub>) and para-quinone compound (tetracyanoquinodimethane, TCNQ) as electron donor and acceptor respectively, proved mainly by optical analysis and electrically tested by four-point probe resistivity measurements. The same synthesis method has been employed to grown ZIF-8 film on Cu foils, a frequently used surface because as current collector for anode. ZIF-8/Cu films have been doped with lithium acetate in order to investigate the lithium ionic conduction inside films and the electrochemical performance through cyclic voltammetry and galvanostatic measurements.
3. ***Direct Growth from solution of Fe-based MIL-frameworks:*** it reports different synthesis strategies adopted to grow carboxylate-based MOF on a Si surface. It has been proved as synthesis conditions drive the MIL heterogenous nucleation in terms of morphology, crystallinity and film thickness. Fe-based MIL-101 and MIL-88 were obtained and chemical and structural characterized. A simple two-step synthesis protocol, based on sol-gel process and post direct growth, has been newly developed to growth a MIL composite on Cu foil consisted of MIL-101 embedded in iron oxides/hydroxides matrix. The hybrid MOF-based composite showed an unique, very attractive electrochemical behaviour.
4. ***Chemical Vapour Deposition of Silicon Nanoparticles:*** Octahedral Si-NPs, intrinsic and doped were synthesized by means inductively coupled plasma chemical vapour deposition. The effect of doping and of size on electrochemical performance were investigated through charge-discharge voltage profile and capacities. Si-NPs were functionalized with ZIF-8 by adopting different synthesis routes in order to optimize the coating in terms of composition, crystallinity and shell porosity.

# Chapter 1

## 1 Anode Materials for Rechargeable Lithium Ion Battery

Lithium ion batteries (LIBs) are leading power sources for portable electronic devices, like laptops, mobile phone, digital cameras and medical microelectronic devices and are nowadays preferred with respect to other widely used technologies based on Pb, Ni-Cd or NiMH.<sup>1</sup> LIBs offer good safety performance and own large volumetric (250 – 670 Wh / L) and gravimetric (100 – 265 Wh / kg) energy density. Among all the alkali metals, Li is the lightest ( $d = 0.535 \text{ g/cm}^3$ ), and one of the most electropositive elements ( $E^\circ = -3.4 \text{ V}$ ).<sup>2</sup> Therefore, LIBs provide high energy density and it is possible to reach voltages up to 4 V compared with the typical voltage of Ni-Cd (1.2 V), resulting a suitable material for high-power applications (Figure 1).<sup>3</sup> Moreover, LIBs do not suffer from memory effect and they are characterized by a slow self-discharge rate (1.5 – 2 V per month).<sup>4</sup> In addition, LIBs do not require particular manutention processes to keep cycle life and moreover do not contain toxic elements.

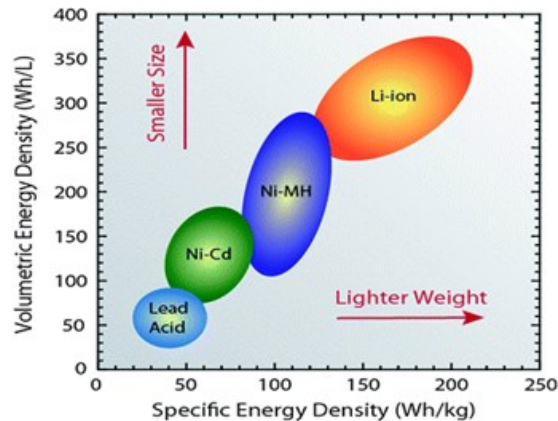


Figure 1: Diagram of specific and volumetric energy density of battery technologies in use (from <http://www.cei.washington.edu/education/science-of-solar/battery-technology/>)



Bulk size cylindrical cells (the smallest is only 5mm in diameter), like pouch or coin cell, are the most common LIBs in use today, particularly for electronic portable devices. Lithium micro-batteries are less frequently used, though ideal for microelectronic integrated circuits and biological / medical devices (Figure 2) because their manufacturing results very difficult.<sup>5</sup> Size reduction (until millimeter scale) and capacity improving are still a great technological challenge and coin cells continue replacing micro-batteries in self-powered microelectronics.<sup>6</sup>

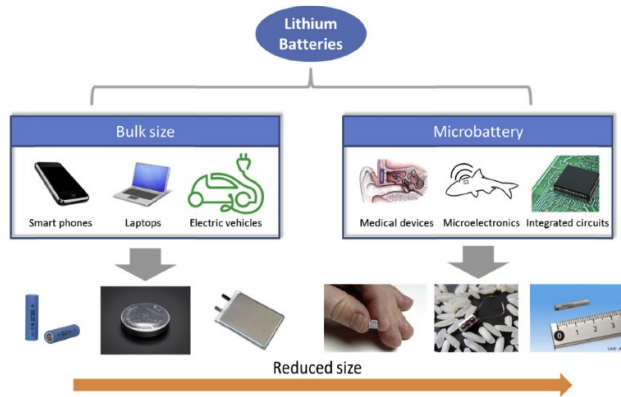


Figure 2: Lithium ion battery form cells and their applications.<sup>6</sup>

Innovative micro-sized pin-type batteries have been implemented by Panasonic in 2014. Though the reduced sizes, their high specific capacity allowed to employ these ones in electronic pens, wearable and medical devices.<sup>7</sup> However, micro-batteries cannot ensure rechargeability for the complexity due to their intrinsic small scale. Technological improvements in terms of manufacturing and power density are required to develop secondary micro-batteries and expand their use in functional integrated systems.<sup>8</sup>

Lithium ion battery consists of composite electrodes and a liquid electrolyte. Decreasing the battery size, the cell assembly results more problematic and the selection of electrode materials is crucial for manufacturing processes.<sup>9</sup> The energy difference between the highest occupied (HOMO) and lowest unoccupied molecular orbitals (LUMO) of the electrolyte, indicated as HOMO LUMO  $E_{gap}$ , and the electrochemical potential of the cathode  $\mu_C$  and of the anode  $\mu_A$  are key factors to address the choice of the related materials.<sup>10</sup> In order to avoid the reduction and the oxidation of electrolyte,  $\mu_A$

must be energetically lower than LUMO and  $\mu_c$  must be energetically higher than HOMO, (Figure 3a). Similarly, the greater the difference between the electrodes electrochemical potentials ( $\mu_A - \mu_C$ ) the higher will be the lithium intercalation ability and the energy density.<sup>11,12</sup>

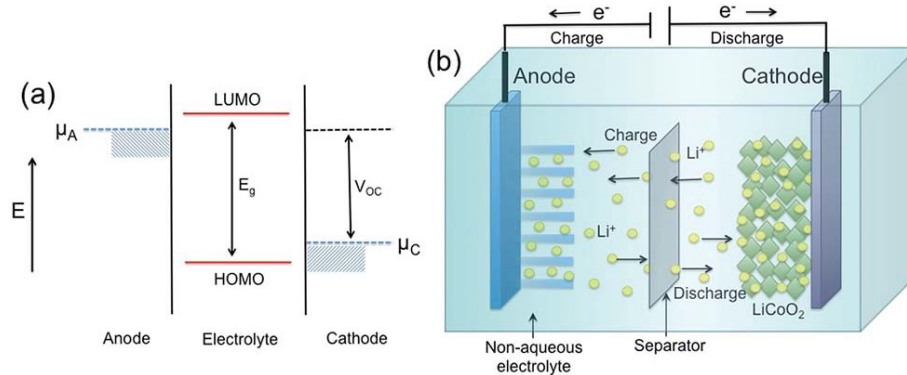


Figure 3: a) Energy diagram of electrochemical potential of electrodes and HOMO -LUMO Egap of electrolyte in LIBs; b) Charge / discharge process in a typical secondary LIBs.<sup>10</sup>

In first generation LIBs, graphite was employed as anode and, intercalation materials, like oxides indicated as  $LiMO_2$  ( $M = Co, Mn, Ni$  or  $V$ ) or a phosphate such as  $LiFePO_4$ , were used as cathode.<sup>13</sup> The electrolyte, which allows ions transport between the electrodes, is composed of a lithium salt, usually  $LiPF_6$ , chosen for its high ionic conductivity and electrochemical stability, in an aprotic organic solvent (Propylene Carbonate, Ethylene Carbonate, Diethyl Carbonate), able to dissolve the salt and conducting current by means of  $Li^+$  ions.<sup>14</sup> The working mechanism of LIBs is based on the extraction of Li ions from the cathode and their insertion into the anode during charging. The process is reversed during discharging with Li ions being extracted from the anode and inserted into the cathode (Figure 3b). The widely use of layered graphitic carbon was due to its long cycle lifetime, abundance and low costs. However, it is characterized by a low theoretical capacity (372 mAh/g) that involves low energy density.<sup>15</sup> In addition, the repeated insertion and extraction of lithium ions, defined as lithiation and de-lithiation processes respectively, cause graphite layers exfoliation and lithium dendritic depositions resulting in short-circuits.<sup>16</sup> In addition, irreversible processes and anode cracking, which are due to the electrolyte decomposition at low potential ( $\sim 100$  mV), shapes a solid electrolyte interphase layer (SEI) close to the surface of the negative electrode.<sup>17</sup> Repeated decomposition of SEI is the main issue of LIBs because of leading to capacity fading.

Safety battery and electrochemical performances have been improved by replacing graphite intercalation compounds with alloy-type anodes.

## 1.1 Alloy Anode: Silicon “quasi” ideal anode

In order to extend LIB’s technology in electrical vehicles, several alloy-type anodes have been proposed. Huggin and Besenhard proposed metal binary alloy ( $\text{Li}_x\text{M}$ ) as negative electrode topology for the first time.<sup>18,19</sup> The metal not only is an electrochemical active element responsible of lithium phase formation but represents also the host matrix that should bear the strain associated to the lithium insertion. Alloy anodes guarantee relatively low cost, environmentally compatibility and moreover high energy density. Respect to conversion type anode, like graphite, in which the lithiation reaction involves the fully reduction of the active material, leading to an only possible intercalate product (like  $\text{LiC}_6$ ); working alloy mechanism involves the formation of different intermetallic  $\text{Li}_x\text{M}$  compound at specific potentials.<sup>20</sup>

Pure elements like Si, Ge, P, Sn and Pb, metal hydrides and metal oxides have been proposed as anode (Figure 4).<sup>21</sup> Having low density and a stoichiometric ratio suitable to lithium accommodation (providing more than an electron they guarantying the formation of different  $\text{Li}_x\text{M}$  phases), they can limit the capacity fade and overcome the limitations of traditional anode materials involving enhanced safety, high-energy density and long cycle life.<sup>22</sup>

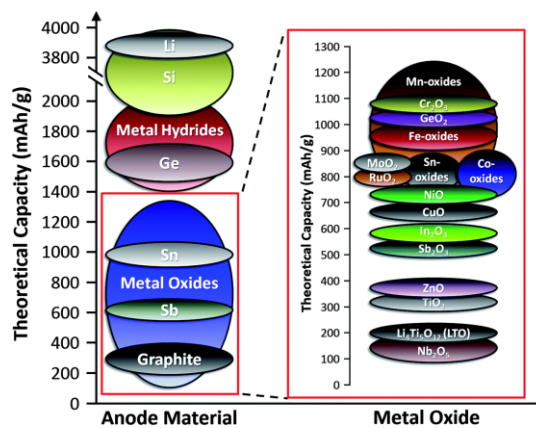


Figure 4: Theoretical capacity of proposed anode for LIBs.<sup>21</sup>

An ideal anode material should possess a high gravimetric and volumetric capacity, high environmental compatibility, low toxicity and low cost. Metallic lithium presents a high specific capacity (3862 mAh/g) but its practical use as electrode negative is limited by its high reactivity, both in water and organic electrolyte, involving overheating and therefore compromising the cell safety. In particular, the high reactivity of lithium accentuates the SEI instability with lithium dendritic formation making its use technologically impossible.<sup>23</sup>

<i>ELEMENT</i>	<i>GRAVIMETRIC CAPACITY (mAh/g)</i>	<i>VOLUMETRIC CAPACITY (mAh/cm<sup>3</sup>)</i>	<i>COST</i>	<i>TOXICITY</i>	<i>SAFETY</i>
<i>Si</i>	<i>4200</i>	<i>2400</i>	<i>Low</i>	<i>No</i>	<i>High</i>
<i>C</i>	372	890	Low	No	Low
<i>Ge</i>	1568	2300	High	High	High
<i>Sn</i>	990	2200	Low	No	High
<i>P</i>	2600	2250	Low	High	Low
<i>Sb</i>	660	1890	Low	High	Low
<i>Pb</i>	549	1790	Low	High	Low

*Table 1: Characteristics of Li-alloy element.*<sup>24</sup>

Among all Li-alloy element, Silicon acts as “quasi-ideal” anode because it possesses a high gravimetric and volumetric capacity close to lithium metallic, high environmental compatibility, low

toxicity and low cost (Table 1). In addition, it is characterized by a low self-discharge voltage (0.2 V / Li<sup>+</sup>) that guarantees a greater safety.<sup>24</sup>

However, high thermal and morphological stability are required to improve SEI stability and guarantee a complete safety device.

### 1.1.1 Limits of Silicon Anode

Though Silicon represents the most promising alloy-type anode its practical implementation in LIBs as electrode negative is strongly limited by the following issues:

- a. *Large volume variation (about 400 %) due to electrochemical lithiation;*
- b. *Instability of SEI;*
- c. *Low electronic conductivity ( $10^{-3}$  S cm<sup>-1</sup>,  $10^{-2}$  S cm<sup>-1</sup> after lithiation).*

- a) Figure 5 shows the Lithium – Silicon diagram phase at different temperatures (Figure 5a) and the voltage profile concerning the first and second cycle and detected for crystalline silicon anode (Figure.5b). Each Li-Si binary phase is associated to a defined temperature and characterized by a distinct voltage plateau. At room temperature and for the first discharge a long plateaus voltage is detected at 100 mV, due to the Si amorphization for the related lithium allowing, and that disappears at second cycle (Figure 5b).<sup>24,25,26.</sup>

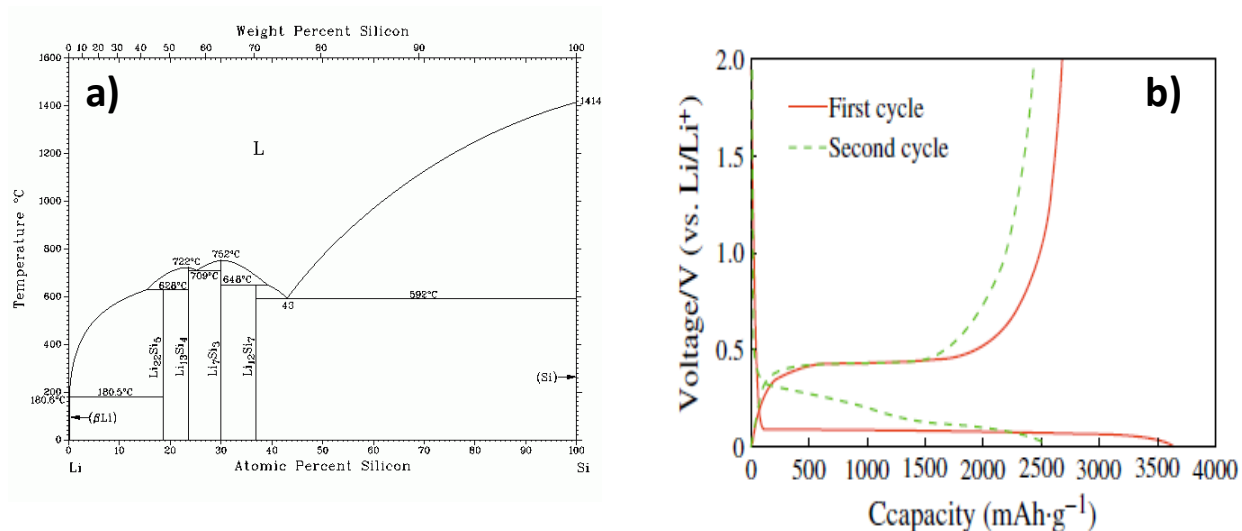
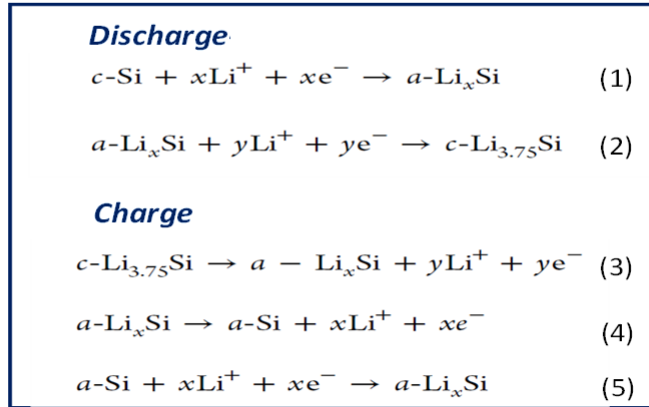


Figure 5: Phase Diagram of system Silicon Lithium (a); Voltage profile of Silicon anode for the first charge/discharge cycle (b).<sup>24</sup>

As showed in the scheme 1, the first charge / discharge process involves Silicon crystalline-amorphous change, called “two - phase region” and highlighted by two voltage plateaus. In detail, the lithium allowing into crystalline Silicon (first discharge), involves the a- $\text{Li}_x\text{Si}$  amorphous phase formation (reaction 1) that changes in c- $\text{Li}_{15}\text{Si}_4$  at around 60 mV (vs  $\text{Li}/\text{Li}^+$ ) after insert the maximum possible lithium amount (reaction 2). The charge is also characterized by a two-phase region due to related de-allowing process and to the c- $\text{Li}_{15}\text{Si}_4$  and a- $\text{Li}_x\text{Si}$  amorphous phases (reaction 3) that it is changes into a-Si with the complete depletion of crystalline Silicon (reaction 4).<sup>24,27</sup>



*Scheme 1: Electrochemical lithiation /delithiation for silicon anode.<sup>24</sup>*

During the second cycle only, amorphous silicon reacts with lithium through the reaction 5. The consecutive allowing / de-allowing processes go on with the reactions 1-5 causing lattice expansion and contraction resulting on a huge volume change of Silicon. The latter one causes the electrical resistance increases and the capacity fade. In addition, the lithiation stress causes surface tensions that propagate quickly toward internal matrix producing cracking until to anode disintegration, (Figure 6-morphologic changes).<sup>28</sup>

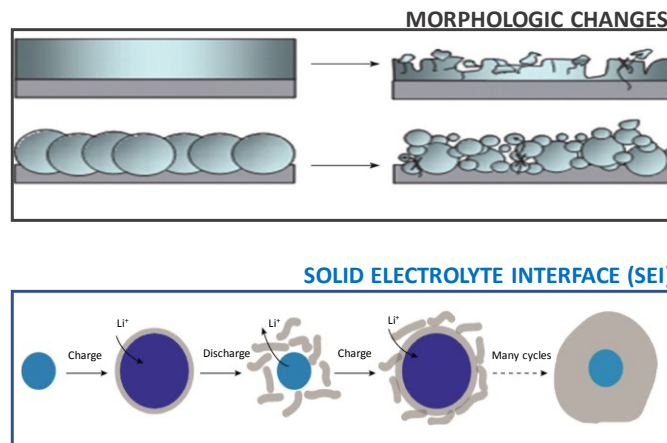


*Figure 6: Cracking and anode disintegration for Si bulk (morphologic change); instability of solid electrolyte interface for Si particles (SEI).<sup>24,28</sup>*

- b) In addition, the electrolyte decomposition during lithiation at low potential shape a thin SEI layer close the anode surface. (Figure 6-*SEI*).<sup>29</sup> The contraction of particles causes a SEI layer fragmentation leaving the particles surface exposed to electrolyte solution. The particle shrinks and swelling processes continue with the charge / discharge cycles and the SEI thickness increases, insulating electrically the particle and rising electrical resistance and compromising cycling stability.<sup>30,31</sup>
- c) In order to develop high-efficient silicon-based battery it is necessary to improve the Si electrical conductivity. It is about  $10^{-3} \text{ S cm}^{-1}$  and increase to  $10^2 \text{ S cm}^{-1}$  after lithiation. In addition, the lithium diffusion coefficient is rather low, with value between  $10^{-14}$  and  $10^{-13} \text{ cm}^2\text{s}^{-1}$ , limiting the rate performance of the Si anode. Hence, the poor electron transport and the short lithium paths increase the battery impedance contributing further to failure mechanism of Si as negative electrode.<sup>32</sup>

### 1.1.2 Solution: Si-based nanomaterials

A suitable solution to overcome the above-mentioned Silicon limits is the use of silicon nanostructures rather than bulk. They offer a higher degree of freedom for the arrangement of the ions, so they can tolerate plastically the stress associated to the lithiation / delithiation process, promoting relaxation and avoiding the pulverization. Respect to a bulk material, the nanostructures provide a greater surface to volume ratio, implicating a reduction of diffusion paths of lithium ions improving kinetic characteristics and leading to a greater capacity density.<sup>33</sup> It has been reported as nanoparticles with size smaller than 150 nm, (critical size to lithiation process), are particularly suitable to bear the stress due lithium allowing and de-allowing guarantying an efficient electrical contact and, therefore a greater cycling reversibility (Figure 7).<sup>34</sup>



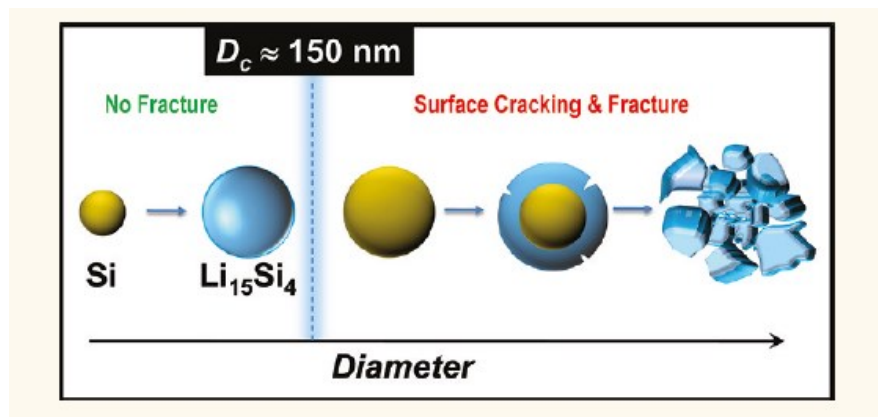


Figure 7: Suitable diameter of Si nanoparticles able to tolerate anode cracking.<sup>34</sup>

In addition, porous silicon nanoparticles result also promising as anode because they offer greater surface area increasing the electrolyte diffusion, improving electrical conductivity and limiting capacity loss.<sup>35</sup>

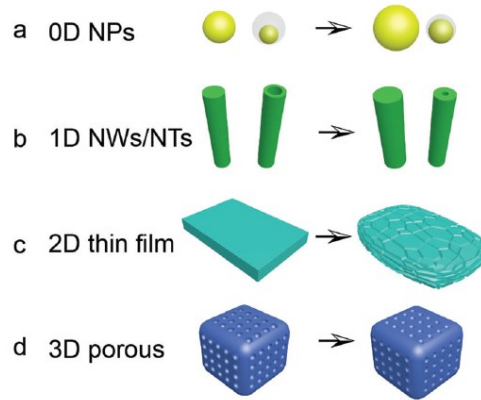
To date, in the literature, there are reported several examples of LIBs based on nanostructured silicon anode (Scheme 2).<sup>36</sup> In details:

- a) *0D-Si*: Nano - sized Si nanoparticles, with diameter about 10 – 30 nm, and characterized by internal holes have been proposed as practical solution to increase the surface area accessible to electrolyte and to improve the lithium diffusion and the capacity retention. To preserve the anode pulverization, core-shell structures based on Si-NPs core and carbon empty shell, (named yolk shell Si-NPs) have been synthesized. The Carbon shell guarantees an appropriate ductility needed to bear lithiation stress and to avoid the thermal drifts. The yolk – shell Si-NPs topology have been obtained through magnesiothermic or aluminiothermic reduction a chemical process that requires high temperatures and more deposition steps during which the nanoparticles sizes cannot be control.<sup>37,38,39,40</sup>
- b) *1D-Si nanowires*: Si NWs grown through bottom-up, more common, top-down method or VLS techniques (like chemical vapor deposition “CVD”, Molecular Beam Epitaxy “MBE” and atomic layer deposition “ALD”). By CVD method it is possible to control the Si NW’s diameter, growth direction and length, however the process temperatures are very high (about 800°C). By modulating synthesis processes, in particular through template presence or acid additive, it is possible to tune the structural properties and therefore the electrochemical lithiation.<sup>41,42,43,44</sup>

*1D-Si nanotubes*: proposed SiNTs; with carbon or Ge, SiO<sub>x</sub>, TiO<sub>2</sub>, and SnO<sub>2</sub> like coating material, are characterized by higher energy density than other topology, like nanorods or nanowires, thanks to empty internal canals that allow to bear the Si expansion. However, there are few examples due to the difficulties to obtain them. SiNTs were synthesized mainly by decomposition of silicon precursors embedded in aluminum oxide matrix.<sup>45,46,47,48</sup>

c) *2D-Si thin film*: deposited through CVD or physical techniques like PVD, evaporation, pulsed laser deposition, electron-beam evaporation, DC or radio frequency magnetron sputtering. Thin films were usually directly deposited on surfaces, like Cu, Ni, stainless, to be integrated in cells. The advantages of thin films are the possibility to control the composition and crystallinity of films, and the insertion of dopants to modulate the electrical properties of silicon. However, the cost of Si thin film manufacturing is still very high and the instability of SEI compromises the electrochemical performance of these Si thin film anodes.<sup>49,50,51,52</sup>

d) *Porous Si nanoparticles*: this topology results particularly attractive thanks to the buffer effect of the nanoparticles that allows to limit the large volume change of silicon. More promising are porous Si nanostructures coated with carbon framework or embedded in carbon or graphene matrix. The combination of porous nanoparticles, with the flexibility and the conductivity of the carbon matrix, ensures to overcome the large volume variation and the poor electron conductivity of silicon. Porous Si particles have been synthesized mainly via self-assembly approach or by decomposition of Si precursors based on Si / polymer composite.<sup>53,54,55,56</sup>



*Scheme 2: Si Nanostructures (Si-NPs) examples: yolk-shell Si-NPs (a), Si nanowires Si NWs and Si nanotubes Si NTs (b), Si thin film (c), 3D porous Si nanoparticles (d).*<sup>36</sup>

### 1.1.3 Doped Si Nanostructures

Silicon doping could be an efficient strategy to overcome Si insulating/semiconductor properties. It is known that the insertion of impurities like phosphorous (P), boron (B), copper (Cu), aluminum (Al), arsenic (As) in the Si lattice allows to insert donor or acceptor levels in Silicon Egap.<sup>57</sup>

Thanks to the high thermal stability and the excellent mechanical properties of Cu, like hardness, strength and ductility, Cu doped Si films with thickness about 10  $\mu\text{m}$  were employed as active electrode film composite. Particularly Cu-doped Si films show a morphology stability and anode integration after 300 cycles guarantying good cycling performances, in terms of long cycle life, capacity retention (93.8 % after 100 cycles) and Columbic efficiency ( $\sim 80\%$ ).<sup>58</sup>

Al-doped Si nanowires were tested as negative electrodes for Mg, Na ion batteries. Through DFT calculations, the energy insertion of Mg, Na, Li ions into Al-doped Si nanowires were obtained. It was proved that high Al concentrations thermodynamically favor the Mg and Na insertion. In addition, the Al doping allows to reduce the Li defect formation energy with respect to the Li energy cohesive. However, Al-doped Si nanowires show a similar behavior to undoped Si, involving very high energy barrier for Li (0.57 and 0.70 eV), Na (1.07-1.19 eV) and Mg (0.97-1.18 eV) ion diffusion.<sup>59</sup>

McSweeney et al. through a combined approach based on electrochemical and structural characterization of doped Si electrodes studied how the electronic density of surface region

influences the crystalline – amorphous changes and therefore the lithiation/de-lithiation processes. In particular, the electrochemical Li loading at Si (100) surface region was investigated for n-type and p-type Si electrodes, achieved through As and B doping respectively. It has been proved as B-doped Si (100) reaches higher Coulombic efficiency over the 25 cycles, (~95%) than highly P-doped Si electrode. The poor capacity retention of P-doped is due to the surface cracking for the formation of silicide lithium alloy. The high morphology stability of B-doped Si (100) allows to bear the lithiation stress and to preserve a polycrystalline structure until 5 cycles.<sup>60</sup>

Computational studies have been carried out to elucidate the effect of dopant type on lithium insertion energy by considering the Lithium insertion Energy into Si lattice ( $E_{\text{insert}}$ ).<sup>57</sup> Long et al. reported positive  $E_{\text{insert}}$  for P-doping whereas negative for B-doping proving as the lithium insertion in P-doped Si is energetically unfavourable.<sup>61</sup> However, it has been proved as low P dopant levels (124 ppm) can influence positively the cycling stability of negative electrode. Despite P concentrations above 120 ppm increase electrical Si conductivity, they do not guarantee greater Coulombic efficiency and good capacity retention.<sup>57</sup> There are not many examples of doped Si as anode for LIBs and the relationship between dopant type and level with their electrochemical performance is not totally clear.

However, it turns out that the increase of electronic conductivity due the dopant insertion doesn't particularly influence the electrochemical performances instead the amorphous phase formation due lithiation process, like  $B_4Li_5$ ,  $Li_3P$  or  $P_2O_5$  limits anode disintegration leading to better rate capability and cycling stability.<sup>62,63,64</sup>

## 1.2 Metal Organic Frameworks for Lithium Ion Battery

Metal Organic Frameworks (MOF) have become recently interesting for energy storage application, like fuel cells, Li or Na ion batteries and supercapacitors.<sup>65</sup> These peculiar hybrid materials are crystalline complexes, similar to coordination polymers shaped from inorganic cations or clusters and organic linkers (Figure 8).<sup>66,67</sup>

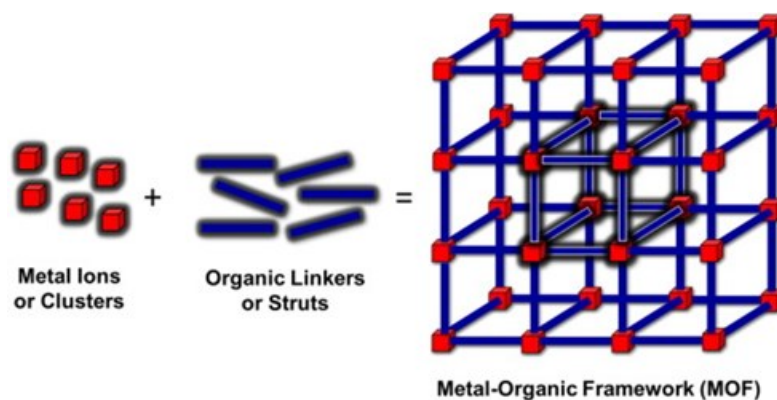


Figure 8: Graphical representation of MOFs.<sup>66</sup>

They are characterized by a high porosity, large surface area and low density and offer high thermal and chemical stability.<sup>65</sup> The electronic configuration of transition metals and the steric encumbrance of organic moieties affect the MOF coordination geometry and the crystalline structure. Indeed, MOFs present dynamic structure with tunable pore size.<sup>68</sup> Flexible ligands as imidazole and aromatic carboxylic acid, and d-transition metals; like Zn, Mn, Co, Fe, Ni; are the most common organic and inorganic precursors used.<sup>69</sup> MOFs' porous structure, their chemical-physical properties and, in particular, their adsorption/transport capability can be varied by tuning the nature of their building blocks (metallic centres and organic ligands) and by inserting functional groups or specific guests inside the porous structure through in situ or post-synthetic routes.<sup>70,71</sup>

MOFs have been employed for application in LIBs both as precursors for mesoporous composite electrodes and as hybrid solid electrolyte for Li ion transport.<sup>72,73</sup> Fe-based MIL-53 obtained with amino-terephthalic acid as starting organic precursor, Cu-TCA (H<sub>3</sub>TCA: tri-carboxy-triphenylamine), ternary MOF based on LiBTC (BTC: trimesic acid) and Cu-TCNQ (TCNQ: tetracyanoquinodimethane) are the more common MOF cathode developed for LIBs.<sup>74,75,76,77.</sup>

Several examples of MOF-based anodes have been synthesized mainly using imidazole and carboxylates as organic linkers. Particularly, *Co-TFBTC* (TFBTC: 2,3,5,6-tetrafluoroterephthalic acid), *Zn(abIM)* (abIM: 2-aminobenzimidazole), and *Mn-BTC* (BTC: trimesic acid) have been proposed as negative electrode.<sup>78,79,80</sup> They show theoretical capacity between 230 – 1080 mAh/g guaranteeing a high energy density. In order to strengthen the application of MOFs as anodes, conjugated carbonyl groups [R-(C=O)-R<sup>1</sup>] and quinone acceptor complexes have been employed as

organic moieties.<sup>81</sup> Their high redox potential and high oxidative ability, involving multi electron transfer reversible reactions, improve their capacity retention. However, the MOFs' instability due to the huge volume variation and to the large voltage hysteresis, requires the use of carbon matrices, polymer additives or the insertion of additional redox active centres and anion radicals, in order to develop MOF-based composites capable of promoting the Li-M alloy formation and preventing the anode pulverization. An attractive class of MOF-based composites consisting of metal oxides or hydroxide embedded in carbon matrix were recently obtained after pyrolysis process using MOFs as template or precursors.<sup>82,83</sup> The MOFs' annealing was employed to produce carbon porous coating of silicon or TiO<sub>2</sub> nanoparticles because the high temperatures cause network collapse which leads to a carbon framework with metallic centres scattered inside it.<sup>84,85</sup> However, it would be important to implement a new strategy of synthesis able to achieve MOF-based systems which guarantee the same electrochemical performances of metallic oxides without using the MOFs pyrolysis.

Furthermore, in order to reduce weight cells and to increase the safety of the solid-state battery MOFs have been proposed as alternative to liquid electrolyte.

The intrinsic MOF structure acts as efficient host for *lithium ionic liquids (LIL)* since it guarantees a porous network inside which the lithium ions are free to move. Recently Zhu et al. reported a novel modifier for solid polymeric electrolytes which consists of an Al-based MOF (MIL-53) used as filler for thin films of polyethylene oxide.<sup>86</sup> In addition, Mg-based MOFs like Mg<sub>2</sub>(2,5-dioxidobenzene-1,4-dicarboxylate), and Zn-based imidazolate MOFs, were used as host materials for Lithium ion-doped ionic liquid (IL).<sup>87,88,89</sup> IL consists of a mixture of 1-ethyl-3-methylimidazolium bis(trifluoromethylsulfonyl)amide(EMI-TFSA) with lithium salts, like lithium bis(trifluoromethanesulfonyl)amide (LiTFSA), or lithium isopropoxide (LiOiPr) or Lithium tetrafluoroborate(LiBF<sub>4</sub>), in order to induce lithium conductivity inside MOF cavities.<sup>90</sup> The good transport properties of the reported composites were attributed to the Lewis acid behaviour of the MOF surface which promotes the Li salt dissociation increasing therefore, the ionic conductivity. In addition, the MOF nanoparticles acting as crossing-linking centres for PEO produce a robust network that guarantees a good thermal stability and an excellent mechanical robustness.

### 1.2.1 MOF Films: Synthetic Methods

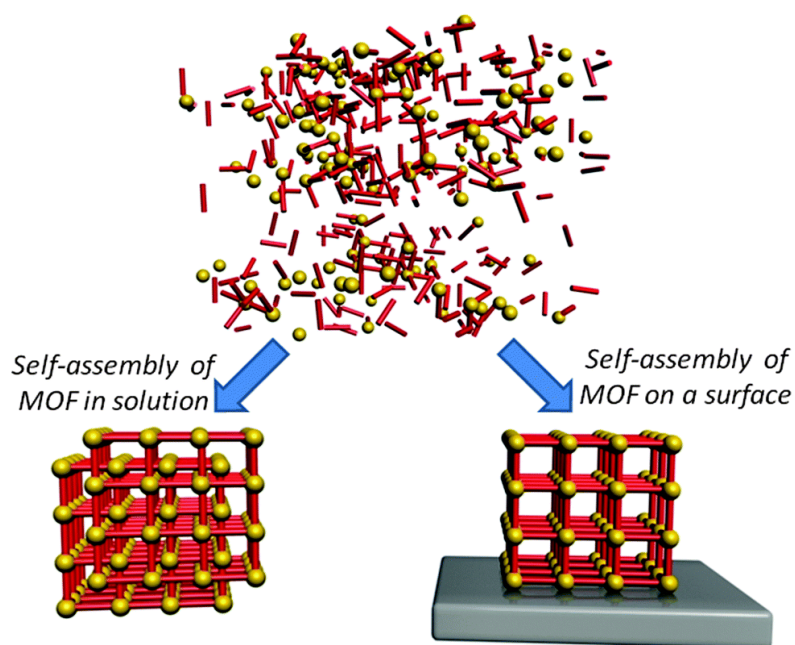
There are several examples of MOF powders in literature, due to the possibility to modulate MOFs assembly and crystalline structure in function of organic and inorganic precursors choice.<sup>67</sup> The MOF powders' synthetic methods are mainly based on solvothermal or hydrothermal routes, and on microwave - assisted, mechanochemical and sonochemical protocols. The synthesis' conditions affect the structural and chemical-physical properties of MOFs allowing to select specific application field (Scheme 3).<sup>91,92</sup>



*Scheme 3: Correlation between main synthetic route of MOF powders, their structural properties and possible applications.<sup>91</sup>*

These synthetic routes are not suitable for film growth because of film cracks and therefore, do not guarantee a homogenous coating. In addition, mechanochemical and sono-chemical methods, involving grinding and ultrasound techniques, generate intrinsic defects compromising the film structure and morphology.<sup>93, 94</sup> In order to optimize heterogeneous nucleation and the layer adhesion, layer-by-layer depositions, liquid-phase epitaxy and rapid thermal depositions ensure thickness control and film homogeneity.<sup>95,96,97</sup> Silicon, quartz, gold surfaces have been pre-functionalized with

Self Assembled Monolayers (SAMs) to drive the chemistry interaction between surface terminations and MOFs precursors.<sup>98,99</sup> SAMs pre-functionalization represents the main synthetic via to obtain surface-anchored MOFs. The surface modification allows to modify its hydrophilicity-hydrophobicity behaviour optimizing covalent anchoring and driving the MOF growth. Surfaces have been functionalized with OH-, NH<sub>2</sub> or COOH-terminated SAMs to achieved highly oriented MOFs film like Zn and Cu-based MOFs.<sup>98,100,101</sup> Another possible strategy to growth MOFs is the pre-deposition trough CVD or ALD techniques of the inorganic precursors. ZIF-8 films were grown on CVD pre-deposited with a ZnO layer that generates Zn<sup>2+</sup> surface centres and activates the MOF nucleation.<sup>102</sup> Therefore, it is needed to implement facile and fast syntheses to obtain a continuous and thickness-controlled coating on determinate surfaces, like Cu or Al, common collectors used in LIBs, silicon or metallic lithium. (Scheme 4).<sup>103</sup>



*Scheme 4: MOFs' Homogenous and Heterogenous nucleation with direct growth of film.<sup>103</sup>*

So doing, by depositing MOF films onto an appropriate substrate it is possible to achieve integrated devices suitable for sensors, electronic and storage applications and, in addition, to rationalize the design of multi-layers system with functional chemical physical properties.



### 1.2.2 Zeolitic Imidazolate Frameworks (ZIF-8)

Zeolitic Imidazolate Frameworks are the most well-known MOFs subclass consisted of tetrahedrally coordinated transition metal, like  $\text{Zn}^{2+}$ ,  $\text{Co}^{2+}$  and 2-methylimidazole, used as organic linker. They are characterized by aluminosilicate structure with M-Im-M (M: Co or Zn and Im: ditopic or functionalized imidazolate) bridges with bond angles of  $145^\circ$  similar to that one of T-O-T (T: Si, Al, P) building units of zeolitic.<sup>104,105</sup> Zeolitic Imidazole Frameworks is a versatile MOF family because changing the metal transition cation and/or functionalizing imidazole moieties over 100 ZIFs networks have been achieved today.<sup>106</sup> ZIF-8 ( $\text{C}_8\text{H}_{10}\text{N}_4\text{Zn}$ ) results in  $\text{ZnN}_4$  clusters organized in sodalite structure with 8 hexagonal and 6 square windows (Figure 9).<sup>107</sup> It has a cubic space group  $I4_3m$ , with lattice parameter of  $16.32 \text{ \AA}$ , characterized by a six-membered ring of  $3.4 \text{ \AA}$  inscribed in a large aperture of  $11.6 \text{ \AA}$ .<sup>104</sup>

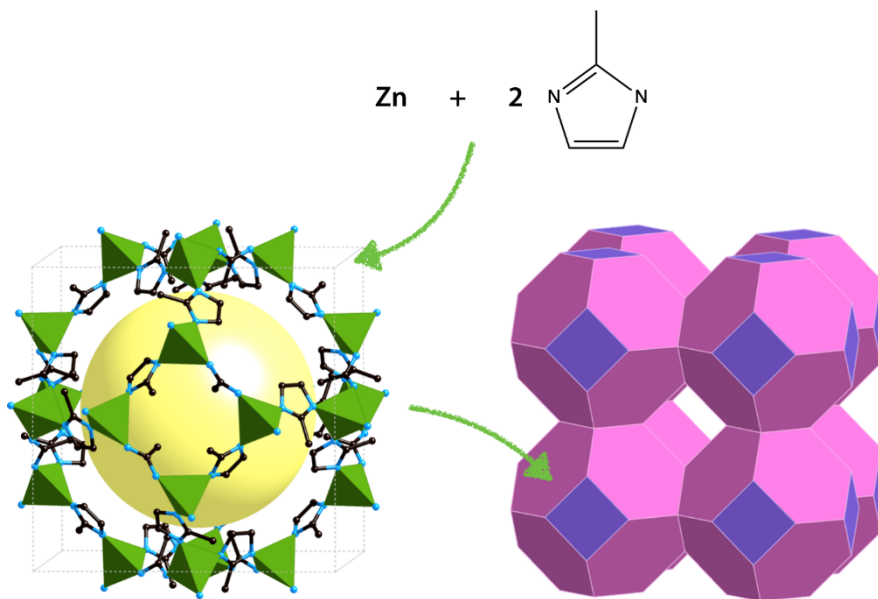


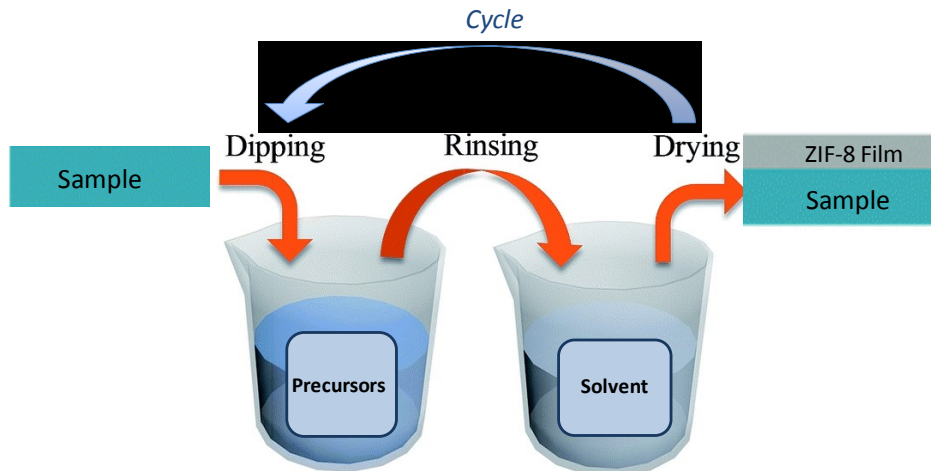
Figure 9: ZIF-8 with sodalite-like structure (from “a big family of MOFs Zeolitic imidazolate frameworks”).

For its permanent porosity and its super-hydrophobic surface ZIF-8 has been applied as sponge-like material for gas separation and adsorption.<sup>108,109</sup> In particular, its pore sizes result suitable for  $\text{CO}_2$  and  $\text{CH}_4$  storage but also for the adsorption of ethanol, acetone and several Volatile Organic Compounds like toluene.<sup>110,111,112</sup> Adsorption properties have been investigated analysing the host-

guest interaction in the post synthesis insertion and the effect of temperature and pressure on structural changes and gas permeability have been also studied.<sup>113</sup>

ZIF-8 being a sturdily built material, guarantee a high thermal stability, above to 500° C, although it has a very low stability under pressure. It has good chemical stability in acid and basic solutions. For this reason, ZIF-8 have been employed as heterogeneous catalyst for Knoevenagel condensation/oxidation reactions or Friedel-Crafts acylation.<sup>114,115</sup>

ZIF-8 synthesis results quite simply with respect to other MOFs and several examples of ZIF-8 powders have been obtained with solvothermal method. Synthesis' parameters like inorganic precursor, solvent, additive presence and reaction times influence the morphology, crystallinity and cavity sizes.<sup>105,116,117,118</sup> It has been proved that the imidazole deprotonation is the key step of ZIF-8 formation and the basicity of the solvent or of possible additives in solution play a crucial role in the reaction kinetics and crystallization rate.<sup>119</sup> Particularly interesting is the development of ZIF-8 films or membranes to carry out porous coating with large surface area and therefore, to assembly ZIF-8 in integrated micro-electronic devices to obtain ZIF-8-coated electrode. Electrochemical, lithographic, and atomic layer depositions have been adopted as synthetic routes to obtain ZIF-8 films.<sup>120,121,122</sup> However, ALD techniques involve high temperatures and, electrochemical methods result complex due to the required several process steps and post-synthetic treatments. For this reason, direct growth of ZIF-8 from solution on pre- or not functionalized surface have been implemented in order to guarantee facile, fast and low-cost protocols. In particular, layer by layer deposition (LBL) and sequential one pot methods (SOP) consisting of dipping the substrate into separated or mixed solution of precursors respectively, can be used to optimize the growth of homogenous ZIF-8 film promoting heterogenous nucleation and can guarantee an accurate thickness control through cycle processes (Scheme 5).<sup>98,123,113</sup> SiO<sub>2</sub>, glass, Cu, Al<sub>2</sub>O<sub>3</sub>, were functionalized with ZIF-8 films in order to increase their surface area improving photocatalytic or sensing activity.<sup>117,124,125</sup>



*Scheme 5: Scheme of SOP synthesis of ZIF-8 film.*

### 1.2.3 Materials of Institute Lavoisier (MIL)

Carboxylate-based MOFs result attractive materials due to their open flexible frameworks. The combination of trivalent metal centres (such as vanadium, chromium, iron, aluminium, gallium, indium, ruthenium and manganese) with carboxylate ligands results in MIL (Material of Institute Lavoisier) architectures, which are more complex than the zeolitic structure and different for surface area and cavity size.<sup>126</sup> MILs are characterized by an excellent thermal and chemical stability and present a flexible tunable structure too.<sup>127</sup> They offer a dynamic response toward external stimuli (solvent, gas adsorption, light and electrical field) in terms of shape, pore size and structural evolution. MIL-type topologies like MIL-53, MIL-68, MIL-100, MIL-47, MIL-101 and MIL-88 have been shaped from carboxylate bridge and mainly  $\text{Cr}^{3+}$  or  $\text{Al}^{3+}$ , less from  $\text{Fe}^{3+}$  centres.<sup>128,129</sup> Fe-based MOFs represent promising materials for environmental pollution since iron is an earth-abundant and environmentally friendly metal. Fe-MILs can be obtained through a low-cost synthesis and thanks to the presence of Fe-O clusters guarantees an intense visible absorption, particularly desirable in photocatalysis field. Fe-based MILs can be employed in energy storage field too.<sup>130,131</sup> Thanks to its intrinsic porosity, thermal stability and redox-active organic-inorganic sites, Fe-MIL-101 results a promising electrode material, whose electrochemical performances are strongly dependent on the synthetic conditions and on the coupling with carbon and/or adhesive materials.<sup>132,133</sup> In addition, Fe-based MIL, such as Fe-MIL-88, are often used as template to achieve

iron oxide, widely proposed as anode of sodium and lithium ion batteries.<sup>134,135</sup> Among all MIL topology, MIL-101 and MIL-88 are framework isomers shaped from the same precursors but with different connectivity. MIL-101 is a cubic Fd3m system characterized by a three-dimensional super-tetrahedra (ST) structure, shaped from inorganic trimers and 1,4-benzene dicarboxylates, results in a mesoporous network with large cell volume ( $702\,000\text{ \AA}^3$ ) and hexagonal windows of 16 and 34 Å, accessible through pentagonal aperture of 12 and 16 Å respectively (Figure10).<sup>136, 137</sup>

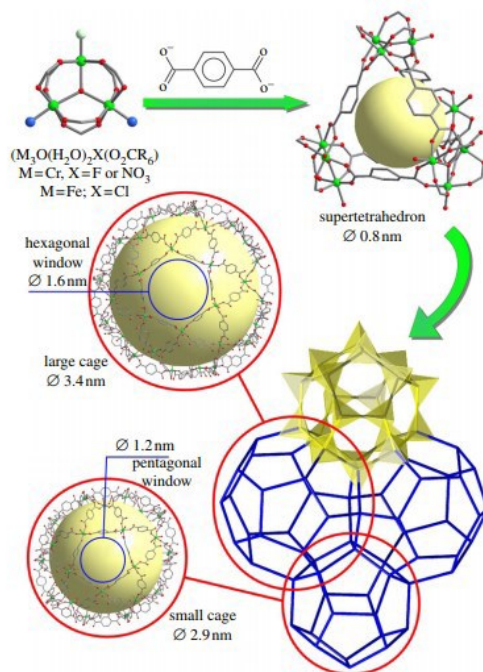


Figure 10: MIL-101 structure.<sup>136</sup>

MIL-88 network built up from trimers of  $M_3O$  octahedra connected by 1,4-benzene dicarboxylate anions (MIL-88-B) arranged in *acs-net* (aligned corner sharing) is a hexagonal P63mmc system featured of 1D microporous tunnels connected by bipyramidal cages with unit cell volume of  $1153\text{ \AA}^3$  (Figure 11).<sup>138,139</sup>

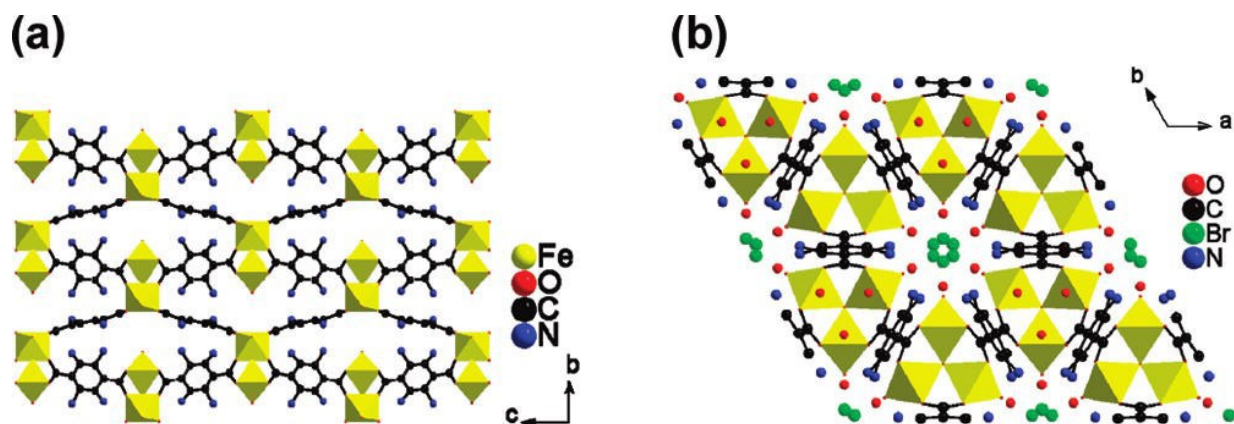


Figure 11: MIL-88 structure along a (a) and c axis (b).<sup>138</sup>

MIL-88 and MIL-101 are polymorphs in equilibrium whereby the rigid MIL-101 structure forms faster and represents the kinetic isomer whereas the flexible MIL-88 topology is more stable and favoured under thermodynamic control.<sup>136</sup> The polymorphic phase transitions affect the structure-property relationship since a specific connectivity involves characteristic physical properties. The stereoselectivity is strongly influenced by synthesis conditions and the formation of MIL-88 or MIL-101 can be achieved by modulating temperature, reaction time and pH. In addition, the choice of solvent, the presence of additives in the reaction media and the concentration of metal precursors represent other parameters which affect the phase formation. It has been proved that the reaction time involves structural evolution and the addition of acid additives, like HCl or glacial acetic acid drives the deprotonation of carboxylic linkers by controlling the crystal sizes and the crystallinity.<sup>140,141,142</sup> Structural and chemical-physical properties of MIL-101 can be influenced by the presence of amino-functionalization. The amino group, that can be also introduced into MIL network through post-synthetic modifications, can act as active interaction site and can significantly affect the host-guest chemistry, which is a point of great importance in research areas such as gas recognition and catalysis.<sup>143</sup>

Several examples of amino-functionalized MIL-101 and MIL-88 (Fe-based) crystals have been obtained through microwave-assisted and solvothermal route in presence of polymer and/or stabilizing agents and through hydro-thermal synthesis using long reaction times (12-24 hours). On the other hand, there are few examples of MIL films, carried out through coating techniques like Langmuir Blodgett and spin-coating which are usually polymer-assisted to optimize the surface

adhesion. Thin films of MIL-88 and MIL-101 have been recently synthesized on self - assembled monolayer of 16-mercaptohexadecanoic acid on Au surface by direct growth from solution. Though the SAMs surface modification allowed to obtain oriented MIL film, more reaction steps and very long immersion time were needed (from 4 to 11 days).<sup>144,145,146,147,140</sup> MOF films represent interesting coating materials since with their complex intrinsic structure allow to develop integrated multilayers devices with tunable properties. Therefore, it would be necessary the implementation of new synthetic routes which through fast and facile protocols lead to MIL layers with specific morphology and featuring.

## **REFERENCES**

---

- (1) Scrosati, B.; Garche, J. Lithium Batteries: Status, Prospects and Future. *J. Power Sources* **2010**, *195*, 2419–2430.
- (2) Teki, R.; Krishnan, R.; Parker, T. C.; Lu, T. M.; Datta, M. K.; Kumta, P. N.; Koratkar, N. Nanostructured Silicon Anodes for Lithium Ion Rechargeable Batteries. *Small* **2009**, *5*, 2236–2242.
- (3) <http://www.cei.washington.edu/education/science-of-solar/battery-technology>
- (4) Sasaki, T.; Ukyo, Y.; Novák, P. Memory Effect in a Lithium-Ion Battery. *Nat. Mater.* **2013**, *12*, 569–575.
- (5) Bock, D. C.; Marschlok, A. C.; Takeuchi, K. J.; Takeuchi, E. S. Batteries Used to Power Implantable Biomedical Devices. *Electrochim. Acta* **2012**, *84*, 155–164.
- (6) Wang, Y.; Liu, B.; Li, Q.; Cartmell, S.; Ferrara, S.; Deng, Z. D.; Xiao, J. Lithium and Lithium Ion Batteries for Applications in Microelectronic Devices: A Review. *J. Power Sources* **2015**, *286*, 330–345.
- (7) <http://news.panasonic.com/press/news/official.data/data.dir/2014/10/en141003-2/en141003-2.html>.
- (8) Wang, Y.; Cartmell, S.; Li, Q.; Xiao, J.; Li, H.; Deng, Z. D.; Zhang, J. G. A Reliable Sealing Method for Microbatteries. *J. Power Sources* **2017**, *341*, 443–447.
- (9) Marom, R.; Amalraj, S. F.; Leifer, N.; Jacob, D.; Aurbach, D. A Review of Advanced and Practical Lithium Battery Materials. *J. Mater. Chem.* **2011**, *21*, 9938–9954.
- (10) Roy, P.; Srivastava, S. K. Nanostructured Anode Materials for Lithium Ion Batteries. *J. Mater. Chem. A* **2015**, *3*, 2454–2484.
- (11) Goodenough, J.B. Evolution of strategies for modern rechargeable batteries, *Accounts of chemical research*, **2012**, *5*, 1053-1061

- 
- (12) Liu, D.; Cao, G. Engineering Nanostructured Electrodes and Fabrication of Film Electrodes for Efficient Lithium Ion Intercalation. *Energy Environ. Sci.* **2010**, *3*, 1218–1237.
- (13) Hassoun, J.; Bonaccorso, F.; Agostini, M.; Angelucci, M.; Betti, M. G.; Cingolani, R.; Gemmi, M.; Mariani, C.; Panero, S.; Pellegrini, V.; Scrosati, B. An Advanced Lithium-Ion Battery Based on a Graphene Anode and a Lithium Iron Phosphate Cathode. *Nano Lett.* **2014**, *14*, 4901–4906.
- (14 ) Zheng, J.; Lochala, J. A.; Kwok, A.; Deng, Z. D.; Xiao, J. Research Progress towards Understanding the Unique Interfaces between Concentrated Electrolytes and Electrodes for Energy Storage Applications. *Adv. Sci.* **2017**, *4*, 1–19.
- (15 ) Roselin, L. S.; Juang, R. S.; Hsieh, C. Te; Sagadevan, S.; Umar, A.; Selvin, R.; Hegazy, H. H. Recent Advances and Perspectives of Carbon-Based Nanostructures as Anode Materials for Li-Ion Batteries. *Materials* **2019**, *12* .
- (16) Malmgren, S.; Ciosek, K.; Lindblad, R.; Plogmaker, S.; Kühn, J.; Rensmo, H.; Edström, K.; Hahlin, M. Consequences of Air Exposure on the Lithiated Graphite SEI. *Electrochim. Acta* **2013**, *105*, 83–91.
- (17 ) Wang, J.; Xu, T.; Huang, X.; Li, H.; Ma, T. Recent Progress of Silicon Composites as Anode Materials for Secondary Batteries. *RSC Adv.* **2016**, *6*, 87778–87790.
- (18 ) Chabre, Y. Chemical Physics of Intercalation II. *Phys. Chem. Finite Syst. From Clust. to Cryst.* **1993**, *305*, 181.
- (19 ) Huggins, R. A. Alternative Materials for Negative Electrodes in Lithium Systems. *Solid State Ionics* **2002**, *152*, 61–68.
- (20 ) Park, C. M.; Kim, J. H.; Kim, H.; Sohn, H. J. Li-Alloy Based Anode Materials for Li Secondary Batteries. *Chem. Soc. Rev.* **2010**, *39*, 3115–3141.
- (21) Spinner, N.; Zhang, L.; Mustain, W. E. Investigation of Metal Oxide Anode Degradation in Lithium-Ion Batteries via Identical-Location TEM. *J. Mater. Chem. A* **2014**, *2*, 1627–1630.
- (22) Osiak, M.; Geaney, H.; Armstrong, E.; O’Dwyer, C. Structuring Materials for Lithium-Ion Batteries: Advancements in Nanomaterial Structure, Composition, and Defined Assembly on Cell Performance. *J. Mater. Chem. A* **2014**, *2*, 9433.



- 
- (23) Xu, W.; Wang, J.; Ding, F.; Chen, X.; Nasybulin, E.; Zhang, Y.; Zhang, J. G. Lithium Metal Anodes for Rechargeable Batteries. *Energy Environ. Sci.* **2014**, *7*, 513–537.
- (24) Ma, D.; Cao, Z.; Hu, A. Si-Based Anode Materials for Li-Ion Batteries: A Mini Review. *Nano-Micro Lett.* **2014**, *6*, 347–358.
- (25) Wen, C. G.; Huggins, R.A. Chemical Diffusion in Intermediate Phases in the Lithium-Silicon System Department of Materials Science and Engineering. *J. Solid State Chem.* **1981**, *37*, 271–278.
- (26) Obrovac, M. N.; Christensen, L. Structural Changes in Silicon Anodes during Lithium Insertion/Extraction. *Electrochem. Solid-State Lett.* **2004**, *7*, A93-A96.
- (27) Li, J.; Dahn, J. R. An in Situ X-Ray Diffraction Study of the Reaction of Li with Crystalline Si. *J. Electrochem. Soc.* **2007**, *154*, 156–161.
- (28) Chan, C. K.; Peng, H.; Liu, G.; Mc Ilwrath, K.; Zhang, X. F.; Huggins, R. A.; Cui, Y. High-Performance Lithium Battery Anodes Using Silicon Nanowires. *Mater. Sustain. Energy A Collect. Peer-Reviewed Res. Rev. Artic. from Nat. Publ. Gr.* **2010**, 187–191.
- (29) Ryu, J. H.; Kim, J. W.; Sung, Y. E.; Oh, S. M. Failure Modes of Silicon Powder Negative Electrode in Lithium Secondary Batteries. *Electrochem. Solid-State Lett.* **2004**, *7*, 306–309.
- (30) Oumellal, Y.; Delpuech, N.; Mazouzi, D.; Dupré, N.; Gaubicher, J.; Moreau, P.; Soudan, P.; Lestriez, B.; Guyomard, D. The Failure Mechanism of Nano-Sized Si-Based Negative Electrodes for Lithium Ion Batteries. *J. Mater. Chem.* **2011**, *21*, 6201–6208.
- (31) Etienne, A.; Tranchot, A.; Douillard, T.; Idrissi, H.; Maire, E.; Roué, L. Evolution of the 3D Microstructure of a Si-Based Electrode for Li-Ion Batteries Investigated by FIB/SEM Tomography. *J. Electrochem. Soc.* **2016**, *163*, A1550–A1559.
- (32) Su, X.; Wu, Q.; Li, J.; Xiao, X.; Lott, A.; Lu, W.; Sheldon, B. W.; Wu, J. Silicon-based nanomaterials for lithium-ion battery: a review. *Adv. Energy Mater.* **2014**, *4*, 1300882- 1300905.
- (33) Rahman, M. A.; Song, G.; Bhatt, A. I.; Wong, Y. C.; Wen, C. Nanostructured Silicon Anodes for High-Performance Lithium-Ion Batteries. *Adv. Funct. Mater.* **2016**, *26*, 647–678.
- (34) Liu, X. H.; Zhong, L.; Huang, S.; Mao, S. X.; Zhu, T.; Huang, J. Y. Size-Dependent Fracture of Silicon Nanoparticles during Lithiation. *ACS Nano* **2012**, *6*, 1522–1531.

- 
- (35) Wang, W.; Favors, Z.; Ionescu, R.; Ye, R.; Bay, H. H.; Ozkan, M.; Ozkan, C. S. Monodisperse Porous Silicon Spheres as Anode Materials for Lithium Ion Batteries. *Sci. Rep.* **2015**, *5*, 2–7.
- (36) Li, J. Y.; Xu, Q.; Li, G.; Yin, Y. X.; Wan, L. J.; Guo, Y. G. Research Progress Regarding Si-Based Anode Materials towards Practical Application in High Energy Density Li-Ion Batteries. *Mater. Chem. Front.* **2017**, *1*, 1691–1708.
- (37) Wu, L.; Yang, J.; Zhou, X.; Zhang, M.; Ren, Y.; Nie, Y. Silicon Nanoparticles Embedded in a Porous Carbon Matrix as a High-Performance Anode for Lithium-Ion Batteries. *J. Mater. Chem. A* **2016**, *4*, 11381–11387.
- (38) Park, J.; Kim, G. P.; Nam, I.; Park, S.; Yi, J. One-Pot Synthesis of Silicon Nanoparticles Trapped in Ordered Mesoporous Carbon for Use as an Anode Material in Lithium-Ion Batteries. *Nanotechnology* **2013**, *24*, 025602-025608.
- (39) Liu, N.; Wu, H.; McDowell, M. T.; Yao, Y.; Wang, C.; Cui, Y. A Yolk-Shell Design for Stabilized and Scalable. *Nano Lett.* **2012**, *12*, 3315–3321.
- (40) Gueon, D.; Kang, D. Y.; Kim, J. S.; Kim, T. Y.; Lee, J. K.; Moon, J. H. Si Nanoparticles-Nested Inverse Opal Carbon Supports for Highly Stable Lithium-Ion Battery Anodes. *J. Mater. Chem. A* **2015**, *3*, 23684–23689.
- (41) Ruffo, R.; Hong, S. S.; Chan, C. K.; Huggins, R. A.; Cui, Y. Impedance Analysis of Silicon Nanowire Lithium Ion Battery Anodes. *J. Phys. Chem. C* **2009**, *113*, 11390–11398.
- (42) Peng, K.; Jie, J.; Zhang, W.; Lee, S. T. Silicon Nanowires for Rechargeable Lithium-Ion Battery Anodes. *Appl. Phys. Lett.* **2008**, *93*, 1–4.
- (43) Nguyen, H. T.; Zamfir, M. R.; Duong, L. D.; Lee, Y. H.; Bondavalli, P.; Pribat, D. Alumina-Coated Silicon-Based Nanowire Arrays for High Quality Li-Ion Battery Anodes. *J. Mater. Chem.* **2012**, *22*, 24618–24626.
- (44) Liu, X. H.; Zheng, H.; Zhong, L.; Huang, S.; Karki, K.; Zhang, L. Q.; Liu, Y.; Kushima, A.; Liang, W. T.; Wang, J. W.; Cho, J. H.; Epstein, E.; Dayeh, S. A.; Picraux, S. T.; Zhu, T.; Li, J.; Sullivan, J. P.; Cumings, J.; Wang, C.; Mao, S. X.; Ye, Z. Z.; Zhang, S.; Huang, J. Y. Anisotropic Swelling and Fracture of Silicon Nanowires during Lithiation. *Nano Lett.* **2011**, *11*, 3312–3318.

- 
- (45) Yu, X.; Xue, F.; Huang, H.; Liu, C.; Yu, J.; Sun, Y.; Dong, X.; Cao, G.; Jung, Y. Synthesis and Electrochemical Properties of Silicon Nanosheets by DC Arc Discharge for Lithium-Ion Batteries. *Nanoscale* **2014**, *6*, 6860–6865.
- (46) Yoo, J. K.; Kim, J.; Jung, Y. S.; Kang, K. Scalable Fabrication of Silicon Nanotubes and Their Application to Energy Storage. *Adv. Mater.* **2012**, *24*, 5452–5456.
- (47) Wu, H.; Chan, G.; Choi, J. W.; Ryu, I.; Yao, Y.; Mcdowell, M. T.; Lee, S. W.; Jackson, A.; Yang, Y.; Hu, L.; Cui, Y. Stable Cycling of Double-Walled Silicon Nanotube Battery Anodes through Solid-Electrolyte Interphase Control. *Nat. Nanotechnol.* **2012**, *7*, 310–315.
- (48) Park, M.H.; Kim, M. G.; Joo, J.; Kim, K.; Kim, J.; Ahn, S.; Cui, Y.; Cho, J. Silicon Nanotube Battery Anodes. *Nano letters* **2009**, *9*, 3844–3847.
- (49) Netz, A.; Huggins, R. A.; Weppner, W. The Formation and Properties of Amorphous Silicon as Negative Electrode Reactant in Lithium Systems. *J. Power Sources* **2003**, *119–121*, 95–100.
- (50) Mukanova, A.; Jetybayeva, A.; Myung, S. T.; Kim, S. S.; Bakenov, Z. A Mini-Review on the Development of Si-Based Thin Film Anodes for Li-Ion Batteries. *Mater. Today Energy* **2018**, *9*, 49–66.
- (51) He, Y.; Yu, X.; Wang, Y.; Li, H.; Huang, X. Alumina-Coated Patterned Amorphous Silicon as the Anode for a Lithium-Ion Battery with High Coulombic Efficiency. *Adv. Mater.* **2011**, *23*, 4938–4941.
- (52) Chen, L. B.; Xie, J. Y.; Yu, H. C.; Wang, T. H. An Amorphous Si Thin Film Anode with High Capacity and Long Cycling Life for Lithium Ion Batteries. *J. Appl. Electrochem.* **2009**, *39*, 1157–1162.
- (53) Liu, Y.; Chen, B.; Cao, F.; Chan, H. L. W.; Zhao, X.; Yuan, J. One-Pot Synthesis of Three-Dimensional Silver-Embedded Porous Silicon Micronparticles for Lithium-Ion Batteries. *J. Mater. Chem.* **2011**, *21*, 17083–17086.
- (54) Kim, H.; Han, B.; Choo, J.; Cho, J. Three-Dimensional Porous Silicon Particles for Use in High-Performance Lithium Secondary Batteries. *Angew. Chemie - Int. Ed.* **2008**, *47*, 10151–10154.

- 
- (55) Jia, H.; Gao, P.; Yang, J.; Wang, J.; Nuli, Y.; Yang, Z. Novel Three-Dimensional Mesoporous Silicon for High Power Lithium-Ion Battery Anode Material. *Adv. Energy Mater.* **2011**, *1*, 1036–1039.
- (56) Gao, P.; Jia, H.; Yang, J.; Nuli, Y.; Wang, J.; Chen, J. Three-Dimensional Porous Silicon-MWNT Heterostructure with Superior Lithium Storage Performance. *Phys. Chem. Chem. Phys.* **2011**, *13*, 20108–20111.
- (57) Domi, Y.; Usui, H.; Shimizu, M.; Kakimoto, Y.; Sakaguchi, H. Effect of Phosphorus-Doping on Electrochemical Performance of Silicon Negative Electrodes in Lithium-Ion Batteries. *ACS Appl. Mater. Interfaces* **2016**, *8*, 7125–7132.
- (58) Wen, Z.; Tian, F. Cu-Doped Silicon Film as Anode for Lithium Ion Batteries Prepared by Ion-Beam Sputtering. *Int. J. Electrochem. Sci.* **2013**, *8*, 10129–10137.
- (59) Legrain, F.; Manzhos, S. Aluminum Doping Improves the Energetics of Lithium, Sodium, and Magnesium Storage in Silicon: A First-Principles Study. *J. Power Sources* **2015**, *274*, 65–70.
- (60) McSweeney, W.; Lotty, O.; Glynn, C.; Geaney, H.; Holmes, J. D.; O'Dwyer, C. The Influence of Carrier Density and Doping Type on Lithium Insertion and Extraction Processes at Silicon Surfaces. *Electrochim. Acta* **2014**, *135*, 356–367.
- (61) Long, B. R.; Chan, M. K. Y.; Greeley, J. P.; Gewirth, A. A. Dopant Modulated Li Insertion in Si for Battery Anodes: Theory and Experiment. *J. Phys. Chem. C* **2011**, *115*, 18916–18921.
- (62) Kim, J. S.; Choi, W.; Byun, D.; Lee, J. K. Electrochemical Characteristics of Phosphorus Doped Silicon for the Anode Material of Lithium Secondary Batteries. *Solid State Ionics* **2012**, *212*, 43–46.
- (63) Jung, C. Y.; Koo, J. B.; Jang, B. Y.; Kim, J. S.; Lee, J. S.; Kim, S. S.; Han, M. H. Effects of Phosphorous Incorporation on the Microstructure of Si Nanoparticles as an Anode Material for Lithium-Ion Battery. *Thin Solid Films* **2015**, *587*, 142–149.
- (64) Deng, C.; Lau, M. L.; Barkholtz, H. M.; Xu, H.; Parrish, R.; Xu, M.; Xu, T.; Liu, Y.; Wang, H.; Connell, J. G.; Smith, K. A.; Xiong, H. Amorphous Boron Nanorod as an Anode Material for Lithium-Ion Batteries at Room Temperature. *Nanoscale* **2017**, *9*, 10757–10763.

- 
- (65) Ricco, R.; Pfeiffer, C.; Sumida, K.; Sumbly, C. J.; Falcaro, P.; Furukawa, S.; Champness, N. R.; Doonan, C. J. Emerging Applications of Metal–organic Frameworks. *CrystEngComm* **2016**, *18*, 6532–6542.
- (66) Dhakshinamoorthy, A.; Garcia, H. Catalysis by Metal Nanoparticles Embedded on Metal–Organic Frameworks. *Chem. Soc. Rev.* **2012**, *41*, 5262–5284.
- (67) Zhang, W. X.; Liao, P. Q.; Lin, R. B.; Wei, Y. S.; Zeng, M. H.; Chen, X. M. Metal Cluster-Based Functional Porous Coordination Polymers. *Coord. Chem. Rev.* **2015**, *293–294*, 263–278.
- (68) Almeida Paz, F. A.; Klinowski, J.; Vilela, S. M. F.; Tomé, J. P. C.; Cavaleiro, J. A. S.; Rocha, J. Ligand Design for Functional Metal–Organic Frameworks. *Chem. Soc. Rev.* **2012**, *41*, 1088–1110.
- (69) Lin, Z. J.; Lü, J.; Hong, M.; Cao, R. Metal–Organic Frameworks Based on Flexible Ligands (FL-MOFs): Structures and Applications. *Chem. Soc. Rev.* **2014**, *43*, 5867–5895.
- (70) Cui, Y.; Li, B.; He, H.; Zhou, W.; Chen, B.; Qian, G. Metal – Organic Frameworks as Platforms for Functional Materials. **2016**.
- (71) Tanabe, K. K.; Cohen, S. M. Postsynthetic Modification of Metal–organic Frameworks—a Progress Report. *Chem. Soc. Rev.* **2011**, *40*, 498–519.
- (72) Zhao, R.; Liang, Z.; Zou, R.; Xu, Q. Metal–Organic Frameworks for Batteries. *Joule* **2018**, *2*, 2235–2259.
- (73) Zhou, Y.; Wu, M.; Luo, Y.; Pang, B.; Su, X.; Zhou, M.; Han, L. Redox Active Azo-Based Metal–Organic Frameworks as Anode Materials for Lithium–Ion Batteries. *New J. Chem.* **2019**, *43*, 1710–1715.
- (74) Hameed, A. S.; Reddy, M. V.; Sarkar, N.; Chowdari, B. V. R.; Vittal, J. J. Synthesis and Electrochemical Investigation of Novel Phosphite Based Layered Cathodes for Li–Ion Batteries. *RSC Adv.* **2015**, *5*, 60630–60637.
- (75) Dühren, S.; Nölle, R.; Wrogemann, J.; Winter, M.; Placke, T. Reversible Anion Storage in a Metal–Organic Framework for Dual–Ion Battery Systems. *J. Electrochem. Soc.* **2019**, *166*, A5474–A5482.

- 
- (76) Nie, P.; Shen, L.; Pang, G.; Zhu, Y.; Xu, G.; Qing, Y.; Dou, H.; Zhang, X. Flexible Metal-Organic Frameworks as Superior Cathodes for Rechargeable Sodium-Ion Batteries. *J. Mater. Chem. A* **2015**, *3*, 16590–16597.
- (77) Peng, Z.; Yi, X.; Liu, Z.; Shang, J.; Wang, D. Triphenylamine-Based Metal-Organic Frameworks as Cathode Materials in Lithium-Ion Batteries with Coexistence of Redox Active Sites, High Working Voltage, and High Rate Stability. *ACS Appl. Mater. Interfaces* **2016**, *8*, 14578–14585.
- (78) Lou, X.; Hu, X.; Li, C.; Ning, Y.; Chen, Q.; Shen, M.; Hu, B. Room-Temperature Synthesis of a Cobalt 2,3,5,6-Tetrafluoroterephthalic Coordination Polymer with Enhanced Capacity and Cycling Stability for Lithium Batteries. *New J. Chem.* **2017**, *41*, 1813–1819.
- (79) Liu, Q.; Yu, L.; Wang, Y.; Ji, Y.; Horvat, J.; Cheng, M. L.; Jia, X.; Wang, G. Manganese-Based Layered Coordination Polymer: Synthesis, Structural Characterization, Magnetic Property, and Electrochemical Performance in Lithium-Ion Batteries. *Inorg. Chem.* **2013**, *52*, 2817–2822.
- (80) Lin, Y.; Zhang, Q.; Zhao, C.; Li, H.; Kong, C.; Shen, C.; Chen, L. An exceptionally stable functionalized metal-organic framework for lithium storage, *Chemical Communications*, **2015**, *51* (4), 697-699
- (81) Amos, P. I.; Hitler, L.; Amusan, O. O.; Akakuru, O. U.; Adeleye, A. T.; Magu, T. O.; Anumah, A.; Hamzat, A. T. Recent Advances in the Use of Carbonyl Compounds as Active Components in Organic-Based Batteries. *J. Adv. Electrochem* **2018**, *4*, 172–176.
- (82) Ma, Y.; He, J.; Kou, Z.; Elshahawy, A. M.; Hu, Y.; Guan, C.; Li, X.; Wang, J. MOF-Derived Vertically Aligned Mesoporous Co<sub>3</sub>O<sub>4</sub> Nanowires for Ultrahigh Capacity Lithium-Ion Batteries Anodes. *Adv. Mater. Interfaces* **2018**, *5*, 1–7.
- (83) Spinner, N.; Zhang, L.; Mustain, W. E. Investigation of Metal Oxide Anode Degradation in Lithium-Ion Batteries via Identical-Location TEM. *J. Mater. Chem. A* **2014**, *2*, 1627–1630.
- (84) Feng, L.; Han, X.; Su, X.; Pang, B.; Luo, Y.; Hu, F.; Zhou, M.; Tao, K.; Xia, Y. Metal-Organic Frameworks Derived Porous Carbon Coated SiO<sub>2</sub> Composite as Superior Anode Material for Lithium Ion Batteries. *J. Alloys Compd.* **2018**, *765*, 512–519.

- 
- (85) Yap, M. H.; Fow, K. L.; Chen, G. Z. Synthesis and Applications of MOF-Derived Porous Nanostructures. *Green Energy Environ.* **2017**, *2*, 218–245.
- (86) Zhu, K.; Liu, Y.; Liu, J. A Fast Charging/discharging All-Solid-State Lithium Ion Battery Based on PEO-MIL-53(Al)-LiTFSI Thin Film Electrolyte. *RSC Adv.* **2014**, *4*, 42278–42284.
- (87) Wiers, B. M.; Foo, M. L.; Balsara, N. P.; Long, J. R. A Solid Lithium Electrolyte via Addition of Lithium Isopropoxide to a Metal-Organic Framework with Open Metal Sites. *J. Am. Chem. Soc.* **2011**, *133*, 14522–14525.
- (88) Angulakshmi, N.; Nahm, K. S.; Nair, J. R.; Gerbaldi, C.; Bongiovanni, R.; Penazzi, N.; Stephan, A. M. Cycling Profile of MgAl<sub>2</sub>O<sub>4</sub>-Incorporated Composite Electrolytes Composed of PEO and LiPF<sub>6</sub> for Lithium Polymer Batteries. *Electrochim. Acta* **2013**, *90*, 179–185.
- (89) Fujie, K.; Ikeda, R.; Otsubo, K.; Yamada, T.; Kitagawa, H. Lithium Ion Diffusion in a Metal-Organic Framework Mediated by an Ionic Liquid. *Chem. Mater.* **2015**, *27*, 7355–7361.
- (90) Fujie, K.; Otsubo, K.; Ikeda, R.; Yamada, T.; Kitagawa, H. Low Temperature Ionic Conductor: Ionic Liquid Incorporated within a Metal–organic Framework. *Chem. Sci.* **2015**, *6*, 4306–4310.
- (91) Bilal, M.; Adeel, M.; Rasheed, T.; Iqbal, H. M. N. Multifunctional Metal-Organic Frameworks-Based Biocatalytic Platforms: Recent Developments and Future Prospects. *J. Mater. Res. Technol.* **2019**, *8*, 2359–2371.
- (92) Y.R. Lee, J. Kim, W.S. Ahn, Synthesis of metal-organic frameworks: A mini review, *Korean J. Chem. Eng.*, **2013**, *30*, 1667–1680.
- (93) Kwon, H. T.; Jeong, H. K.; Lee, A. S.; An, H. S.; Lee, T.; Jang, E.; Lee, J. S.; Choi, J. Defect-Induced Ripening of Zeolitic-Imidazolate Framework ZIF-8 and Its Implication to Vapor-Phase Membrane Synthesis. *Chem. Commun.* **2016**, *52*, 11669–11672.
- (94) Zhang, C.; Han, C.; Sholl, D. S.; Schmidt, J. R. Computational Characterization of Defects in Metal-Organic Frameworks: Spontaneous and Water-Induced Point Defects in ZIF-8. *J. Phys. Chem. Lett.* **2016**, *7*, 459–464.

- 
- (95) Chernikova, V.; Shekhah, O.; Eddaoudi, M. Advanced Fabrication Method for the Preparation of MOF Thin Films: Liquid-Phase Epitaxy Approach Meets Spin Coating Method. *ACS Appl. Mater. Interfaces* **2016**, *8*, 20459–20464.
- (96) Yoo, Y.; Jeong, H. K. Rapid Fabrication of Metal Organic Framework Thin Films Using Microwave-Induced Thermal Deposition. *Chem. Commun.* **2008**, *21*, 2441–2443.
- (97) Shah, M. N.; Gonzalez, M. A.; McCarthy, M. C.; Jeong, H.-K. An Unconventional Rapid Synthesis of High Performance Metal–Organic Framework Membranes. *Langmuir* **2013**, *29*, 7896–7902.
- (98) Kida, K.; Fujita, K.; Shimada, T.; Tanaka, S.; Miyake, Y. Layer-by-Layer Aqueous Rapid Synthesis of ZIF-8 Films on a Reactive Surface. *Dalt. Trans.* **2013**, *42* (31), 11128–11135.
- (99) Heinke, L.; Tu, M.; Wannapaiboon, S.; Fischer, R. A.; Wöll, C. Surface-Mounted Metal–Organic Frameworks for Applications in Sensing and Separation. *Microporous Mesoporous Mater.* **2014**, *216*, 200–215.
- (100) Shekhah, O.; Wang, H.; Kowarik, S.; Schreiber, F.; Paulus, M.; Tolan, M.; Sternemann, C.; Evers, F.; Zacher, D.; Fischer, R. A.; Wo, C.; Uni, V. Ja076210U.Pdf. **2007**, 15118–15119.
- (101) Shekhah, O.; Eddaoudi, M. The Liquid Phase Epitaxy Method for the Construction of Oriented ZIF-8 Thin Films with Controlled Growth on Functionalized Surfaces. *Chem. Commun.* **2013**, *49*, 10079–10081.
- (102) Wu, M.; Ye, H.; Zhao, F.; Zeng, B. High-Quality Metal–Organic Framework ZIF-8 Membrane Supported on Electrodeposited ZnO/2-Methylimidazole Nanocomposite: Efficient Adsorbent for the Enrichment of Acidic Drugs. *Sci. Rep.* **2017**, *7*, 39778–39786.
- (103) Muller, M. Self-Assembled Monolayers as Templates for Metal–Organic Framework Thin-Films-Preparation and Applications.
- (104) Venna, S. R.; Jasinski, J. B.; Carreon, M. A. Structural Evolution of Zeolitic Imidazolate Framework-8. *J. Am. Chem. Soc.* **2010**, *132*, 18030–18033.
- (105) Lai, L. S.; Yeong, Y. F.; Lau, K. K.; Shariff, A. M. Effect of Synthesis Parameters on the Formation of ZIF-8 under Microwave-Assisted Solvothermal. *Procedia Eng.* **2016**, *148*, 35–42.



---

(106) Tan, J. C.; Bennett, T. D.; Cheetham, A. K. Chemical Structure, Network Topology, and Porosity Effects on the Mechanical Properties of Zeolitic Imidazolate Frameworks. *Proc. Natl. Acad. Sci. U. S. A.* **2010**, *107*, 9938–9943.

(107) <http://crystallmaker.com>

(108) Tan, J. C.; Bennett, T. D.; Cheetham, A. K. Chemical Structure, Network Topology, and Porosity Effects on the Mechanical Properties of Zeolitic Imidazolate Frameworks. *Proc. Natl. Acad. Sci. U. S. A.* **2010**, *107*, 9938–9943.

(109) Ortiz, A. U.; Freitas, A. P.; Boutin, A.; Fuchs, A. H.; Coudert, F. X. What Makes Zeolitic Imidazolate Frameworks Hydrophobic or Hydrophilic: The Impact of Geometry and Functionalization on Water Adsorption. *Phys. Chem. Chem. Phys.* **2014**, *16*, 9940–9949.

(110) McEwen, J.; Hayman, J. D.; Ozgur Yazaydin, A. A Comparative Study of CO<sub>2</sub>, CH<sub>4</sub> and N<sub>2</sub> Adsorption in ZIF-8, Zeolite-13X and BPL Activated Carbon. *Chem. Phys.* **2013**, *412*, 72–76.

(111) Zhang, K.; Lively, R. P.; Dose, M. E.; Brown, A. J.; Zhang, C.; Chung, J.; Nair, S.; Koros, W. J.; Chance, R. R. Alcohol and Water Adsorption in Zeolitic Imidazolate Frameworks. *Chem. Commun.* **2013**, *49*, 3245–3247.

(112) Chu, F.; Zheng, Y.; Wen, B.; Zhou, L.; Yan, J.; Chen, Y. Adsorption of Toluene with Water on Zeolitic Imidazolate Framework-8/graphene Oxide Hybrid Nanocomposites in a Humid Atmosphere. *RSC Adv.* **2018**, *8*, 2426–2432.

(113) Monforte, F.; Mannino, G.; Alberti, A.; Smecca, E.; Italia, M.; Motta, A.; Tudisco, C.; Condorelli, G. G. Heterogeneous Growth of Continuous ZIF-8 Films on Low-Temperature Amorphous Silicon. *Appl. Surf. Sci.* **2018**, *473* (September 2018), 182–189.

(114) Tran, U. PN.; Le, K. KA.; Phan, N. TS. 20. Expanding applications of metal organic frameworks: zeolite imidazolate framework ZIF-8 as an efficient heterogeneous catalyst for the Knoevenagel reaction. *ACS Catalysis*, **2011**, *1*, 120–127.

(115) Lee, Y. R.; Do, X. H.; Park S. B., Hwang, S. S.; Baek, K. Y. Dual-Functionalized ZIF-8 as an Efficient Acid-Base Bifunctional Catalyst for the One-Pot Tandem Reaction. *Catalysis Today* **2019**, *10.1016/j.cattod.2019.06.076*.

- 
- (116) Maya, F.; Palomino Cabello, C.; Clavijo, S.; Estela, J. M.; Cerdà, V.; Turnes Palomino, G. Zeolitic Imidazolate Framework Dispersions for the Fast and Highly Efficient Extraction of Organic Micropollutants. *RSC Adv.* **2015**, *5*, 28203–28210.
- (117) Papporello, R. L.; Miró, E. E.; Zamaro, J. M. Secondary Growth of ZIF-8 Films onto Copper-Based Foils. Insight into Surface Interactions. *Microporous Mesoporous Mater.* **2015**, *211*, 64–72.
- (118) Cravillon, J.; Nayuk, R.; Springer, S.; Feldhoff, A.; Huber, K.; Wiebcke, M. Controlling Zeolitic Imidazolate Framework Nano- and Microcrystal Formation: Insight into Crystal Growth by Time-Resolved in Situ Static Light Scattering. *Chem. Mater.* **2011**, *23*, 2130–2141.
- (119) Jian, M.; Liu, B.; Liu, R.; Qu, J.; Wang, H.; Zhang, X. Water-Based Synthesis of Zeolitic Imidazolate Framework-8 with High Morphology Level at Room Temperature. *RSC Adv.* **2015**, *5*, 48433–48441.
- (120) Worrall, S. D.; Mann, H.; Rogers, A.; Bissett, M. A.; Attfield, M. P.; Dryfe, R. A. W. Electrochemical Deposition of Zeolitic Imidazolate Framework Electrode Coatings for Supercapacitor Electrodes. *Electrochim. Acta* **2016**, *197*, 228–240.
- (121) Drobek, M.; Bechelany, M.; Vallicari, C.; Abou Chaaya, A.; Charmette, C.; Salvador-Levehang, C.; Miele, P.; Julbe, A. An Innovative Approach for the Preparation of Confined ZIF-8 Membranes by Conversion of ZnO ALD Layers. *J. Memb. Sci.* **2015**, *475*, 39–46.
- (122) Dalstein, O.; Ceratti, D. R.; Boissière, C.; Grosso, D.; Cattoni, A.; Faustini, M. Nanoimprinted, Submicrometric, MOF-Based 2D Photonic Structures: Toward Easy Selective Vapors Sensing by a Smartphone Camera. *Adv. Funct. Mater.* **2016**, *26*, 81–90.
- (123) Tuninetti, J. S.; Rafti, M.; Azzaroni, O. Early Stages of ZIF-8 Film Growth: The Enhancement Effect of Primers Exposing Sulfonate Groups as Surface-Confined Nucleation Agents. *RSC Adv.* **2015**, *5*, 73958–73962.
- (124) Cui, B.; Audu, C. O.; Liao, Y.; Nguyen, S. T.; Farha, O. K.; Hupp, J. T.; Grayson, M. Thermal Conductivity of ZIF-8 Thin-Film under Ambient Gas Pressure. *ACS Appl. Mater. Interfaces* **2017**, *9*, 28139–28143.

- 
- (125) Lu, G.; Hupp, J. T. Metal-Organic Frameworks as Sensors: A ZIF-8 Based Fabry-Perot Device as a Selective Sensor for Chemical Vapors and Gases. *J. Am. Chem. Soc.* **2010**, *132*, 7832–7833.
- (126) Barea, E.; Montoro, C.; Navarro, J. A. R. Toxic Gas Removal-Metal-Organic Frameworks for the Capture and Degradation of Toxic Gases and Vapours. *Chem. Soc. Rev.* **2014**, *43*, 5419–5430.
- (127) Liu, Q.; Ning, L.; Zheng, S.; Tao, M.; Shi, Y.; He, Y. Adsorption of Carbon Dioxide by MIL-101(Cr): Regeneration Conditions and Influence of Flue Gas Contaminants. *Sci. Rep.* **2013**, *3*, 2916–2921.
- (128) Knebel, A.; Zhou, C.; Huang, A.; Zhang, J.; Kustov, L.; Caro, J. Smart Metal-Organic Frameworks (MOFs): Switching Gas Permeation through MOF Membranes by External Stimuli. *Chemical Engineering and Technology*, **2018**, *41*, 224–234.
- (129) Hamon, L.; Llewellyn, P. L.; Devic, T.; Ghoufi, A.; Clet, G.; Guillerm, V.; Pirngruber, G. D.; Maurin, G.; Serre, C.; Driver, G.; Beek, W. Van; Jolima, E.; Vimont, A.; Daturi, M.; Je, S.; Orientale, A. A. V. Co-Adsorption and Separation of CO<sub>2</sub> - CH<sub>4</sub> Mixtures in the Highly Flexible MIL-53 (Cr) MOF. *Journal of the American Chemical Society*, **2009**, *53*, 17490–17499.
- (130) Wang, D.; Wang, M.; Li, Z. Fe-Based Metal-Organic Frameworks (MOFs) for Highly Selective Photocatalytic Benzene Hydroxylation to Phenol Fe-Based Metal-Organic Frameworks (MOFs) for Highly Selective Photocatalytic Benzene Hydroxylation to Phenol. *ACS Catalysis*, **2015**, *5*, 6852–6857.
- (131) Qu, L. L.; Wang, J.; Xu, T. Y.; Chen, Q. Y.; Chen, J. H.; Shi, C. J. Iron(III)-Based Metal-Organic Frameworks as Oxygen-Evolving Photocatalysts for Water Oxidation. *Sustain. Energy Fuels* **2018**, *2*, 2109–2114.
- (132) Yamada, T.; Shiraishi, K.; Kitagawa, H.; Kimizuka, N. Applicability of MIL-101(Fe) as a Cathode of Lithium Ion Batteries. *Chem. Commun.* **2017**, *53*, 8215–8218.
- (133) Xu, G.; Nie, P.; Dou, H.; Ding, B.; Li, L.; Zhang, X. Exploring Metal Organic Frameworks for Energy Storage in Batteries and Supercapacitors. *Mater. Today* **2017**, *20*, 191–209.

- 
- (134) Zhang, C.; Huang, K. MOF-Derived Iron as an Active Energy Storage Material for Intermediate-Temperature Solid Oxide Iron-Air Redox Batteries. *Chem. Commun.* **2017**, *53*, 10564–10567.
- (135) Salunkhe, R. R.; Kaneti, Y. V.; Yamauchi, Y. Metal-Organic Framework-Derived Nanoporous Metal Oxides toward Supercapacitor Applications: Progress and Prospects. *ACS Nano* **2017**, *11*, 5293–5308.
- (136) Carson, F.; Su, J.; Platero-Prats, A.E.; Wan, W.; Yun, Y.; Samain, L.; Zou, X. Framework Isomerism in Vanadium Metal – Organic Frameworks: MIL-88B(V) and MIL-101(V). Crystal growth and design. **2013**, *13*, 5036-5044.
- (137) Lebedev, O. I.; Millange, F.; Serre, C.; Tendeloo, G.V.; Férey, G. First Direct Imaging of Giant Pores of the Metal - Organic Framework MIL-101. *Chem. Mater.* **2005**, *17*, 6525–6527.
- (138) Serre, C.; Millange, F.; Surblé, S.; Férey, G. A Route to the Synthesis of Trivalent Transition-Metal Porous Carboxylates with Trimeric Secondary Building Units. *Angew. Chemie - Int. Ed.* **2004**, *43*, 6286–6289.
- (139) Surblé, S.; Serre, C.; Mellot-Draznieks, C.; Millange, F.; Férey, G. A New Isoreticular Class of Metal-Organic-Frameworks with the MIL-88 Topology. *Chem. Commun.* **2006**, *3*, 284–286.
- (140) Scherb, C.; Williams, J. J.; Hinterholzinger, F.; Bauer, S.; Stock, N.; Bein, T. Implementing Chemical Functionality into Oriented Films of Metal–organic Frameworks on Self-Assembled Monolayers. *J. Mater. Chem.* **2011**, *21*, 14849.
- (141) Feng, D.; Wang, K.; Wei, Z.; Chen, Y. P.; Simon, C. M.; Arvapally, R. K.; Martin, R. L.; Bosch, M.; Liu, T. F.; Fordham, S.; Yuan, D.; Omary, M. A.; Haranczyk, M.; Smit, B.; Zhou, H. C. Kinetically Tuned Dimensional Augmentation as a Versatile Synthetic Route towards Robust Metal-Organic Frameworks. *Nat. Commun.* **2014**, *5*.
- (142) Li, C. P.; Wu, J. M.; Du, M. Inducing Effect of Additive Agents on Coordination Assembly of silver(I) Nitrate with 3,5-Bis(2-Pyridyl)-4-Amino-1,2,4-Triazole: Supramolecular Isomerism and Interconversion. *Inorg. Chem.* **2011**, *50*, 9284–9289.

- 
- (143) Lin, Y.; Kong, C.; Chen, L. Amine-Functionalized Metal-Organic Frameworks: Structure, Synthesis and Applications. *RSC Adv.* **2016**, *6*, 32598–32614.
- (144) Zhang, Z.; Li, X.; Liu, B.; Zhao, Q.; Chen, G. Hexagonal Microspindle of NH<sub>2</sub>-MIL-101(Fe) Metal-Organic Frameworks with Visible-Light-Induced Photocatalytic Activity for the Degradation of Toluene. *RSC Adv.* **2016**, *6*, 4289–4295.
- (145) Serra-Crespo, P.; Ramos-Fernandez, E. V.; Gascon, J.; Kapteijn, F. Synthesis and Characterization of an Amino Functionalized MIL-101(Al): Separation and Catalytic Properties. *Chem. Mater.* **2011**, *23*, 2565–2572.
- (146) Pham, M. H.; Vuong, G. T.; Vu, A. T.; Do, T. O. Novel Route to Size-Controlled Fe-MIL-88B-NH<sub>2</sub> Metal-Organic Framework Nanocrystals. *Langmuir* **2011**, *27*, 15261–15267.
- (147) Zhang, Z.; Li, X.; Liu, B.; Zhao, Q.; Chen, G. Hexagonal Microspindle of NH<sub>2</sub>-MIL-101(Fe) Metal-Organic Frameworks with Visible-Light-Induced Photocatalytic Activity for the Degradation of Toluene. *RSC Adv.* **2016**, *6*, 4289–4295.

## Chapter 2

### 2 Direct Growth from Solution of ZIF-8 Films

ZIF-8 films have been directly grown from solution on Cu foils and Si-based surfaces. The synthetic route, feasible at room temperature and without organic or polymer additive, is based on the Sequential One-Pot protocol (SOP) that consists in cyclic processes during which the substrate was firstly dipped into mix solution of two precursors and then rinsed in the reaction solvent. Alcoholic solution of Zinc Nitrate and 2-methylimidazole were used as inorganic and organic precursors, respectively. By changing the number of cycles and the solvent, i.e. carrying out ten and five cycles in methanol and ethanol respectively, it has been possible to control the layer thickness and over all to investigate the solvent's effect on the ZIF-8 growth rate. Slowing down the homogenous and heterogenous nucleation by modulating the synthesis conditions it has been possible to investigate how the surface groups control the ZIF-8 film deposition. In particular, amorphous silicon (a-Si), H-terminated Si (100), SiO<sub>2</sub> and quartz have been employed to study the effect of the surface chemistry on ZIF-8 nucleation and growth. a-Si was deposited through low-temperature (50° C) CVD assisted by plasma inductively coupled (ICP-CVD). A combined approach based on experimental and theoretical data has given a coherent explanation of ZIF-8 film formation mechanism.

ZIF-8 films grown on quartz surfaces were also used as host materials to trap donor-acceptor electron pair complex like iodine (I<sub>2</sub>) and tetracyanoquinodimethane (TCNQ). The ZIF-8 stability towards solvents with different polarity was tested in order to choose the specific doping strategies, based on post and in situ synthesis protocols. Chemical composition analysis and optical characterizations proved the effective I<sub>2</sub> and TCNQ doping. The insulating quartz substrate was chosen to investigate the response behaviour in terms of electrical resistivity of ZIF-8 films to dopants insertion.

The above-mentioned SOP synthesis protocol has allowed to easily grow ZIF-8 films also on copper foils, a traditional collector for anodes in lithium ion batteries. The high basicity of Cu surface involves fast homogeneous and heterogenous nucleation leading to thick and poorly crystalline ZIF-8 films. ZIF-8/Cu films doped with lithium acetate were also prepared to evaluate post synthetic doping.

The change in chemical composition of ZIF-8/Cu films after  $\text{Li}^+$  doping was studied by FTIR spectroscopy.

Through the assembly of  $\text{Li}^+$  doped ZIF-8/Cu and undoped ZIF-8/Cu in lithium ion cells and their electrochemical characterization, like voltammetry cyclic and galvanostatic measurements, it has been investigated how the lithium doping can influence the charge/discharge profile of lithium ion cells. ZIF-8/Cu electrodes result electrochemical active and show intrinsic, partial, reversible charge transfer process respect to Cu foils.

## **2.1 Synthesis of ZIF-8 films on Si-based surfaces**

The challenge of this work is the development of new synthetic approaches for ZIF-8 film fabrication based on scalable and reproducible processes near room temperature, avoiding waste of chemical products in order to reduce environmental impact. To this scope, the key factors which drive the heterogeneous nucleation and growth of ZIF-8 films were studied. Several studies focused on the mechanisms of the homogeneous nucleation of ZIF-8 crystals formation. It has been widely reported that the choice of the solvent, the precursors type and their concentrations strongly affect the MOF formation in solution. ZIF-8 has been obtained through several synthetic methods using aprotic and/or protic solvents, like water, alcohol and amines involving specific mechanism and reaction times. The key step of ZIF-8 formation is the imidazole deprotonation either as isolate molecule or as Zn-imidazole complex. It has been proved as polar solvents and basic additives like, sodium formate or n-butylamine, facilitate the deprotonation reaction, speeding up the clusters formation and crystals growth. However, the dependence of heterogeneous growth on the surface chemistry is still unclear, and, further studies are required to better optimize the ZIF-8 films formation.

Here, the role of the surface chemistry and the solvent on the ZIF-8 growth have been studied by employing a variety of Si-based substrates, e.g H-terminated Si, quartz, native SiO<sub>2</sub> and, in particular, a-Si, with the aim of developing efficient and facile synthetic routes. Film preparation was carried out at room temperature using a mixed Zn nitrate and imidazole solution in MeOH or EtOH. Structural and morphological characterizations and chemical composition analysis proved that using MeOH, nucleation occurred both in solution and on the surface leading to ZIF-8 powders and homogenous films denser than those obtained from ethanol solution. In particular, continuous ZIF-8 films were obtained on a-Si and H-terminated Si (100). On the other hand, the ZIF-8 coating was less homogeneous on quartz, whereas, on SiO<sub>2</sub>, negligible coatings were formed. The fast homogeneous nucleation in methanol solution does not allow to detect the influence of surface chemistry on ZIF-8 growth. By employing ethanol and decreasing the reaction cycles, growth rate decreases involving negligible crystal formation in solution and thinner films, compared to the ones achieved from MeOH. Slower growth rates have been intentionally used in order to distinguish the four surfaces and to understand how experimentally optimize ZIF-8 growth. These differences have been related to the silanol density of the surfaces and to the Lewis basic strength which affect imidazole moiety deprotonation.

The advantages of this study are:

- The formation of a new bilayer ZIF-8/a-Si, never realized in the literature before, considerably empowering the applications of ZIF-8 also to rough surfaces, like copper foils or aluminum, that can be easily covered by a-Si. Thanks to its cost-effectiveness and compatibility with several materials, ZIF-8/a-Si is a highly promising system for the integration a large variety of devices (electrochemical, photovoltaic and photo-electrochemical, water splitting sensor);
- a coherent and experimentally validated model based on DFT calculations that describes the ZIF-8 growth onto Si-based surfaces as a function of silanols density gives a clear explanation of the effect of surfaces and solvents allowing to optimize the heterogeneous growth of ZIF-8 films;
- the determination by a fast, non-destructive and non-contact optical technique important parameters, like growth rate and film density; these results are crucial to optimize the synthetic protocol in order to obtain a continuous growth.



### 2.1.1 Experimental Section

*Thin film substrate preparation.* Amorphous Si (a-Si) was deposited using an inductive-coupled plasma chemical vapour deposition reactor (ICP-CVD) near room temperature (50°C) at low pressure (20 mTorr) and a power 500 W using a mixture of Ar (1sccm) and SiH<sub>4</sub> (30sccm).<sup>148,149</sup>

*Bulk substrates.* native SiO<sub>2</sub> grown on Cz-Si(100) and quartz were used as received; in contrast H-terminated Cz-Si(100) was obtained by Cz-Si dipping in HF (1%) for 90s in order to remove the native SiO<sub>2</sub>. The substrate was then washed quickly in deionized water, dried under N<sub>2</sub> flow and immediately introduced in the reaction solution for ZIF-8 film growth.

*ZIF-8 films growth.* Two solutions of 250 ml of Zn(NO<sub>3</sub>)<sub>2</sub> (12,5 mM) and 250 ml of HmeIm (25 mM) have been prepared using either MeOH or EtOH as solvent. During each cycle, the substrates were dipped in a mix solution consisted of 10 ml Zn(NO<sub>3</sub>)<sub>2</sub> (12,5 mM) and 10 ml HmeIm (25 mM) for 30 minutes at room temperature and without stirring.<sup>150</sup> Subsequently the samples were rinsed in the reaction solvent (MeOH or EtOH) and, finally dried under N<sub>2</sub> flow. From one to ten cycles were performed in MeOH or EtOH, respectively.

*ZIF-8 films characterizations.* Ellipsometric measurements were performed using a VASE instrument (J.A. Woollam) which is especially suited for transparent samples like glass and quartz in order to measure on the same position ellipsometric and transmittance data thanks to a vertical 9-29 configuration. Optical spectra were recorded from 300 nm to 2100 nm at 55°, 60° and 65° incident angle values near the Brewster angle of the transparent substrate. The optical model was built for each layer constituting the sample. The layer thickness was initially evaluated by a simple Cauchy model assuming  $k=0$  in the infrared spectral region. The complete ZIF-8 layer optical constant were modelled by using two gaussian oscillators. Special care was taken to evaluate the optical constants for the quartz substrate taking into account backside reflection and un-polarized light. Data fitting has been obtained through the whole range of measurements (300–2100 nm) including direct transmittance data for better estimation of layer thickness.

XPS spectra were run with a PHI 5600 multi-technique ESCA-Auger spectrometer equipped with a monochromatic Al K $\alpha$  X-ray source. Analyses were carried out with a photo-electron angle of 45° (relative to the sample surface) with an acceptance angle of  $\pm 7^\circ$ . The XPS binding energy (BE)

scale was calibrated by centring the C 1s peak due to hydrocarbon moieties and “adventitious” carbon at 285.0 eV. XPS atomic concentration was evaluated by estimating the integrated area of C1s, O1s, Si 2p, Zn 3p and N1s peaks corrected for the corresponding relative atomic sensitivity factor ( $S_x$ ) based on empirical data reported by Wagner and corrected for the transmission function of the spectrometer. Sensitivity factor for Zn 2p<sub>3/2</sub> was empirically determined from ZIF-8 powders. Note that atomic concentration of Zn has been estimated averaging Zn 3p and Zn 2p<sub>3/2</sub> signals.

X-ray diffraction (XRD) patterns were collected with a D8 Discover (Bruker AXS) diffractometer equipped with a high-precision goniometer (0.0001°), a thin-film attachment (long soller slits) and a Cu-K $\alpha$  source. The acquisitions were done in grazing incidence geometry with incident angle of 0.4°. This corresponds to a penetration depth of approximately 50 nm. The acquisition time was the same for all the diffraction patterns.

Field emission scanning electron microscope (Zeiss Supra35 FE-SEM) equipped with EDX microanalysis system (Oxford Instruments, X-MAX, 80 mm<sup>2</sup>) was used to observe morphology.

*Computational Details.* DFT-based simulations were performed with the CP2K/Quickstep package, using a hybrid Gaussian and plane wave method.<sup>151</sup> A double quality DZVP Gaussian basis set was employed for all atoms. The Goedecker-Teter-Hutter<sup>152</sup> pseudopotentials together with a 400 Ry plane wave cutoff were used to expand the densities obtained with the Perdew-Burke-Ernzerhof (PBE) exchange-correlation density functional.<sup>153</sup> A surface dipole correction was employed along the z axis to avoid unrealistic dipole interactions among the slabs.<sup>154</sup> Molecular graphics were produced by the CHEMCRAFT graphical package.<sup>155</sup> Solvent effects were taken into account for the proton release process of the imidazole molecule by using the self-consistent continuum solvation (SCCS) model of Andreussi et al.<sup>156</sup> the Zn<sup>2+</sup> coordinated imidazole have been modelled using two methyl groups and two imidazole groups with a tetrahedral environment around the Zn center. In order to model surface structures, bulk Si and quartz cell were optimized. On the optimized bulk cells, the 100 plane has been cut for both Si and SiO<sub>2</sub>. A seven-layer slab was built using a 20 Å vacuum region between slabs. The coordinates of the deepest layer were fixed to model bulk constrains.

### 2.1.2 Results and Discussions

A coherent model of heterogenous nucleation of ZIF-8 film on Si-based substrates was developed experimentally by changing the solvent, methanol or ethanol, and carrying out single and cyclic processes. As below reported the role of the solvent on the growth of ZIF-8 film was investigated through optical, morphological and structural characterizations while the role of the surface chemistry through qualitative and quantitative XPS analysis. In addition, a theoretical model based on DFT calculations of the ZIF-8 growth onto Si surfaces explained the relationship between the surface reactivity and silanols density.

- **Ellipsometric Spectroscopy**

In order to investigate the role of the solvent on nucleation and film growth, ZIF-8 layers were grown on quartz and glass as substrates and using both methanol and ethanol. In addition, SOP cycle and 1-step processes have been carried out to study the influence of the synthesis via on ZIF-8 growth rate. Kinetic data and optical properties of ZIF-8 layers have been acquired through ellipsometric measurements, for the first time. Figure 12a, shows the ZIF-8 growth rates as function of the time for 1-step and cyclic processes of 30 min each, plotted as blue and green curves for the synthesis in ethanol and methanol respectively. As reported, 1 step-process does not guarantee a constant growth rate and cyclic process is necessary to obtain a uniformly thick ZIF-8 layer. In addition, MeOH solvent involves a faster growth rate compared to ethanol. The refractive index measured with the Cauchy formula between 1 and 2eV where it is constant, increases and tends to saturate above 200 min cumulative process in both solvents but it is higher in MeOH proving as the film is thicker than the EtOH film.

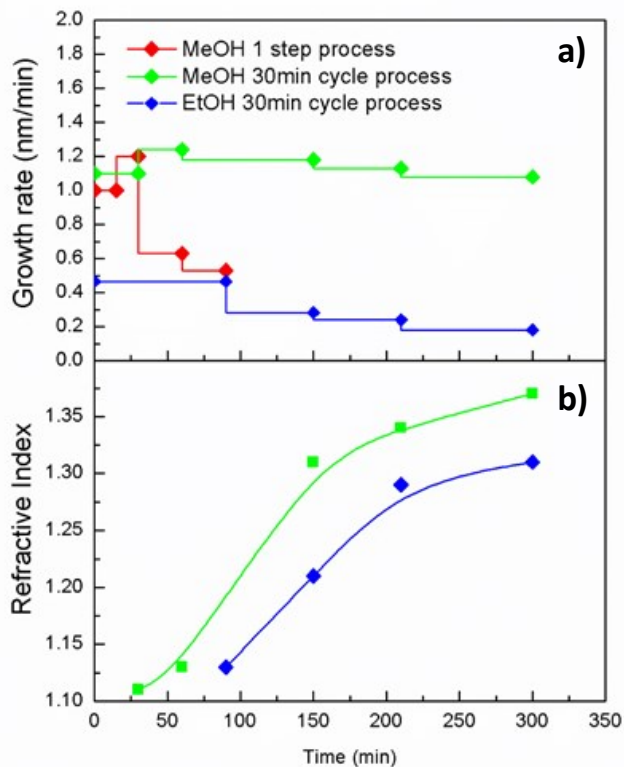


Figure 12: Growth rate (a) and refractive index (b) as function of time of ZIF-8 layers grown in MeOH and EtOH.<sup>186</sup>

The refractive index values reported in Figure 12b, are low with respect to other materials (e.g.  $n(\text{SiO}_2) = 1.47$ ) due to the MOF porous and empty structure. Furthermore, ZIF-8 film obtained from methanol solution presents a higher refractive index over the whole investigated range (from infrared to the deep UV) compared to that one concerning synthesis in EtOH. This can be attributed to the formation of a denser layer using MeOH, (being on purpose the thickness of 60 nm in both cases).

A quartz substrate able to guarantee an optimal (>95%) transmission of light in the whole range was used as surface to grow ZIF-8 film by 10 cycles in MeOH and EtOH, in order to measure optical gap of ZIF-8 (Figure 13).

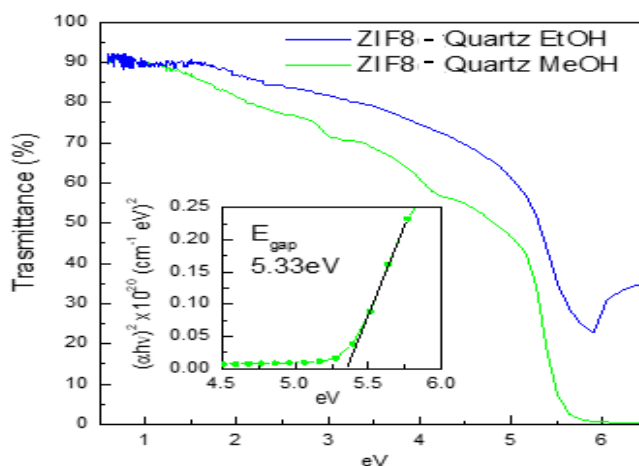


Figure 13: Transmittance measurements of ZIF-8 layers grown with cyclic processes in MeOH and EtOH at identical number of cycles. Note the layer grown in MeOH has formed a continuous layer reducing the transmitted light near zero at energies above the band gap.

The band gap was calculated as linear extrapolation typical of a Tauc plot to be 5.33 eV, according to other theoretical studies in the literature. The transmittance of ZIF-8 grown in MeOH attests again the layer has fully covered the substrate because it goes to zero at values near and above the band gap.

- **X-Ray Diffraction**

The role of the solvent on ZIF-8 growth was investigated by carrying out x-ray diffraction analyses on the same 10 and 5 cycles in methanol and ethanol samples, respectively. Figure 14 reports XRD patterns of ZIF-8 films grown by 10 SOP cycles of 30 min from MeOH on quartz, Si (100), amorphous Silicon (a-Si) and SiO<sub>2</sub>. Patterns of samples on quartz, Si and a-Si are similar, consisting of a main diffraction peak at  $2\theta = 7.4^\circ$  attributable to (011) reflection of crystalline ZIF-8 according to the reported XRD ICCD data.<sup>157,158,159</sup> A less intense replica at  $2\theta = 14.8^\circ$  is also visible in the pattern.<sup>160</sup> The full width at half maximum (FWHM) accounts for ordered crystallites of average size 35 nm for Si and quartz as estimated using the Scherrer formula ( $D = 0.9\lambda/\beta\cos\theta$ , being  $\beta$  a function of the FWHM, corrected with the instrumental broadening). The interplanar spacing for the (011) planes is 1.19 nm. A slightly different scenario can be depicted on a-Si the peak is less intense,

the d-spacing is 1.2 nm and the average crystallites size is 40 nm. The XRD pattern of SiO<sub>2</sub> does not show any characteristic signals of ZIF-8 phase.

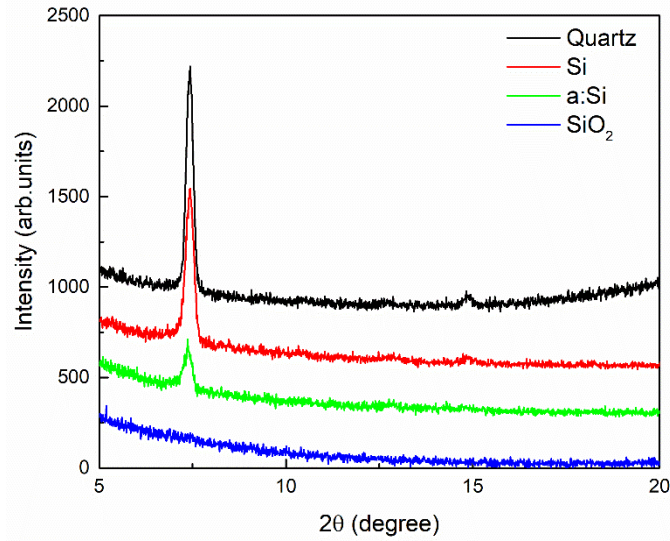


*Figure 14: XRD diffractogram of ZIF-8 films grown on quartz, Si (100), a-Si and SiO<sub>2</sub> obtained through 10 SOP cycles in methanol solution.*

In order to decrease the homogenous and heterogenous ZIF-8 nucleation and to investigate the surface effect 10 SOP cycles have been carried out using EtOH as solvent. Figure 15 reports the relative XRD data showing as the same ZIF-8 materials using EtOH as solvent have been obtained. As expected, due to the lower growth rate, less intense peaks are observed.

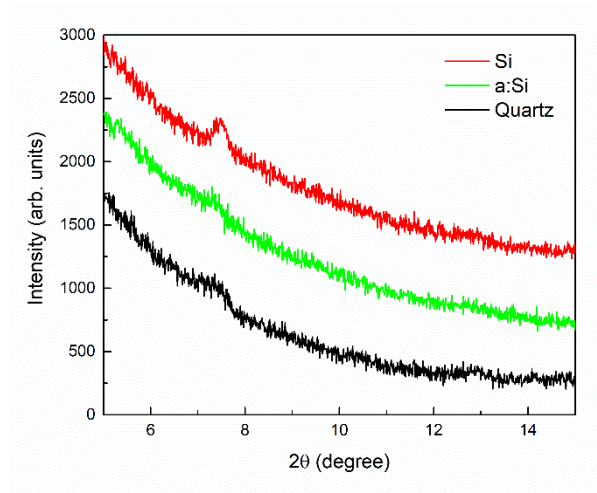


Figure 15: XRD diffractogram of ZIF-8 films grown on quartz, Si (100) and a-Si obtained through 10 SOP cycles in ethanol solution.

- **Sem characterization**

The above-mentioned ellipsometry and XRD outcomes prove that the film thickness and crystallinity are strongly dependent on the solvent polarity. These data have been further confirmed by the following SEM analysis. Low and high-magnification SEM images of film morphologies are reported in Figure 16. Film growth in MeOH on Si and a-Si leads to a continuous coating, which consists of homogeneous and well-formed crystals in the case of Si (Figure 16b) and a-Si (Figure 16c). A less homogeneous film with large crystals embedded in a layer of tiny grains were obtained on quartz substrate (Figure 16a). For this substrate, several cracks are also visible in the SEM micrographs.

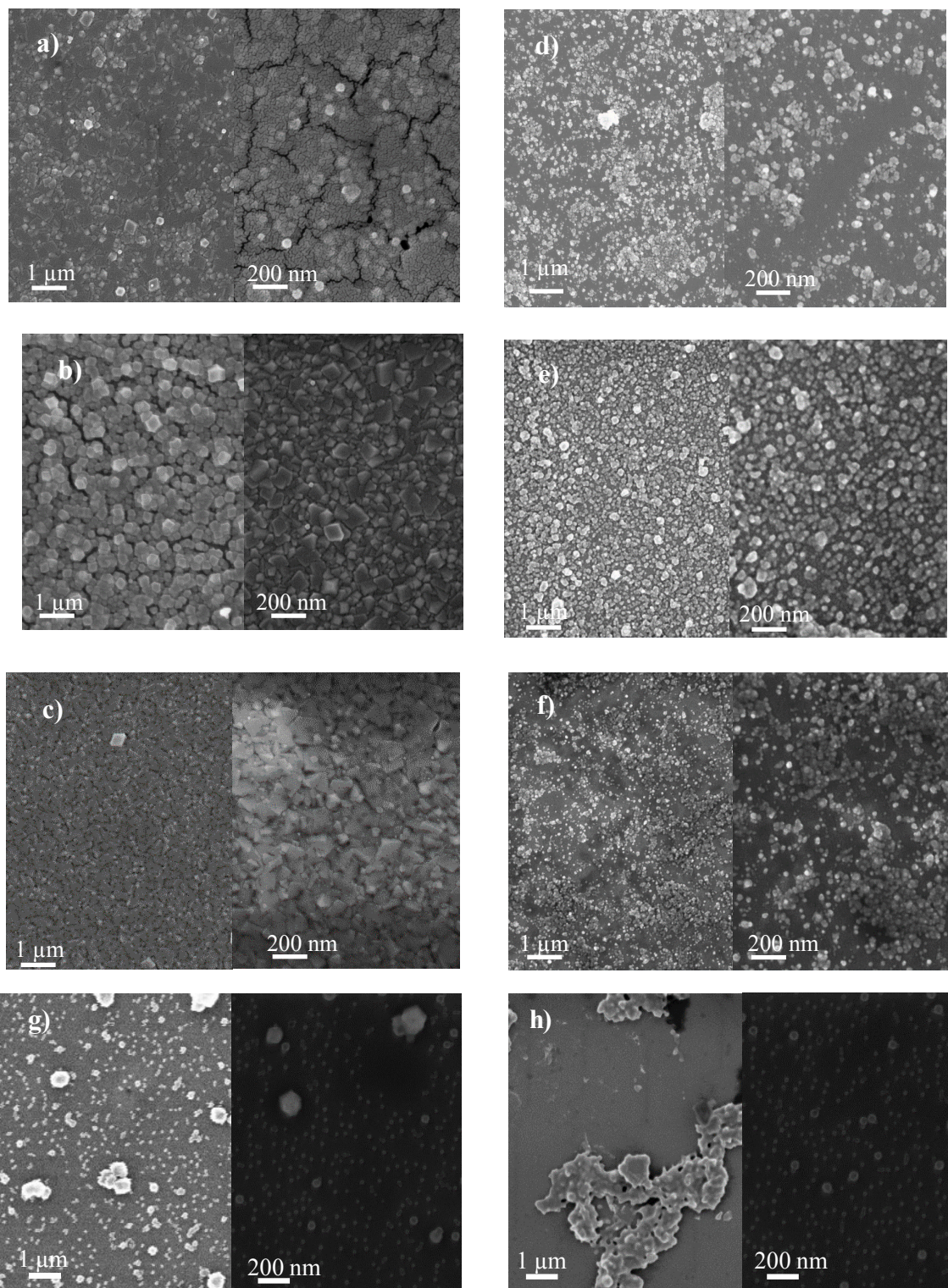


Figure 16: SEM images of ZIF-8 layers grown on quartz, Si, a-Si and SiO<sub>2</sub> from MeOH (a-b-c-g) and EtOH (d-e-f-h).



A less continuous coating, in some cases with large uncovered areas, have been overall obtained when using EtOH as solvent (Figure 16 d-e-f-h). The substrate coverage is higher on Si (Figure 16e), and it decreases moving from Si to a-Si and to quartz. On SiO<sub>2</sub>, SEM images show a negligible ZIF-8 coating, particularly for the synthesis in EtOH (Figure 16h).

- **XPS characterization**

To highlight the effect of the four surfaces and to investigate the ZIF-8 nucleation, a single deposition cycle of 30 minutes, has been carried out using either methanol or ethanol as solvent. Figure 17 reports the XPS deconvolution peaks of N 1s and Zn 2p<sub>3/2</sub> bands of ZIF-8 samples grown on the four substrates. The four all samples show N 1s signals as sum of two components, at 399.3 eV attributed to deprotonated imidazole nitrogen atoms, as proved for bulk ZIF-8, and at 400.8 eV, related to the not-deprotonated N-H moieties of unreacted adsorbed imidazole molecules.

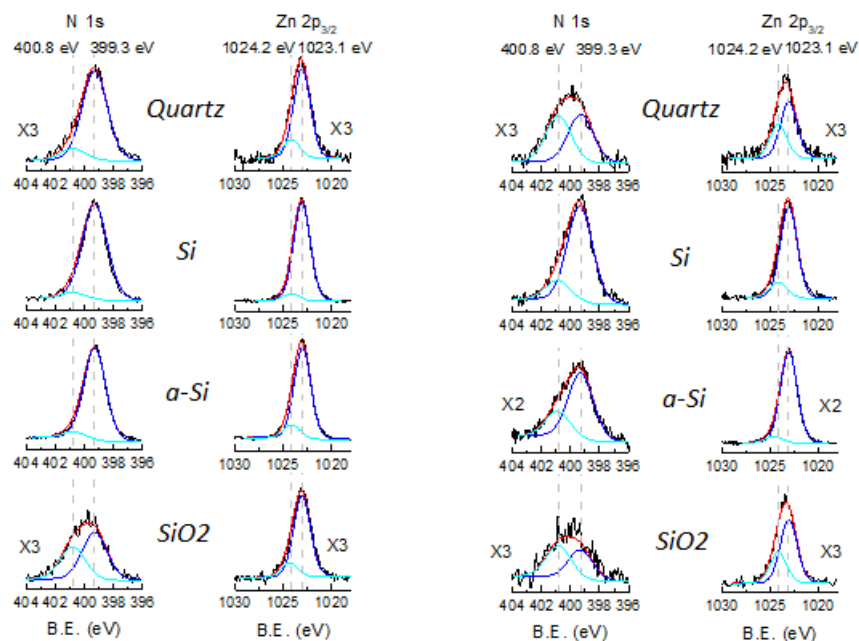


Figure 17: XPS spectra of N 1s and Zn 2p<sub>3/2</sub> of samples grown after 1 SOP cycle of 10 min from methanol (left) and ethanol solution (right) on quartz, Si, a-Si and SiO<sub>2</sub>.<sup>186</sup>

The relative intensity of the two components can be modulated with the solvent and substrate (Table 2).

<i>XPS Atomic Concentration %</i>						
<i>Reaction solvent MeOH</i>						
SAMPLE	Si	C	O	N	Zn	N:Zn
Si	0.9	71.4	3.9	19.2	4.6	4.2
a-Si	0.1	71.8	3.0	20.2	4.9	4.1
Quartz	0.9	67.8	5.9	19.8	5.7	3.5
SiO <sub>2</sub>	37.7	18.7	36.1	5.3	2.1	2.7
<i>Reaction solvent EtOH</i>						
	Si 2p	C 1s	O 1s	N 1s	Zn	N:Zn
Si	1.4	73.2	7.2	14.6	3.6	4.0
a-Si	11.5	52.2	16.6	15.6	3.9	4.0
Quartz	21.8	22.8	46.4	5.8	3.3	1.75
SiO <sub>2</sub>	39.0	24.1	34.8	1.4	0.8	1.75
<i>Reference</i>						
Powder		67.2	2.5	24.4	5.9	4.1

Table 2: XPS atomic concentration of ZIF-8 films grown on the four substrates from MeOH and EtOH solutions. The XPS atomic concentration of ZIF-8 powders has been added as reference.<sup>186</sup>

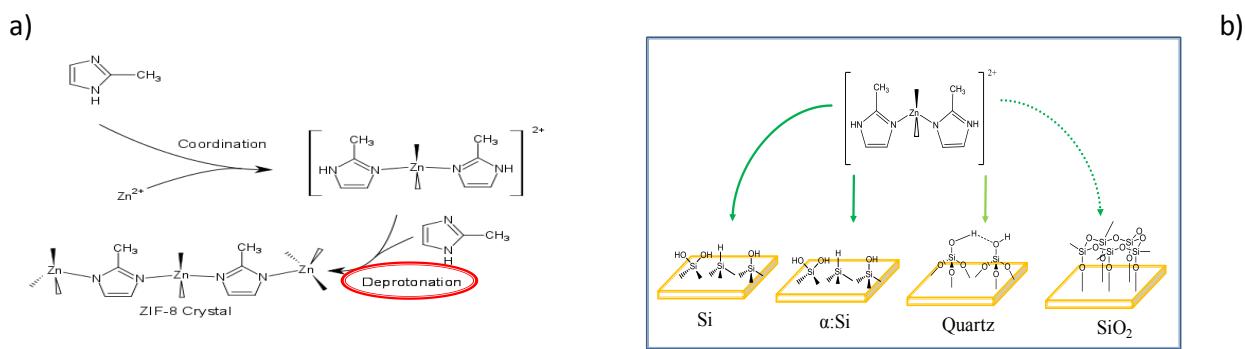
From methanol solution, the film grown on Si, a-Si and quartz mainly show mainly the low BE N 1s component (399.3 eV) associated to fully formed ZIF-8. On the other hand, for ZIF-8 grown on SiO<sub>2</sub> sample, the intensity of the high BE N 1s component (400.8eV) is comparable to that one at 399.3 eV, indicating a slower nucleation on SiO<sub>2</sub> respect to the other three surfaces. By using ethanol as solvent, the intensity of the high BE N 1s component (400.8eV) is higher proving as the imidazole is still not full deprotonated and, in particular, the 399.3 eV/ 400.8 eV component ratio decreases with the following order: Si> a-Si>quartz>SiO<sub>2</sub>. The XPS outcomes confirms the above mentioned optical data, and they prove that i) nucleation in ethanol is slower compared that in

methanol, and ii) heterogeneous nucleation rate increases with the following order  $\text{SiO}_2 < \text{quartz} < \alpha\text{-Si} < \text{Si}$ .

The XPS signal of Zn  $2p_{3/2}$  consists also of two components, at 1023.1 eV similar to the relative of bulk ZIF-8 and at 1024.2 eV associated to hydroxides or nitrates. Similarly, the different intensity ratios of Zn  $2p_{3/2}$  components depend on the substrate and solvent and it can be associated to different nucleation rates. As already observed for N 1s, the nucleation rate, increases according to the following trend ethanol < methanol and  $\text{SiO}_2 < \text{quartz} < \alpha\text{-Si} < \text{Si}$ , confirming the results observed for N 1s.

- **Theoretical model and DFT-based simulations**

By considering the above-reported experimental data and according the previous literature studies on the homogeneous formation of ZIF-8 that indicate as the key step for the crystal growth is the imidazole deprotonation either of isolate imidazoles or of  $\text{Zn}^{2+}$  coordinated imidazoles (Scheme. 6a)<sup>161</sup>; a ZIF-8 formation mechanism has been proposed for the four Si-based investigated (Scheme 6b).



*Scheme 6: Proposed ZIF-8 formation mechanism for Si-based surfaces based on silanols density.*

Surface differences towards ZIF-8 functionalization have been related to their silanol density and to the Lewis basic strength which affect imidazole moiety deprotonation. H-terminated Si(100) and amorphous Si turned out to be the most reactive surfaces, whereas on quartz and, especially, on  $\text{SiO}_2$  reactivity was much lower.

DFT calculations were used to develop a theoretical model of the ZIF-8 growth considering the solvents and surfaces chemistry. Figure 18 shows the key formation step of ZIF-8 crystals consisting on the imidazole (or of its  $\text{Zn}^{2+}$  cluster) deprotonation.<sup>161,162,159</sup> Taking into account the deprotonation energies of the imidazole and of the  $\text{Zn}^{2+}$  coordinated imidazole, the Zn complex results favoured of about 15 kcal/mol compared to the imidazole. In addition, the effect of the solvent is studied, and results indicate that methanol owning a dielectric constant ( $\epsilon$ ) of 32.613 D induces better stabilization than ethanol ( $\Delta = 0.5$  kcal/mol) ( $\epsilon = 24.852$  D).

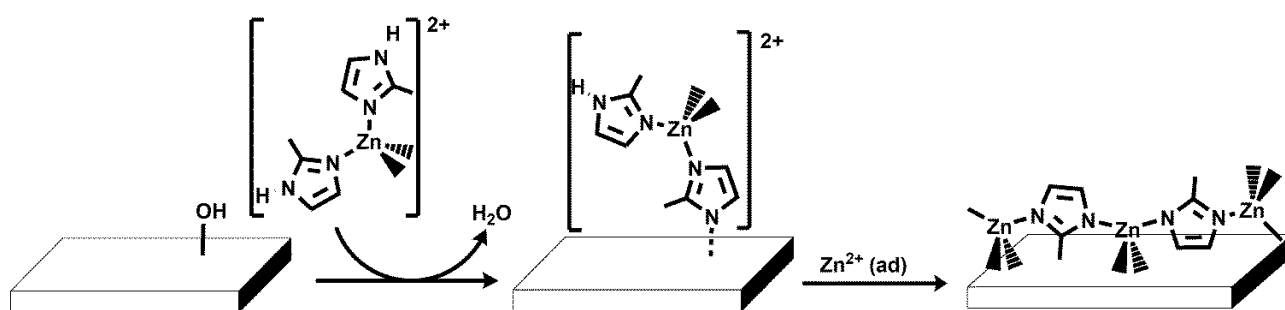
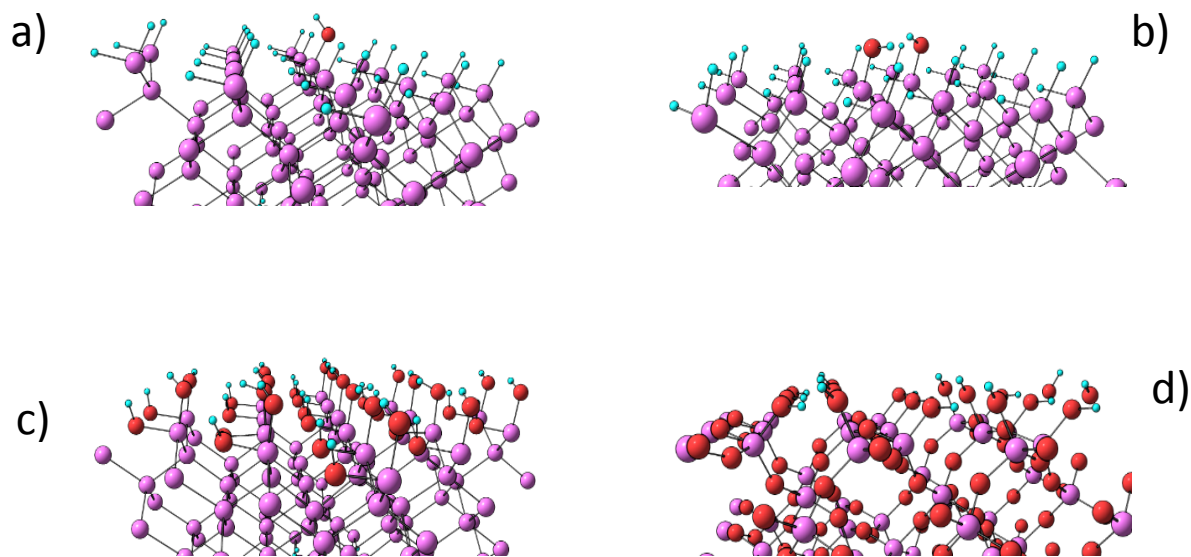


Figure 18: The modelled nucleation step employed in DFT calculations to study the different surfaces effect.<sup>186</sup>

Calculation results shows that the hydroxyl groups of the surface deprotonate the imidazole of the Zn clusters with the formation of water molecule (figure 18).



*Figure 19: Surfaces model of the first step of the ZIF-8 growth: a) Si(100) with one hydroxyl group; b) Si(100) with two vicinal hydroxyl groups, c) Si(100) saturated of hydroxyl groups, d) totally hydroxylated SiO<sub>2</sub>(100).<sup>186</sup>*

This first step is endergonic, involves an adsorbed intermediate formation, and it acts as an energy barrier for the following ZIF-8 deposition. Particularly, the deprotonated imidazole of the intermediate reacts with Zn<sup>2+</sup> ions adsorbed on surface determining the ZIF-8 film growth.

Another model was developed by considering the four substrate and the only simpler imidazole. Four Si(100) surfaces have been adopted having a different oxygen density: a) with one hydroxyl group, b) with two oxygen groups, c) saturated of hydroxyl groups and, d) a totally hydroxylated SiO<sub>2</sub>(100) surface ( Figure 19).

By increasing the oxygen content on the surface, the first nucleation step requires more energy. In particular, for Si(100) with two hydroxyl groups (Figure 19 b), 2 kcal/mol extra are needed compared the case of Fig 19 a; Si(100) saturated of hydroxyl groups (Figure 19 c) 2.7 kcal/mol extra and the SiO<sub>2</sub>(100) surface (Figure 19 d), 13.1 kcal/mol extra. Si (100) with one hydroxyl group favours the first ZIF-8 deposition process (Figure 19 a). Therefore, the inhibition of the ZIF-8 deposition on the surface increases with the oxygen content and, in turn, the hydroxyl density, according which the experimental data.

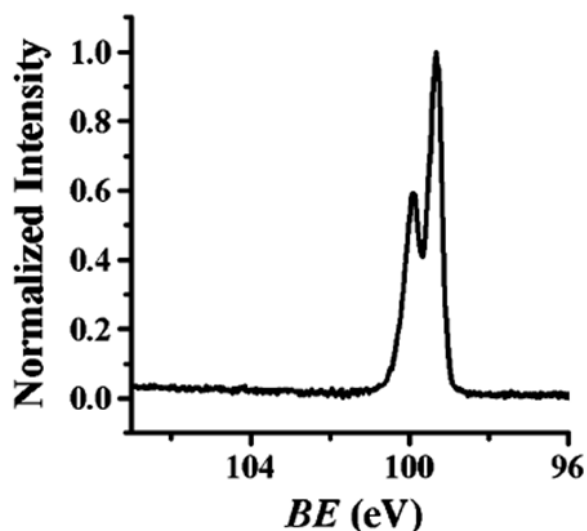


Figure 20: Si 2p XPS spectra of Si-H obtained through HF-etching after 1h.<sup>163</sup>

Figure 20 shows Si 2p XPS signal of Si-H surface obtained through HF-etching after 1 h and prove that the oxygen content is very low. Since Si mainly consists of hydride (Si-H<sub>x</sub>) terminations with a low density of hydroxyl groups due to oxidation phenomena, its Si-OH groups are isolated, and they are free to react and to promote proton exchange. The reactivity of hydroxyl groups decreases with their density because of increase the inter cross-link and possible H-bonds formation. In addition, surface reactivity decreases also with the overall oxygen content, thus making quartz, and native SiO<sub>2</sub> less reactive surfaces compared to Si.

Figure 21a shows a 100nm-thick a-Si sample adopted to measured H concentration through Elastic Recoil Detection Analysis (ERDA).<sup>164</sup> It has been assuming that most of the H was incorporated during the growth process and its concentration profile is roughly constant (Figure 21 b). In fact, if the sample is too thin the amount of adventitious H dominates over the H due to the deposition process which is significantly underestimated. Under identical process condition H content in thin layers used for ZIF-8 growth can be assumed to be as high as  $1.2 \times 10^{22}$  H/cm<sup>3</sup> or 25% atomic.

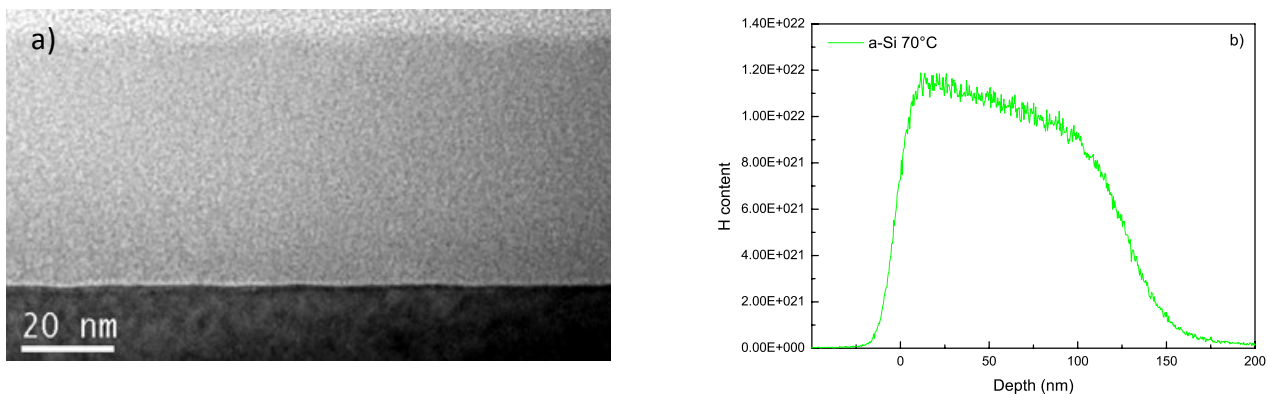


Figure 21: a) Transmission electron microscopy of 100nm-thick a-Si layer grown on bulk Si at low temperature used for H content; b) H-content in a-Si as measured by Elastic Recoil Detection Analysis (ERDA).

XPS signals of Si-H surface and Hydrogen profile of a-Si achieved through ERDA analysis above-reported, represent an un ulterior experimental prove of the low oxygen content on Si and a-Si surface. Therefore, Si and a-Si characterized by higher density of isolated silanols result the most reactive substrates towards ZIF-8 functionalization.

In order to study the role of  $Zn^{2+}$  ions on the ZIF-8 formation before the imidazole deprotonation, all four surfaces were dipped for 10 min into a  $Zn(NO_3)_2$  ethanol solution and after rinsed in ethanol, and dried under  $N_2$  flow. XPS spectra of Zn  $2p_{3/2}$  signal reported in Figure 22 shows the presence of Zn  $2p_{3/2}$  component at 1024.2 eV attributable to adsorbed  $Zn^{2+}$  hydroxides or nitrates.

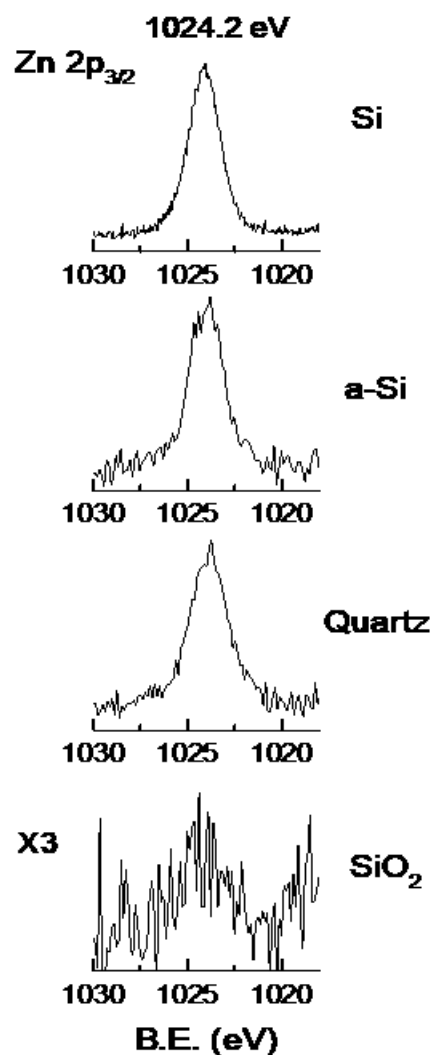


Figure 22: XPS Zn 2p region of the four surfaces after treatment with ethanolic solutions of  $Zn(NO_3)_2$  (12.5 mM) for 10 min.

Table 3 reports the atomic concentration of Si 2p, C 1s, O 1s and Zn 2p for all four surface after treatment with  $Zn(NO_3)_2$  ethanol solution. In order to evaluate the amount of adsorbed ions the atomic ratio between Zn and the substrate atoms (i.e Si and O) is also reported and prove that it is much lower for SiO<sub>2</sub> compared to the other three surfaces. The above calculated high energy barrier (13.1 kcal/mol) of SiO<sub>2</sub> surfaces and the low amount of adsorbed Zn<sup>2+</sup> ions available to interact with the adsorbed intermediate, confirm the poor reactivity of SiO<sub>2</sub> towards ZIF-8 functionalization.

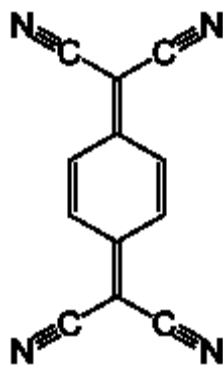


Substrate	Si	C	O	Zn	$\frac{\text{Zn}}{(\text{Si} + \text{O})} \times 100$
Si	41.9	35.9	21.4	0.8	1.3
a-Si	25.8	37.5	35.7	1	1.6
Quartz	30.9	13.2	54.9	1	1.2
SiO <sub>2</sub>	37.7	28.2	34.0	0.1	0.1

Table 3: Atomic concentrations of the four surfaces after treatment (10 min) with Zn(NO<sub>3</sub>)<sub>2</sub> ethanol solutions (12.5 mM)

## 2.2 Doping of ZIF-8/Quartz films with Iodine and TCNQ

Several strategies based on in-situ synthesis using  $\pi$ -conjugated organic linkers as precursors or on post-doping of MOF with redox-active molecules have been implemented to improve their electrical conductivity.<sup>165,166,167,168</sup> The insertion of acceptor-donor electron species inside MOF cavities allow to obtain host-guest systems able to match the overlap between  $\pi$  and d orbitals of organic and metal centres and to guarantee a suitable electron charge transfer.<sup>169</sup> Tetracyanoquinodimethane (TCNQ) with molecular formula is [(NC)<sub>2</sub>CC<sub>6</sub>H<sub>4</sub>C(CN)<sub>2</sub>] is a strong electron acceptor due to its cyanocarbon atoms and the its  $\pi$ -system extension and it is characterized by a large electron affinity (2.8 eV) in gas phase, suitable to achieve low-dimensional conductors and charge-transfer compounds.<sup>170,171</sup>



*Scheme 7: Scheme of Tetracyanoquinodimethane (TCNQ).*

TCNQ acts as an efficient multi-redox-active molecule because can easily accept two or more electrons. TCNQ and its radical anion  $\text{TCNQ}^-$  are suitable for electronic, optical and organic semiconductors.<sup>172</sup> Several examples of TCNQ-based complexes owning electrical conductance close to metals have been developed, like TCNQ-TTF (TTF: tetrathiafulvalene),<sup>173</sup> hybrid metal-to-ligand charge-transfer systems (MLCT)<sup>174</sup> and surface-supported structures using Au, Ag and Cu as substrates.<sup>175,176</sup> In addition, electrical properties of MOF-based thin films were modulated by TCNQ insertion. As recently reported, the electrical conductivity of  $\text{Cu}_3(\text{BTC})_2$  film can be tunable through TCNQ infiltration.<sup>177</sup> However, there are few examples of TCNQ-doped MOFs and this could represent a promising synthesis method to obtain N-doped hybrid frameworks.<sup>178</sup>

Likewise, electrophilic addition of halogens represents a chemical reaction to covalently link nucleophile MOF sites like nitrogen or carbon atoms.<sup>179</sup> Iodine and Bromine have been widely used to bond  $\pi$  electron systems like olefin and to form 1:1 electron donor-acceptor complexes with imidazole derivatives.<sup>180,181</sup> Halogen bonding are particularly exploited to achieve luminescent MOF and MLCT complexes too.<sup>182,179</sup> Particularly, iodine linked to pyridinic nitrogen of imidazole leads to n-type charge transfer complexes. In addition, hole doping of  $\text{Co}_3(\text{NDC})_3$  films through  $\text{I}_2$  insertion have been carry out to achieve an oxidative MOF doping leading to p-type semiconductor and allowing to extend the MOFs applications in electronic and optical devices.<sup>178</sup> On the other hand, ZIF-8 embedded in a rubber polymeric matrix has been employed as host material to trap iodine vapour, useful in sensing field.<sup>183</sup> Therefore, dopant insertion like  $\text{I}_2$  and TCNQ, not only involves morphological changes but also allows to modulate chemical-physical and electrical properties of MOF thin films.

On this background, the doping of ZIF-8/quartz films with TCNQ and I<sub>2</sub> is reported in the following sections. The guest's insertion has been investigated through chemical and optical characterizations and the resistivity change of the ZIF-8 films after doping were tested by four point probe electrical characterization.

### 2.2.1 Iodine Doping of ZIF-8/Quartz films

ZIF-8/quartz films were doped with I<sub>2</sub> through in situ synthesis during ZIF-8 growth and by post synthesis via based on infiltration of the sample into dopant solution. Chemical stability of ZIF-8 films in solvents with different polarity was firstly tested. ZIF-8/quartz films were dipped into water, methanol or ethanol separately for 30 min. As shown in Figure 23, ZIF-8/quartz film is unchanged after dipping in water (Figure 23 a), whereas it undergoes a dissolution in methanol and ethanol (Figure 23 b).

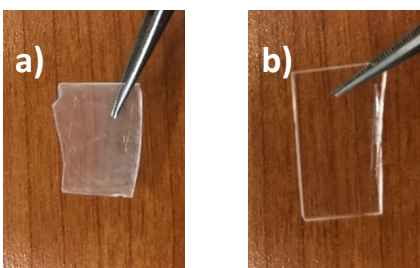


Figure 23: (a) ZIF-8/Quartz film after dipping of 30 min in water and in methanol; and (b) in ethanol.

Due to remarkable in water stability of ZIF-8, iodine doping via post-synthesis was carried out in water (ZIF-8@I<sub>2</sub>\_H<sub>2</sub>O) whereas methanol has been used as reaction solvent for ZIF-8 synthesis and its simultaneous I<sub>2</sub>-doping (ZIF-8@I<sub>2</sub>\_MeOH).

*Route a: ZIF-8@I<sub>2</sub>\_MeOH:* quartz substrate was dipped for 30 min into mix solution consisted of 5 ml of a methanolic solution of Zn(NO<sub>3</sub>)<sub>2</sub>×6H<sub>2</sub>O (12.5mM, 250 ml MeOH), 2 ml di I<sub>2</sub> (6,8 mM, 250 ml di MeOH) and 5 ml di MeIm (25 mM, 250 ml di MeOH). This one represents a reaction cycle and it has been repeated 10 times for the ZIF-8@I<sub>2</sub> film synthesis.

*Route b: ZIF-8@I<sub>2</sub>\_H<sub>2</sub>O:* ZIF-8/Quartz film was dried at 130°C for 1h in order to remove methanol amount inside ZIF-8 cavities trapping during synthesis. Then, the sample was dipped for 3 hours at room temperature in a Lugol reactive solution obtained dissolving 1.52 gr of KI and 0.76 gr di I<sub>2</sub> into 60 ml di H<sub>2</sub>O.

Optical characterization has been allowed to detect the iodine presence in the ZIF-8/quartz films and proves that the host-guest system formation (ZIF-8@I<sub>2</sub>). Figure 24 reports the UV-vis spectra of ZIF-8@I<sub>2</sub> obtained through 10 SOP cycle from methanol solution (Figure 24 a) and through post-synthesis way in water solution (Figure 24 b)

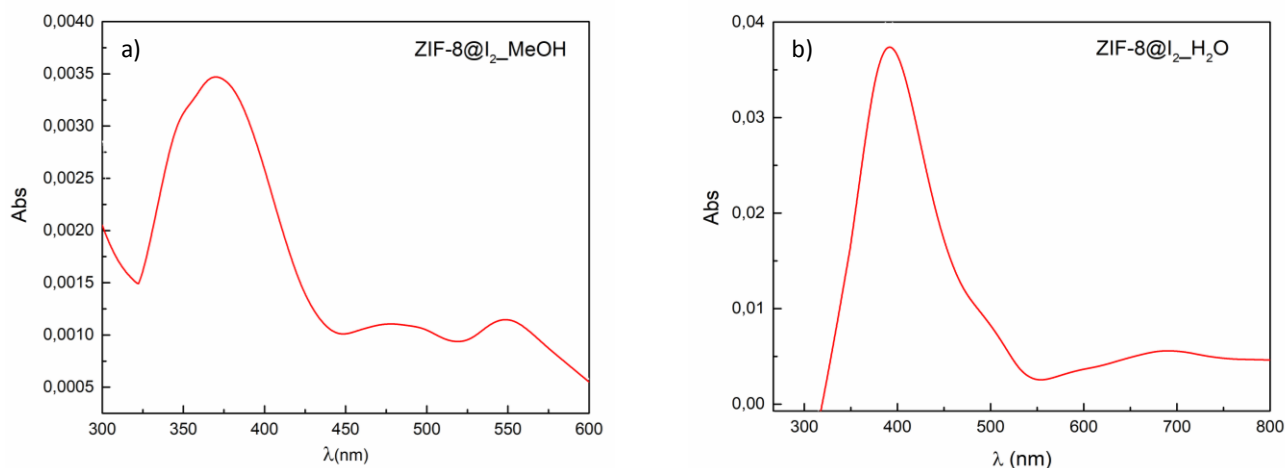


Figure 24: UV-vis of ZIF@I<sub>2</sub> system obtained through route a (a); and through route b (b).

Despite there are not typical absorption peaks of ZIF-8, due to its absorption in the region below 300 nm, both spectra show a band between 360 and 400 nm related to I<sub>3</sub><sup>-</sup> and I<sup>-</sup> species.<sup>184</sup> As shown in Figure 24 b, the absorption results more intense for ZIF-8@I<sub>2</sub> sample obtained through post-synthesis in water than the related achieved by synthesis in methanol. In addition, for ZIF-8@I<sub>2</sub>\_H<sub>2</sub>O sample the band at about 700 nm is recorded and attributable to I<sup>-</sup> formation.<sup>185</sup>

As further prove of ZIF-8@I<sub>2</sub> host-guest formation, chemical composition analysis was carried out through XPS. The table 4 reports XPS atomic concentrations of the ZIF-8@I<sub>2</sub>\_MeOH sample. The detected Zn:N atomic ration, close to theoretical value (1:4),<sup>186</sup> proves as the addition of iodine into mix ZIF-8 precursors solution does not compromise the formation of ZIF-8 crystals.

<i>XPS atomic concentrations ZIF-8@I<sub>2</sub>_MeOH</i>						
Si 2p <sub>3/2</sub>	C 1s	O 1s	N 1s	Zn 2p <sub>3/2</sub>	I 3d <sub>5/2</sub>	I 4d <sub>5/2</sub>
6.8	70.2	15.4	4.5	1.1	1.0	1.0

Table 4: XPS atomic concentrations of Si 2p<sub>3/2</sub>, C 1s, O 1s, N 1s, Zn 2p<sub>3/2</sub>; I 3d<sub>5/2</sub> and I 4d<sub>5/2</sub> of the ZIF-8@I<sub>2</sub>\_MeOH.

In addition to XPS quantitative analysis, Figure 25 shows the XPS signal of I 3d<sub>5/2</sub> as single peak centred at about 617 eV and attributable to I<sub>3</sub><sup>-</sup> presence.

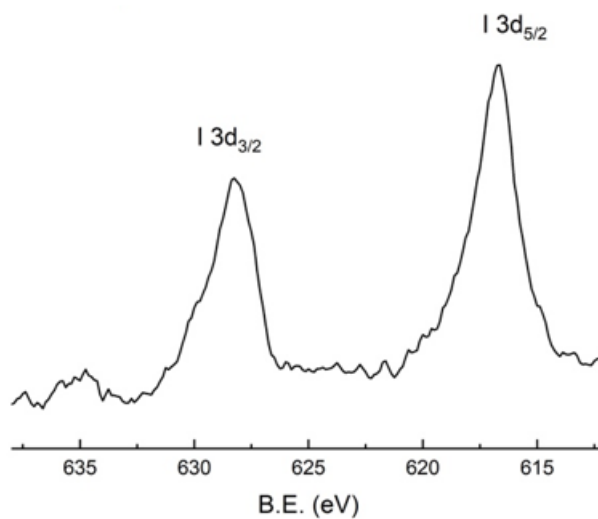


Figure 25: XPS signal of I 3d<sub>5/2</sub> of ZIF-8@I<sub>2</sub>\_MeOH sample.

By analysing the XPS atomic concentration of ZIF-8@I<sub>2</sub>\_H<sub>2</sub>O sample, reported in Table 5, it is clear as post-doping synthesis in water allow to insert more iodine inside ZIF-8 cavities. Indeed, the I 3d<sub>5/2</sub> atomic concentrations results higher than that one recorded for ZIF-8@I<sub>2</sub>\_MeOH sample.

<i>XPS atomic concentrations ZIF-8@I<sub>2</sub>_H<sub>2</sub>O</i>							
Si 2p <sub>3/2</sub>	C 1s	O 1s	N 1s	Zn 2p <sub>3/2</sub>	I 3d <sub>5/2</sub>	I 4d <sub>5/2</sub>	K 2p
5.3	43.4	32.6	5.0	1.31	4.3	4.2	3.9

Table 5: XPS atomic concentrations of Si 2p<sub>3/2</sub>, C 1s, O 1s, N 1s, Zn 2p<sub>3/2</sub>; I 3d<sub>5/2</sub>, I 4d<sub>5/2</sub> and K 2p of the **ZIF-8@I<sub>2</sub>\_H<sub>2</sub>O**.

Figure 26a shows the XPS signal of I 3d<sub>5/2</sub> of ZIF-8@I<sub>2</sub>\_H<sub>2</sub>O that results shifted to higher binding energy (620. 2eV) respect to the relative recorded for ZIF-8@I<sub>2</sub>\_MeOH due to the I formation.<sup>187</sup> In addition, K 2p signal has been also detected due the KI introduction in reactive Lugol solution (Figure 26b).

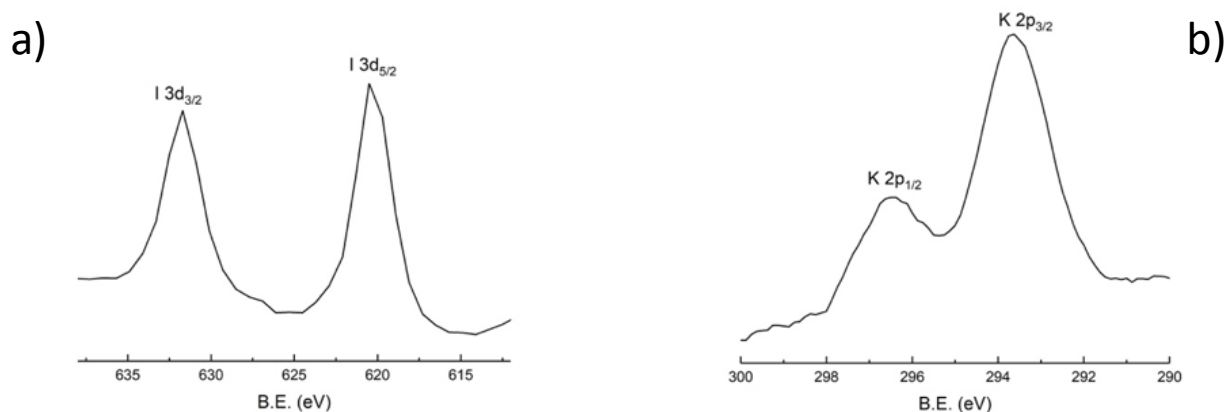


Figure 26: XPS signal of I 3d<sub>5</sub> and K 2p of ZIF-8@I<sub>2</sub>\_H<sub>2</sub>O sample.

XPS outcomes confirm the above-mentioned optical data proving as the post-doping of ZIF-8 film in water solution does not compromise the ZIF-8 integration and its composition, N:Zn atomic ratio is equal to theoretical value also after iodine treatment, and guarantees a greater iodine amounts trapped inside ZIF-8 cavities than one achieved through the synthesis in MeOH.

### 2.2.2 TCNQ Doping of ZIF-8/Quartz films

As widely reported in literature, MOF infiltration into a  $\text{CH}_2\text{Cl}_2$  saturated solution of TCNQ over long time (2 days) is the more common method to achieve N-rich MOF acting as n-type semiconductors.<sup>188</sup>

In situ synthesis approach simultaneous to doping has been adopted to achieve doped ZIF-8/quartz films with TCNQ in order to avoid ZIF-8 dissolution into  $\text{CH}_2\text{Cl}_2$ . In addition, the relationship between TCNQ concentrations and ZIF-8 chemical composition has been investigated through XPS analysis. Particularly, two sample through low and high TCNQ level doping were obtained.

Low TCNQ doping (2 ml) was carried out by introducing 2 ml of 5 mM  $\text{CH}_2\text{Cl}_2$  solution of TCNQ into mix solution consisted of 5 ml of 12.5 mM methanol solution of  $\text{Zn}(\text{NO}_3)_2 \times 6\text{H}_2\text{O}$  and 5 ml of 25 mM methanol solution of MeIm.

High TCNQ doping (4ml) was carried out by introducing 4 ml of 5 mM  $\text{CH}_2\text{Cl}_2$  solution of TCNQ into mix solution consisted of 2 ml of 12.5 mM methanol solution of  $\text{Zn}(\text{NO}_3)_2 \times 6\text{H}_2\text{O}$  and 2 ml of 25 mM methanol solution of MeIm.

The ZIF-8/quartz@TCNQ films were characterized through Uv-vis to test the occurred high and low doping (Figure 27).

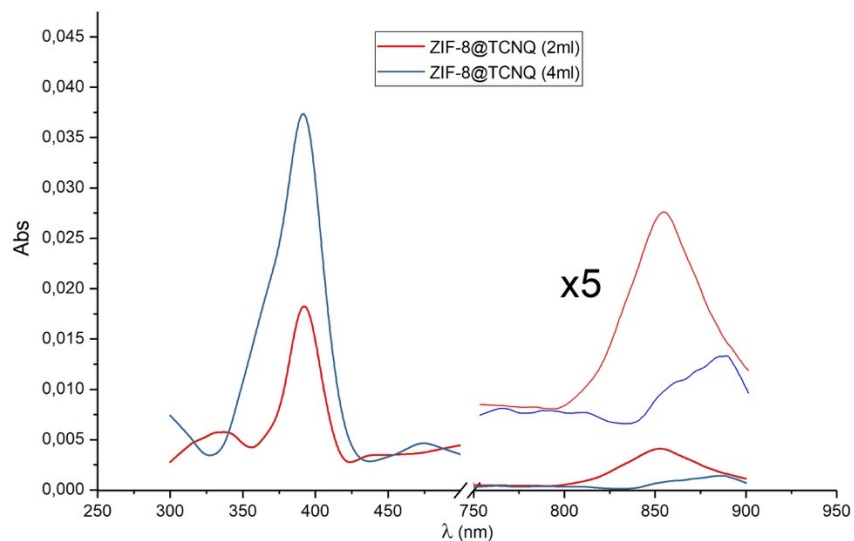
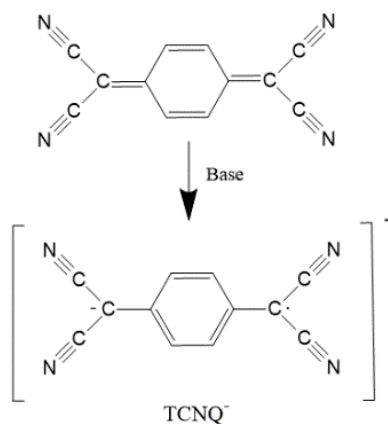


Figure 27: UV-vis spectra of doped ZIF-8/quartz film with 4 ml (high-doping, -) of and 2 ml (low-doping, -) of saturated  $\text{CH}_2\text{Cl}_2$  solution of TCNQ.

The absorption spectra consist of two bands at 391 nm and 850 nm attributable to  $\text{TCNQ}^\circ$  and  $\text{TCNQ}^-$  formation (Figure 27). The  $\text{TCNQ}^\circ/\text{TCNQ}^-$  equilibrium is dependent on polarity of the solvent and the TCNQ dissociation is more prominent at high pH as reported in the following reaction<sup>189</sup> (Scheme 8).



Scheme 8: TCNQ dissociation to form  $\text{TCNQ}^-$  in basic conditions.



The absorption peaks at about 850 nm result less intense than that ones at 391 nm, indicating as the dopant is present as TCNQ° inside ZIF-8 cavities or on its surface.<sup>190</sup>

TCNQ can also act as organic linker and coordinate Zn<sup>2+</sup> cation competing with 2-methylimidazole. FTIR spectroscopy has allowed to prove as TCNQ acts only as guest without compromise the ZIF-8 structure. Indeed, FTIR spectra of ZIF-8@TCNQ systems obtained through low and high doping are comparable to that one of ZIF-8/quartz film, and they show IR signals; at 3135 cm<sup>-1</sup> and at 2900 cm<sup>-1</sup> attributable to N-H and C-N stretching, respectively, at 3100 and 1350 cm<sup>-1</sup> assignable to C-H group of imidazole linker, and a weak signal at about 500 cm<sup>-1</sup> due to coordination bond Zn-N.<sup>191,192</sup>

The relationship between the doping levels and the ZIF-8 chemical composition was investigated through XPS characterizations of the both ZIF-8@TCNQ systems. Table 6 shows as the high doping, concerning the in-situ synthesis of ZIF-8 with the addition of 4 ml of TCNQ determines a higher N 1s concentration proving that TCNQ addition lead to a N-rich MOF formation. However, N:Zn atomic ratio that should be about 4 for the ZIF-8 structure<sup>186</sup>, results higher (7 - 7.8) also for the sample obtained through low-doping indicating the presence of TNCQ inside ZIF-8 cavities.

<u>XPS atomic concentrations ZIF-8@TCNQ (2 ml)</u>				
<i>Si 2p3</i>	<i>C 1s</i>	<i>O 1s</i>	<i>N 1s</i>	<i>Zn 2p3/2</i>
2.5	75.8	12.9	7.8	1.0
<u>XPS atomic concentrations ZIF-8@TCNQ (4 ml)</u>				
<i>Si 2p3</i>	<i>C 1s</i>	<i>O 1s</i>	<i>N 1s</i>	<i>Zn 2p3/2</i>
5.7	70.3	10.2	12.0	1.8

*Table 6: XPS atomic concentrations of Si 2p3, C 1s, O 1s, N 1s, Zn 2p3/2 of the ZIF-8@TCNQ obtained through low (2 ml) and high (4ml) doping in-situ synthesis.*

### 2.2.3 Electrical Characterization

Four-point probe resistivity measurements have allowed to prove that the electrical response of ZIF-8 films changes in function of the dopant-type. In particular, not-doped ZIF-8/quartz film has been used as benchmark and compared with ZIF@I<sub>2</sub> host-guest systems, obtained through in-situ synthesis using MeOH as reaction solvent and post-doping via in water, and ZIF-8@TCNQ obtained through high doping in situ synthesis.

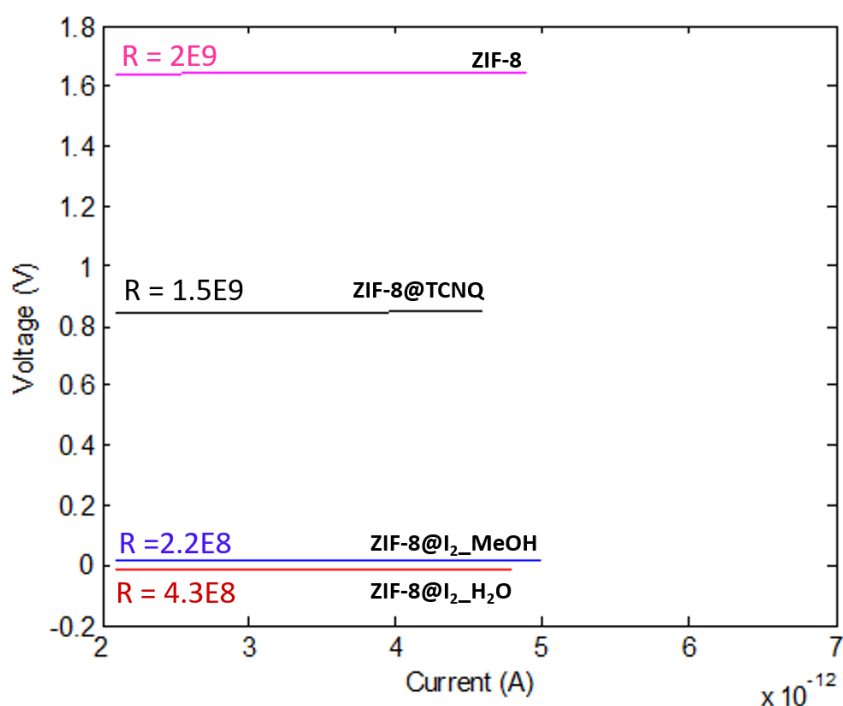


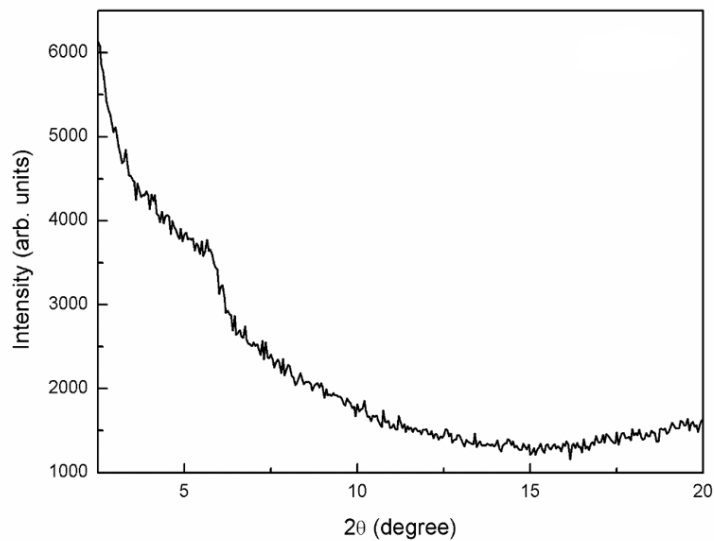
Figure 28: Four-point probe resistivity characterization of not-doped ZIF-8 and ZIF-8@I<sub>2</sub>\_MeOH; ZIF-8@I<sub>2</sub>\_H<sub>2</sub>O, ZIF-8@TCNQ films.

Figure 28 shows the electrical resistivity value of ZIF-8 before and after doping with I<sub>2</sub> and TCNQ. The measurements were carried out by employing a Rc of  $1.6 \times 10^{12} \Omega$  and as above-reported the iodine doping involves a resistivity decrease of ZIF-8 film by an order of magnitude. In particular, the I<sub>2</sub> doping carried out in water results more promising because of it determines an electrical resistivity value changes from  $2.0 \times 10^9 \Omega$ , detected for not-doped ZIF-8, to  $4.3 \times 10^8 \Omega$ . A slightly

electrical difference is detected between ZIF-8@I<sub>2</sub>\_MeOH and ZIF-8@I<sub>2</sub>\_H<sub>2</sub>O. Whereas, TCNQ doping doesn't involve remarkable resistivity improvement of the ZIF-8 material. The electrical resistivity of ZIF-8@TCNQ synthesized via low doping has not been reported because is equal to the relative sample achieved through the high doping. Therefore, the development of doped ZIF-8 films results a novel and valid example of responsive coating for integrated devices, particularly promising in sensor or electrochemical storage field.

### **2.3 Synthesis of ZIF-8 films on Copper foil**

In order to assembly ZIF—8 based lithium ion cells it is necessary to grow ZIF-8 films on a copper substrate, which is a common collector for anode electrodes. Copper foils present surfaces characterized by a strong basic behaviour able to guarantee fast imidazole deprotonation, key step of ZIF-8 crystal formation. ZIF-8 films were grown directly from methanol solution through the SOP protocol above described.<sup>150</sup> In detail, 10 SOP cycles were carried out into MeOH mix solution of Zinc nitrate and 2-methylimidazole at room temperature without any additive. The surface basicity involves fast homogenous and heterogenous nucleation leading to thicker film than those obtained on Si-based surface. However, the high growth rate does not allow to control the crystallinity degree of the film leading to an amorphous ZIF-8 coating. Indeed, in the diffractogram of the ZIF-8/Cu sample, reported in Figure 29, the characteristic diffraction peaks of ZIF-8 are missing and the broad shoulder at low 2θ is attributable to the formation of poorly crystalline material.



*Figure 29: XRD diffractogram of ZIF-8 film grown through 10 SOP cycles from methanol solution on Cu foil.*

ZIF-8 formation was instead proved by FTIR spectroscopy. Figure 30 shows the IR spectra of ZIF-8 film grown on Cu foil and, as reference, the ZIF-8 powder. The two IR spectra are comparable and show identical main vibration modes of the ZIF-8 characteristic functional groups.

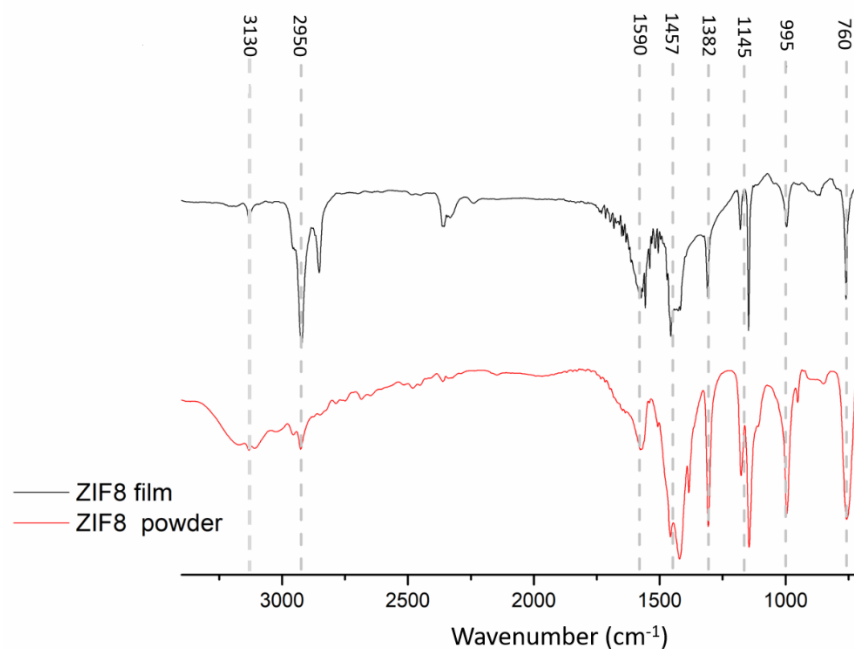


Figure 30: IR spectra of ZIF-8 powder (-) and ZIF-8 film (-) grown on Cu foil through SOP method.

In detail, signals at  $790\text{ cm}^{-1}$  and at  $2950\text{ cm}^{-1}$  are due to the stretching modes of aliphatic C-H whereas the infrared peak at  $3130\text{ cm}^{-1}$  is attributable to aromatic C-H bending. The signals in the region between  $1382$  and  $1457\text{ cm}^{-1}$  are due to aromatic ring vibrations. Whereas, the vibration modes in the region between  $995\text{ cm}^{-1}$  and  $1145\text{ cm}^{-1}$  and the signal centred at  $1590\text{ cm}^{-1}$  are assignable to C-N and C=N functional groups.<sup>191,192</sup> SEM images of ZIF-8/Cu sample obtained after 10 SOP cycles from methanol solution proves the formation of a homogenous and continuous ZIF-8 coating on Cu surface. Figure 31a shows an inter-grown layer consisted of hexagonal closed-packed structures, typical ZIF-8 morphology. In addition, the thickness of Cu coating is about  $3\mu\text{m}$  and was detected through ZIF-8 film cross-section analysis (Figure 31b)

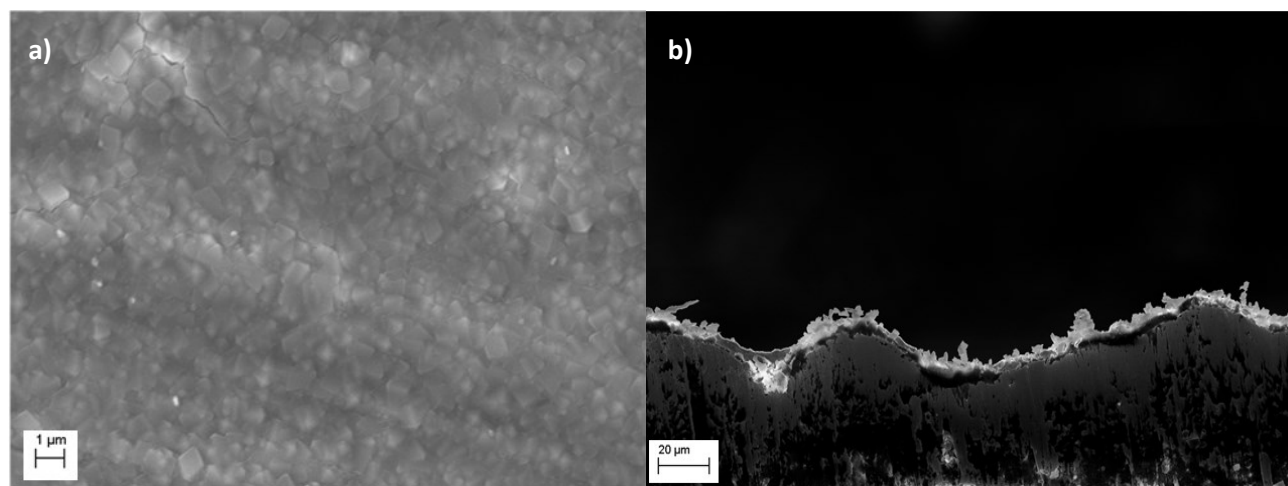


Figure 31: SEM image (a) and cross-section (b) of ZIF-8 film grown on Cu foil through SOP method.

### 2.3.1 Doping of Cu/ZIF-8 films with Lithium acetate

Post synthetic treatments of ZIF-8/Cu films with lithium acetate (LiOAc) have allowed to introduce lithium ions inside their cavities developing  $\text{Li}^+$  doped ZIF-8/Cu electrode through fast and facile route. In Particular, two different doping levels were carried out by using high and low concentrations of lithium acetate, named high and low doping routes. Before LiOAc doping, MeOH trapped inside ZIF-8 pores was removed through post annealing treatments of ZIF-8/Cu films at  $130^\circ\text{C}$  for 30 min. Then, low doping route was implemented by dipping the ZIF-8/Cu sample into 10 ml solution of LiOAc (10 mM) using ethanol and water as solvents in 1:2 ratio. High LiOAc doping was carried out in the same conditions but using 10 ml solution of LiOAc (40 mM). Both doping reactions was carried out at room temperature and for 4h.

FTIR spectroscopy has allowed to detect the chemical composition difference between ZIF-8 undoped and ZIF-8@ $\text{Li}^+$  samples. As shown in Figure 32, the sample ZIF-8@ $\text{Li}^+$  low doping presents a comparable spectrum to ZIF-8 undoped. Particularly, both ZIF-8 undoped and ZIF-8@ $\text{Li}^+$  low doping, show the typical absorption peaks of ZIF-8 as above reported in Figure 32. However, the IR signals of ZIF-8@ $\text{Li}^+$  low doping are slightly less intense of that one's of ZIF-8 undoped proving as the low LiOAc concentration doesn't lead to particular ZIF-8 chemical composition changes. Whereas, ZIF-8@ $\text{Li}^+$  high doping shows less intense signals and the peaks centred in the

region between 1400 and 1600  $\text{cm}^{-1}$  consists of a broad band attributable to the presence of acetate groups whose signals overlap with ZIF-8 bands at 1583  $\text{cm}^{-1}$  and 1440  $\text{cm}^{-1}$ .<sup>193</sup>

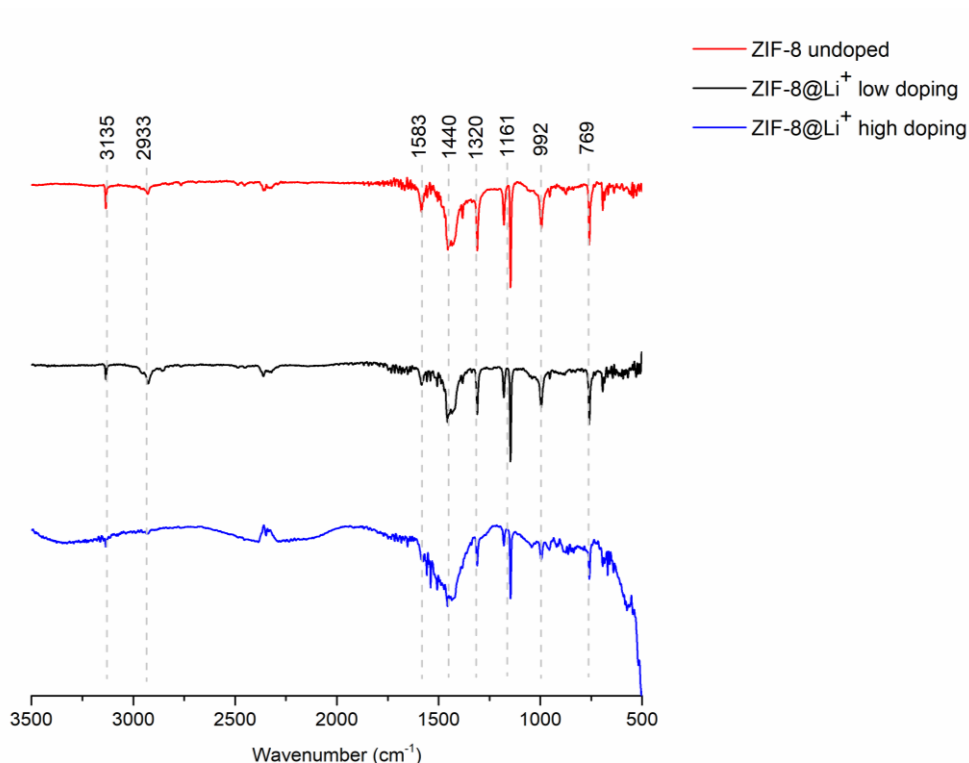
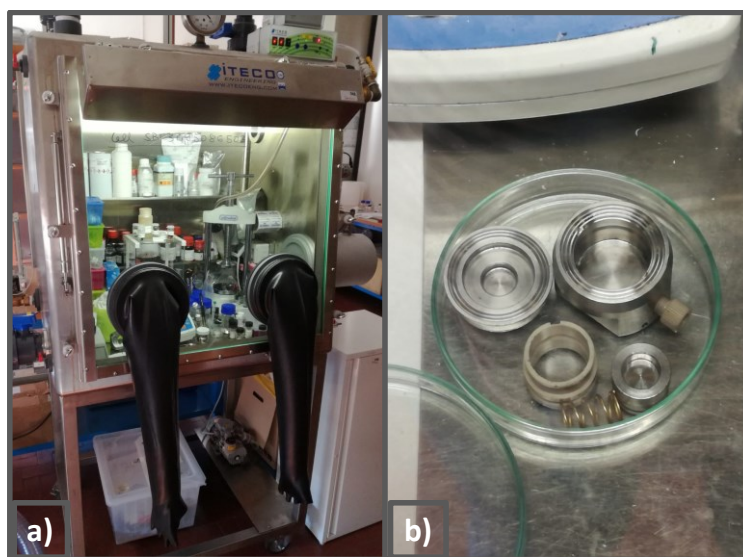


Figure 32: IR spectra of ZIF-8/Cu film undoped (-), of ZIF-8@Li<sup>+</sup> obtained through low doping via (-) and ZIF-8@Li<sup>+</sup> obtained through high doping via (-).

### 2.3.2 Electrochemical Characterization of ZIF-8/Cu electrode

Undoped and Li<sup>+</sup> doped ZIF-8/Cu films were assembled in lithium ion cells in order to test their electrochemical behaviour. In Particular, cyclic voltammetry and galvanostatic measurements were carried out to investigate the electrochemical activity of the ZIF-8 thin films as function of lithium voltage range and to study the reversibility of redox charge-discharge processes. The cells were

assembled in an Ar glove box kept in anhydrous conditions ( $\text{ppm}(\text{H}_2\text{O}) < 0.1$ ) (Figure 33 a) and by using EL-Cell Std as devices (Figure 33 b). Figure 34 shows the different steps of coin cell assembly of the electrode half-cells in glove-box, starting from a coin cell base (Figure 34 a) where the active material is placed (Figure 34 b). Then, a separator with LP30 electrolyte, consisting of a 1 molality solution of hexafluorophosphate,  $\text{LiPF}_6$ , dissolved into a mixture of ethylene carbonate and dimethyl carbonate, 1:1 in volume, is deposited (Figure 34c-d) and lithium foil is used as metal film (Figure 34e). The cell is sealed through appropriate spring and spacer (Figure 34 f) and closed with a coin cell lid in order to obtain the EL-Cell Std reported in Figure 35a. Galvanostatic cycling was carried out by connecting the achieved EL-Cell to a defined channel of battery analyser (Figure 35b-c), in the range 3mV-10mV and employing a current density of  $J: 5\mu\text{A cm}^{-2}$ .



*Figure 33: Picture of Ar glove box (6a) and of the components of EL-Cell Std (6b).*



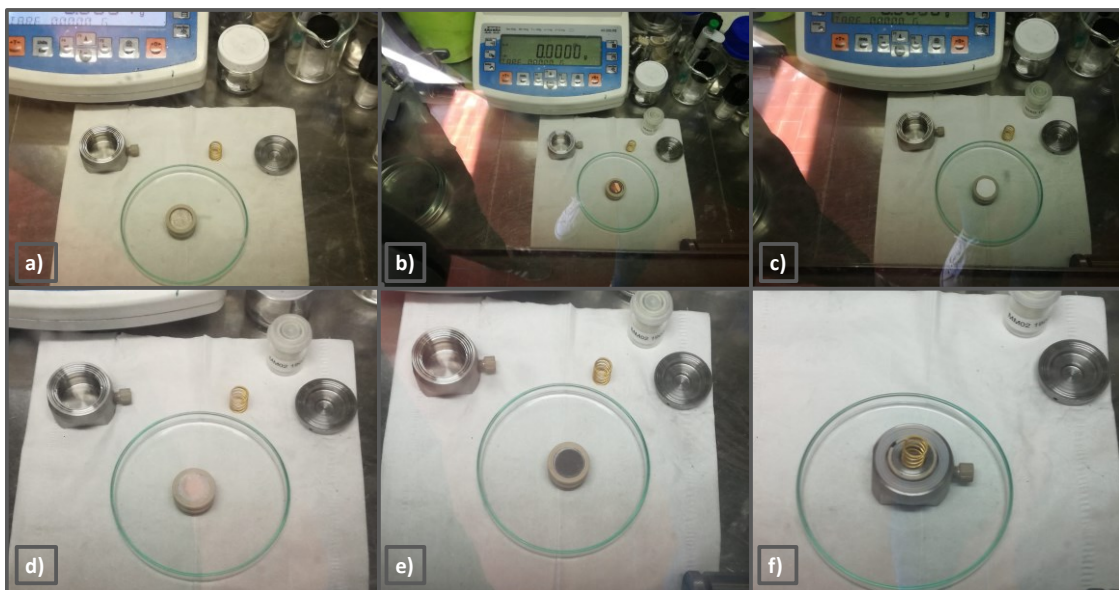


Figure 34: Steps of coin cell assembly: a) coin cell base, b) active material consisted of ZIF-8/Cu electrode, c) separator, d) LP30 electrolyte, e) lithium foil; f) spring and coin cell lid.

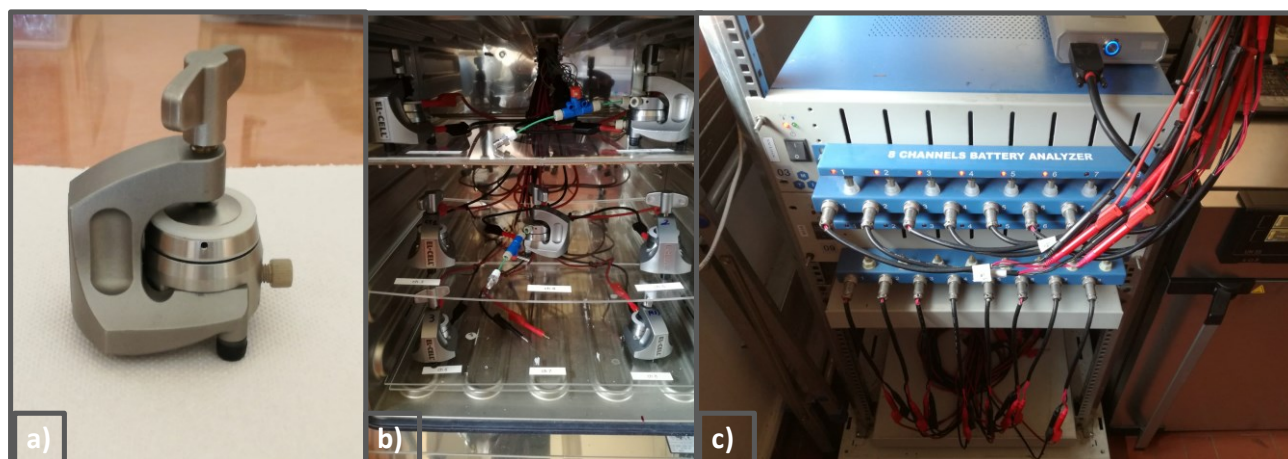


Figure 35: El-Cell std (a) and channel battery analyser (b-c).

- Galvanostatic Measurements

All three samples showed a moderate lithium electrolyte permeability and guarantee a suitable ionic charge transfer but doesn't contribute to capacity increase. Figure 36 reports charge/discharge

capacity density as function of cycle number of the ZIF-8 undoped and ZIF-8@Li<sup>+</sup> electrodes achieved through high and low doping route.

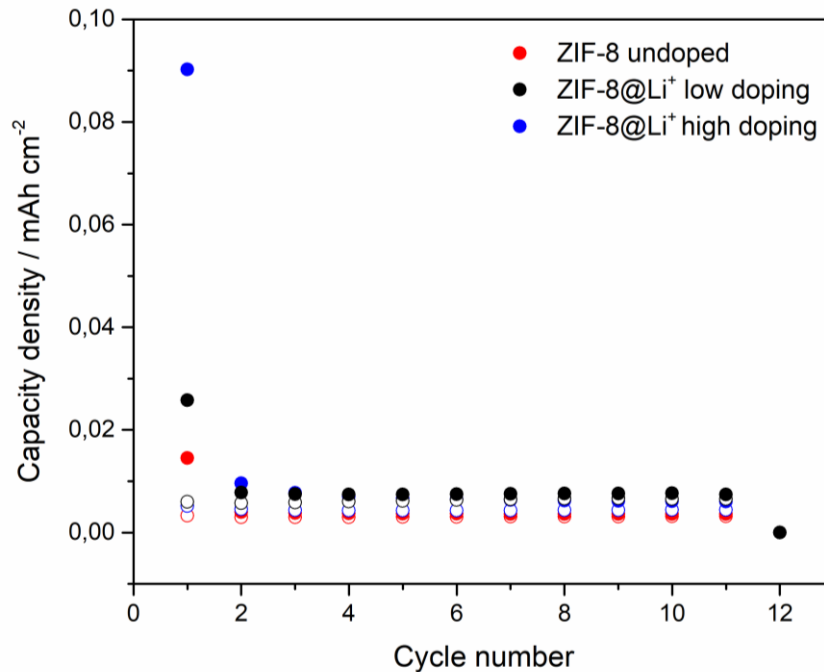


Figure 36: Capacity density  $\text{mAh cm}^{-2}$  of ZIF-8 undoped (red), ZIF-8@Li<sup>+</sup> low doping (black) and ZIF-8@Li<sup>+</sup> high doping (blue) for 10 charge (empty symbol)-discharge (filled symbol) processes in the range  $5\text{mV}$ - $3\text{mV}$  and with density current of  $5\mu\text{A cm}^{-2}$ .

The capacity density values are very low with stabilization capacity about  $0.01 \text{ mAh cm}^{-2}$ . The capacity density of for ZIF-8@Li<sup>+</sup> high doping sample at first discharge results greater with value of  $0.09 \text{ mAh cm}^{-2}$  indicating that the lithium acetate insertion give some the electrochemical activity of the ZIF-8 electrode, but this activity strongly decrease after the first discharge indicating the presence of some irreversible degradation. Whereas ZIF-8 undoped and ZIF-8@Li<sup>+</sup> low doping samples shows a comparable first discharge capacity density

The electrochemical lithium loading has been investigated through charge/discharge voltage profiles as function of the capacity density related to the first three redox lithiation/delithiation processes. As shown in Figure 37, the span of voltage plateau increases with the LiOAc concentration. Indeed, ZIF-8@Li<sup>+</sup> high doping has an intrinsic electrochemical activity presenting two pseudo plateaus at about 1.6 and 1.2 mV, which disappears after the first three cycles. Whereas ZIF-8@Li<sup>+</sup> high doping shows a continue voltage slope and ZIF-8 undoped is characterized by an electrochemical Li unreactivity.

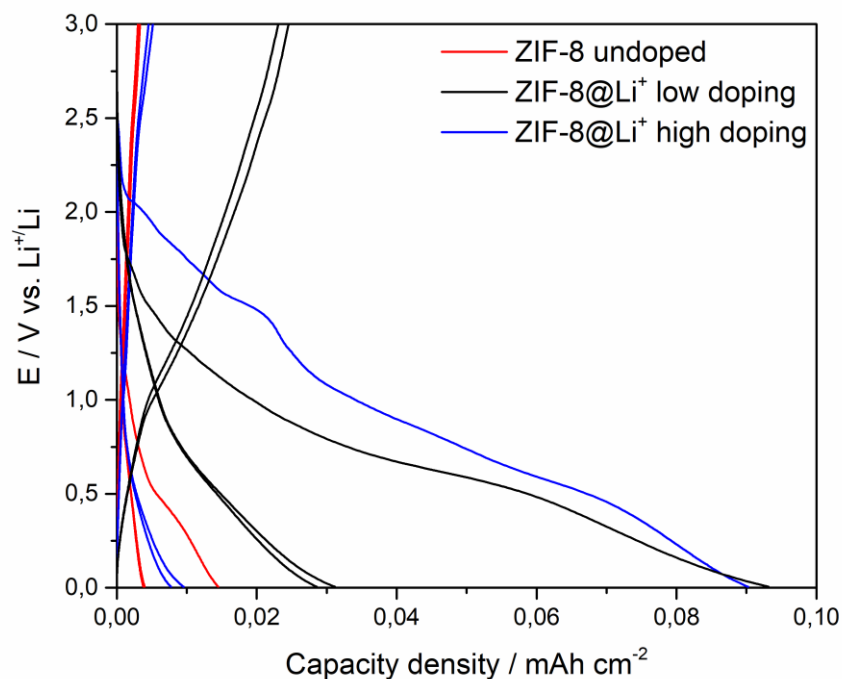


Figure 37: Voltage profile as function of Capacity density mAh cm<sup>-2</sup> of ZIF-8 undoped ( - ), ZIF-8@Li<sup>+</sup> low doping ( - ) and ZIF-8@Li<sup>+</sup> high doping ( - ) for first three charge-discharge processes.

The galvanostatic performances of the Cu/ZIF-8 undoped and Li<sup>+</sup> doped films demonstrated that the high porosity and large surface area of ZIF-8 guarantee a suitable permeability of electrolyte and by modulating the LiOAc doping it is possible to control the electrochemical loading of ZIF-8 films.

- Cyclic Voltammetry

The voltage profiles in Figure 38 describe the redox processes related to lithiation and delithiation of ZIF-8/Cu electrodes. Cyclic Voltammetry (CV) experiments have allowed to confirm the above reported galvanostatic outcomes and therefore the electrochemical activity of the ZIF-8/Cu thin films and as, it changes as function of the film chemical nature. CV test was carried out in the range 3mV-10mV and with scan rate of 0.5 mV/s. Figure 38a reports the voltage profile of (-) Li /EC:DMC 1:1 v/v LiPF<sub>6</sub> 1m/ W.E. (+) cell using as working electrode Cu benchmark. Figure 38b and 38c show the voltage profile of (-) Li /EC:DMC 1:1 v/v LiPF<sub>6</sub> 1m/ W.E. (+) cells using as working electrodes ZIF-8 undoped and ZIF-8@Li<sup>+</sup> high doping, respectively. The CV curve of ZIF-8@Li<sup>+</sup> low doping is not shown because of they present the same profile of ZIF-8 undoped.

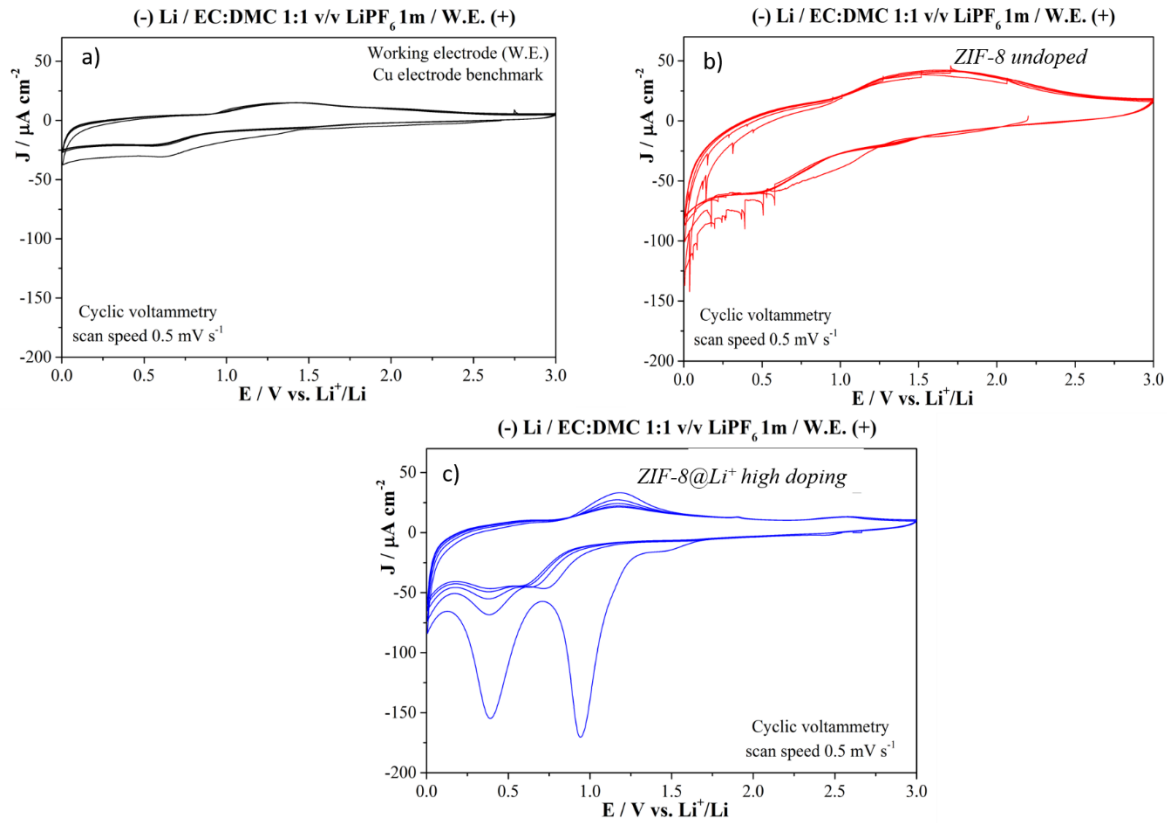


Figure 38: Voltage profile  $E/V$  vs.  $\text{Li}^+/\text{Li}$  as function of Current density  $J/\mu\text{A cm}^{-2}$  of Cu benchmark (7a, -) of ZIF-8 undoped (7b, -) and of ZIF-8@Li<sup>+</sup> high doping (7c, -).

Both the ZIF-8/Cu electrodes, undoped and Li<sup>+</sup> doped, show an intrinsic reversible electrochemical activity respect to the CV curve of Cu benchmark, even though some irreversible processes have been observed for the Li<sup>+</sup> doped sample. In particular., the ZIF-8 undoped shows a two reduction signals at ~ 0.5 V and 0.2 V vs Li, respectively. The electrochemical noise is probably attributable to contact losses during experimental CV test. The electrochemical activity of ZIF-8@Li<sup>+</sup> high doping electrode results more noticeable both in first and following redox processes than that one of ZIF-8 undoped. ZIF-8@Li<sup>+</sup> high doping electrode shows, two intense reduction peaks at ~ 0.95 and 0.4 V vs Li in the first cathodic process, and discrete electrochemical activity at V < 0.1V vs Li. In addition, ZIF-8@Li<sup>+</sup> high doping electrode shows a single oxidation peak at ~ 1.2 V vs Li and two weak signals at ~1.8 and 2.5 V vs Li. The electrochemical activity of ZIF-8@Li<sup>+</sup> high doping electrode decreases with the cycle number and the reduction signal at ~ 0.95 V shifts towards lower Li voltages (0.75 - 0.65 V), suggesting the occurrence of some irreversible reduction processes

## REFERENCES

---

- (148) Mannino, G.; Ruggeri, R.; Alberti, A.; Privitera, V.; Fortunato, G.; Maiolo, L. Electrical Properties of Ultrathin SiO<sub>2</sub> Layer Deposited at 50°C by Inductively Coupled Plasma-Enhanced Chemical Vapor Deposition. *Appl. Phys. Express* **2012**, *5*, 021103-021105.
- (149) Mannino, G.; Spinella, C.; Ruggeri, R.; Mio, A.; Rimini, E. Transient Crystal Grain Nucleation in As Doped Amorphous Silicon. *Mater. Lett.* **2014**, *126*, 28–31.
- (150) Lu, G.; Hupp, J. T. Metal-Organic Frameworks as Sensors: A ZIF-8 Based Fabry-Perot Device as a Selective Sensor for Chemical Vapors and Gases. *J. Am. Chem. Soc.* **2010**, *132*, 7832–7833.
- (151) The CP2K developers group. <http://www.cp2k.org>
- (152) Goedecker, S.; Teter, M.; Hutter, J. Separable due-space Gaussian pseudopotentials, *Phys. Rev. B* **1996**, *54*, 1703-1710.
- (153) Perdew, J.P.; Burke, K.; Ernzerhof, M. Generalized Gradient Approximation Made Simple, *Phys. Rev. Lett.* **1996**, *77* 3865–3868.
- (154) Bengtsson, L. Dipole correction for surface supercell calculations, *Phys. Rev. B*, 1999, *59*, 12301–12304.
- (155) The chemcraft developers group. <https://www.chemcraftprog.com>
- (156) Andreussi, O.; Dabo, I.; Marzari, N.; Andreussi, O.; Dabo, I.; Marzari, N. Revised self-consistent continuum solvation in electronic-structure calculations, *J. Chem. Phys.*, **2012**, *136*, 064102-064121.
- (157) Gražulis, S.; Merkys, A.; Vaitkus, A.; Okulič-Kazarinas, M. Computing stoichiometric molecular composition from crystal structures, *J. Appl. Cryst.* **2015**, *48*, 85-91.
- (158) Gražulis, S.; Daškevič, A.; Merkys, A.; Chateigner, D.; Lutterotti, L.; Quirós, M.; Serebryanaya, N.R.; Moeck, P.; Downs, R.T.; LeBail, A. Crystallography Open Database (COD): an

---

open-access collection of crystal structures and platform for world-wide collaboration, *Nucleic Acids Res.* **2012**, *40*, D420-D427.

(159) He, M.; Yao, J.; Lunxi, L.; Zhong, Z.; Chen, F.; Wang, H. Aqueous solution synthesis of ZIF-8 films on a porous nylon substrate by contra diffusion method, *Microporous and Mesoporous Materials* **2013**, *179*, 10-16.

(160) Shekhah, O.; Eddaoudi, M. The liquid phase epitaxy method for the construction of oriented ZIF-8 thin films with controlled growth on functionalized surfaces, *Chem. Commun.* **2013**, *49*, 10079-10081.

(161) Jian, M.; Liu, B.; Liu, R.; Qu, J.; Wang, H.; Zhang, X. Water-Based Synthesis of Zeolitic Imidazolate Framework-8 with High Morphology Level at Room Temperature. *RSC Adv.* **2015**, *5*, 48433–48441.

(162) Lai, L.S.; Yeong, Y.F.; Ani, N.C.; Lau, K.K.; Shariff, A.M. Effect of synthesis parameters on the formation of zeolitic imidazolate framework 8 (ZIF-8) nanoparticles for CO<sub>2</sub> adsorption, *Sci. Technol.* **2014**, *32*, 520–528.

(163) Condorelli, G.G.; Motta, A.; Favazza, M.; Fragalà, I.L.; Busi, M.; Menozzi, E.; Dalcanale, E.; Crstofolini, L. Grafting Cavitands on the Si (100) surface. *Langmuir*, **2006**, *22*, 11126-11133.

(164) Ruggeri, R.; Privitera, V.; Spinella, C.; Fazio, E.; Neri, F.; De Bastiani, R.; GGrimaldi, M.G.; Ausilia, M.; Stefano, D.; Marco, D.; Mannino, G. Crystallization of Deposited Amorphous Silicon by Infrared Laser Irradiation, *J. Electrochem. Soc.* **2011**, *158*, H25–H29.

(165) Kulhánek, J.; Bureš, F.; Ludwig, M. Convenient Methods for Preparing  $\pi$ -Conjugated Linkers as Building Blocks for Modular Chemistry. *Beilstein J. Org. Chem.* **2009**, *5*, 1–5.

(166) Moreno, J. M.; Veltý, A.; Díaz, U.; Corma, A. Synthesis of 2D and 3D MOFs with Tuneable Lewis Acidity from Preformed 1D Hybrid Sub-Domains. *Chem. Sci.* **2019**, *10*, 2053–2066.

(167) Qin, J. S.; Yuan, S.; Wang, Q.; Alsalmé, A.; Zhou, H. C. Mixed-Linker Strategy for the Construction of Multifunctional Metal-Organic Frameworks. *J. Mater. Chem. A* **2017**, *5*, 4280–4291.

- 
- (168) Wang, Z.; Cohen, S. M. Postsynthetic Modification of Metal-Organic Frameworks. *Chem. Soc. Rev.* **2009**, *38*, 1315–1329.
- (169) Miyasaka, H. Control of Charge Transfer in Donor/acceptor Metal-Organic Frameworks. *Acc. Chem. Res.* **2013**, *46*, 248–257.
- (170) Shiozawa, H.; Bayer, B. C.; Peterlik, H.; Meyer, J. C.; Lang, W.; Pichler, T. Doping of Metal-Organic Frameworks towards Resistive Sensing. *Sci. Rep.* **2017**, *7*, 1–8.
- (171) Ma, L.; Hu, P.; Jiang, H.; Kloc, C.; Sun, H.; Soci, C.; Voityuk, A. A.; Michel-Beyerle, M. E.; Gurzadyan, G. G. Single Photon Triggered Dianion Formation in TCNQ and F 4 TCNQ Crystals. *Sci. Rep.* **2016**, *6*, 1–7.
- (172) Kirtley, J. R.; Mannhart, J. When TTF Met TCNQ. *Nat. Mater.* **2008**, *7*, 520–521.
- (173) Park, C.; Atalla, V.; Smith, S.; Yoon, M. Understanding the Charge Transfer at the Interface of Electron Donors and Acceptors: TTF-TCNQ as an Example. *ACS Appl. Mater. Interfaces* **2017**, *9*, 27266–27272.
- (174) Niehaus, T. A.; Hofbeck, T.; Yersin, H. Charge-Transfer Excited States in Phosphorescent Organo-Transition Metal Compounds: A Difficult Case for Time Dependent Density Functional Theory *RSC Adv.* **2015**, *5*, 63318–63329.
- (175) Blowey, P. J.; Velari, S.; Rochford, L. A.; Duncan, D. A.; Warr, D. A.; Lee, T. L.; De Vita, A.; Costantini, G.; Woodruff, D. P. Re-Evaluating How Charge Transfer Modifies the Conformation of Adsorbed Molecules. *Nanoscale* **2018**, *10*, 14984–14992.
- (176) Otero, R.; Vázquez de Parga, A. L.; Gallego, J. M. Electronic, Structural and Chemical Effects of Charge-Transfer at Organic/inorganic Interfaces. *Surf. Sci. Rep.* **2017**, *72*, 105–145.
- (177) Talin, A. A.; Centrone, A.; Ford, A. C.; Foster, M. E.; Stavila, V.; Haney, P.; Kinney, R. A.; Szalai, V.; El Gabaly, F.; Yoon, H. P.; Léonard, F.; Allendorf, M. D. Tunable Electrical Conductivity in Metal-Organic Framework Thin-Film Devices. *Science*. **2014**, *343*, 66–69.
- (178) Shiozawa, H.; Bayer, B. C.; Peterlik, H.; Meyer, J. C.; Lang, W.; Pichler, T. Doping of Metal-Organic Frameworks towards Resistive Sensing. *Sci. Rep.* **2017**, *7*, 2439–2446.



- 
- (179) Ding, X.; Tuikka, M.; Haukka, M. Halogen Bonding in Crystal Engineering. **2012**, *10.1021/ar5001555*.
- (180) El-Shabouri, S. R.; Emara, K. M.; Khashaba, P. Y.; Mohamed, A. M. Charge-Transfer Complexation for Spectrophotometric Assay of Certain Imidazole Antifungal Drugs. *Anal. Lett.* **1998**, *31*, 1367–1385.
- (181) Mahmoud, R. A.; El-samahy, A. A.; Rabia, M. M. Electron Donor-Acceptor Complexes of Iodine with Imidazole and some its Derivates. *Bulletin de la société Chimiques Belges*, **1983**, *92*, 923–928.
- (182) Priimagi, A.; Cavallo, G.; Metrangolo, P.; Resnati, G. The Halogen Bond in the Design of Functional Supramolecular Materials: Recent Advances. *Acc. Chem. Res.* **2013**, *46*, 2686–2695.
- (183) Xie, W.; Cui, D.; Zhang, S.-R.; Xu, Y.-H.; Jiang, D.-L. Iodine Capture in Porous Organic Polymers and Metal–organic Frameworks Materials. *Mater. Horizons* **2019**, *10.1039/C8MH01656A*.
- (184) Awtrey, A. D.; Connick, R. E. The Absorption Spectra of I<sub>2</sub>, I<sub>3</sub><sup>-</sup>, I<sup>-</sup>, IO<sub>3</sub><sup>-</sup>, S<sub>4</sub>O<sub>6</sub><sup>-</sup> and S<sub>2</sub>O<sub>3</sub><sup>-</sup>. Heat of the Reaction I<sub>3</sub><sup>-</sup> = I<sub>2</sub> + I<sup>-</sup>. *J. Am. Chem. Soc.* **1951**, *73*, 1842–1843.
- (185) Wei, Y.; Liu, C.G.; Mo, L.P. Ultraviolet absorption spectra of iodine, iodide ion and triiodide ion, *Guang pu*, **2005**, *25*, 86-88.
- (186) Monforte, F.; Mannino, G.; Alberti, A.; Smecca, E.; Italia, M.; Motta, A.; Tudisco, C.; Condorelli, G. G. Heterogeneous Growth of Continuous ZIF-8 Films on Low-Temperature Amorphous Silicon. *Appl. Surf. Sci.* **2018**, *473* (September 2018), 182–189.
- (187) Sherwood, P.; M. A. X-Ray Photoelectron Spectroscopic Studies of Some Iodine Compounds. *J. Chem. Soc. Faraday Trans. 2 Mol. Chem. Phys.* **1976**, *72*, 1805–1820.
- (188) Chen, T. H.; Popov, I.; Kaveevivitchai, W.; Miljanić, O. Š. Metal-Organic Frameworks: Rise of the Ligands. *Chem. Mater.* **2014**, *26*, 4322–4325.
- (189) Boyd, R. H.; Phillips, W. D. Solution Dimerization of the Tetracyanoquinodimethane Ion Radical. *J. Chem. Phys.* **1965**, *43*, 2927–2929.

---

(190) Shimomura, S.; Matsuda, R.; Tsujino, T.; Kawamura, T.; Kitagawa, S. TCNQ Dianion-Based Coordination Polymer Whose Open Framework Shows Charge-Transfer Type Guest Inclusion. *J. Am. Chem. Soc.* **2006**, *128*, 16416–16417.

(191) Kaur, H.; Mohanta, G. C.; Gupta, V.; Kukkar, D.; Tyagi, S. Synthesis and Characterization of ZIF-8 Nanoparticles for Controlled Release of 6-Mercaptopurine Drug. *J. Drug Deliv. Sci. Technol.* **2017**, *41*, 106–112.

(192) Zhang, Y.; Jia, Y.; Hou, L. Synthesis of Zeolitic Imidazolate Framework-8 on Polyester Fiber for PM 2.5 Removal. *RSC Adv.* **2018**, *8*, 31471–31477.

(193) Ito, K.; Bernstein, H. J. The Vibrational Spectra of the Formate, Acetate, and Oxalate Ions. *Can. J. Chem.* **1956**, *34*, 170–178.

## Chapter 3

### 3 Direct Growth from Solution of Fe-Based MIL-Frameworks

Fe-based MIL frameworks, consisted of  $\text{FeO}_x$ -terephthalate units, respect to other MOF topologies are characterized by a complex flexible structure with tunable pore size.<sup>194,195,196</sup> Among all MIL topology, MIL-101 and MIL-88, consisted of trinuclear transition metal carboxylates complexes (metal like  $\text{Cr}^{3+}$ ,  $\text{Fe}^{3+}$ ,  $\text{V}^{3+}$ ,  $\text{Al}^{3+}$ ;  $\text{I}^{3+}$  or  $\text{Sc}^{3+}$ ) conventionally described as trigonal prism, are framework isomers distinguishable for their intrinsic crystal structure.<sup>197,198</sup>

Extreme synthetic conditions are required to MIL crystal formation. In particular, long reaction times, above one day, high temperatures and additive use are needed to MIL nucleation.<sup>199,200,201</sup>

Design of MIL film is even more difficult because of both their intrinsic structure and the surface terminations affect the MOF nucleation and growth in terms of morphology and thickness.<sup>202,203,204</sup>

Surfaces pre-functionalization by carboxylate-based monolayers can drive MIL nucleation through covalent interactions between  $\text{-COO}^-$  surface terminations and  $\text{Fe}^{3+}$  centres or  $\text{FeO}$  clusters in solution.<sup>205</sup> However, the few examples of Fe-MIL film, have been mainly obtained through powder

deposition techniques like Langmuir Blodgett and spin or dip coating involving more deposition steps and long reaction time.<sup>204,206,207</sup> Therefore, the implementation of novel synthesis routes,

characterized by facile and fast protocols, is needed to growth MIL film or membrane. Thanks to its hydrophobic-hydrophilic dual nature, MIL is a versatile coating with an excellent reactivity towards both polar and non-polar molecules.<sup>208</sup> On the other hand, the introducing of functional groups like -

$\text{OH}$  and  $\text{-NH}_2$  on the MIL frameworks allows to control the surface chemistry and to modulate the chemical-physical properties ensuring the selectivity needed for application fields like sensor or catalysis.<sup>209,210,211</sup> In addition, Fe-based MIL films are suitable for energy storage devices because

their reversible  $\text{Fe}^{2+}/\text{Fe}^{3+}$  redox transitions, make them active materials for electrochemical cells.<sup>212,213</sup> Direct growth from solution is a promising alternative synthetic route to directly deposit

MIL on collector like copper or aluminium avoiding powders deposition processes followed by repeated annealing's that can cause cracks and structural defect. In this chapter, the direct growth of different MIL topologies is reported. NH<sub>2</sub>-MIL-101 and NH<sub>2</sub>-MIL-88 were obtained on bare and pre-functionalized Si surfaces through different synthetic routes proving that the synthetic protocol affects not only the growth rate but also the film's morphology and thickness. A novel two-step strategy based on sol-gel deposition of iron oxide and followed by the growth of MOF from a carboxylic acid solution, was implemented to realize MIL-based composite. EIS spectroscopy shows that the Cu/MIL electrode has a very low intrinsic electrical resistivity, therefore representing a promising hybrid active material.

### 3.1 Synthesis of Fe-MIL-frameworks on Si Surface

Iron-based MIL thin films were directly grown from solution on Si (100) surface via three different synthetic routes. By modulating experimental parameters such as the introduction of acid additives directly in solution (i.e. acetic acid), the reaction times and the presence of carboxylates-based self-assembled monolayers (SAMs), it was possible to control the morphology, the thickness and crystallinity of films and, more important, the phase (NH<sub>2</sub>-MIL-101 or NH<sub>2</sub>-MIL-88). Monolayers constituted of pure, well defined and monodispersed NH<sub>2</sub>-MIL-101 octahedral crystals were obtained after 4h in the presence of acetic acid, which favours crystallization following reduced growth rate. Longer reaction times (8h) lead to well-crystallized NH<sub>2</sub>-MIL-88 hexagonal grains embedded in a matrix of tiny NH<sub>2</sub>-MIL-101 crystals. In the absence of acetic acid, the deposition is faster but leads to poorly crystalline films mainly consisting of mixtures of NH<sub>2</sub>-MIL-88 and NH<sub>2</sub>-MIL-101 grains already after 4 h. Surface pre-functionalization with 4-vinylbenzoic acid SAMs allows to optimize both the crystallization and the growth rate leading to thicker crystalline films of NH<sub>2</sub>-MIL-88 already after 4h. XPS analysis showed that NH<sub>2</sub>-MIL-88 crystals obtained on carboxylate SAMs are mixed with iron oxide.

The advantages of this study are:

- The realization of iron-based MIL- film allows to obtain redox active coating for electrode surface. The use of iron salts as inorganic precursors involves low-cost and environmentally friendly synthesis. In addition, Fe-based MIL guarantees a reversible redox Fe<sup>2+</sup>/Fe<sup>3+</sup> equilibrium suitable to electrochemical storage device.

- Synthesis of MIL films through direct growth from solution allowed to develop facile strategies at moderately temperatures involving short reaction times respect that one reported in literature.
- The different synthesis protocols lead to MIL films distinguishable by morphology, composition, thickness layer and crystallinity.

The growth rate was optimized by implementing a novel synthesis strategy based on MIL growth on carboxylate-based Si surface. Carboxylate SAM increased the heterogenous nucleation which leads to a continuous film of NH<sub>2</sub>-MIL-88 after only 4h. In addition, the covalent interactions between COO<sup>-</sup> termination of Si surface and Fe<sup>3+</sup> centres promoted the formation an iron oxide matrix in which MIL framework is embedded.

### 3.1.1 Synthesis strategy to control MIL morphology and film coating

Native SiO<sub>2</sub> grown on Czochralski-grown B doped Si (100) substrate (2×2 cm in size) was dipped in HF (1%) for 90s in order to obtain H-terminated Si surface and remove the native surface oxide. The substrate was quickly rinsed in deionized water, dried in a stream of nitrogen and immediately introduced in the reaction solution for MOF film growth. Fe-based NH<sub>2</sub>-MIL films was obtained through solvothermal reaction by dipping Si surface in a DMF solution consisted of Iron (III) chloride hexahydrate and 2-aminoterephthalic acid, used as metal and organic precursors, respectively; with molar ratios of 1:1. Three synthetic methods were implemented to obtained different NH<sub>2</sub>-MIL structures: the direct growth from solution in acid conditions with the addition of glacial acetic acid (*GAA route*), the direct growth without acid additive use (*free-additive route*) and, the growth on 4-vinylbenzoic acid SAM (*4-VBA route*) reported in the next paragraph. The DMF mix solutions were placed in an oil bath at 120° C for all three above-mentioned routes, by varying the dipping time between 4 and 16 hours. Lastly, the sample was rinsed in DMF and dried in a stream of nitrogen.

*MIL film characterization:* The Ellipsometric measurements were performed using a VASE instrument (J.A. Woollam) which is better suited for transparent samples in order to measure on the same position ellipsometric and transmittance data thanks to a vertical 9-29 configuration.

Field emission scanning electron microscope (Zeiss Supra35 FE-SEM) equipped with EDX microanalysis system (Oxford Instruments, X-MAX, 80 mm<sup>2</sup>) was used to observe morphology.

XPS spectra were run with a PHI 5600 multi-technique ESCA-Auger spectrometer equipped with a monochromatic Al K $\alpha$  X-ray source. Analyses were carried out with a photo-electron angle of 45° (relative to the sample surface) with an acceptance angle of  $\pm 7^\circ$ . The XPS binding energy (BE) scale was calibrated by centring the C 1s peak due to hydrocarbon moieties and “adventitious” carbon at 285.0 eV. XPS atomic concentration was evaluated by estimating the integrated area of C1s, O1s, Si 2p<sub>3</sub>, N1s, Cl 2p, Fe 2p<sub>3/2</sub>, Fe 3p peaks corrected for the corresponding relative atomic sensitivity factor ( $S_x$ ) based on empirical data reported by Wagner and corrected for the transmission function of the spectrometer.

The crystal structure of MIL film was determined by X-ray diffraction methods. Intensity data were obtained at 190 K on a Bruker APEX II equipped with a charge-coupled device area detector and a graphite monochromator (Mo K $\alpha$  radiation  $\lambda = 0.71073 \text{ \AA}$ ).

### **3.1.2 GAA and free-additive synthetic strategies to achieve Fe-Based MIL films**

Fe-based MIL were directly grown on Si (100) from a DMF solution of FeCl<sub>3</sub> and 2-amino terephthalic acid by increasing the dipping time from 30 min up to 3.5 hours in order to evaluate the surface coverage. Figure 39 reports the direct transmittance measurements of the samples obtained at increasing dipping time from 300 nm to 2100 nm at normal incidence.

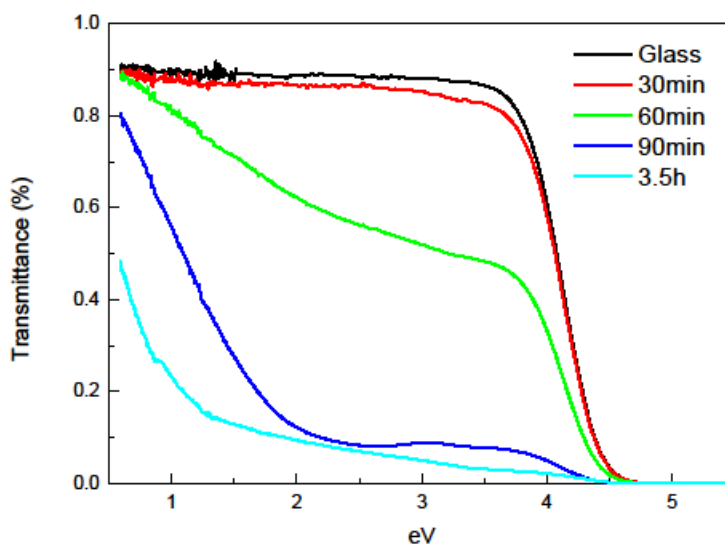


Figure 39: Transmittance spectrum of MIL film compared to bare glass and, as function of dipping time

Substrate coverage, compared to bare glass substrate, is negligible at 30 min whereas it is almost complete for 3.5 hours where only far infrared wavelengths are partially transmitted. The films transmittance drop recorded after 3h suggests the needed reaction time to MIL formation confirming the data reported by Carson et al.<sup>198</sup> By considering the optical outcomes, a layer of isolated NH<sub>2</sub>-MIL-101(Fe) crystals was grown from a DMF solution using 2-aminoterephthalic acid and FeCl<sub>3</sub>×6H<sub>2</sub>O as reactants and acetic acid as additive (GAA route) after 4h. The crystals are characterized by a regular and well-defined octahedral shape with sizes ranging from 150 to 300 nm (Figure 40).

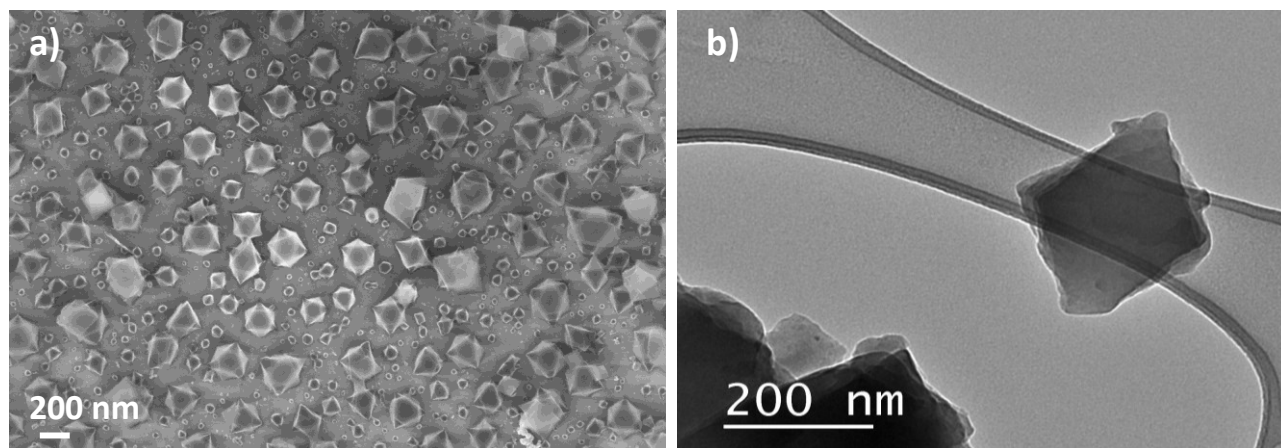
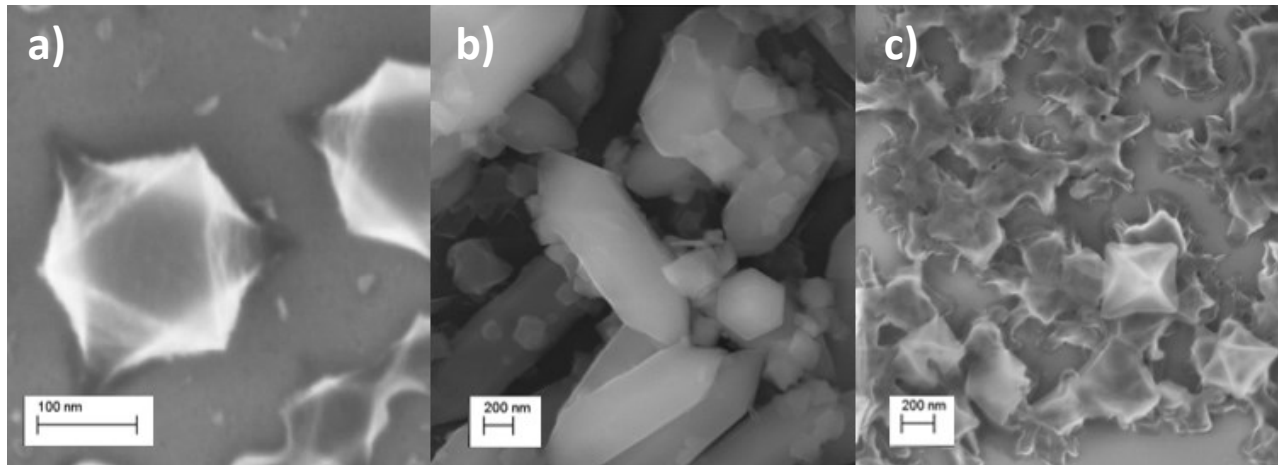


Figure 40: SEM (a) and TEM (b) images of  $\text{NH}_2\text{-MIL-101(Fe)}$  layers.<sup>214</sup>

In both cases, SEM and TEM analyses show that the layers consist of octahedrons, which are typical of MIL-101 crystals due to their cubic symmetry,<sup>215,216</sup> observed mainly along the [111] direction.

In order to investigate as the reaction time influences the MIL morphology,  $\text{NH}_2\text{-MIL-101}$  film were grown on Si surface through GAA route for 8h and 16h. Figure 41 shows the comparison of the MIL morphology in function of increased times. For longer reaction time (8h), besides the small octahedral MIL-101 grains, hexagonal crystals with the characteristic needle shape of  $\text{NH}_2\text{-MIL-88}$ ,<sup>217</sup> were formed (Figure 41 b). The transition from one structure to another occurs because MIL-101 and MIL-88 are polymorphs in equilibrium, and the specific framework formation depends on the reaction times, temperature and pH.<sup>198</sup> Increasing the reaction times up to 16 hours, flat islands with poorly defined shapes (Figure 41 c) were observed.





*Figure 41: High resolution SEM images of a) typical octahedral crystals obtained both through the GAA after 4h; b) typical needle-like crystals obtained through the GAA route after 8h; (c) morphology of films obtained through the GAA route after 16 h.*

Free-additive route was also adopted and compared to the results observed in the presence of acetic acid.  $\text{NH}_2\text{-MIL-101}$  was obtained through the same synthetic route and times (from 4 to 16 h), without using acetic acid. Figure 42 compare morphologies of  $\text{NH}_2\text{-MIL}$  films achieved at 4h, 8h, and 16h using GAA, (Figure 42 a, b and c) respectively; and  $\text{NH}_2\text{-MIL}$  films through free-additive one (Figure 42 d, e and f).

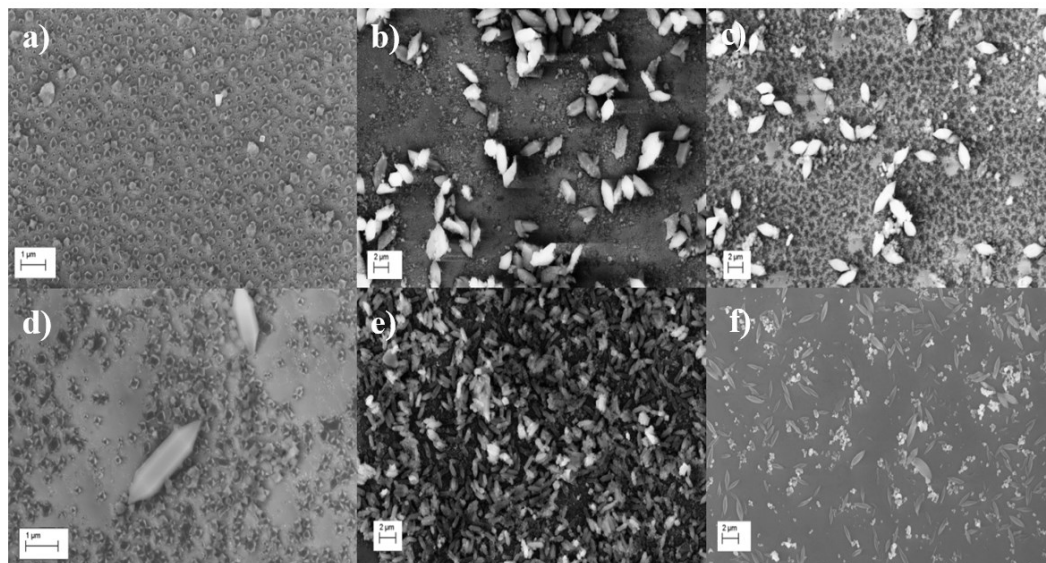


*Figure 42: SEM images of NH<sub>2</sub>-MIL films, obtained through the GAA route after 4h (a), 8h (b) and 16h (c); and NH<sub>2</sub>-MIL films obtained through the free-additive route after 4h (d), 8h (e) and 16 h (f).*

Using the free-additive route and after 4h, a discontinuous dual structure coverage layer, mainly made of octahedral MIL-101 crystals (Figure. 42 d), and some hexagonal MIL-88 crystals was obtained. Longer reaction times (up to 8h) favour the formation of a denser coverage consisting of hexagonal crystals embedded in a net of tiny (Figure 42 e) grains, while a further increase of the reaction times (16h) leads to a poor coverage with only few crystals grown on the surface (Figure 42 f). The morphology of the latter indicates that dipping times above 8h for the free-additive route lead to low amount of MIL material.

Table 7 shows the Fe/Si atomic ratios (obtained from EDX and XPS measurement) of samples grown for different times (4h, 8h and 16h) with or without the presence of additives.

<u>Route</u>	<u>GAA</u>			<u>Free-additive</u>		
<i>Time</i>	4h	8h	16h	4h	8h	16h
	EDX / XPS	EDX / XPS	EDX / XPS	EDX / XPS	EDX / XPS	EDX / XPS
Si 2p	67.1 / 20.5	46.0 / 5.3	39.5 / 3.2	67.5 / 18.0	44.8 / 1.4	87.8
O 1s	5.9 / 37.1	10.3 / 27.5	12.7 / 28.1	5.7 / 36.7	11.3 / 19.4	2.4
C	26.3 / 33.6	42.7 / 51.4	46.7 / 53.7	23.3 / 36.3	42.5 / 74.8	9.5
Fe	0.39 / 2.3	0.84 / 4.2	1.0 / 4.1	0.40 / 2.4	0.96 / 1.1	0.2
N	- / 3.5	- / 6.1	- / 5.6	- / 3.5	- / 1.2	-
Cl	0.05 / 0.7	0.14 / 1.4	0.11 / 1.2	0.07 / 0.8	0.41 / 0.4	0.05
Fe / Si	0.006 / 0.11	0.018 / 0.79	0.025 / 1.28	0.006 / 0.13	0.21 / 0.79	0.002

*Table 7: EDX and XPS atomic concentration of MIL films grown by GAA and free-additive route and at different time (4, 8, 16 h).*

The time-dependence of the film/substrate ratios, shown on the above-reported table; suggests that both with and without acetic acid the amount of deposited material increases with the reaction time until a maximum reached at about 8h. For longer deposition times, material is depleted from the surface likely through a process of re-dissolution and homogeneous precipitation of powders.

Further information on both the chemical nature and the amount of the deposited material were obtained through FTIR spectroscopy.

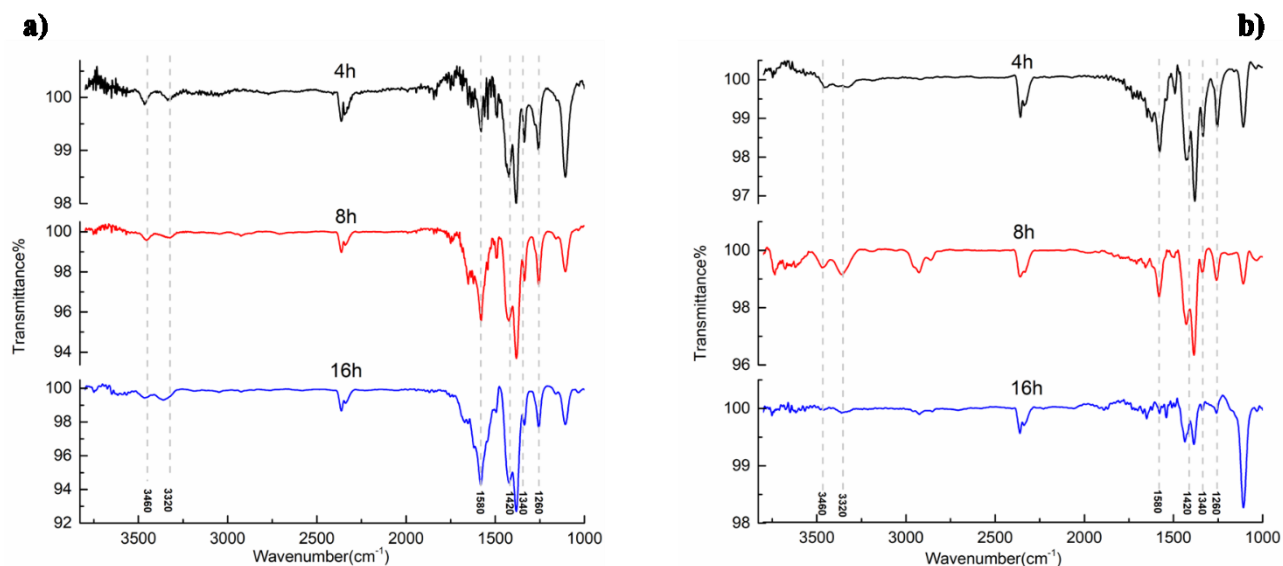


Figure 43: FTIR spectra of the samples obtained by GAA (a) and by free-additive route (b) as function of dipping time.

Figure 43 shows the FTIR spectra related to the samples obtained by GAA route (a) and by free-additive route (b) and reported as function of the dipping time. The signals at  $1580\text{ cm}^{-1}$  and around  $1420\text{--}1390\text{ cm}^{-1}$ , detectable in each MIL sample, are attributable to terephthalate bands and, particularly; are characteristic of asymmetric and symmetric stretching of  $\text{-COO}^-$  groups. In addition, the peaks at  $3460$  and  $3320\text{ cm}^{-1}$  can be ascribed to the asymmetric and symmetric  $\nu(\text{N-H})$  of the amino group, respectively, and the signals at  $1260$  and  $1340\text{ cm}^{-1}$ , to the C-N stretching. The intensity of the above-described IR vibrational modes confirm the MIL surface coverage observed in Figure 42. In particular, the IR signals of  $\text{COO}^-$  and C-N stretching result more intense in the 8h and 16h samples obtained through GAA route (a) and clearer in the 4h and 8h samples concerning the free-additive route (b).<sup>218,219,220, 221</sup>

Film crystallinity has been investigated through XRD measurements. Patterns of the films obtained after 4h, 8h and 16h of reaction through GAA and free-additive route are reported in Figure 44a and 44b respectively.

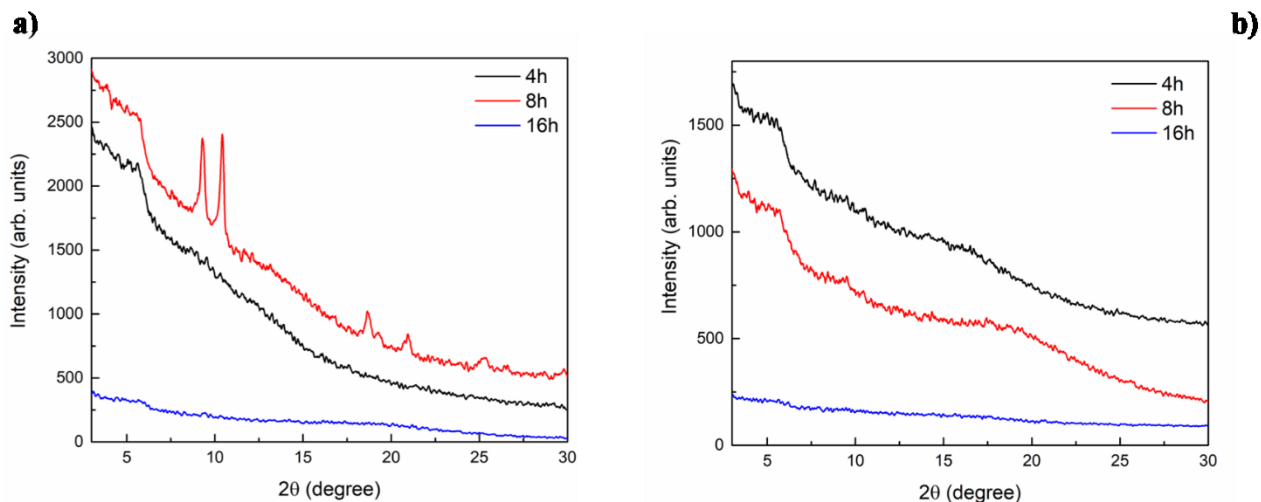


Figure 44: XRD diffractogram of the samples obtained by GAA (a) and free-additive (b) route as function of dipping time.

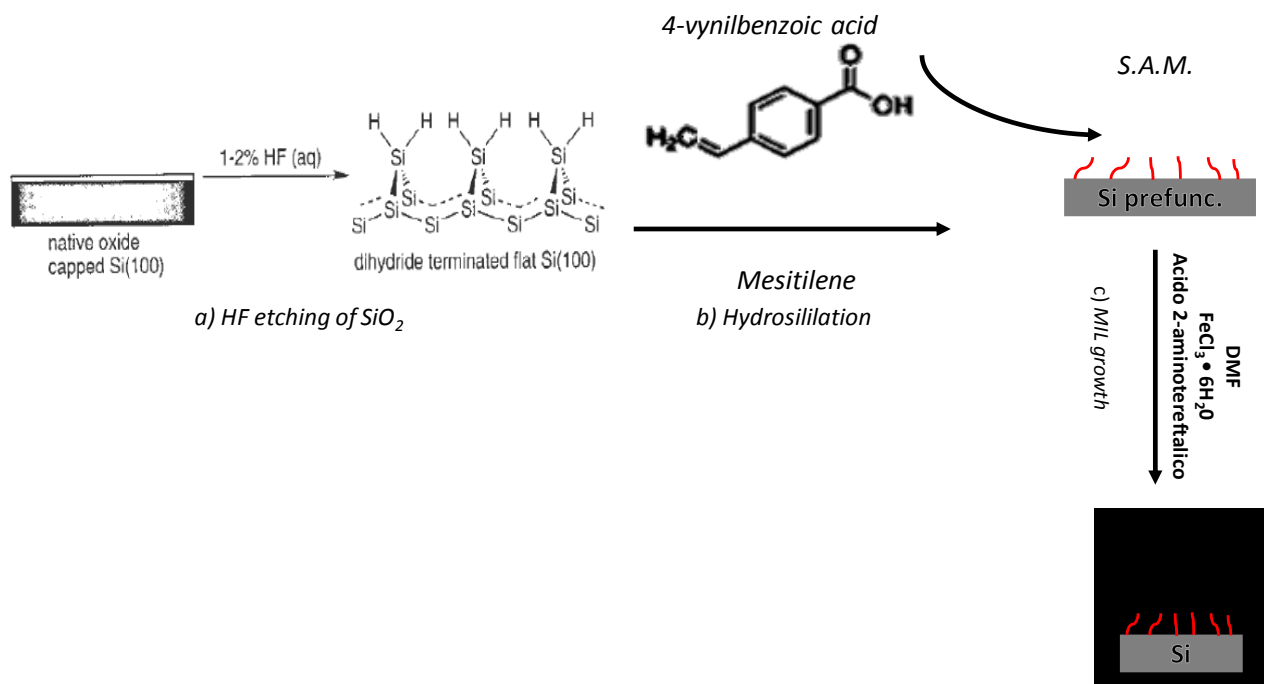
In the case of 4h-grown film through GAA route, we can observe a broad peak at about  $5.5^\circ$  attributable to the large and not-intergrown  $\text{NH}_2\text{-MIL-101}$  crystals. Whereas, sharp and intense XRD reflections are detected for the sample obtained after 8h with acid additive (Figure 44a). The above-reported diffraction peaks at  $9.3^\circ$ ;  $10.4^\circ$ ;  $18.6^\circ$ ;  $20.9^\circ$ ;  $25.3^\circ$  are characteristic of the MIL-88 structure.<sup>222</sup>

Negligible signals are present in the diffraction patterns of the corresponding films grown for 16 hours, suggesting that it consists of amorphous coating. XRD patterns of the samples obtained through free-additive routes (Figure 44b) show a broad peak at low  $2\theta$  for all the three ones corresponding at different dipping times, more intense for the 4h, 8h-grown films due to their greater coverage.

The reported XRD outcomes prove again that the presence of acid additive, like CH<sub>3</sub>COOH, controls the rate of nucleation, the crystal sizes and the crystallinity. In particular, glacial acetic acid drives the deprotonation of carboxylic linkers accelerating the rate of the heterogenous nucleation but does not guarantee a long-range order.<sup>223</sup>

### 3.1.3 4-VBA synthetic strategy to achieve Fe-based MIL-88 film

In order to optimize the heterogenous nucleation of MIL film and to investigate how the carboxylate surface terminations affect the growth rate, the morphology and the coverage, 4-vynilbenzoic acid was used to functionalize the Si surface. Indeed, a new synthesis strategy of NH<sub>2</sub>-MIL-88 (Fe based) based on a carboxylic acid prefunctionalization was implemented (Scheme 9). Through hydrosililation, 4-vynilbenzoic acid (*4-VBA route*) was covalently anchored on the Si surface. The HF-etched substrate was firstly placed in a N<sub>2</sub> purged reaction chamber for 2 h, after was introduced into a 10 mL mesitylene solution ( $5 \times 10^{-3}$  M) of 4-vynilbenzoic acid. The reaction mixture was left to react at 180°C for 2 h. The silicon surface was recovered from the reaction mixture and repeatedly washed with dichloromethane and acetone in an ultrasonic bath and dried under a stream of nitrogen. NH<sub>2</sub>-MIL-88(Fe) films were obtained through solvothermal reaction by dipping the Si surface in a DMF solution consisted of iron (III) chloride hexahydrate and 2-aminoterephthalic acid, used as metal and organic precursors, respectively; with molar ratios of 1:1 and without acid additive use. The DMF mix solutions were placed in an oil bath at 120° C and by varying the dipping time between 4 and 8 hours.



*Scheme 9: Scheme of the reaction steps of MOF film on SAMs surface: HF etching of SiO<sub>2</sub> (a), Hydrosilylation reaction with 4-vinylbenzoic acid (b), Direct growth from solution of MIL film (c) with the formation MOF film.*

- *Crystal structure analysis and morphological characterization*

Figure 45a and 45b report the SEM images of NH<sub>2</sub>-MIL-88 film obtained through VBA route after 4h and 8h respectively.

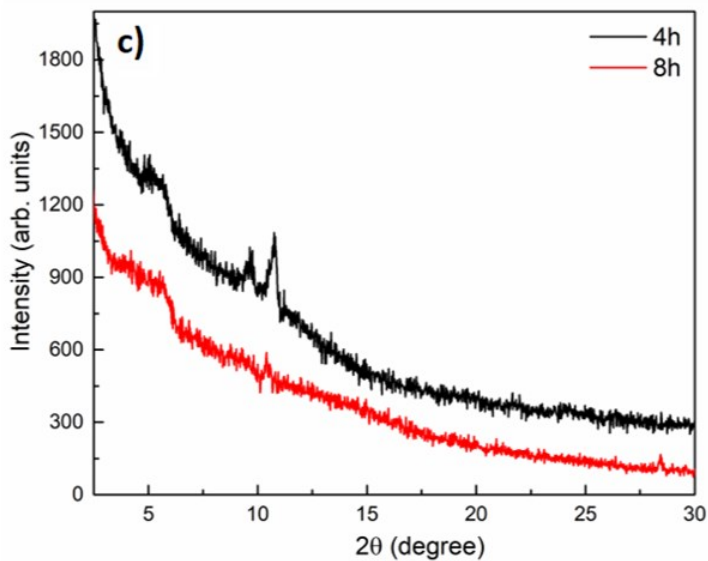
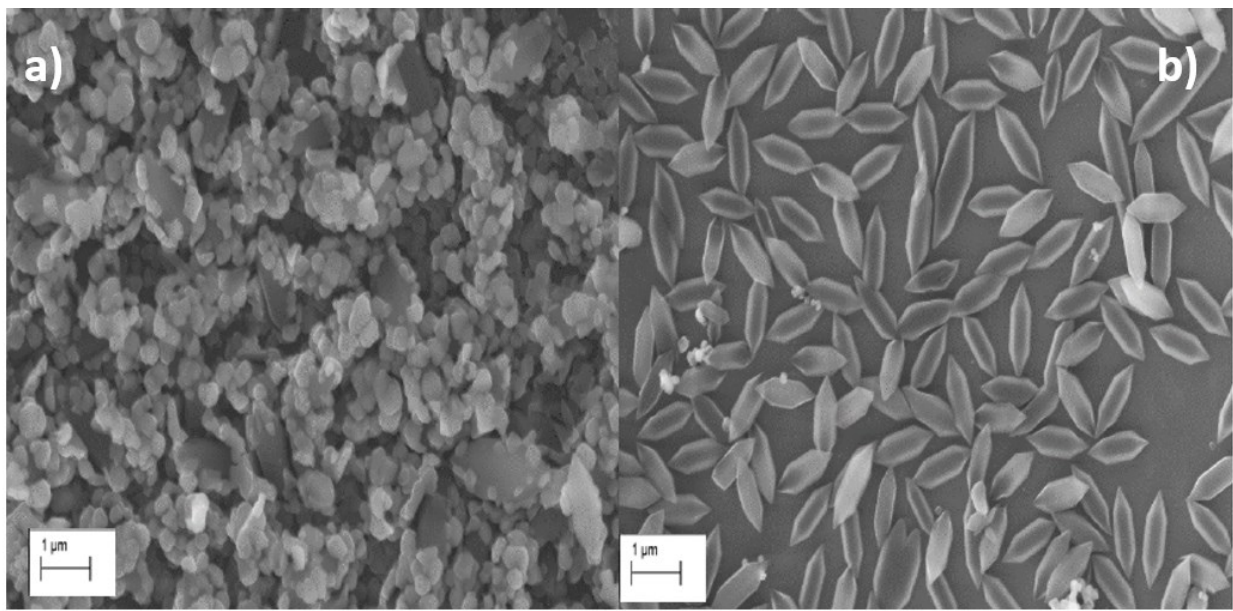


Figure 45: SEM images of  $\text{NH}_2\text{-MIL-88}$  film obtained by 4-VBA route after 4h (a), 8h (b). XRD data (c) of  $\text{NH}_2\text{-MIL-88}$  film obtained by 4-VBA as function of dipping time (d).

Respect to the above-mentioned methods, the direct growth on carboxylic acid SAMs allows to achieve a thin inter-grown layer of tiny  $\text{NH}_2\text{-MIL-88}$  grains after only 4 dipping hours (Figure 45a). By increasing reaction time up to 8h, the surface coating is poor but  $\text{NH}_2\text{-MIL-88}$  crystals increase in size shaping isolated defined hexagonal  $\text{NH}_2\text{-MIL-88}$  crystals (Figure 44b). XRD patterns



reported in Figure 45c as function of dipping time confirm the formation of MIL-88 phase after 4h showing its characteristic reflection peaks at about  $9,3^\circ$  and  $10,4^\circ$ .<sup>222</sup> In addition, it is again visible the broad peak at low  $2\theta$ . Its position is characteristic of MIL-101 phase and is probably attributable to not-grown MIL-101 nuclei proving the isomerism equilibrium between MIL-101 and MIL-88. For 8h-grown sample the low-angle signal results broader and only the reflection peak at  $10,4^\circ$  is slightly observable due to the low amount of deposited material.

- *Chemical composition through FTIR and XPS analysis*

FTIR spectra of 4h and 8h-grown samples, reported in Figure 46, obtained through 4-VBA route show the same vibrational modes detected for the films grown onto bare silicon (Figure 46).

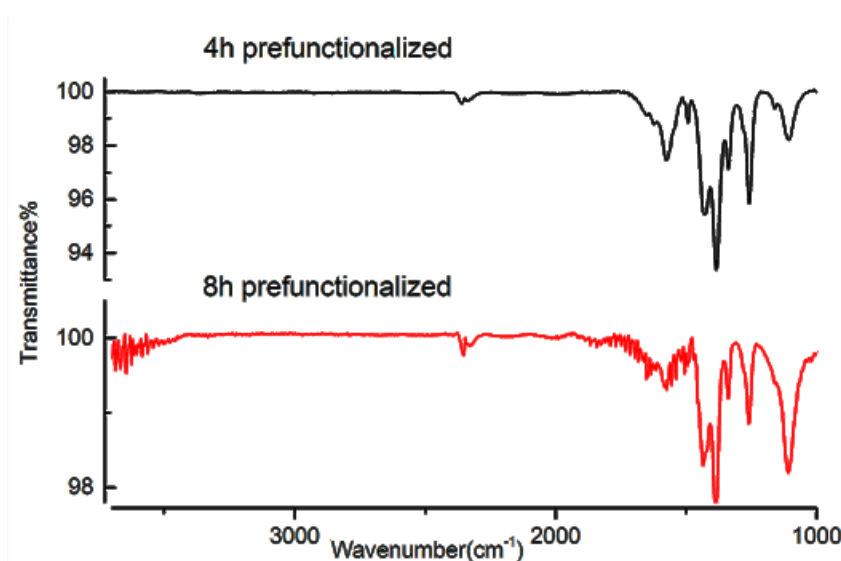


*Figure 46: IR spectra of  $\text{NH}_2$ -MIL-88 films grown by 4-VBA route after 4h (black) and after 8h (red)*

In this case, we can observe as the IR peaks, result already more intense after only 4 dipping hours compared to the samples obtained with the protocols described in the previous paragraph. The

optical data and SEM morphology indicate that the carboxylic pre-functionalization accelerates the growth of NH<sub>2</sub>-MIL-88 guarantying both the crystallinity and a good surface coverage, whereas, extended reaction times, from 8h on, induce the solubilization of the deposited materials.

In addition, chemical composition of the NH<sub>2</sub>-MIL-88 film growth through by 4-VBA route were investigated through XPS and EDX analysis. From the Fe/Si atomic ratios of the samples 4h and 8h-grown samples (Table 8), it is clear that the amount of deposited material and, therefore, the film thickness decrease with the increase of the reaction time from 4 to 8h, differently from the outcomes of the GAA and free-additive syntheses reported on table 7.

<i>Route: 4-VBA</i>		
<i>Time</i>	4h	8h
	EDX / XPS	EDX / XPS
Si	40.2/ 10.8	90.2/ 8.7
O	35.4 / 29.3	6.2/ 22.2
C	13.7 / 46.6	2.8/ 62.6
Fe	10.43 / 4.8	0.56/ 1.8
N	- / 2.1	-/ 2.8
Cl	0.2 / -	0.15/ -
Fe / Si	0.179/0.461	0.006/0.207

*Table 8: EDX and XPS atomic concentration of NH<sub>2</sub>-MIL-88 films grown by 4-VBA route and after 4, and 8h.*

In addition, no XPS signal of Cl 2p is detected and the O 1s signal (Figure 47a) is different with respect to the one recorded for films obtained through GAA route (Figure 47b).

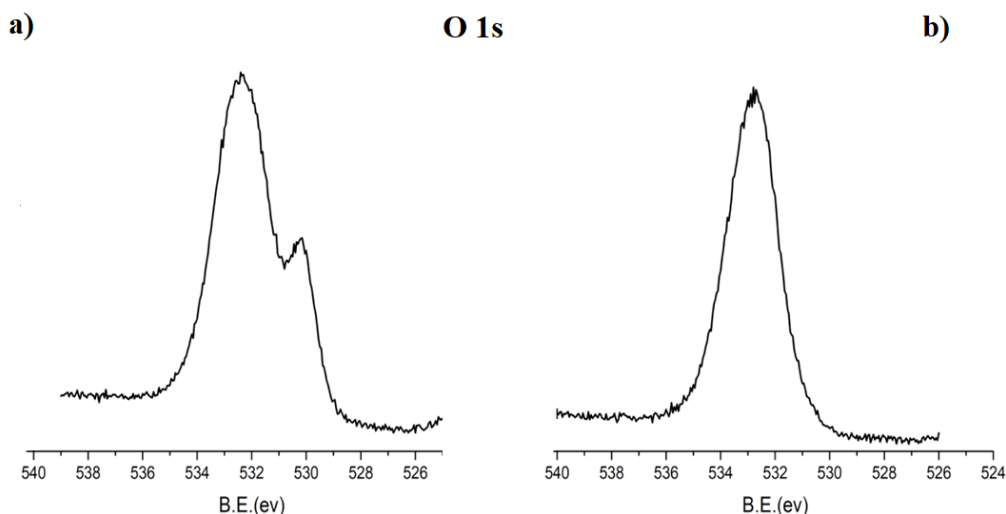


Figure 47: XPS spectra of O1s region of  $\text{NH}_2\text{-MIL-88}$  films grown by 4-VBA route after 4h (a) and of the all  $\text{NH}_2\text{-MIL-88}$  films grown by GAA route.

The low binding energy peak at about 530 eV, clearly observed only for the sample grown via 4-VBA (4h), is attributable to the presence of iron oxide<sup>224</sup> and it is probably produced from reaction between carboxylate surface terminations and the ferric salt in growth solution. Single O 1s peaks, as that one reported in Figure 47b, instead were detected for all other described films. Therefore, the carboxylate SAMs allows to obtain, after only 4h, a continuous film of  $\text{NH}_2\text{-MIL-88}$  accelerating the growth rate and guarantying the crystallinity; and leads to, the formation of a iron oxide/MIL-101 composite.

### 3.2 Synthesis of MIL-based composites on Copper foils

Metal Oxides (MOs)–based composites are promising materials for electrochemical storage applications.<sup>225,226,227,228</sup> MOs are widely used as active electrodes because they are characterized by good capacity retention and long cycling stability.<sup>229,230</sup> In these systems the MOF offers a flexible coordination network characterized by a high surface area, a low density and a tunable pore size.<sup>231,232,233</sup> Additionally, appropriate functionalities can be added to the MOF organic building blocks through post synthetic modifications to modulate MOF properties.<sup>234,235</sup> Despite their advantages, pure MOFs are not much used for electrochemical applications due to their poor

chemical stability and low electrical conductivity which reduce their energy storage capabilities.<sup>227,236</sup> Indeed, Metal-Organic Frameworks (MOFs) have been frequently used as precursors of MOs-based composites through high-temperature annealing processes, but they have rarely been used as pure MOF electrodes due to their low electrical conductivity and poor chemical stability.<sup>237,238,239</sup> However, hybrid MOF/MO composite materials can combine the MOF advantages such as low density, high surface areas and flexible frameworks, with the electrical efficiency of metal oxides. Transition metal oxides (like Fe<sub>2</sub>O<sub>3</sub>, Co<sub>3</sub>O<sub>4</sub>, Cu<sub>2</sub>O, RuO<sub>2</sub>, TiO<sub>2</sub>), are, indeed, efficient active electrode capable of performing reversible conversion reactions assuring an accurate control of the redox potential.<sup>229,240</sup> In addition, hybrid nanostructures consist of metal oxides embedded in the carbon matrix improve the electrochemical performances compared to the pure oxides due to the short-ion diffusion and to the increased conductivity.<sup>241,242</sup> Among various transition metal oxides, iron oxides being environmentally friendly and characterized by high theoretical capacity, high corrosion resistance and wide working potential range, have been widely employed as anode materials.<sup>243,244</sup> The most common synthetic methods to achieve iron oxides-based electrodes are sol-gel routes and MOF pyrolysis.<sup>245,246</sup> Fe-MIL-88 and Fe-MIL-101 are the MOF precursors mainly used for the pyrolysis which typically collapse shaping mesoporous carbon shell around the iron oxide core after the thermal treatment.<sup>247,248</sup> In this context, the development of facile synthetic routes to fabricate hybrid composites consisting of MOFs and transition metal oxides joined in a common matrix would lead to new and efficient materials able to overcome some of the issues of the current electrochemical cells, like the capacity fade and the poor capacity retention. For this purpose, it would be necessary to optimize the heterogenous nucleation of MOF on conductive surfaces like highly doped-silicon, aluminium or copper foils in order to directly grow integrated multilayers device and avoid repeated steps of powder deposition.

### **3.2.1 Growth of Iron Oxy-Hydroxide MIL composite**

A novel MOF-based hybrid film was synthesized on a Cu substrate via a two-step route. FeOOH was first deposited on Cu foils through a sol-gel process, then Fe-NH<sub>2</sub>-MIL-101 was grown using both the FeOOH matrix, which provided the Fe<sup>3+</sup> centers needed for the MOF formation, and a 2-amino terephthalic acid ethanol solution. The obtained Cu/FeOOH-MIL-101 composite is made up

of the FeOOH goethite and the NH<sub>2</sub>-MIL-101 phases and features a hybrid porous heterostructure. The electrochemical features of the composite structure were investigated using electrochemical impedance spectroscopy (EIS). The unique impedance behavior of the  $\alpha$ -FeOOH/MOF proves its potential as high surface area metal oxide/MOF-based electrode for energy storage and sensing applications.

The originality and scientific relevance of this work can be summarized as follows:

1. Development of a novel two-step synthesis of porous  $\alpha$ -FeOOH/NH<sub>2</sub>-MIL-101(Fe) film on Cu. The synthetic protocol is based on i) the sol-gel deposition of an iron oxides/hydroxides layer that acts as inorganic MOF precursor and, then, ii) on the direct growth of NH<sub>2</sub>-MIL-101(Fe) on the iron oxides/hydroxides film using a solution containing the MOF organic building block only, namely the 2-aminoterephthalate acid. A mild, template-free, low-temperature (80°C) and low-cost synthetic protocol was implemented to obtain Cu/MO/MOF composite films which can be easily integrated to produce micro and nano devices;
2. EIS analysis demonstrated that the porous Cu/ $\alpha$ -FeOOH/NH<sub>2</sub>-MIL-101(Fe) composite represents a promising high surface electrode material. Although the  $\alpha$ -FeOOH/NH<sub>2</sub>-MIL-101(Fe) film showed a high ESR value, it has good circuit parameters comparable to the sol-gel deposited iron oxides/hydroxides layer. In particular, both systems behave like non-ideal capacitors with a value of charge transfer resistance of about 1100  $\Omega$ , which is lower than the Cu benchmark. For this reason,  $\alpha$ -FeOOH/NH<sub>2</sub>-MIL-101, despite the insulating character of NH<sub>2</sub>-MIL-101, can be used as high surface area metal hydroxide/MOF-based electrodes for applications such as energy storage and sensing.

### **3.2.2 Iron Oxy-hydroxide MIL composite: *Structural and chemical characterization***

Iron oxide/hydroxide layer was deposited on Copper foil through sol-gel deposition using iron (III) nitrate as precursor and 2-methoxyethanol as solvent. Firstly, Fe(NO<sub>3</sub>)<sub>3</sub> × 9H<sub>2</sub>O was solubilized in a solution of 2-methoxyethanol and acetylacetone in a molar ratio of 10:1. The latter solution (0.2 M) was stirring and kept at room temperature for 2h. Then the precursor solution (15 ml) was dropped

on a copper foil, cleaned with a mixture of acetone/isopropanol/ethanol, in a spin-coater at a spinning rate of 1000 - 2000 rpm for 30 sec. Four spin-coating steps were repeated to increase the layer thickness. In addition, a drying treatment at 100°C was carried out after each cycle to allow a suitable adhesion on surface. The sample was, then, annealed at 150°C (heating rate of 5°C/min) for 4h to eliminate the organic components without inducing film crystallization.

Later, composite films were directly grown from solution on FeOOH layer; which acts as source of Fe<sup>3+</sup> ions. In particular, the samples of iron oxides/hydroxides layer deposited on the Cu foils were dipped into an ethanol solution (15 ml) of 2-amino terephthalic acid (0.16 gr). The system was kept under reflux for 4h in an 80°C oil bath. Samples were then washed in ethanol and dried under N<sub>2</sub> flow.

The morphology of MIL-composite was investigated through SEM morphology, its crystallinity by XRD diffraction and chemical composition of the film was studied through FTIR and XPS spectroscopy.

Figure 48 shows the SEM images of the morphologies of the sol-gel deposited FeOOH (Figure 48a) and the  $\alpha$ -FeOOH/MIL-101 composite (Figure 48b and c). As reference the morphology of the bare copper foil (Figure 48d) is shown too. The sol-gel deposited FeOOH is a homogenous and continuous film characterized by a “bunch” morphology, typical of iron oxide material (Figure 48a). MIL-101 growth into amorphous FeOOH matrix increases the layer porosity (Figure 48b) through the formation of agglomerated clusters of rod-like crystals (Figure 48c), typical shape of crystalline  $\alpha$ -FeOOH (goethite).

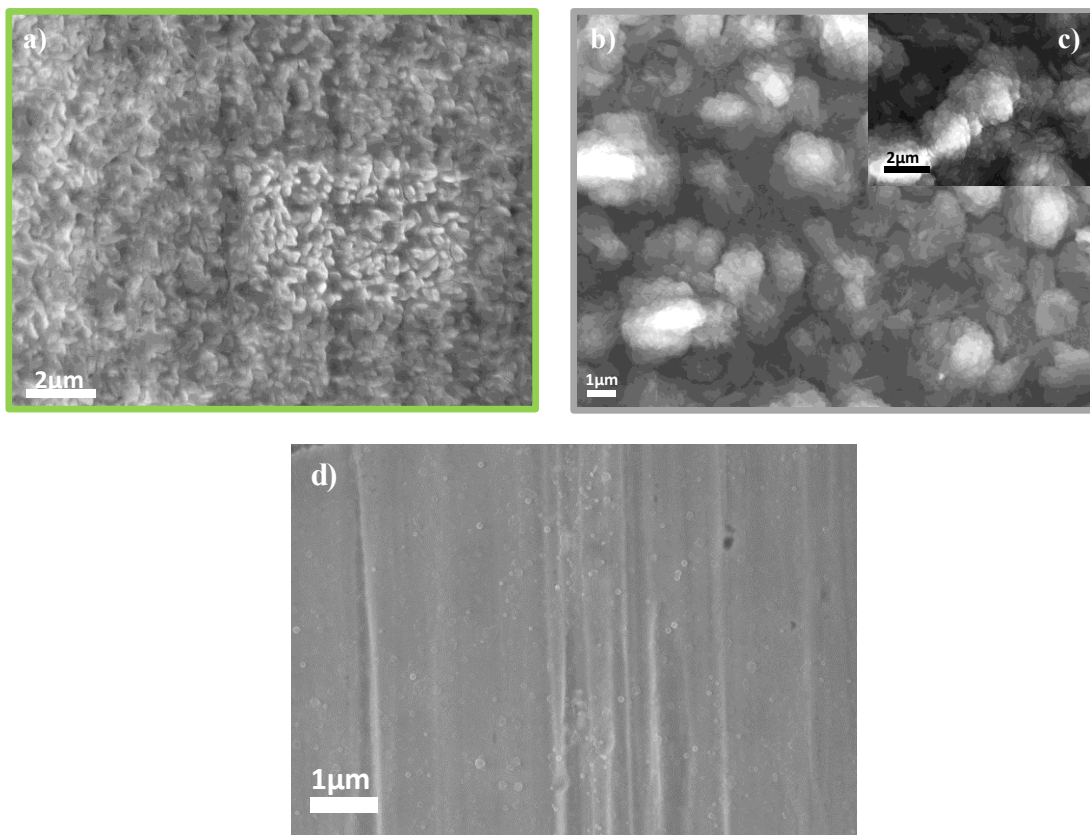


Figure 48: SEM image of a) FeOOH deposited via sol-gel on Cu foil; b) low and c) high-magnification SEM image of  $\alpha$ -FeOOH/MIL-101 composite; d) bare Cu foil surface.

The structure of obtained films was determined by X-ray diffraction (XRD) measurements. The XRD pattern of sol-gel deposited FeOOH films (not shown) does not show any peak associated to the deposit but only those related to the Cu substrate. On the other hand, after MIL-101 growth some new features can be observed.  $\alpha$ -FeOOH/MIL-101 composite pattern (Figure 49) shows a weak reflection at  $5.5^\circ$  assigned to the (311) crystallographic planes of NH<sub>2</sub>-MIL-101. The weak and noisy signals at about  $12^\circ$  and  $17^\circ$  are probably related to (222) and (422) planes of NH<sub>2</sub>-MIL-101<sup>249,250</sup> but are poorly detectable in the obtained thin film. The broad signals at about  $22.2^\circ$ ,  $26.4^\circ$  and  $36.4^\circ$  can be assigned to the (110), (021) and (111) reflections of crystalline  $\alpha$ -FeOOH (goethite) likely formed during the growth of MIL-101 films.<sup>251</sup>

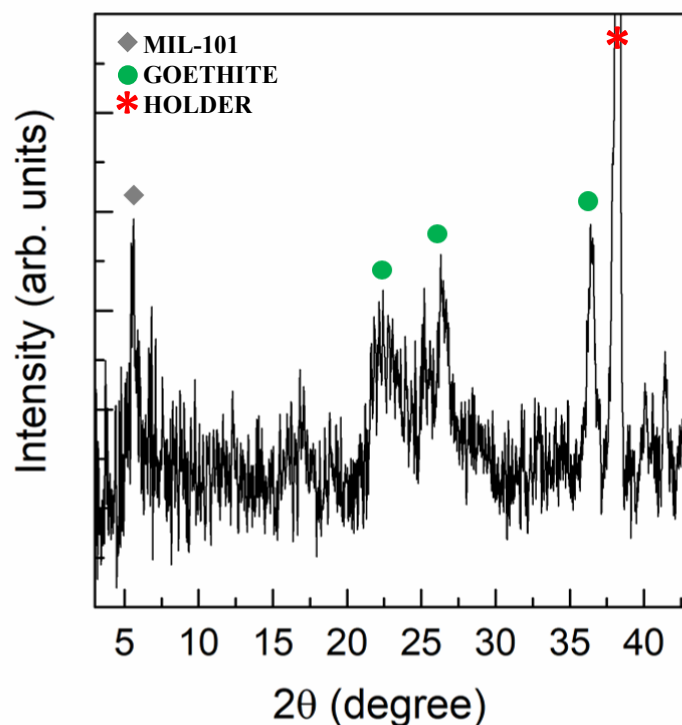


Figure 49: XRD diffractogram of  $\alpha$ -FeOOH/MIL-101 composite grown on Cu/FeOOH foil.<sup>252</sup>

Complementary information on the nature of the  $\alpha$ -FeOOH/MIL-101 composite was obtained by Fourier Transmission InfraRed Spectroscopy (FTIR). Figure 50a shows the spectra of sol-gel deposited  $\alpha$ -FeOOH (green line and Figure 50b) and of the  $\alpha$ -FeOOH/MIL-101 composite (dark line). The spectrum of the deposit is consistent with the presence of FeOOH. As expected for an inorganic compound, FeOOH signals are much weaker than the ones of MIL-101. The most intense signals are the broad bands at  $3430\text{ cm}^{-1}$  and at  $1600\text{ cm}^{-1}$  assigned to the stretching and bending vibrations of the -OH groups of FeOOH.<sup>251</sup> Other characteristic FeOOH signals are the Fe-O stretching modes at  $860\text{ cm}^{-1}$  and at  $660\text{ cm}^{-1}$ .<sup>253</sup> In addition, the defined peak localized at  $2430\text{ cm}^{-1}$  is likely due to  $\text{CO}_3^{2-}$  which is typically formed by reaction of FeOOH with atmospheric  $\text{CO}_2$ . Finally, the double peak observed in the region at about  $1030\text{ cm}^{-1}$  can be assigned to nitrate functional groups of the  $\text{Fe}(\text{NO}_3)_3$  precursor.<sup>253,254</sup> The IR spectrum of  $\alpha$ -FeOOH/MIL-101 composite shows much stronger signals mainly due to the terephthalate ligand which cover the much less intense



bands of the FeOOH component. In particular, the signals at  $1590\text{-}1510\text{ cm}^{-1}$  and in the  $1300\text{-}1400\text{ cm}^{-1}$  region are typical of asymmetric and symmetric stretchings of  $\text{-COO}^-$  groups of the terephthalate.<sup>250,253,255</sup> However, the presence of terephthalic acid molecules is also detected through the signal at  $1690\text{ cm}^{-1}$ .<sup>253,256</sup> The doublet at  $3226\text{ cm}^{-1}$  and  $3189\text{ cm}^{-1}$  is due to the  $\nu$  (N-H) of the amino group, and the signal at  $1140\text{ cm}^{-1}$  is due to the C-N stretching of aromatic  $\text{NH}_2$ . In addition, in the  $1700\text{-}1100\text{ cm}^{-1}$  region the signals due to the deformation vibrations of the terephthalic acid aromatic ring are also present.<sup>250,253</sup> Finally, the weak and broad shoulder at  $3430\text{ cm}^{-1}$  can be associated to the OH stretching of FeOOH.

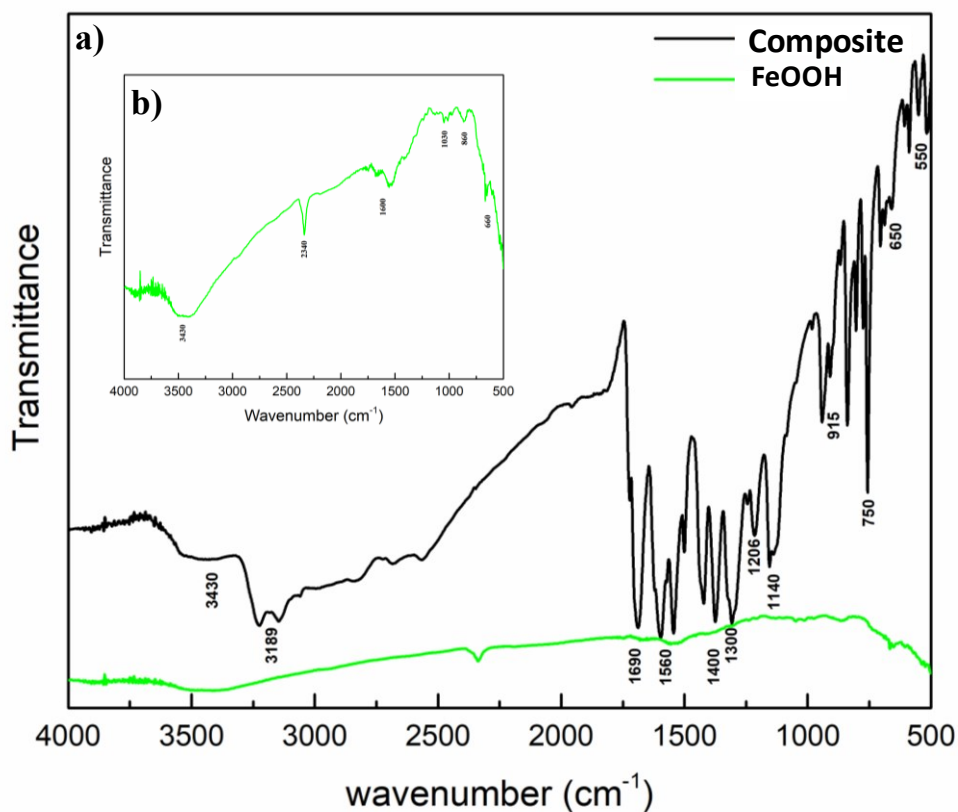


Figure 50: a) FTIR spectrum of FeOOH layer (green, and 50b) and  $\alpha$ -FeOOH/MIL-101 composite (dark).

The chemical composition of the composite surface through X-ray Photoelectron Spectroscopy (XPS). XPS spectra showed the signals due to Fe (1.5%), O (27%), N (2.5%), C (64%) and of the Cu substrate (1.8%). The Fe/N atomic ratio is 3:5 which is consistent with the theoretical value of the molecular formula  $[\text{Fe}_3(\text{O})\text{X}(\text{DMF})_2(\text{aminoterephthalate})_3]$  (X= Cl<sup>-</sup> or OH<sup>-</sup>, Solvent= DMF) of NH<sub>2</sub>-MIL-101 obtained from DMF solution. The carbon and oxygen excess compared to the theoretical values (Fe/C/O nominal = 3/30/16) is due to the ubiquitous presence of the “adventitious” carbon as well as of carbonate species (as confirmed by FTIR spectrum) and of the oxidized substrate (CuO). Note that the Cu signals in the XPS spectrum is likely due to rough morphology of the deposit with the presence of columnar structures (Figure 48 a) which increase the surface area but leave uncovered the areas on the Cu substrates among the column.

Information on the chemical nature of the composite surface were obtained through X-ray Photoelectron Spectroscopy (XPS). Figure 51 shows the high resolution XPS spectral region of the composite components: Fe2p<sub>3/2</sub>, O1s, C1s, O1s, and N1s. Fe2p<sub>3/2</sub> signal (Figure 51a) consists of two main components at 709.1 and 711.4 eV indicating the presence of Fe<sup>2+</sup> and Fe<sup>3+</sup> respectively.<sup>257</sup> A third low band is due to the Fe<sup>2+</sup> shake-up at about 715 eV. The Fe<sup>3+</sup> component can be due to both the α-FeOOH and NH<sub>2</sub>-MIL-101 phases, while the Fe<sup>2+</sup> is likely due to amorphous FeO.<sup>258</sup> The shape of C 1s band (Figure 51b) is the result of the contribution of different species. The most intense peak in this region is observed at 285.0 eV and it is typically associated to aliphatic and aromatic hydrocarbon atoms as well as to the “adventitious” carbon. The feature at 288.9 eV is characteristic of carboxylic groups. However, the position of this peak is intermediate between the value (289.3 eV) reported for the COOH groups of the terephthalic acid<sup>253</sup> and the typical values (288.6-288.2) reported for carboxylate (COO<sup>-</sup>) groups.<sup>256</sup> This feature can be, therefore, the results of the contribution of two components at 289.3 eV and at 288.6 eV due to adsorbed terephthalic acid and to the terephthalate ligands of the MOF respectively. This result is consistent with the FTIR outcomes which suggests the presence of free terephthalic acid besides the terephthalate ligand of the NH<sub>2</sub>-MIL-101 framework. The last component around 286.1 eV can be associated to adventitious C-O species as well as to the C-N atoms of the amino-terephthalic/terephthalate species. As expected, a N1s signal at 400.2 eV (Figure 51c) is also present due to the above mentioned amino-terephthalic/terephthalate species. The spectrum of O 1s (Figure 51d) shows a main component at 532.1 eV and two shoulders at 529.2 eV and 533.9 eV. The main component is

consistent with the presence of hydroxides and of the carboxylate groups of the MOF. The weak signal at low binding energies (529.2 eV) can be assigned to metal oxides while the shoulder at 533.9 eV is likely due to adsorbed water.

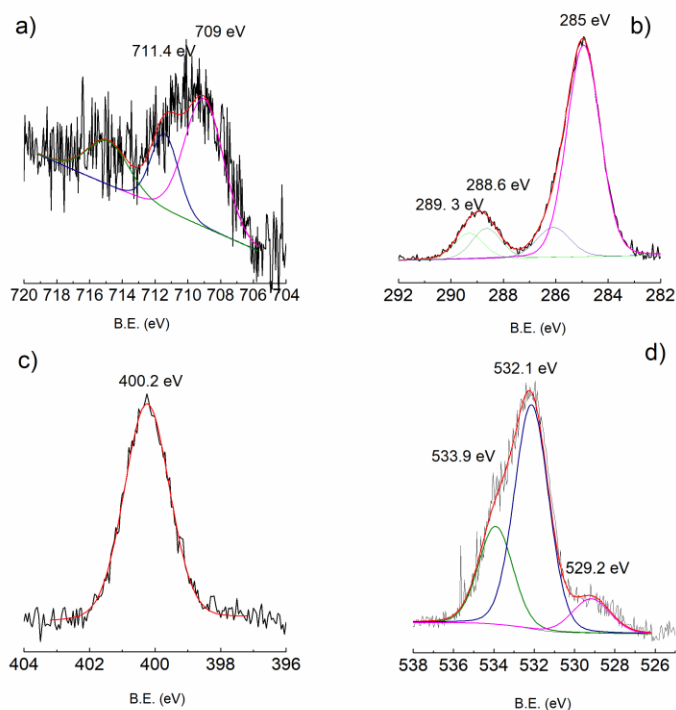


Figure 51: XPS spectra of (a)  $Fe2p_{3/2}$ , (b)  $C1s$ , (c)  $N1s$  and (d)  $O1s$  of  $\alpha\text{-FeOOH}/\text{NH}_2\text{-MIL-101}$  composite.<sup>252</sup>

### 3.2.3 Iron Oxy-hydroxide MIL composite: *Electrochemical characterization*

Electrochemical impedance spectroscopy (EIS) is considered a powerful tool to get insight into the electrochemical behaviour of MOF-based composite system.<sup>259,260</sup> Figure 52a compares the Nyquist plots (real part vs imaginary part of the impedance) of a bare Cu foil (black squares), amorphous sol-gel iron oxides/hydroxides (top inset) and  $\alpha\text{-FeOOH}/\text{NH}_2\text{-MIL-101}$  composite (bottom inset).

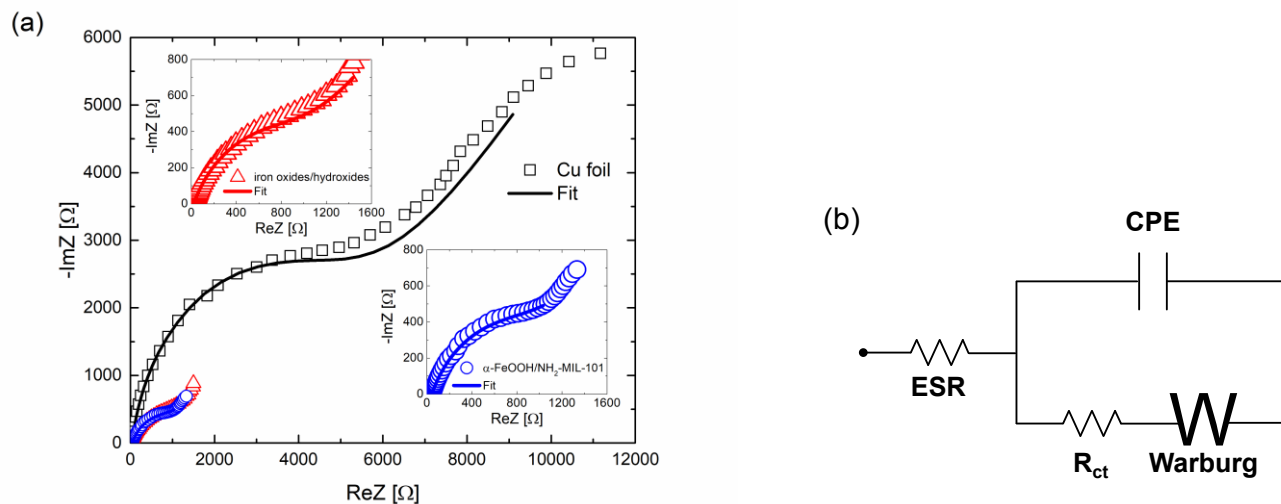


Figure 52: (a) Nyquist plots of a Cu foil (black squares), iron oxides/hydroxides (red triangles),  $\alpha$ -FeOOH/NH<sub>2</sub>-MIL-101 composite (blue circles) recorded at 0 V vs open circuit potential with a 10 mV superimposed AC voltage in the frequency range  $10^4 \div 10^{-1}$  Hz in 0.1 M KCl electrolytic solution containing 5 mM  $[\text{Fe}(\text{CN})_6]^{3-/4-}$ . The insets are the magnified region of the Nyquist plots of the iron oxides/hydroxides film (top inset) and  $\alpha$ -FeOOH/NH<sub>2</sub>-MIL-101 composite (bottom inset); (b) Equivalent circuit model used for the fit of the Nyquist plots: an equivalent series resistance (ESR) is connected in series with a constant phase element (CPE) in parallel with the charge transfer resistance ( $R_{ct}$ ) and a Warburg element ( $W$ ).<sup>252</sup>

Sample	$R_{\text{ESR}}$ [ $\Omega$ ]	$R_{ct}$ [ $\Omega$ ]	$A_w$ [ $\Omega \text{ s}^{-1/2}$ ]	CPE [ $\text{F s}^{(n-1)}$ ]	n
Cu foil	40±3	5201±354	9012±765	(2.02±0.07) $10^{-6}$	0.885±0.004
Iron oxides/hydroxides film	22±1	1157±39	958±57	(6.6±0.1) $10^{-5}$	0.673±0.002
$\alpha$ -FeOOH/NH <sub>2</sub> -MIL-101	44±1	1117±73	1087±283	(5.3±0.2) $10^{-5}$	0.663±0.005

Table 9: Fitting parameters obtained from the equivalent circuit model reported in Figure 52b.

All plots display a semicircular arc in the high frequency region and an almost straight line in the low frequency region. The beginning of the semicircle is the equivalent series resistance (ESR), which represents the combined resistance of the electrolyte, active material/substrate interface and substrate. The semicircle is due to the double layer capacitance, described by the constant phase element (CPE) to take into account the non-ideality of the capacitor, in parallel with the charge transfer resistance at the electrolyte/electrode interface ( $R_{ct}$ ). The straight line is related to the diffusion resistance of the ions within the electrode material and is represented by a Warburg element (CPE with  $45^\circ$  phase) in series with  $R_{ct}$ . This peculiar shape can be fitted based on the equivalent circuit model reported in Figure 52b.<sup>261</sup> The resulting fitting parameters are reported in Table 9. Except for the ESR values, the iron oxides/hydroxides film and the  $\alpha$ -FeOOH/NH<sub>2</sub>-MIL-101 present similar circuit parameters, as expected from the very similar impedance curves shown in Figure 52a. In fact, ESR reduces after the sol-gel deposition of the iron oxides/hydroxides film (40→22  $\Omega$ ) and increases after the formation of the hybrid NH<sub>2</sub>-MIL-101 structure (22→44  $\Omega$ ) due to the lower conductivity of the MOF. However, the  $R_{ct}$  of the the iron oxides/hydroxides films and of the  $\alpha$ -FeOOH/NH<sub>2</sub>-MIL-101 samples is almost the same (~1100  $\Omega$ ) and it is significantly lower than the one of the Cu foil (~5000  $\Omega$ ). Moreover, the CPE values of the iron oxides/hydroxides film and of the  $\alpha$ -FeOOH/NH<sub>2</sub>-MIL-101 are similar (~50-65  $\mu\text{F s}^{(n-1)}$ ) and obviously higher than those of the Cu foil (~2 $\mu\text{F s}^{(n-1)}$ ) because of their larger surface area. Also, the value of n indicates that the capacitive behavior of the Cu foil (n=0.885) is close to that of an ideal capacitor (n=1), while both the iron oxides/hydroxides film and  $\alpha$ -FeOOH/NH<sub>2</sub>-MIL-101 (n~0.67) behave like non-ideal capacitor due to their porous nature. Finally, the value of the Warburg coefficient  $A_w$  of the iron oxides/hydroxides film and  $\alpha$ -FeOOH/NH<sub>2</sub>-MIL-101 suggests an easier diffusion of ions within the electrode. Therefore, the  $\alpha$ -FeOOH/NH<sub>2</sub>-MIL-101 composite electrode offers the synergistic

properties of the two components ( $\alpha$ -FeOOH and MOF) without deteriorating the electrochemical features of the classical iron oxides/hydroxides electrodes.

## REFERENCES

---

- (194) Kanj, A. B.; Müller, K.; Heinke, L. Stimuli-Responsive Metal-Organic Frameworks with Photoswitchable Azobenzene Side Groups. *Macromol. Rapid Commun.* **2018**, *39*, 1–14.
- (195) Barea, E.; Montoro, C.; Navarro, J. A. R. Toxic Gas Removal-Metal-Organic Frameworks for the Capture and Degradation of Toxic Gases and Vapours. *Chem. Soc. Rev.* **2014**, *43*, 5419–5430.
- (196) Hamon, L.; Llewellyn, P. L.; Devic, T.; Ghoufi, A.; Clet, G.; Guillerm, V.; Pirngruber, G. D.; Maurin, G.; Serre, C.; Driver, G.; Beek, W. Van; Jolimai, E.; Vimont, A.; Daturi, M.; Je, S.; Orientale, A. A. V. Co-Adsorption and Separation of CO<sub>2</sub> - CH<sub>4</sub> Mixtures in the Highly Flexible MIL-53 (Cr) MOF. **2009**, *53*, 17490–17499.
- (197) Bauer, S.; Serre, C.; Devic, T.; Horcajada, P.; Marrot, J.; Ferey, G.; Stock, N. High-Throughput Assisted Rationalization of the Formation of Metal Organic Frameworks in the Iron (III) Aminoterephthalate Solvothermal System. *Inorganic Chemistry* **2008**, *47*, 7568–7576.
- (198) Carson, F.; Su, J.; Platero-Prats, A.E.; Wan, W.; Yun, Y.; Samain, L.; Zou, X. Framework Isomerism in Vanadium Metal – Organic Frameworks: MIL-88B(V) and MIL-101(V). *Crystal growth & design* **2013**, *13*, 5036-5044.
- (199) Pham, M. H.; Vuong, G. T.; Vu, A. T.; Do, T. O. Novel Route to Size-Controlled Fe-MIL-88B-NH<sub>2</sub> Metal-Organic Framework Nanocrystals. *Langmuir* **2011**, *27*, 15261–15267.
- (200) Serra-Crespo, P.; Ramos-Fernandez, E. V.; Gascon, J.; Kapteijn, F. Synthesis and Characterization of an Amino Functionalized MIL-101(Al): Separation and Catalytic Properties. *Chem. Mater.* **2011**, *23*, 2565–2572.
- (201) Zhang, Z.; Li, X.; Liu, B.; Zhao, Q.; Chen, G. Hexagonal Microspindle of NH<sub>2</sub>-MIL-101(Fe) Metal-Organic Frameworks with Visible-Light-Induced Photocatalytic Activity for the Degradation of Toluene. *RSC Adv.* **2016**, *6*, 4289–4295.

- 
- (202) Monforte, F.; Mannino, G.; Alberti, A.; Smecca, E.; Italia, M.; Motta, A.; Tudisco, C.; Condorelli, G. G. Heterogeneous Growth of Continuous ZIF-8 Films on Low-Temperature Amorphous Silicon. *Appl. Surf. Sci.* **2018**, *473*, 182–189.
- (203) Hu, Y.; Dong, X.; Nan, J.; Jin, W.; Ren, X.; Xu, N.; Lee, Y. M. Metal-Organic Framework Membranes Fabricated via Reactive Seeding. *Chem. Commun.* **2011**, *47*, 737–739.
- (204) Benito, J.; Fenero, M.; Sorribas, S.; Zornoza, B.; Msayib, K. J.; McKeown, N. B.; Téllez, C.; Coronas, J.; Gascón, I. Fabrication of Ultrathin Films Containing the Metal Organic Framework Fe-MIL-88B-NH<sub>2</sub> by the Langmuir-Blodgett Technique. *Colloids and Surfaces A: Physicochem. Eng. Asp.* **2015**, *470*, 161–170.
- (205) Scherb, C.; Williams, J. J.; Hinterholzinger, F.; Bauer, S.; Stock, N.; Bein, T. Implementing Chemical Functionality into Oriented Films of Metal-organic Frameworks on Self-Assembled Monolayers. *J. Mater. Chem.* **2011**, *21*, 14849-14856.
- (206) Jiang, D.; Burrows, A. D.; Xiong, Y.; Edler, K. J. Facile Synthesis of Crack-Free Metal-Organic Framework Films on Alumina by a Dip-Coating Route in the Presence of Polyethylenimine. *J. Mater. Chem. A* **2013**, *1*, 5497–5500.
- (207) Huang, Y.; Tao, C. A.; Chen, R.; Sheng, L.; Wang, J. Comparison of Fabrication Methods of Metal-Organic Framework Optical Thin Films. *Nanomaterials* **2018**, *8*, 1–10.
- (208) Rivera-Torrente, M.; Filez, M.; Hardian, R.; Reynolds, E.; Seoane, B.; Coulet, M. V.; Oropeza Palacio, F. E.; Hofmann, J. P.; Fischer, R. A.; Goodwin, A. L.; Llewellyn, P. L.; Weckhuysen, B. M. Metal-Organic Frameworks as Catalyst Supports: Influence of Lattice Disorder on Metal Nanoparticle Formation. *Chem. - A Eur. J.* **2018**, *24*, 7498–7506.
- (209) Lin, Y.; Kong, C.; Chen, L. Amine-Functionalized Metal-Organic Frameworks: Structure, Synthesis and Applications. *RSC Adv.* **2016**, *6*, 32598–32614.
- (210) Yot, P. G.; Yang, K.; Guillerm, V.; Ragon, F.; Dmitriev, V.; Parisiades, P.; Elkaïm, E.; Devic, T.; Horcajada, P.; Serre, C.; Stock, N.; Mowat, J. P. S.; Wright, P. A.; Férey, G.; Maurin, G. Impact of the Metal Centre and Functionalization on the Mechanical Behaviour of MIL-53 Metal-Organic Frameworks. *Eur. J. Inorg. Chem.* **2016**, *2016*, 4424–4429.



- 
- (211) Liu, L.; Zhou, Y.; Liu, S.; Xu, M. The Applications of Metal–Organic Frameworks in Electrochemical Sensors. *ChemElectroChem* **2018**, *5*, 6–19.
- (212) Baumann, A. E.; Burns, D. A.; Liu, B.; Thoi, V. S. Metal-Organic Framework Functionalization and Design Strategies for Advanced Electrochemical Energy Storage Devices. *Commun. Chem.* **2019**, *2*, 1-14.
- (213) Pan, F.; Wang, Q. Redox Species of Redox Flow Batteries: A Review. *Molecules* **2015**, *20*, 20499–20517.
- (214) Monforte, F.; Falsaperna, M.; Pellegrino, A.L.; Bongiorno, C.; Motta, A.; Mannino, G.; Condorelli, G.G. Direct Growth on Si (100) of Isolated Octahedral Mil-101 (Fe) Crystals for the Separation of Aromatic Vapors. *The Journal of Physical Chemistry C*, **2019**, 10.1021/acs.jpcc.9b09880.
- (215) Lebedev, O. I.; Millange, F.; Serre, C. First Direct Imaging of Giant Pores of the Metal - Organic Framework MIL-101. **2020**, *5*, 6525–6527.
- (216) Bhattacharjee, S.; Chen, C.; Ahn, W. RSC Advances. Chromium terephthalate metal-organic framework MIL-101: synthesis, functionalization, and applications for adsorption and catalysis. *RSC Adv.* **2014**, *4*, 52500–52525.
- (217) Ma, M.; Noei, H.; Mienert, B.; Niesel, J.; Bill, E.; Muhler, M.; Fischer, R. A.; Wang, Y.; Schatzschneider, U.; Metzler-Nolte, N. Iron Metal-Organic Frameworks MIL-88B and NH<sub>2</sub>-MIL-88B for the Loading and Delivery of the Gasotransmitter Carbon Monoxide. *Chem. - A Eur. J.* **2013**, *19*, 6785–6790.
- (218) Zhou, F.; Zhou, J.; Gao, X.; Kong, C.; Chen, L. Facile Synthesis of MOFs with Uncoordinated Carboxyl Groups for Selective CO<sub>2</sub> Capture via Postsynthetic Covalent Modification. *RSC Adv.* **2017**, *7*, 3713–3719.
- (219) Sun, J.; Yu, G.; Huo, Q.; Kan, Q.; Guan, J. Epoxidation of Styrene over Fe(Cr)-MIL-101 Metal-Organic Frameworks. *RSC Adv.* **2014**, *4*, 38048–38054.
- (220) Vuong, G. T.; Pham, M. H.; Do, T. O. Direct Synthesis and Mechanism of the Formation of Mixed Metal Fe<sub>2</sub>Ni-MIL-88B. *CrystEngComm* **2013**, *15*, 9694–9703.

- 
- (221) Serre, C.; Millange, F.; Thouvenot, C.; Noguès, M.; Marsolier, G.; Louër, D.; Férey, G. Very Large Breathing Effect in the First Nanoporous chromium(III)-Based Solids: MIL-53 or  $\text{CrIII}(\text{OH}) \cdot \{\text{O}_2\text{C}-\text{C}_6\text{H}_4-\text{CO}_2\} \cdot \{\text{HO}_2\text{C}-\text{C}_6\text{H}_4-\text{CO}_2\text{H}\}_x \cdot \text{H}_2\text{O}_y$ . *J. Am. Chem. Soc.* **2002**, *124*, 13519–13526.
- (222) Shi, L.; Wang, T.; Zhang, H.; Chang, K.; Meng, X.; Liu, H.; Ye, J. An Amine-Functionalized Iron(III) Metal–Organic Framework as Efficient Visible-Light Photocatalyst for Cr(VI) Reduction. *Adv. Sci.* **2015**, *2*, 1–8.
- (223) Yuan, S.; Feng, L.; Wang, K.; Pang, J.; Bosch, M.; Lollar, C.; Sun, Y.; Qin, J.; Yang, X.; Zhang, P.; Wang, Q.; Zou, L.; Zhang, Y.; Zhang, L.; Fang, Y.; Li, J.; Zhou, H. C. Stable Metal–Organic Frameworks: Design, Synthesis, and Applications. *Adv. Mater.* **2018**, *30*, 1–35.
- (224) Barik, R.; Pandey, B.; Shashi, A.; Mamata, M. A Facile Single Step Synthesis of Flowery Shape Pure/lithium Doped 3D Iron Oxides. *Journal of Material Chemistry A* **2014**, *2*, 12380–12389.
- (225) Xu, Y.; Li, Q.; Xue, H.; Pang, H. Metal-Organic Frameworks for Direct Electrochemical Applications. *Coord. Chem. Rev.* **2018**, *376*, 292–318.
- (226) Patwardhan, S.; Schatz, G. C. Theoretical Investigation of Charge Transfer in Metal Organic Frameworks for Electrochemical Device Applications. *J. Phys. Chem. C* **2015**, *119*, 24238–24247.
- (227) Xue, Y.; Zheng, S.; Xue, H.; Pang, H. Metal-Organic Framework Composites and Their Electrochemical Applications. *J. Mater. Chem. A* **2019**, *7*, 7301-7327.
- (228) Sundriyal, S.; Kaur, H.; Bhardwaj, S. K.; Mishra, S.; Kim, K. H.; Deep, A. Metal-Organic Frameworks and Their Composites as Efficient Electrodes for Supercapacitor Applications. *Coord. Chem. Rev.* **2018**, *369*, 15–38.
- (229) Martinet, S. Nanomaterials for Rechargeable Lithium Batteries. *Nanomaterial for Sustainable Energy.* **2016**, 471–512.
- (230) Wu, H. Bin; Chen, J. S.; Hng, H. H.; Lou, X. W. Nanostructured Metal Oxide-Based Materials as Advanced Anodes for Lithium-Ion Batteries. *Nanoscale* **2012**, *4*, 2526–2542

- 
- (231) Chae, H.K.; Siberio-Perez, D. Y.; Kim, J.; Go, Y.; Eddaoudi, M.; Matzger, A.J.; O’Keeffe, M.; Yaghi, O.M. A Route to High Surface Area, Porosity and Inclusion of Large Molecules in Crystals. *Nature*, **2004**, *427*, 523–527.
- (232) Davis, M. E. Ordered Porous Materials for Emerging Applications. *Nature* **2002**, *417*, 813–821.
- (233) Zhang, W. X.; Liao, P. Q.; Lin, R. B.; Wei, Y. S.; Zeng, M. H.; Chen, X. M. Metal Cluster-Based Functional Porous Coordination Polymers. *Coord. Chem. Rev.* **2015**, *293–294*, 263–278.
- (234) Cui, Y.; Li, B.; He, H.; Zhou, W.; Chen, B.; Qian, G. Metal-Organic Frameworks as Platforms for Functional Materials. *Acc. Chem. Res.* **2016**, *49*, 483–493
- (235) Tanabe, K. K.; Cohen, S. M. Postsynthetic Modification of Metal–organic Frameworks—a Progress Report. *Chem. Soc. Rev.* **2011**, *40*, 498–519.
- (236) Campbell, M. G.; Dincă, M. Metal–organic Frameworks as Active Materials in Electronic Sensor Devices. *Sensors* **2017**, *17*, 1–11.
- (237) Oar-Arteta, L.; Wezendonk, T.; Sun, X.; Kapteijn, F.; Gascon, J. Metal Organic Frameworks as Precursors for the Manufacture of Advanced Catalytic Materials. *Mater. Chem. Front.* **2017**, *1*, 1709–1745.
- (238) Pastore, V. J.; Cook, T. R.; Rzyayev, J. Polymer-MOF Hybrid Composites with High Porosity and Stability through Surface-Selective Ligand Exchange. *Chem. Mater.* **2018**, *30*, 8639-8649.
- (239) Li, Y.; Xu, Y.; Yang, W.; Shen, W.; Xue, H.; Pang, H. MOF-Derived Metal Oxide Composites for Advanced Electrochemical Energy Storage. *Small* **2018**, *14*, 1–24.
- (240) Wu, H. Bin; Chen, J. S.; Hng, H. H.; Lou, X. W. Nanostructured Metal Oxide-Based Materials as Advanced Anodes for Lithium-Ion Batteries. *Nanoscale* **2012**, *4*, 2526–2542.
- (241) Zhang, E.; Wang, B.; Yu, X.; Zhu, J.; Wang, L.; Lu, B.  $\beta$ -FeOOH on Carbon Nanotubes as a Cathode Material for Na-Ion Batteries. *Energy Storage Mater.* **2017**, *8*, 147–152.
- (242) Wu, Z. S.; Zhou, G.; Yin, L. C.; Ren, W.; Li, F.; Cheng, H. M. Graphene/metal Oxide Composite Electrode Materials for Energy Storage. *Nano Energy* **2012**, *1*, 107–131.

- 
- (243) Yu, L.; Wang, L. P.; Xi, S.; Yang, P.; Du, Y.; Srinivasan, M.; Xu, Z. J.  $\beta$ -FeOOH: An Earth-Abundant High-Capacity Negative Electrode Material for Sodium-Ion Batteries. *Chem. Mater.* **2015**, *27*, 5340–5348.
- (244) Gao, M.; Zhou, P.; Wang, P.; Wang, J.; Liang, C.; Zhang, J.; Liu, Y. FeO/C Anode Materials of High Capacity and Cycle Stability for Lithium-Ion Batteries Synthesized by Carbothermal Reduction. *J. Alloys Compd.* **2013**, *565*, 97–103.
- (245) Abdel-Samad, H.; Watson, P. R. An XPS Study of the Adsorption of Chromate on Goethite ( $\alpha$ -FeOOH). *Appl. Surf. Sci.* **1997**, *108*, 371–377.
- (246) Wezendonk, T. A.; Santos, V. P.; Nasalevich, M. A.; Warringa, Q. S. E.; Dugulan, A. I.; Chojecki, A.; Koeken, A. C. J.; Ruitenbeek, M.; Meima, G.; Islam, H. U.; et al. Elucidating the Nature of Fe Species during Pyrolysis of the Fe-BTC MOF into Highly Active and Stable Fischer-Tropsch Catalysts. *ACS Catal.* **2016**, *6*, 3236–3247.
- (247) Xu, X.; Cao, R.; Jeong, S.; Cho, J. Spindle-like mesoporous  $\alpha$ -Fe<sub>2</sub>O<sub>3</sub> anode material prepared from MOF template for high-rate lithium batterie. *Nano Lett.* **2012**, *12*, 4988-4991.
- (248) Li, C.; Hu, Q.; Li, Y.; Zhou, H.; Lv, Z.; Yang, X.; Liu, L.; Guo, H. Hierarchical Hollow Fe<sub>2</sub>O<sub>3</sub> @MIL-101(Fe)/C Derived from Metal-Organic Frameworks for Superior Sodium Storage. *Sci. Rep.* **2016**, *6*, 1–8.
- (249) Yin, D.; Li, C.; Ren, H.; Shekhah, O.; Liu, J.; Liang, C. Efficient Pd@MIL-101(Cr) Hetero-Catalysts for 2-Butyne-1,4-Diol Hydrogenation Exhibiting High Selectivity. *RSC Adv.* **2017**, *7*, 1626–1633.
- (250) Xie, Q.; Li, Y.; Lv, Z.; Zhou, H.; Yang, X.; Chen, J.; Guo, H. Effective Adsorption and Removal of Phosphate from Acqueous Solution and Eutrophic Water by Fe-based MOFs of MIL-1101 *Sci. Rep.*, **2017**, *7*, 1–15.
- (251) Ghosh, M. K.; Poinern, G. E. J.; Issa, T. B.; Singh, P. Arsenic Adsorption on Goethite Nanoparticles Produced through Hydrazine Sulfate Assisted Synthesis Method. *Korean J. Chem. Eng.* **2012**, *29*, 95–102.

- 
- (252) Monforte, F.; Urso, M.; Alberti, A.; Smecca, E.; Mirabella, S.; Bongiorno, C.; Mannino, G.; Condorelli, G.G. New Synthetic Route for the growth of  $\alpha$ -FeOOH/NH<sub>2</sub>-Mil-101 Films on Copper Foil for High Surface Electrode. *ACS Omega*, **2019**, 10.1021/acsomega.9b01840.
- (253) Stoia, M.; Istrate, R.; Păcurariu, C. Investigation of Magnetite Nanoparticles Stability in Air by Thermal Analysis and FTIR Spectroscopy. *J. Therm. Anal. Calorim.* **2016**, *125*, 1185–1198
- (254) Sharma, G.; Jeevanandam, P. Synthesis of Self-Assembled Prismatic Iron Oxide Nanoparticles by a Novel Thermal Decomposition Route. *RSC Adv.* **2013**, *3*, 189–200.
- (255) Sun, J.; Yu, G.; Huo, Q.; Kan, Q.; Guan, J. Epoxidation of Styrene over Fe(Cr)-MIL-101 Metal–organic Frameworks. *RSC Adv.* **2014**, *4*, 38048–38054.
- (256) Liang, R.; Jing, F.; Shen, L.; Qin, N.; Wu, L. MIL-53(Fe) as a Highly Efficient Bifunctional Photocatalyst for the Simultaneous Reduction of Cr(VI) and Oxidation of Dyes. *J. Hazard. Mater.* **2015**, *287*, 364–372.
- (257) Gao, C.; Chen, S.; Quan, X.; Yu, H.; Zhang, Y. Enhanced Fenton-like Catalysis by Iron-Based Metal Organic Frameworks for Degradation of Organic Pollutants. *J. Catal.* **2017**, *356*, 125–132.
- (258) Luo, H.; Su, H.; Dong, C.; Li, X. Passivation and Electrochemical Behavior of 316L Stainless Steel in Chlorinated Simulated Concrete Pore Solution. *Appl. Surf. Sci.* **2017**, *400*, 38–48.
- (259) Zhang, Y.; Bo, X.; Luhana, C.; Wang, H.; Li, M.; Guo, L. Facile Synthesis of a Cu-Based MOF Confined in Macroporous Carbon Hybrid Material with Enhanced Electrocatalytic Ability. *Chem. Commun.* **2013**, *49*, 6885–6887.
- (260) Yang, J.; Zhao, F.; Zeng, B. One-Step Synthesis of a Copper-Based Metal-Organic Framework-Graphene Nanocomposite with Enhanced Electrocatalytic Activity. *RSC Adv.* **2015**, *5*, 22060–22065.
- (261) Urso, M.; Torrisi, G.; Boninelli, S.; Bongiorno, C.; Priolo, F.; Mirabella, S. Ni(OH)<sub>2</sub>@Ni Core-Shell Nanochains as Low-Cost High-Rate Performance Electrode for Energy Storage Applications. *Sci. Rep.* **2019**, *9*, 7736.-

## Chapter 4

### 4 Octahedral Silicon Nanoparticles: an *Innovative* Negative Electrode Material in Lithium Cells

The use of Si nanocrystals instead of bulk Si is considered a good strategy to overcome the well-known poor bulk-Si anodes cyclability and quick fading in electrochemical performances.<sup>262</sup> With respect to other conversion-type anode materials, like graphite, Si is an alloying element that guarantee different  $\text{Li}_w\text{M}$  phases formation<sup>263,264</sup> as reported in Figure 53.

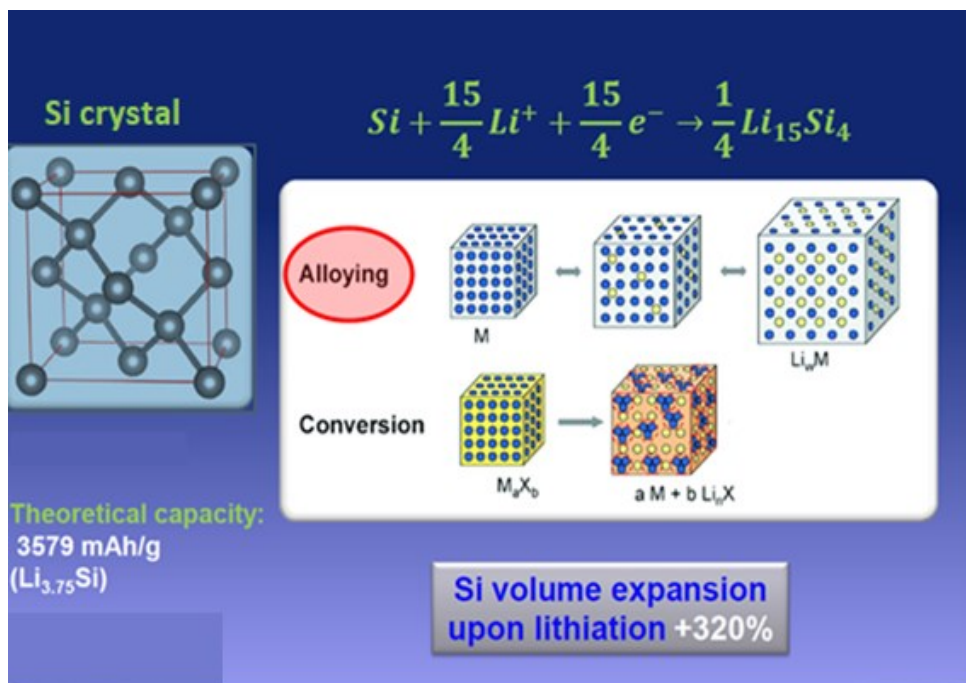


Figure 53: Lithium Alloying into Si crystal with the formation of  $\text{Li}_{15}\text{Si}_4$  phase at room temperature.

At room temperature, the maximum possible Li insertion into Si crystal leads to  $\text{Li}_{15}\text{Si}_4$  alloy in which Si host lattice can host 3,75 atoms of Lithium. The theoretical capacity associated to  $\text{Li}_{15}\text{Si}_4$  formation is  $3579 \text{ mAhg}^{-1}$ , very close to capacity value of metallic Li ( $3860 \text{ mAhg}^{-1}$ ).<sup>265,266,267</sup> However, the lithium insertion causes the volume expansion of Si lattice up to 400%, much more pronounced during first discharging process, that represents a critical activation step for Si crystal and it involves the formation of  $\text{Li}_x\text{Si}_y$  amorphous phase.<sup>264</sup>

To date, in the literature there are reported several examples of LIBs based on Si thin films and/or nanowires, nanotubes and spherical Si nanoparticles with size smaller than 150 nm in order to increase the diffusion of Li ions along the surface and, therefore, enhance the rate of charge/discharge cycles.<sup>268,269,270,271,272</sup>

In this context, a new technology of lithium ions battery was developed using octahedral Si nanoparticles (Si-NPs) as active material. The novel octahedral shape and the peculiar morphology, coupled with larger size, have allowed to bear the large volume change of the Si due to the lithiation / delithiation process showing excellent electrochemical performance in terms of Lithium loading and cycling reversibility. The nanoparticles have been synthesized using chemical vapor deposition assisted by inductively coupled plasma (ICP-CVD). It consists of high-density plasma synthesis, a versatile processes method in the synthesis of Si-NPs. This process is solvent-free, is fully compatible in any industrial plant and is easily up-scalable on very large substrate area. Thanks to the intrinsic characteristics of ICP-CVD system, it has been possible to obtain, through low-cost and low-temperature synthesis, a variety of Si-NPs in terms of crystalline structure, size and chemical composition. Intrinsic Si-NPs with size between 50 and 250 nm were synthesized by simply increasing the process time maintaining constant the precursor gas mixture. In contrast adding a gas containing P or B we obtained doped Si-NPs of the desired size. The relationship between Si-NPs size and electrochemical Li loading has been studied by varying the operating conditions of the galvanostatic cycling experiments and it has allowed to select the suitable size to design a novel anode material composite. Once the best size has been selected, phosphorous and boron doped Si-NPs have been carried out. The n- and p-type Si-NPs has been achieved not only to increase the electrical conductivity of the Si but also to investigate as the dopant's insertion influences the morphology of the Si-NPs and therefore the  $\text{Li}^+$  accommodation in the crystal structure during the charge/discharge process.

Finally, Si-NPs were functionalized with ZIF-8 in order to develop an advanced integrated anode based on active Si-NPs and flexible solid-state electrolyte. By considering the electrochemical outcomings of ZIF-8 reported on Chapter 2, the ZIF-8 coating should act as efficient host for lithium ionic liquids (LIL) and guarantees a hybrid porous network where the lithium ions freely move. The hybrid micro-porous network of the ZIF-8 combined to the peculiar morphology of Si-NPs will lead to develop a high-capacity anode capable to overcome drawbacks of a pure Si electrode, like its large volume change following the lithiation processes and the instability of SEI interface. Si-NPs functionalization with ZIF-8 was a simple and cost-effective process carried out through the direct growth from solution. By varying the synthesis parameters, it has been possible to obtain Si-NPs with a different shell in terms of morphology, crystallinity and coating porosity.

In detail, the chapter is articulated in:

- The description of the CVD processes and an outline of the inductively coupled plasma reactor;
- Formation mechanism of octahedral Si-NPs by means ICP-CVD and their characterization by TEM analysis;
- Electrodes preparation and their assembly in lithium ion battery;
- Study of the role of the sizes of the intrinsic Si-NPs on the electrochemical performances through charge-discharge cycling and voltage profile;
- Electrochemical Li loading of n-type and p-type Si-NPs investigated through galvanostatic measurements;
- Functionalization of Si-NPs with ZIF-8 through two different synthesis protocols.

#### **4.1 Chemical Vapour Deposition: ICP-CVD system.**

Chemical Vapour deposition (CVD) is one of the more common chemical process to the synthesis of Si thin film.<sup>273,274,275</sup> With respect to physical vapour deposition methods, like sputtering and evaporation, CVD involves a chemical conversion from gases precursors to a solid deposit.<sup>276</sup> It offers several advantages, like:



- i) a variety of layers depending on gas precursors;
- ii) a controlled layer thickness with low surface roughness;
- iii) the capability of coating complex shapes;
- iv) a high deposition rate.

Figure 54 shows the typical steps of the nucleation and the growth of the chemical vapor deposition process.

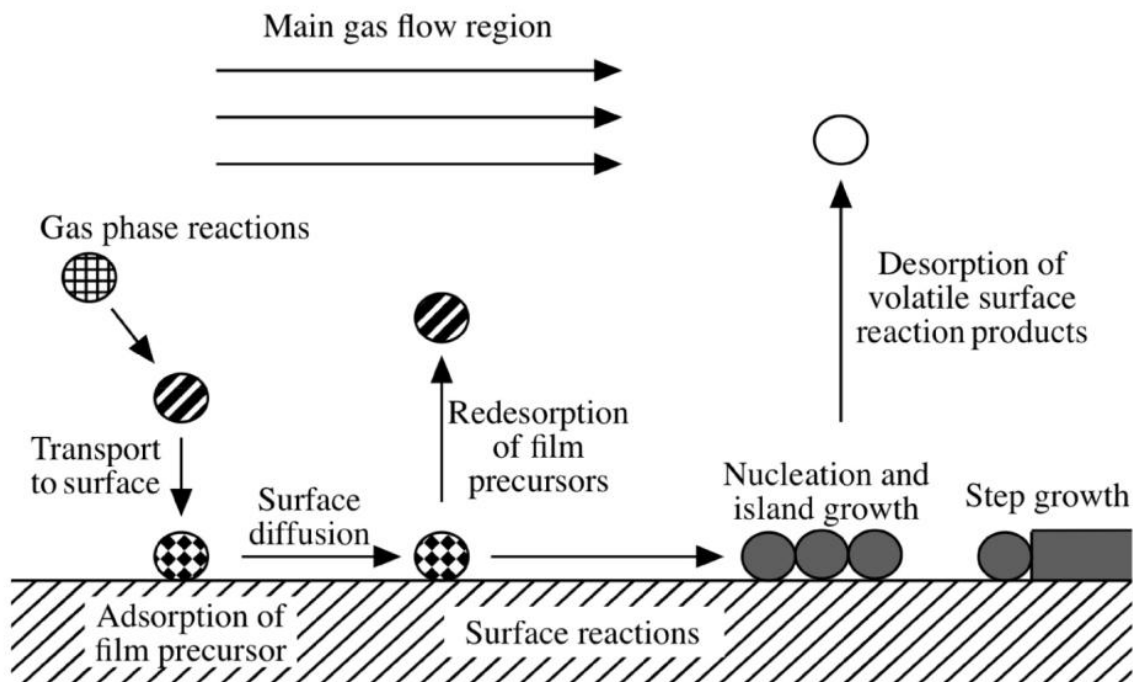


Figure 54: Different steps involved in CVD process.

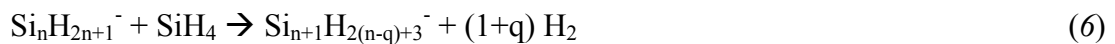
The main transport processes and chemical reaction involved in CVD are:

- i) introduction of the gas precursors in the deposition chamber;
- ii) gas's transport and diffusion onto substrate surface;
- iii) chemical reaction between the gas reagents and solid substrate;
- iv) nucleation and growth of the deposited layer;
- v) desorption of the volatile reaction products from solid surface.

There are several CVD systems typologies, but the two main categories are distinguishable from energy provided as input to activation process: the thermal CVD and the plasma CVD.<sup>277</sup> A thermal CVD process requires high temperatures (800°C and above) to break the precursors gas molecule and is out of the scope of this work. Instead we focus only on the plasma CVD that have the advantage of using much lower temperature (<600°C). These reactors are generally based on a parallel configuration (Figure 55) in which the two electrodes are the capacitor plates linked by the radiofrequency and the sample stays in between the two electrodes. Thanks to the use of a plasma, the substrate temperature can be lowered in 350-600°C range. Among them a subcategory is represented by the Inductively Coupled Plasma Chemical Vapour Deposition (ICP-CVD). Thanks to its vertical geometry, contrary to capacitive plasma configuration, ICP-CVD is based on an inductive coupling of the plasma allowing a much more plasma density (up to 10<sup>11</sup> ions /cm<sup>3</sup>).<sup>278,279</sup> High density plasma is so effective that the sample is located outside the radiofrequency region and furthermore the substrate can be kept near room temperature (70°C)<sup>280,281</sup> involving the formation of a compact amorphous layer through ionization reactions (1-2):



When using a high plasma density in combination with a sufficiently high pressure, the reactive ionized species are so closely packed that Si radicals coalesce in the gas phase promoting the Si nanoparticles formation and limiting the Si amorphous deposition through electron impact dissociation reactions like (3-6):<sup>282,283,284</sup>



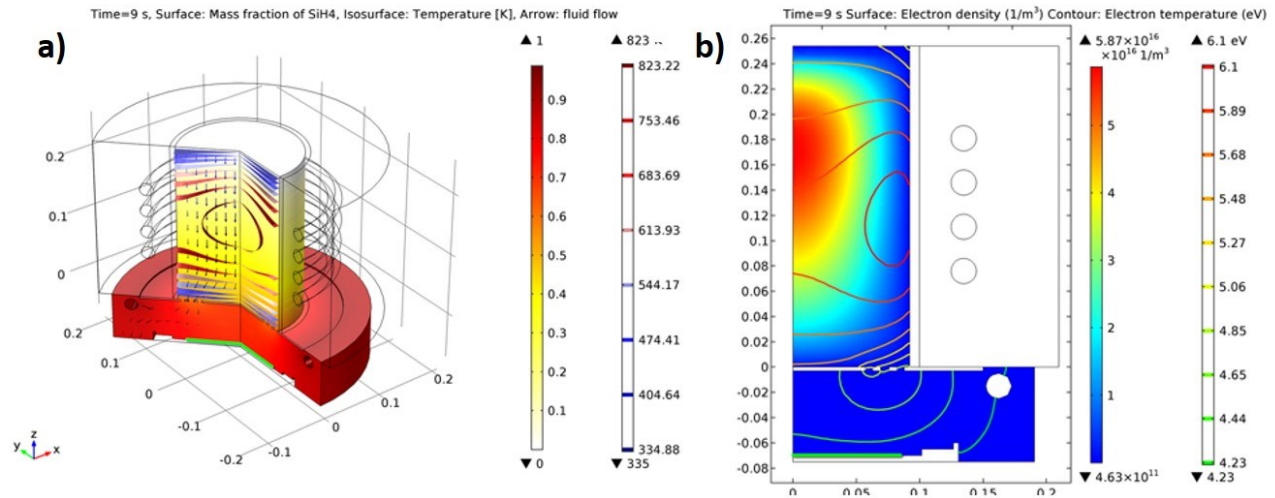


Figure 55:(a) 3D schematic of plasma reactor where the mass fraction of SiH<sub>4</sub> is shown as colour-map: the colours of isothermal surfaces indicate the gas temperature in K; the arrows indicate the fluid flow; (b) Electron density map in colour scale in an axial symmetric section of the plasma reactor: the lines' colour of the isothermal surfaces indicates the electron temperature in eV.<sup>285</sup>

Figure 55a shows a schematic of the inductively coupled plasma reactor: cylindrical plasma chamber, surrounded by coils, on top of the deposition chamber where the substrate (green) is positioned. The two parts of the reactor are in communication thanks to a disk with several holes. The arrows describe the fluid flow. Ar flux is injected homogeneously from the top of the plasma chamber, while the process gas (SiH<sub>4</sub> and, if needed for doping, a mixture of SiH<sub>4</sub> and phosphine, PH<sub>3</sub>, and/or trimethylborane, TMB) inlet is in the deposition chamber. The coloured part represents the mass fraction of SiH<sub>4</sub>. The largest portion of SiH<sub>4</sub> is confined in the deposition chamber, although a not negligible part of the fluxed gas goes inside the plasma chamber. Colours in Figure 55a indicate the gas temperature at isothermal surfaces: it is higher in the core of the plasma chamber, but it is relatively low close to the substrate. Figure 55b shows an axial-symmetric section of the plasma reactor. The coloured part represents the plasma region. Here, the colour scale depends on the electron density which is higher in the core region of the plasma chamber with respect to the outer one. Coloured lines in Figure 55b represent the iso-temperature lines in terms of electron temperature.

#### 4.1.1 Formation Mechanism of Si-NPs and structural characterization by TEM analysis

In the typical experimental setup, Ar gas flows through the cylindrical chamber and is excited by radio-frequency (RF) to form an high-density plasma ( $2\div 6 \times 10^{11}$  ions/cm<sup>3</sup>), the SiH<sub>4</sub> is injected at near the substrate and is decomposed by the large amount of electrons coming out from the plasma region. An argon-silane (Ar-SiH<sub>4</sub>) gas mixture is formed at low pressures in a cylindrical reaction chamber with 6 inches of diameter. Radio-frequency power of 500 W at 13.56 MHz is applied through a matching network to the two copper ring electrodes. The reflected power is only a small fraction (<1 %) of the forward power. Base pressure is as low as  $5 \times 10^{-7}$  Torr. Typical flow rates are 20 sccm for SiH<sub>4</sub> and 1 sccm for Ar that is used just to ignite the plasma. The non-thermal synthesis and the low operating pressure allow to achieve larger Si clusters limiting amorphous Si deposition.

The ICP-CVD key parameters that control the Si-NPs deposition are:

- i) radio-frequency power;
- ii) pressure;
- iii) gas flux;
- iv) time.

The critical parameter is indeed the pressure because at low pressure Si radicals are not close enough to coalesce into the Si-NPs and in contrast a sufficiently high pressure triggers the synthesis of Si-NPs. The RF power and gas flux determine the density of Si-NPs, whereas the size is controlled by the process time.

Shorter times (2-9 s) involves isotropic growth with the formation of spherical nanoparticles (Figure 56a - 56b). By increasing the deposition time (from 20 and up to 90 s) Si-NPs undergo a volume expansion and their growth is strictly dependent on crystallographic orientations, promoting the transformation of the sphere into an octahedron where the most energetically favoured planes limit the size growth. (Figure 56c - 56d).

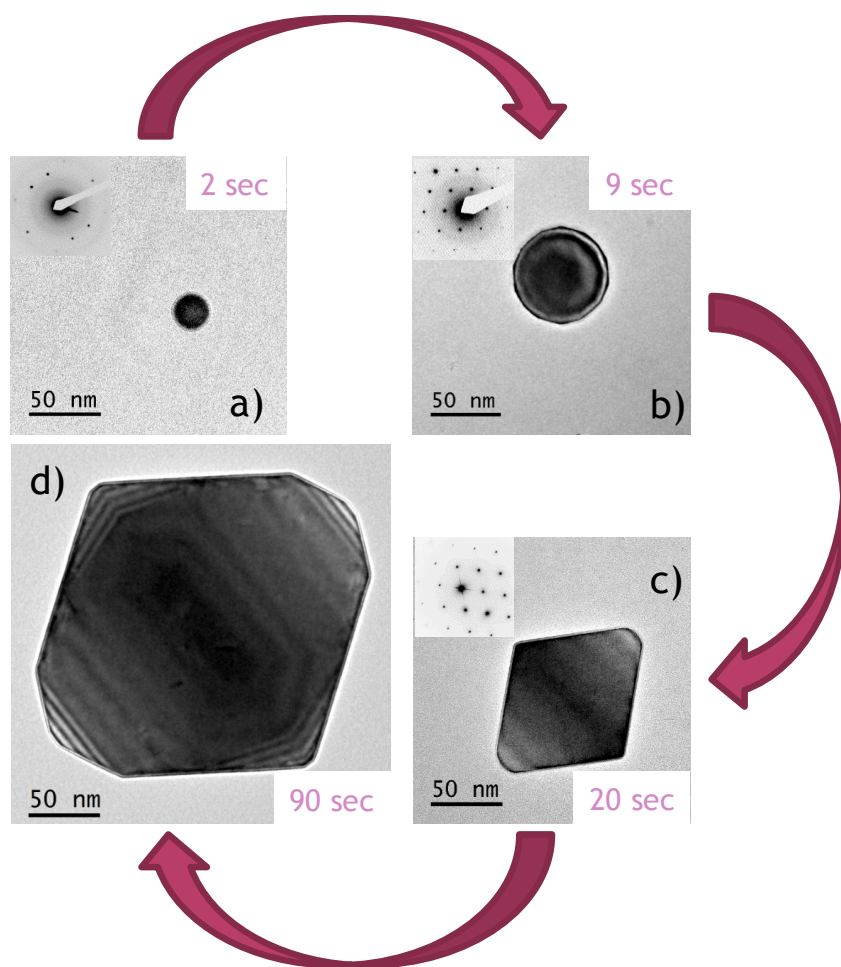
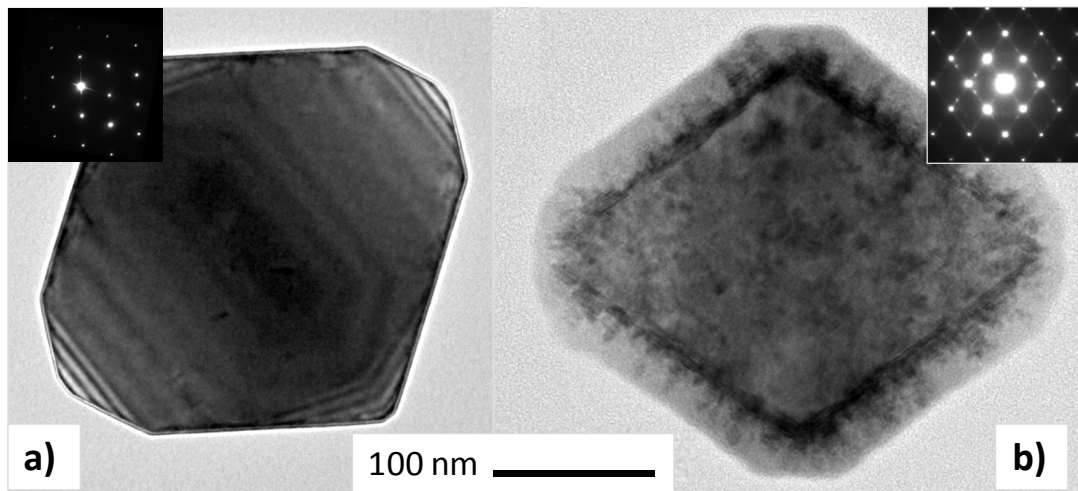


Figure 56: Structural evolution of Si-NPs with the increasing deposition times detected through TEM analysis

In order to investigate as the Si-NPs size condition the electrochemical Lithium loading, Si-NPs with size in the range 50-200 nm were synthesized by varying the process time from 5 to 90 s. In addition, n and p-doped Si-NPs were obtained by introducing a low amount of phosphine and trimethylborane as precursor gases. The presence of any other species in the gas mixture indeed alters the evolution path of the Si-NPs formation.

Intrinsic and doped Si-NPs obtained after 90 s are still characterized by an octahedral shape,<sup>286,287</sup> as reported in Figure 57, but with different crystallinity degree. The intrinsic Si-NPs are fully crystalline octahedrons (Figure 57a) exposing large {111} planes, because of their lower surface

energy with respect to  $\{311\}$  and  $\{110\}$  planes that, in fact, have smaller surface and form the tip and they are also present along the Si-NP edges (not-visible through TEM image). Diffraction pattern of Si-NPs (inset Figure 57a) is that of a perfect Si lattice. By introducing  $\text{PH}_3$  and TMB, respectively, as dopants in the deposition chamber Si-NPs (Figure 57b) has a core-shell structure, where the core is again fully crystalline but it is surrounded by a defective shell as seen in the inset in Figure 57b. In fact, differently from the diffraction pattern of crystalline Si lattice as reported in Figure 57a, extra spots from twins and stacking faults defects are visible near the spots.



*Figure 57: TEM images of (a) intrinsic and (b) doped-Si-NP after 90 s plasma process. While the intrinsic Si-NPs are fully crystalline, the P-Si-NPs consist of a perfect crystalline core surrounded by a defective shell. In the inset their corresponding diffraction.*

In order to implement these Si-NPs into the battery anode the synthesis process has been repeated as many times as needed to obtain a few tents of mg. SEM morphology of Si-NPs reported in Figure 58 confirms the formation of a porous layer composed of well-separated octahedral Si-NPs stacked in columnar structures.<sup>288</sup>

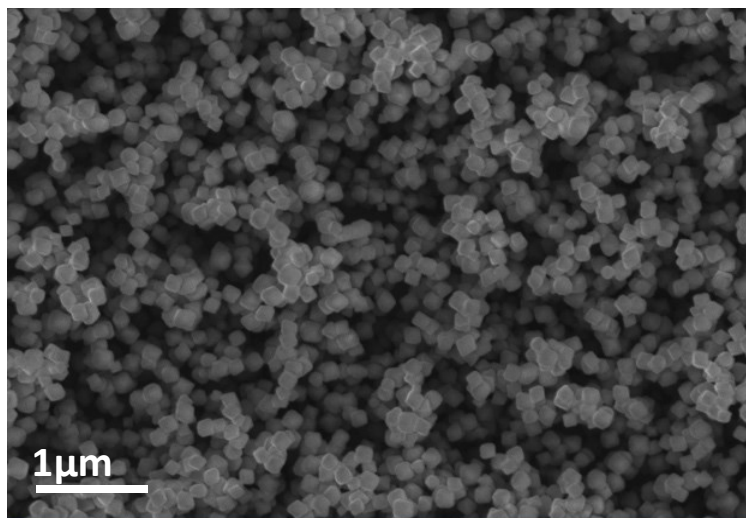


*Figure 58: SEM image of a 2 $\mu$ m thick-layer consisted of octahedral Si-NPs.<sup>284</sup>*

## **4.2 Electrodes Preparation and their assembly in LiBs**

In order to investigate as the size of Si-NPs and the peculiar octahedral shape determine the electrochemical performances of Lithium cells, small (15s), medium (45s) and large (90s) octahedral Si-NPs with size in the range between 50 and 200 nm were synthesized. The typical preparation route of electrode negative involves the realization of a mixed slurry past using carbon as additive, a polymer as binder such as polyacrylic acid (PAA) or polyvinylidenefluorure (PVdF) and a suitable solvent to guarantee a suspension stability, like N-methylpyrrolidone (NMP). Being the carbon ductile and highly conductive it allows to bear the Si volume variation reducing the capacity loss due to irreversible reactions. Whereas, polymeric binder allows to homogeneously deposit the mixed slurry paste on Cu surface, employed as common collector.

Figure 59 shows the different steps of the electrode manufacture. The Si-based anodes have been prepared from a suspension in NMP in which Si-NPs, carbon and PAA, are mixed in the 3:1:1 weight ratio.

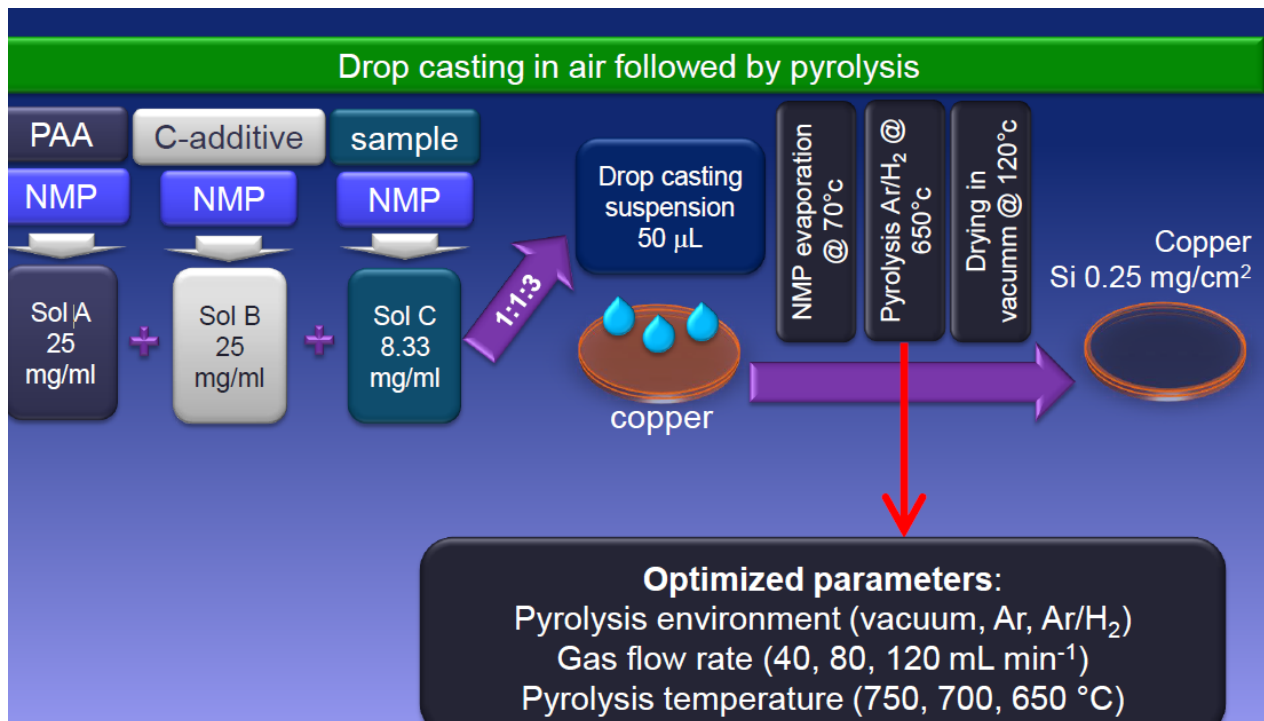


Figure 59: Electrode preparation based on the deposition of the mixed slurry paste consisted of PAA, C additive and Si-NPs on Cu surface and the following pyrolysis processes.

The mixture has been ultrasonicated for 20 minutes and 50  $\mu\text{L}$  of the final dispersion were drop-cast onto a 15mm<sup>2</sup> copper disk and dried under vacuum at 70 °C to evaporate the NMP. The as-prepared electrodes are placed at the center of a quartz tube furnace for a pyrolysis process in the range 650-750° C optimized by varying the gas mixture (vacuum, Ar and Ar/H<sub>2</sub>) and gas flow rate (from 40 to 120 mL/min). Finally, the dry process at 120 °C in vacuum, has permitted to complete the polymer degradation in order to obtain carbon/Si composite (0.25 mg/cm<sup>2</sup>) deposited on Cu surface uniformly.

The cells were assembled in the Ar glove box kept in anhydrous atmosphere ( $\text{H}_2\text{O} < 0.1$  ppm) and by using EI-Cell Std as devices (as reported on Chapter 2, Figure. 33, 34, 35), the lithium foil as counter electrode and LP30 as liquid electrolyte, consisted of a 1 molality solution of hexafluorophosphate,  $\text{LiPF}_6$ , dissolved into a mixture of ethylene carbonate and dimethyl carbonate, 1:1 in volume. Galvanostatic cycling of (+)Si-NPs/ EC:DMC 1:1  $\text{LiPF}_6$  (1molality 25  $\mu\text{L cm}^{-2}$ )/Li(-)



were carried out in the range 10 mV-2 V during the activation step at current density of C/33 and in the range 0.1-1 V for the following cycles at C/10 in order to stabilize the initial amorphization of Si-NPs and to investigate the reversibility of redox charge-discharge processes.

#### 4.2.1 Electrochemical Li loading of intrinsic Si-NPs

Galvanostatic charge-discharge processes have been modulated at different current density allowing to prove the considerable electrochemical activity of the Si-NPs and the dependence of the reversibility of electrochemical Li loading on the Si-NPs size. Figure 60 describes the electrochemical performance of the (+)Si-NPs/ EC:DMC 1:1 LiPF<sub>6</sub> (1 molality 25  $\mu\text{L cm}^{-2}$ )/Li(-) in which active material consists of small intrinsic Si-NPs. In particular, Figure 60a and 60b show the charge-discharge voltage profile as function of the specific capacity at C/10 and C/33 respectively. By decreasing the current density from 350  $\text{mA g}^{-1}$  to 106  $\text{mA g}^{-1}$  achieved at C/10 and C/33, the voltage profile doesn't undergo notable changes. During the first lithiation detected at C/10, 300  $\text{mAh g}^{-1}$  capacity coincides with the sloping section of the curve taking place in the 2.2-0.1 V potential window accounting for SEI formation at crystals-electrolyte interface. Whereas at C/33, 500  $\text{mAh g}^{-1}$  capacity is related to the sloping voltage in the range 2.2-0.1 V. Subsequently, the long-lasting plateau sets at 100 mV vs. Li<sup>+</sup>/Li and it is related to amorphization of crystalline Si particles taking place during the very first lithium insertion, starting at the particle surface and proceeding internally towards the particle core. The second charge/discharge cycle is characterized by a lower hysteresis compared to the first cycle and the occurring electrochemical mechanisms are composed by two pseudo plateaus during the lithiation, taking place at about 0.25 and 0.5 V and a single delithiation plateau, occurring at 0.4 V.

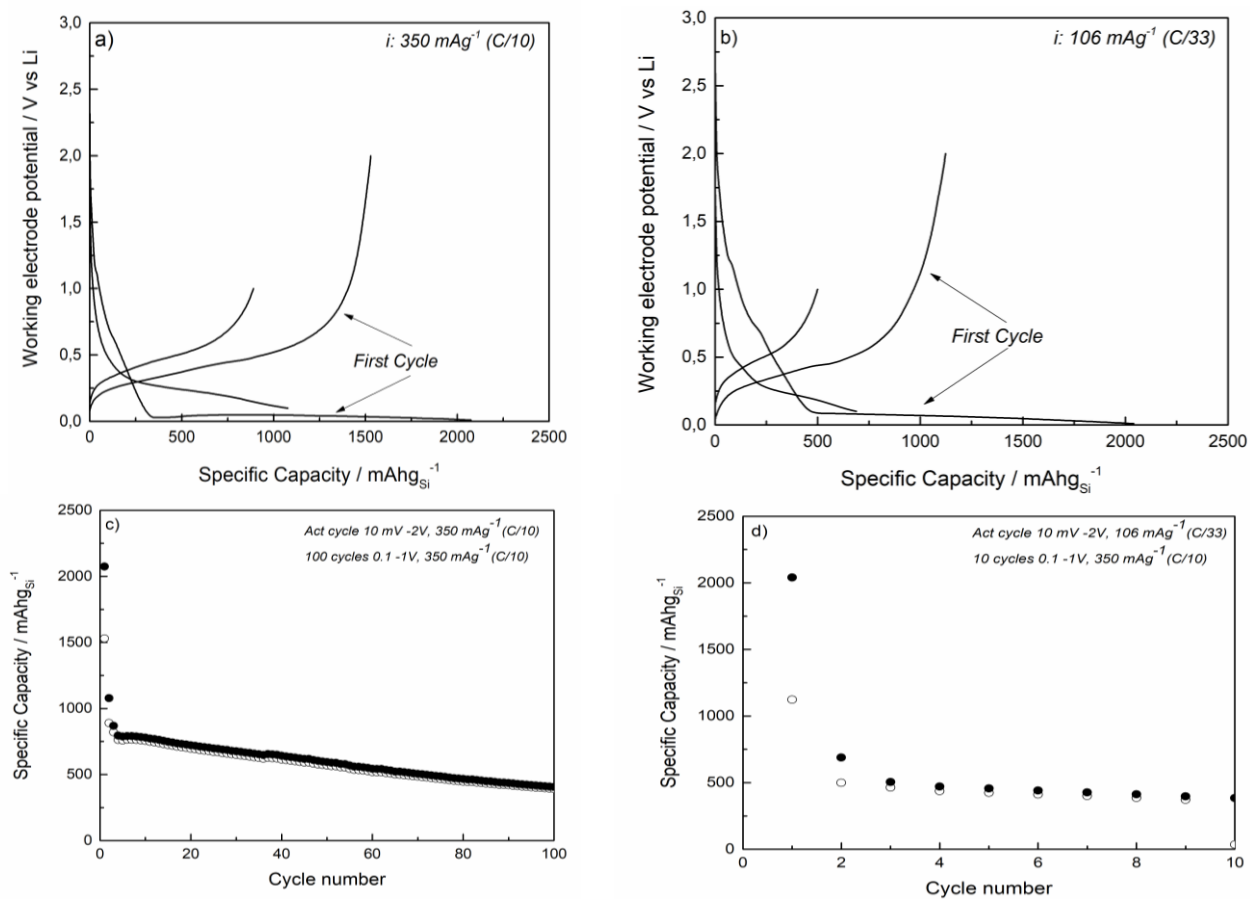


Figure 60: Galvanostatic characterization of small Si-NPs: a)-b) charge-discharge voltage profile detected at C/10 and C/33; c-d) charge-discharge capacities detected at C/10 and C/33 (empty symbols: charge values; filled symbols: discharge values)

The specific capacity of small intrinsic Si-NPs as function of the cycle number detected at C/10 and C/33 are reported in Figure 60c and 60d respectively, and are summarised in table 10.

<b>Small Intrinsic Si-NPs</b>					
	<i>1st discharge capacity mAhg<sup>-1</sup></i>	<i>%Theoretical Capacity</i>	<i>Li eq. 1st discharge</i>	<i>Coulombic Efficiency 1st cycle</i>	<i>Rev. Li eq. 2nd cycles</i>
<i>C/10</i>	2074	58%	2.17	74%	1.12
<i>C/33</i>	2244	63%	2.35	53%	0.77

Table 10: Electrochemical performances of small intrinsic Si-NPs during the 1st and 2nd cycles.

Small intrinsic Si-NPs during the first cycle at C/10 show a discharge capacity of 2074 mAhg<sup>-1</sup> (Figure 60c) attributable to a Li<sub>2.17</sub>Si alloy formation and reaching to a theoretical capacity of to 58% (vs 3579 mAhg<sup>-1</sup> of Si theoretical). In addition; small Si-NPs show a reversible electrochemical cycling reaching to a coulombic efficiency of 74% and leading to a Li<sub>1.12</sub>Si alloy at 2nd cycle. By decreasing the current density to C/33 (Figure 60d), small Si-NPs show a slight improvement of the electrochemical performance during the first discharge reaching to a theoretical capacity of to 63% (vs 3579 mAhg<sup>-1</sup> of Si theoretical) but the Coulombic efficiency decreases to 53%, proving as the reversible electrochemical Li loading isn't particularly favoured at lower current density.

The electrochemical Li loading of medium sized intrinsic Si-NPs shows a trend completely different respect to that one seen for the smaller Si-NPs. By decreasing the current density from C/10 to C/33, medium Si-NPs present a quasi-ideal behaviour, reaching a discharge capacity of 3522 mAhg<sup>-1</sup> vs 3579 mAhg<sup>-1</sup> of Si. In detail, the voltage profile reports in Figure 61a and detected at C/10 doesn't show the plateau typical of activation step proving that the Si amorphization doesn't take place. Whereas, during the first lithiation detected at C/33, 600 mAhg<sup>-1</sup> capacity coincides with the sloping section of the curve taking place in the 3.0 - 0.1 V potential range (Figure 61b). In addition, the long-lasting plateau sets at 100 mV vs. Li<sup>+</sup>/Li and it results wider

than the relative detected for the small Si-NPs (Figure 60b). Similarly, the plateau sets at about 0.3 V and it is detected during the first de-lithiation process at C/33 resulting on greater than the relative seen for small Si-NPs. The second charge/discharge cycle are characterized by two lithiation plateaus, taking place at 0.25 and 0.5 V, and a two de-lithiation plateau, occurring at about 0.3 and 0.7 V.

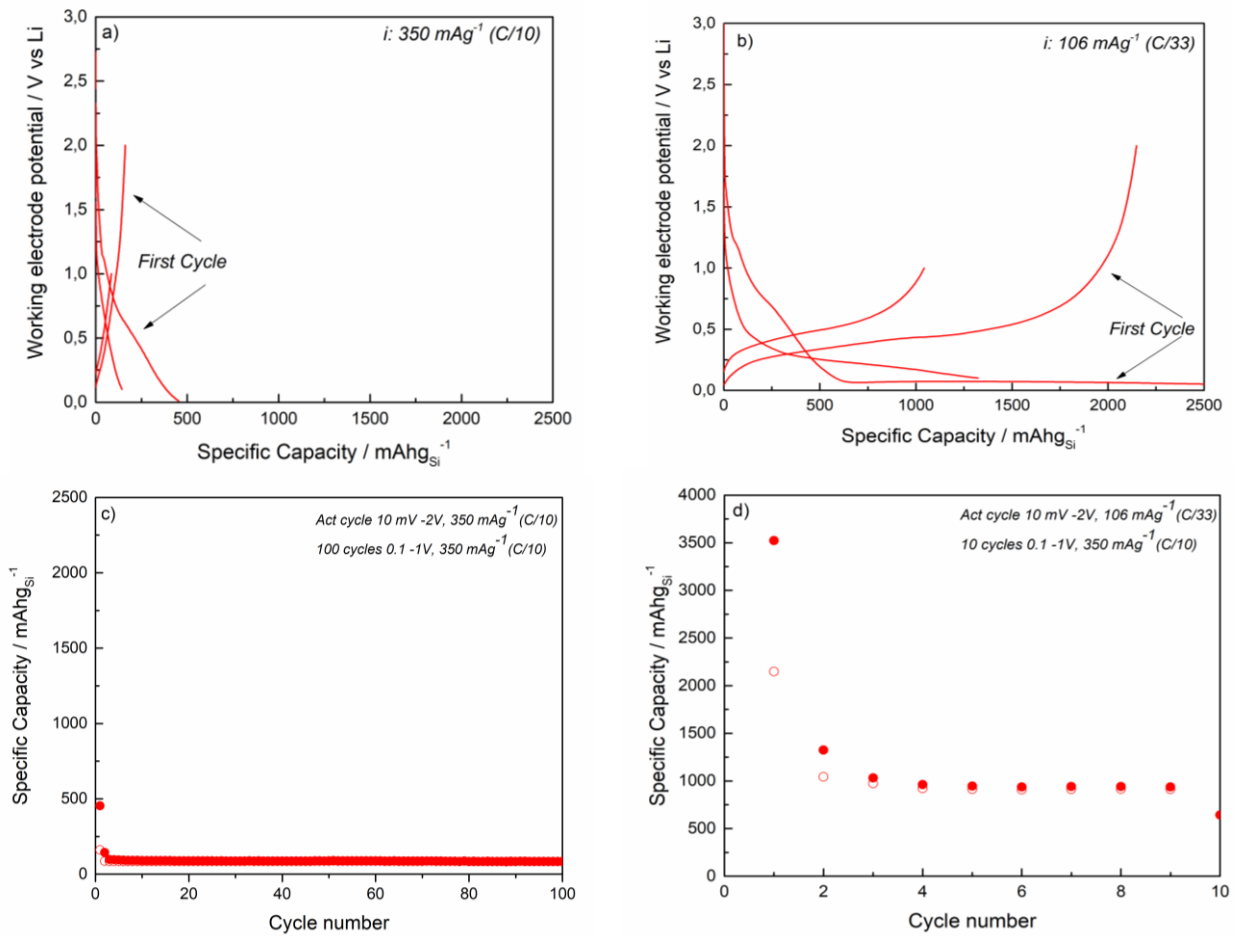


Figure 61: Galvanostatic characterization of medium Si-NPs: a)-b) charge-discharge voltage profile detected at C/10 and C/33; c-d) charge-discharge capacities detected at C/10 and C/33 (empty symbols: charge values; filled symbols: discharge values).

The specific capacity of small intrinsic Si-NPs as function of the cycle number detected at C/10 and C/33 are reported in Figure 61c and 61d respectively, and are summarised in table 11.

<b>Medium Intrinsic Si-NPs</b>					
	<i>1st discharge capacity mAhg<sup>-1</sup></i>	<i>%Theoretical Capacity</i>	<i>Li eq. 1st discharge</i>	<i>Coulombic Efficiency 1st cycle</i>	<i>Rev. Li eq. 2nd cycles</i>
<i>C/10</i>	453	13%	0.47	35%	0.17
<i>C/33</i>	3522	98%	3.69	61%	1.38

Table 11: Electrochemical performances of medium intrinsic Si-NPs during the 1st and 2nd cycles.

Medium intrinsic Si-NPs during the first cycle at C/10 show a discharge capacity of 453 mAhg<sup>-1</sup> (Figure 61c), lower than one detected for small Si-NPs and attributable to a Li<sub>0.47</sub>Si alloy reaching to a theoretical capacity of to 13%. In addition; small Si-NPs show a reversible electrochemical cycling reaching to a Coulombic efficiency of 35% and leading to a Li<sub>0.17</sub>Si alloy at 2nd cycle. By decreasing the current density to C/33, medium Si-NPs show an excellent improvement of their electrochemical performances. In detail, they present a first discharge capacity of 3522 mAhg<sup>-1</sup> (Figure 61d), really close to theoretical value of the Si anode and reaching a theoretical capacity of 61% attributable to the Li<sub>3.69</sub>Si phase formation proving as the cycling at C/33 involve a better amorphization stability and more cycling reversibility.

Despite the overall particle dimension above 200 nm, considered as a threshold value above which the particles easily crack during the lithiation; the electrochemical Li loading and the cycling reversibility of the large Si-NPs result very good, particularly at C/33. The first lithiation detected at C/10, is characterized by two pseudo plateaus at about 1.25 and 0.75 V. Whereas, the first lithiation, detected at C/33, is characterized by a three pseudo plateaus at about 1.25, 0.75 and 0.3 V and it presents a longer lasting plateau sets at about 0.5 V vs Li<sup>+</sup>/Li related to amorphization of

crystalline Si particles (Figure 62a). The first de-lithiation processes of the large Si-NPs show a voltage plateau at C/33, sets at 0.5V (Figure 62b), whereas the charge process at C/10 doesn't show any voltage plateau. In addition, the voltage profiles related to the second lithiation and de-lithiation processes at C/33 proving as the cycling reversibility of the large Si-NPs improves with the decrease of the current density.

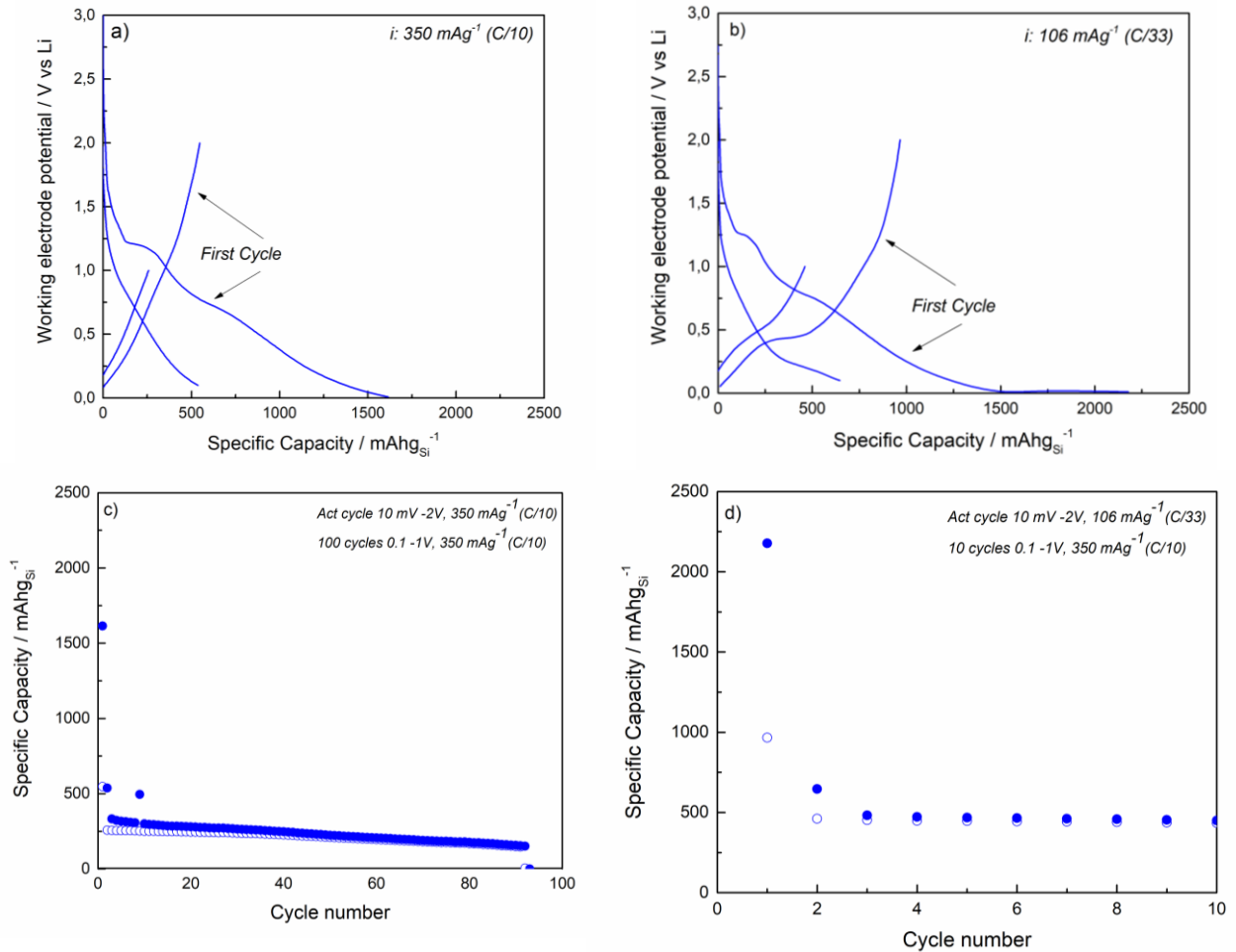


Figure 62: Galvanostatic characterization of large Si-NPs: a)-b) charge-discharge voltage profile detected at C/10 and C/33; c)-d) charge-discharge capacities detected at C/10 and C/33 (empty symbols: charge values; filled symbols: discharge values).

The specific capacity of the large intrinsic Si-NPs as function of the cycle number detected at C/10 and at C/33 are reported in Figure 62c and 62d respectively, and can be explained by considering the table 12.

<b>Large Intrinsic Si-NPs</b>					
	<i>1st discharge capacity mAhg<sup>-1</sup></i>	<i>%Theoretical Capacity</i>	<i>Li eq. 1st discharge</i>	<i>Coulombic Efficiency 1st cycle</i>	<i>Rev. Li eq. 2nd cycles</i>
<i>C/10</i>	1614	45%	1.69	34%	0.27
<i>C/33</i>	2177	61%	2.28	45%	0.67

Table 12: Electrochemical performances of large intrinsic Si-NPs during the 1st and 2nd cycles.

Large intrinsic Si-NPs during the first cycle at C/10 show a discharge capacity of 1614 mAhg<sup>-1</sup> (Figure 62c), attributable to a Li<sub>1.69</sub>Si alloy formation and they reach to a theoretical capacity of to 45%. In addition; the large Si-NPs show a reversible electrochemical cycling reaching to a Coulombic efficiency of 34% and leading to a Li<sub>0.27</sub>Si alloy at 2nd cycle. By decreasing the current density to C/33, large Si-NPs show better electrochemical performances. In detail, they present a first discharge capacity of 2177 mAhg<sup>-1</sup> (Figure 62d), strictly close to theoretical value of the Si anode reaching a theoretical capacity of 61% and attributable to the Li<sub>2.28</sub>Si phase formation proving as the cycling at C/33 involve a better stable amorphization and more reversible electrochemical Li loading.

The study of the role of the octahedral Si-NPs sizes on electrochemical Li loading has allowed to select the better size to limit the deleterious phase transitions commonly occurring during lithium alloying. With respect to the examples reported in literature, medium intrinsic Si-NPs strongly activates the electrochemical alloying with lithium showing an excellent reversible cycling ability.

Medium octahedral Si-NPs not only results a high-capacity anode but also behave as quasi-ideal negative electrode. This effect is probably due to the novel octahedral shape that is capable of bear the lithiation stress avoiding the anode disintegration and therefore, limiting the capacity fade.

#### 4.2.2 LiBs Anode based on doped Si-NPs

In order to investigate as the doping of Si-NPs influences the electrochemical Lithium loading, n and p-type Si-NPs were synthesized by introducing PH<sub>3</sub> and TMB gases during the process in addition to SiH<sub>4</sub> and Ar. It is way it is possible to modulate the doping levels by varying the gas fluxes. In contrast to the few examples of doped Si-NPs-based anode reported in literature and obtained through very high dopant concentrations, here octahedral Si-NPs were doped by employing a relatively low dopant gas flux. Since medium intrinsic octahedral Si-NPs act as high-capacity anodes, as reported in the previous paragraph, the same process time (45 s) has been used only adding the dopant gas to obtain doped Si-NPs. Again, Si-NPs have been deposited on Cu collector through the same steps reported in Figure 59 and galvanostatic cycling of (+)doped Si-NPs/ EC:DMC 1:1 LiPF<sub>6</sub> 1 molality 25  $\mu\text{L cm}^{-2}/\text{Li}(-)$  were carried out by adopting the same current densities used for intrinsic Si-NPs.

Figure 63 shows the electrochemical performance of the (+) P-doped Si-NPs/ EC:DMC 1:1 LiPF<sub>6</sub> 1m 25  $\mu\text{L cm}^{-2}/\text{Li}(-)$  in which active material consists of P-doped Si-NPs. In particular, Figure 63a and 63b show the charge-discharge voltage profile as function of the specific capacity at C/10 and C/33 respectively. The first lithiation detected at C/10, is characterized by two pseudo plateaus at about 1.15, 0.3 V (Figure 63a). The first lithiation, detected at C/33, is characterized by a two clear pseudo plateaus at about 1.25, 0.8 V and a less well-defined plateau at 0.3 V (Figure 63b). The first de-lithiation processes of the P-doped Si-NPs doesn't show any voltage plateau both at C/33 and C/10 (Figure 63a and 63b). Therefore, by decreasing the current density from C/10 to C/33, the voltage profile of P-doped Si-NPs doesn't undergo a specific change.



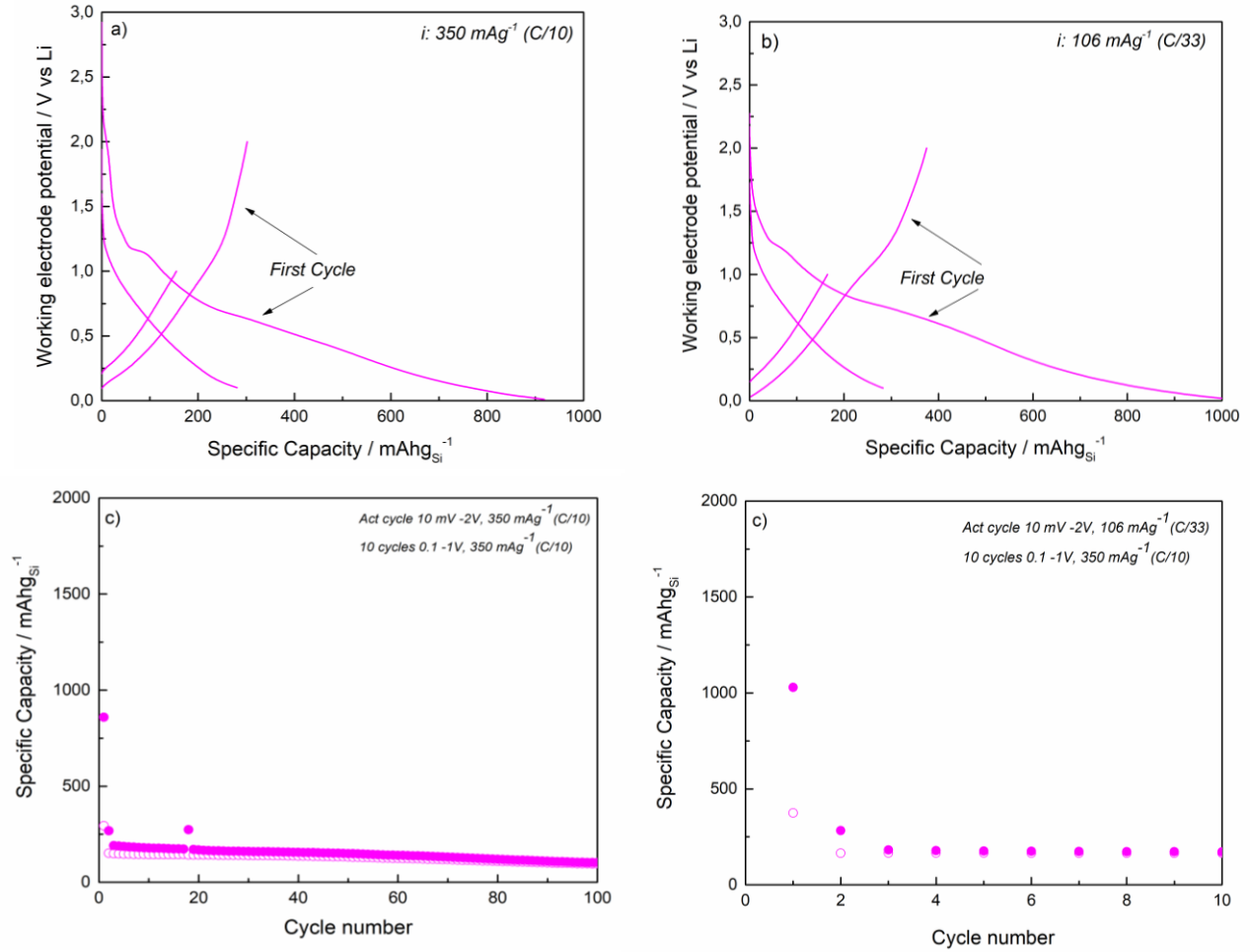


Figure 63: Galvanostatic characterization of medium P-doped Si-NPs: a)-b) charge-discharge voltage profile detected at C/10 and C/33; c-d) charge-discharge capacities detected at C/10 and C/33 (empty symbols: charge values; filled symbols: discharge values).

The specific capacity of P-doped Si-NPs as function of the cycle number detected at C/10 and at C/33 are reported in Figure 63c and 63d respectively, and are summarised in table 13.

<b>Medium P-doped Si-NPs</b>					
	<i>1st discharge capacity mAhg<sup>-1</sup></i>	<i>%Theoretical Capacity</i>	<i>Li eq. 1st discharge</i>	<i>Coulombic Efficiency 1st cycle</i>	<i>Rev. Li eq. 2nd cycles</i>
<i>C/10</i>	858	24%	0.9	34%	0.3
<i>C/33</i>	1028	29%	1.1	36%	0.3

Table 13: Electrochemical performances of medium P-Si-NPs during the 1st and 2nd cycles.

P-doped Si-NPs show a similar electrochemical performance by decreasing the current density from C/10 to C/33. Indeed, they present a first discharge capacity of 858 mAhg<sup>-1</sup> (Figure 63c), that increases to 1028 mAhg<sup>-1</sup> (Figure 63d), attributable to a Li<sub>0.1</sub>Si alloy formation at C/33. The coulombic efficiency of P-doped Si-NPs at C/10 and C/33 is similar and it varies from 34 to 36%, respectively.

The electrochemical behaviour of medium sized B-doped Si-NPs is described in Figure 64. Particularly, Figure 64a and 64b show the charge-discharge voltage profile as function of the specific capacity at C/10 and C/33 respectively. The first lithiation detected at C/10, is characterized by a sloping section of the curve taking place in the 2.2-0.1 V potential followed by long-lasting plateau sets at 100 mV vs. Li<sup>+</sup>/Li and it is related to amorphization of crystalline Si particles taking place during the very first lithium insertion, starting at the particle surface and proceeding radially towards the particle core. The first lithiation, detected at C/33, is characterized by a longer sloping section of the curve taking place in the 3.0-0.1 V. In addition, the lasting plateau sets at 100 mV and associated to amorphization Si result wider than that one detected at C/10.

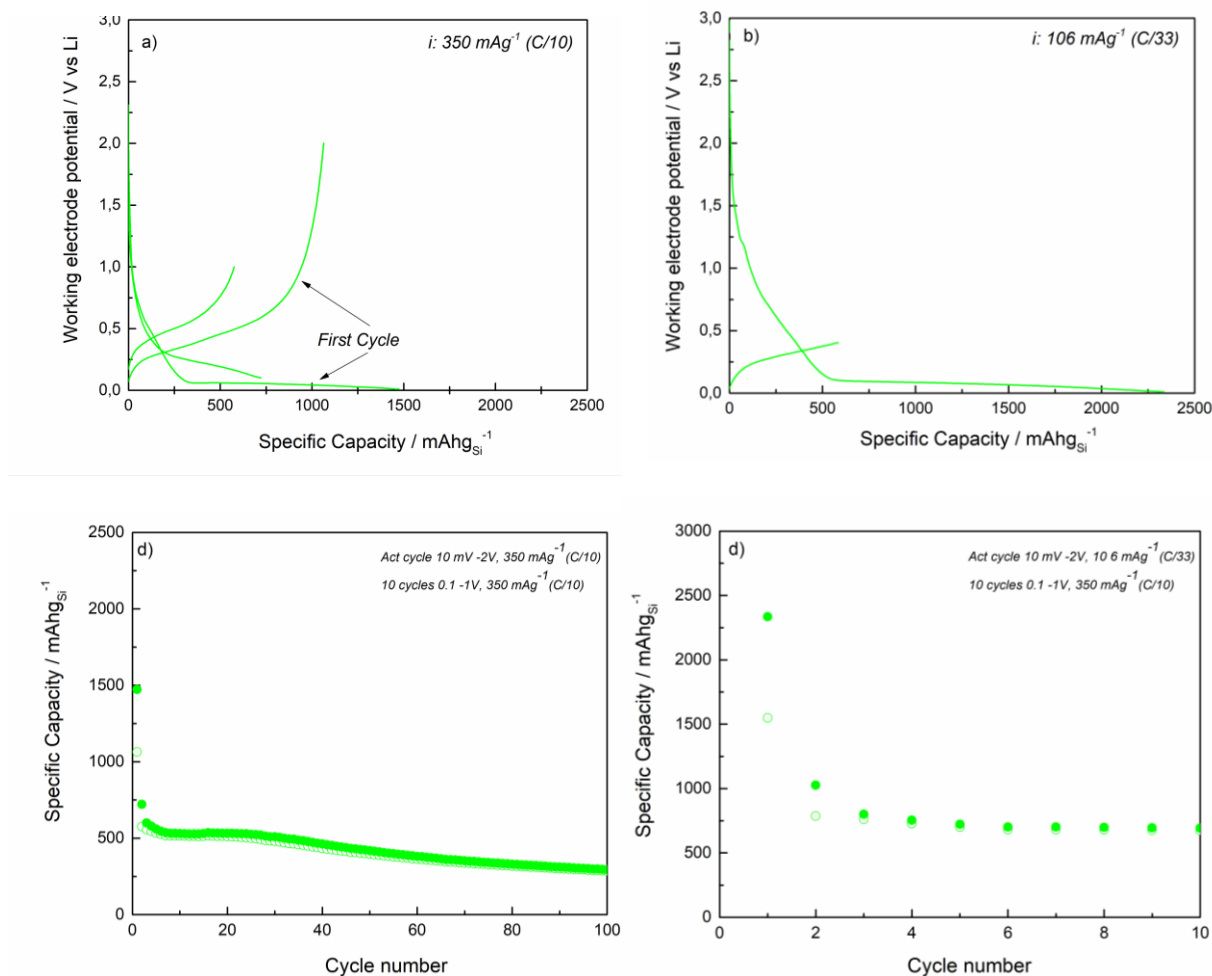


Figure 64: Galvanostatic characterization of medium B-doped Si-NPs: a)-b) charge-discharge voltage profile detected at C/10 and C/33; c-d) charge-discharge capacities detected at C/10 and C/33 (empty symbols: charge values; filled symbols: discharge values).

The specific capacity of B-doped Si-NPs as function of the cycle number detected at C/10 and at C/33 are reported in Figure 64c and 64d respectively, and are summarised in table 14.

<b>Medium B-doped Si-NPs</b>					
	<i>1st discharge capacity mAhg<sup>-1</sup></i>	<i>%Theoretical Capacity</i>	<i>Li eq. 1st discharge</i>	<i>Coulombic Efficiency 1st cycle</i>	<i>Rev. Li eq. 2nd cycles</i>
<i>C/10</i>	1473	24%	1.5	72%	0.7
<i>C/33</i>	2335	41%	2.4	25%	1.0

Table 14: Electrochemical performances of medium B-Si-NPs during the 1st and 2nd cycles.

B-doped Si-NPs show a first discharge capacity of 1473 mAhg<sup>-1</sup> at C/10 (Figure 64c), that it increases to 2335 mAhg<sup>-1</sup> (Figure 64d), attributable to a Li<sub>2.4</sub>Si alloy formation, at C/33 and reaching a theoretical capacity of 41%, proving as the cycling at C/33 involve a better amorphization stability and more cycling reversibility.

The electrochemical performances of doped Si-NPs demonstrate as the B-doping strongly activates the electrochemical alloying with lithium involving better cycling reversibility. As reported in literature, these effects are probably due to the additional amorphous phase formation, like B<sub>4</sub>Li<sub>5</sub>, after lithium alloying as reported in literature.

### **4.3 Functionalization of octahedral Si-NPs with ZIF-8**

Thanks to the peculiar octahedral shape, innovative Si-NPs-based anode has been developed for LIBs. As above reported, by modulating the size and the chemical composition of Si-NPs it is possible to optimize the electrochemical Li loading and improve the cycling reversibility. In particular, medium intrinsic Si-NPs and medium B-doped Si-NPs behave as high-capacity anodes leading to excellent electrochemical performance in terms of lithium ion uptake and capacity retention. However, the continue lithiation and delithiation processes will result in a structural stress and volume variations of also in octahedral Si-NPs, although less evident than in spherical Si-NPs. In order to guarantee an efficient electric contact and to limit the possible irreversible processes, the assembly of Si-NPs in a carbon porous matrix leads to a composite thin films capable of tuning the properties of the electrode/electrolyte interface in the Li cell. The develop of Si-NPs/ZIF-8 core shell allows to combine the excellent anode properties of Si-NPs with the partial reversible electrochemical activity of the ZIF-8. The carbon framework of ZIF-8, its porosity and large surface guarantee a flexible matrix that it should be capable to bear the lithiation stress and the electrolyte diffusion without compromise the capacity featuring. Therefore, the ZIF-8 should represent a mesoporous composite electrode and a hybrid solid electrolyte for Li ion transport.

The present paragraph reports the following studies:

- The chemical composition of octahedral Si-NPs has been investigated through XPS analysis in order to understand the nature of their surface and to optimize their functionalization with ZIF-8.
- By adopting different synthesis protocols, it has been possible to modulate the thickness and the chemical compositions of ZIF-8 coating. Particularly the functionalization of Si-NPs it has been carried out by using methanol and ethanol as solvent.

#### **4.3.1 XPS analysis of octahedral Si-NPs**

Octahedral Si-NPs with a size exceeding 100 nm (45 s process time) in average were synthesized by means of non-thermal induced coupled plasma chemical vapour deposition. Figure 65 shows the XPS deconvolution of Si-NPs achieved after 15 min in air.

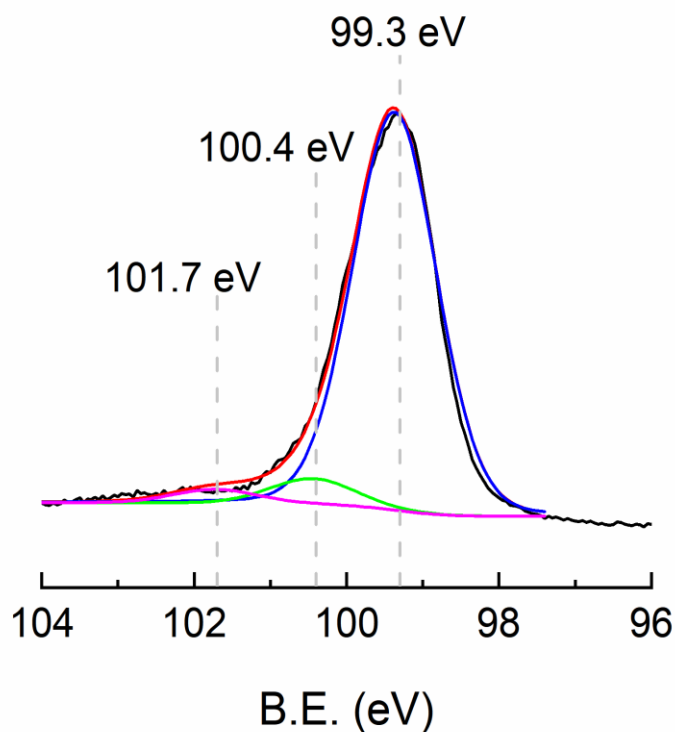


Figure 65: XPS deconvolution of Si 2p signal of Si-NPs deposited by ICP-CVD.

Si 2p signal consists of a defined peak centred at 99.3 eV and two broad components at 100.4 and 101.7 eV, respectively. The more intense peak at lower binding energy is attributable to Si-Si bonds formation,<sup>289</sup> whereas the broader and weaker signals at higher binding energy are due to the starting oxidation of Si-NPs and SiO<sub>x</sub> species formation. Particularly, the XPS bands at 100.4 and 101.8 eV are due to Si<sup>+1</sup> and Si<sup>+2</sup> arising from oxidized Si.<sup>290</sup> The surface chemistry of Si-NPs results similar to hydrogen-terminated Si surface. Indeed, the above described XPS spectrum is comparable to that one of Si-H surface obtained through HF etching<sup>291</sup> and characterized by an initial oxidation as reported on Chapter 2 (Figure 20).

In particular, the XPS chemical composition of Si-NPs indicates a hydrogen terminated surface and therefore, characterized by a greater density of isolated silanols. So doing, Si-NPs should favourite the imidazole deprotonation and accelerate the they should result quite reactive towards ZIF-8 functionalization.

#### **4.3.2 Si-NPs functionalization with ZIF-8**

Octahedral Si-NPs were deposited on SiO<sub>2</sub> surface by means ICP-CVD. A radio-frequency power of 500W was applied and an argon-silane (Ar-SiH<sub>4</sub>) gas mixture (20 sccm /1 sccm) was used. The base pressure and the process time were kept at  $5 \times 10^{-7}$  Torr and 90 sec, respectively. Two solutions of 250 ml of Zn(NO<sub>3</sub>)<sub>2</sub> (12,5 mM) and 250 ml of HmeIm (25 mM) have been prepared using either MeOH or EtOH as solvent. During each cycle, the substrates were dipped in a mix solution consisted of 10 ml Zn(NO<sub>3</sub>)<sub>2</sub> (12,5 mM) and 10 ml HmeIm (25 mM) for 30 minutes at room temperature and without stirring.<sup>292</sup> Subsequently the samples were rinsed in the reaction solvent (MeOH or EtOH) and, finally dried under N<sub>2</sub> flow. From one to ten cycles were performed in MeOH or EtOH, respectively.

Figure 66a shows the XRD patterns of Si-NPs/ZIF-8 structures obtained after ten deposition cycles form methanol solution. Respect to the surfaces, Si, amorphous Si and quartz reported on the Chapter 2, the diffractogram of Si-NPs/ZIF-8 shows not only the main diffraction peak at 7.33 attributable to (011) reflection but also the peaks at 10.3 and 12.7 due to (002) and (112) reflections.<sup>293</sup>

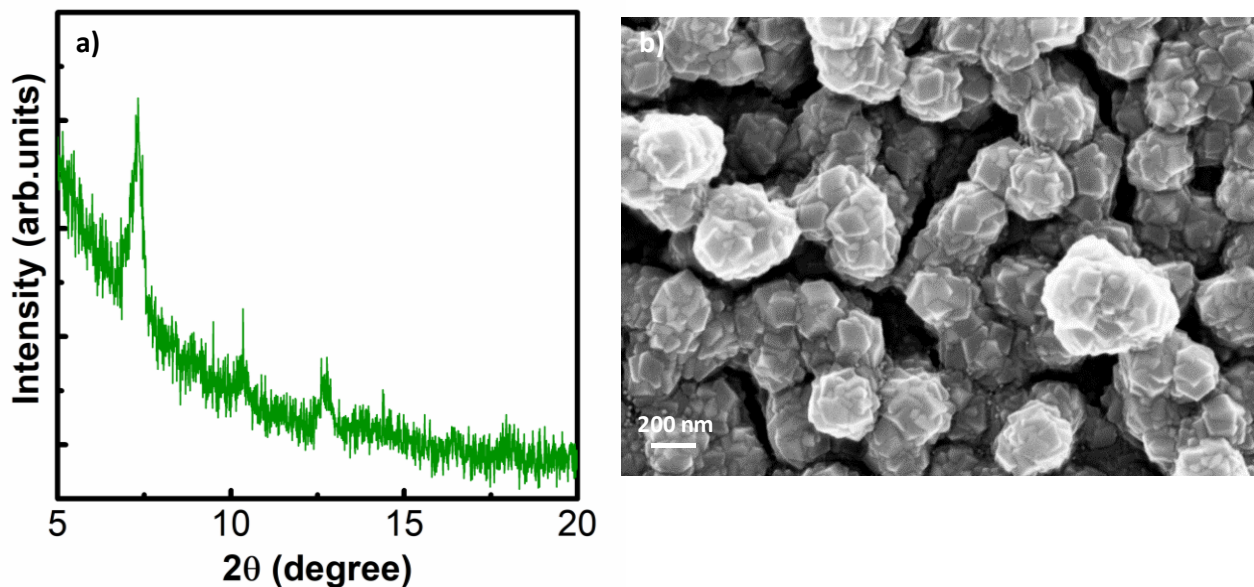


*Figure 66: (a) XRD patterns (b) and SEM morphology of Si-NPs/ZIF-8 structures obtained after 10 deposition cycles in MeOH.*

Figure 66b shows the SEM morphology of Si-NPs/ZIF-8 structures proving the increase of surface porosity of Si-NPs due to the ZIF-8 matrix in which the nanostructures are embedded.

Figure 67a shows the XRD patterns of Si-NPs/ZIF-8 structures obtained after ten deposition cycles from ethanol solution. In this case, any characteristic diffraction signal of ZIF-8 isn't present, confirming the data reported on the Chapter 2 and; in particular, the lower growth rate in ethanol solution.



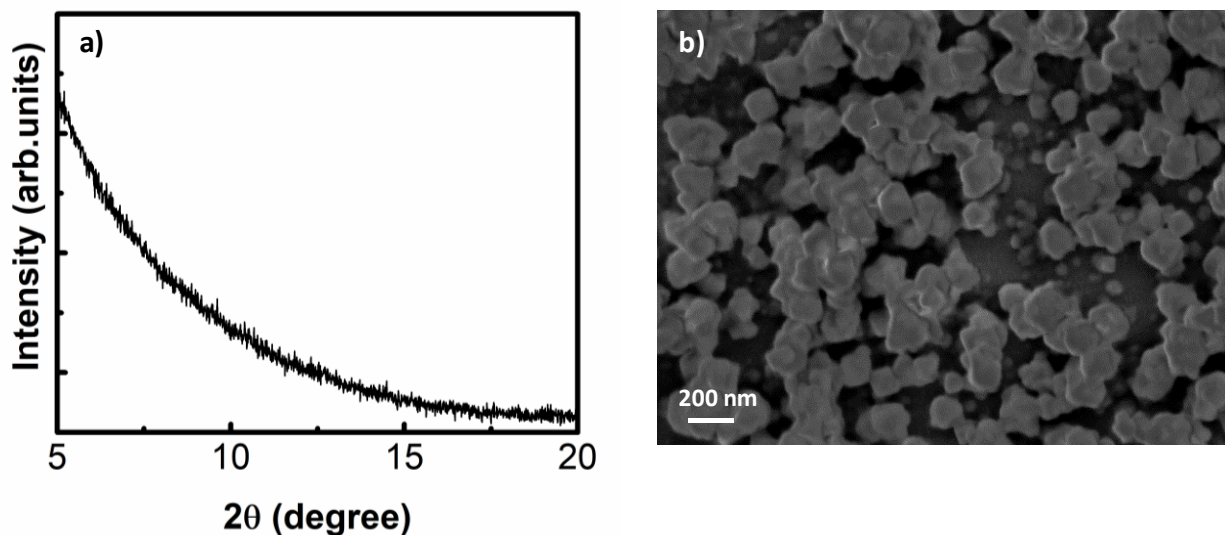


Figure 67: (a) XRD patterns (b) and SEM morphology of Si-NPs/ZIF-8 structures obtained after 10 deposition cycles in EtOH.

Similarly, SEM image of Si-NPs/ZIF-8 structures obtained after 10 cycles in ethanol shows a less ZIF-8 deposited indicating once again as the ZIF-8 functionalization form ethanol solution leads to thinner coating (Figure 67 b).

The chemical composition of Si-NPs/ZIF-8 structures was investigated by XPS quantitative analysis.

<i>XPS atomic concentration of Si-NPs/ZIF-8_10 deposition cycles</i>						
	<i>Si 2p</i>	<i>C 1s</i>	<i>O 1s</i>	<i>N 1s</i>	<i>Zn 2p<sub>3/2</sub></i>	<i>N/Zn</i>
<b>MeOH</b>	<b>2.2</b>	54.9	35.3	6.1	1.5	<b>4.1</b>
<b>EtOH</b>	<b>15.6</b>	47.1	20.6	12.7	4.0	<b>3.2</b>

Table 15: XPS quantitative of Si-NPs obtained after 10 SOP cycles from MeOH and EtOH

Table 15 reports the atomic concentration of Si 2p, C 1s, O 1s, N 1s and Zn 2p<sub>3/2</sub> for Si-NPs/ZIF-8 structures after 10 deposition cycles from methanol and ethanol solution. It is quite clear as the synthesis in ethanol solution is slower, leading to a greater contribute of the substrate. Indeed, XPS atomic concentration of Si 2p is 15.6% vs 2.2% related to the synthesis in MeOH. In addition, N/Zn atomic ratio results 4.1 and close to the theoretical value (4.0) for the Si-NPs/ZIF-8 achieved for the synthesis in methanol solution. Whereas, N/Zn atomic ratio is still only 3.2 after 10 deposition cycles from ethanol solution.

In order to prove the high reactivity of Si-NPs towards ZIF-8 functionalization, 1 deposition cycle of ten minutes was carried out from methanol solution.

As show in Figure 68a the XPS signal of N 1s of Si-NPs/ZIF-8 structures obtained after 1 cycle in MeOH, consists of a single peak centred at 399.3 eV attributable to deprotonated imidazole nitrogen atoms. The Zn 2p<sub>3/2</sub> XPS signal results a sum of two peaks, one at higher B.E. due to hydroxides or nitrates presence and one of higher intensity centred at 1023.1 (Figure 68 b), due to ZIF-8 crystals formation as proved for bulk ZIF-8 and reported on the Chapter 2.

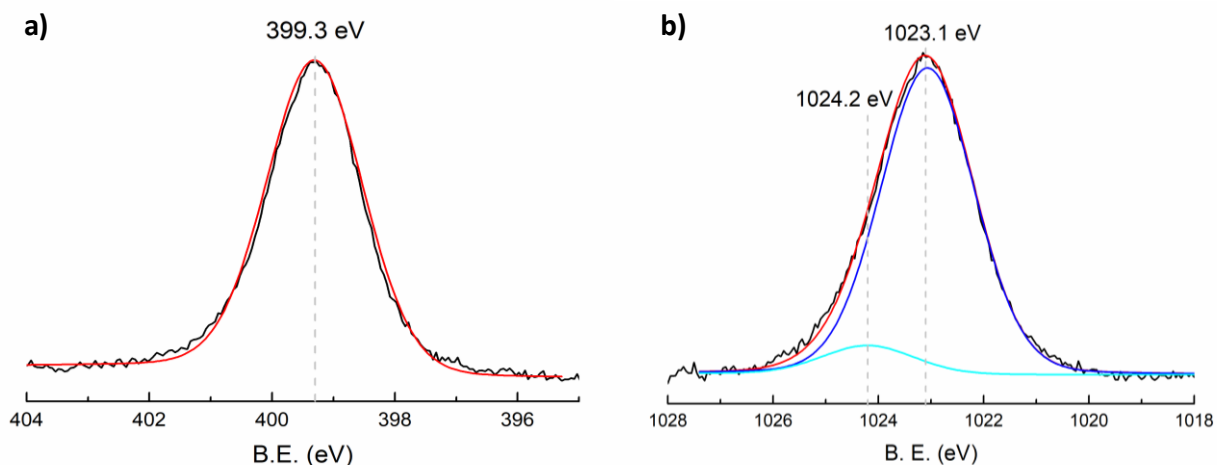


Figure 68: XPS deconvolution of N 1s (a) and Zn 2p<sub>3/2</sub> signals of Si-NPs/ZIF-8 structures obtained after 1 deposition cycle of 10 min in MeOH.

Table 16 reports the atomic concentration of Si 2p, C 1s, O1s, N 1s and Zn 2p<sub>3/2</sub> for Si-NPs/ZIF-8 structures after 1 deposition cycles from MeOH.

<i>XPS atomic concentration of Si-NPs/ZIF-8_1 deposition cycle from MeOH</i>					
<i>Si 2p</i>	<i>C 1s</i>	<i>O 1s</i>	<i>N 1s</i>	<i>Zn 2p<sub>3/2</sub></i>	<i>N/Zn</i>
<b>2.3</b>	65.1	5.7	21.9	5.1	<b>4.3</b>

Table 16: XPS quantitative of Si-NPs obtained after 1 SOP cycle from MeOH solution

N/Zn atomic ratio for the Si-NPs/ZIF-8 structures results 4.3 and the atomic concentration of Si 2p is very low after 10 min. These outcomes prove as the structure and the surface chemistry of Si-NPs accelerate the imidazole deprotonation involving very fast ZIF-8 growth.

In summary, the vertical configuration of ICP CVD, involving non-thermal and high-density plasma synthesis, guarantee the formation of large Si-NPs limiting Si amorphous deposition. In addition, the intrinsic versatility of ICP CVD process allows to control and modulate the structure and the chemical composition of Si-NPs. By varying the deposition time, it has been possible to select the more suitable size to the design of a novel high-capacity active material for negative electrode in LIBs. Octahedral medium Si-NPs, with size exceeding 150 nm and obtained setting the time deposition at 45 sec, have showed a quasi-ideal voltage profile during the first discharge proving as the structure bears the lithiation stress guarantying an excellent electrochemical Li loading and a reversible electrochemical cycling. The ICP-CVD synthesis of P and B-doped Si-NPs, obtained through very low dopants levels, has allowed to test how the Si-NPs doping can avoiding the anode disintegration limiting the capacity fade. Particularly, Medium Octahedral B-doped Si-NPs strongly activates the electrochemical Li<sup>+</sup> alloying probably following the formation of amorphous B<sub>4</sub>Li<sub>5</sub> phases. Finally, the hydrogen-terminated surface of Si-NPs results particularly reactive towards to the functionalization with hybrid organic-inorganic materials, like ZIF-8. Indeed, through facile and fast synthesis from solution it has been possible to obtain core-shell structures characterized by a nanostructured-Si core and a carbon highly porous shell.

## REFERENCES

---

- (262) Su, X.; Wu, Q.; Li, J.; Xiao, X.; Lott, A.; Lu, W.; Sheldon, B. W.; Wu, J. Silicon-based Nanomaterials for lithium Ion Battery. *Adv. Energy Mater.* **2014**, *4*, 1300882-1300904.
- (263) Zhang, W. J. A Review of the Electrochemical Performance of Alloy Anodes for Lithium-Ion Batteries. *J. Power Sources* **2011**, *196*, 13–24.
- (264) Ma, D.; Cao, Z.; Hu, A. Si-Based Anode Materials for Li-Ion Batteries: A Mini Review. *Nano-Micro Lett.* **2014**, *6*, 347–358.
- (265) Doh, C. H.; Oh, M. W.; Han, B. C. Lithium Alloying Potentials of Silicon as Anode of Lithium Secondary Batteries. *Asian J. Chem.* **2013**, *25*, 5739–5743.
- (266) Cheng, X. B.; Huang, J. Q.; Zhang, Q. Review - Li Metal Anode in Working Lithium-Sulfur Batteries. *J. Electrochem. Soc.* **2018**, *165*, A6058–A6072.
- (267) Rezqita, A.; Vasilchina, H.; Hamid, R.; Sauer, M.; Foelske, A.; Täubert, C.; Kronberger, H. Silicon/mesoporous Carbon (Si/mc) Derived from Phenolic Resin for High Energy Anode Materials for Li-Ion Batteries: Role of Hf Etching and Vinylene Carbonate (vc) Additive. *Batteries* **2019**, *5*, 11-22.
- (268) Li, J. Y.; Xu, Q.; Li, G.; Yin, Y. X.; Wan, L. J.; Guo, Y. G. Research Progress Regarding Si-Based Anode Materials towards Practical Application in High Energy Density Li-Ion Batteries. *Mater. Chem. Front.* **2017**, *1*, 1691–1708.
- (269) Wu, L.; Yang, J.; Zhou, X.; Zhang, M.; Ren, Y.; Nie, Y. Silicon Nanoparticles Embedded in a Porous Carbon Matrix as a High-Performance Anode for Lithium-Ion Batteries. *J. Mater. Chem. A* **2016**, *4*, 11381–11387.
- (270) Yu, X.; Xue, F.; Huang, H.; Liu, C.; Yu, J.; Sun, Y.; Dong, X.; Cao, G.; Jung, Y. Synthesis and Electrochemical Properties of Silicon Nanosheets by DC Arc Discharge for Lithium-Ion Batteries. *Nanoscale* **2014**, *6*, 6860–6865.
- (271) Netz, A.; Huggins, R. A.; Weppner, W. The Formation and Properties of Amorphous Silicon as Negative Electrode Reactant in Lithium Systems. *J. Power Sources* **2003**, *119–121*, 95–100.

- 
- (272) Liu, Y.; Chen, B.; Cao, F.; Chan, H. L. W.; Zhao, X.; Yuan, J. One-Pot Synthesis of Three-Dimensional Silver-Embedded Porous Silicon Micronparticles for Lithium-Ion Batteries. *J. Mater. Chem.* **2011**, *21*, 17083–17086.
- (270) Kempster, A. The Principles and Applications of Chemical Vapour Deposition. *Trans. IMF* **1992**, *70*, 68–75.
- (274) Jadhavar, A.; Pawbake, A.; Waykar, R.; Jadkar, V.; Kulkarni, R.; Bhorde, A.; Rondiya, S.; Funde, A.; Patil, D.; Date, A.; Pathan, H.; Jadkar, S. Growth of Hydrogenated Nano-Crystalline Silicon (nc-Si:H) Films by Plasma Enhanced Chemical Vapor Deposition (PE-CVD). *Energy Procedia* **2017**, *110*, 45–52.
- (275) Cabarrocas I. and Roca P., Deposition techniques and processes involved in the growth of amorphous and microcrystalline silicon thin films; *Physics and technology of amorphous-crystalline heterostructure silicon solar cells* **2012**, 131-160
- (276) Abegunde, O. O.; Akinlabi, E. T.; Oladijo, O. P. Overview of Thin Film Deposition Techniques **2019**, *6*, 174–199.
- (277) Sivaram, S. *Chemical Vapor Deposition - Thermal and Plasma Deposition of Electronic Materials* Springer Science & Business Media **2013**.
- (278) Mannino, G.; Alberti, A.; Ruggeri, R.; Libertino, S.; Pennisi, A. R.; Faraci, G. Octahedral Faceted Si Nanoparticles as Optical Traps with Enormous Yield Amplification. *Sci. Rep.* **2015**, *5*, 1–7.
- (279) Faraci, G.; Pennisi, A. R.; Alberti, A.; Ruggeri, R.; Mannino, G. Giant Photoluminescence Emission in Crystalline Faceted Si Grains. *Sci. Rep.* **2013**, *3*, 2674-2679.
- (280) Kortshagen, U. Nonthermal Plasma Synthesis of Semiconductor Nanocrystals. *J. Phys. D. Appl. Phys.* **2009**, *42*, 113001-113022.
- (281) Ravi, L.; Girshick, S. L. Coagulation of Nanoparticles in a Plasma. *Phys. Rev. E - Stat. Nonlinear, Soft Matter Phys.* **2009**, *79*, 1–9.

- 
- (282) De Bleecker, K.; Bogaerts, A.; Goedheer, W.; Gijbels, R. Investigation of Growth Mechanisms of Clusters in a Silane Discharge with the Use of a Fluid Model. *IEEE Trans. Plasma Sci.* **2004**, *32*, 691–698.
- (283) Kee, R.; Coltrin, M.; Glarborg, P. Chemically Reacting Flow: Theory and Practice. **2005**
- (284) Gudmundsson, J. T.; Kouznetsov, I. G. Oxygen Discharges Diluted with Argon: Dissociation Processes. *Plasma Sources Sci. Technol. Plasma Sources Sci. Technol* **2007**, *16*, 399–399.
- (285) Cascio, M.; Deretzis, I.; Fisicaro, G.; Falci, G.; Mannino, G.; La Magna, A. Tailoring Active Defect Centers During the Growth of IV Crystals. MDPI proceedings, in press, 2019.
- (286) Stekolnikov, A. A.; Bechstedt, F. Shape of Free and Constrained Group-IV Crystallites: Influence of Surface Energies. *Phys. Rev. B* **2009**, *72*, 125326-125334.
- (287) Barnard, A. S.; Zapol, P. A Model for the Phase Stability of Arbitrary Nanoparticles as a Function of Size and Shape. *J. Chem. Phys.* **2004**, *121*, 4276-4284.
- (288) De Jong, E. M. L. D.; Mannino, G.; Alberti, A.; Ruggeri, R.; Italia, M.; Zontone, F.; Chushkin, Y. Strong Infrared Photoluminescence in Highly Porous Layers of Large Faceted Si Crystalline Nanoparticles. *Nat. Publ. Gr.* **2016**, 4–12.
- (289) Jaksa, G.; Stefane, B.; Kovac, J. AFM and XPS Study of Aminosilanes with different numbers of bonding sites on a Silicon wafer. *Surface and Interface Analysis*, **2014**, *45*, 1709-1713.
- (290) Kitao, A.; Imakita, K.; Fujii, M. An Investigation into Second Harmonic Generation by Si-Rich SiNx Thin Films Deposited by RF Sputtering over a Wide Range of Si Concentrations. *Journal of Physics D: Applied Physics* **2014**, *47*, 215101- 215108.
- (291) Holovsky, J.; De Wolf, S.; Jiricek, P.; Ballif, C. Attenuated Total Reflectance Fourier-Transform Infrared Spectroscopic Investigation of Silicon Heterojunction Solar Cells. *Review of Scientific Instruments* **2015**, *86*, 073108-073116.
- (292) Lu, G.; Hupp, J. T. Metal-Organic Frameworks as Sensors: A ZIF-8 Based Fabry-Perot Device as a Selective Sensor for Chemical Vapors and Gases. *J. Am. Chem. Soc.* **2010**, *132*, 7832–7833.

---

(293) Jiunn, J.; Kang, J.; Poh, E.; Seng, B. Synthesis and Size Control of Zeolitic Imidazolate Framework-8 ( ZIF-8 ): From the Perspective of Reaction Kinetics and Thermodynamics of Nucleation Synthesis and Size Control of Zeolitic Imidazolate Framework-8 ( ZIF-8 ): From the Perspective of Reaction Kinetics and Thermodynamics of Nucleation. *Mater. Chem. Phys.* **2018**, *216* (September), 393–401.

## CONCLUSIONS

The present PhD thesis reports the development of innovative and high-capacity anodes for secondary lithium ion batteries based on octahedral Silicon nanoparticles and hybrid films of Metal Organic Frameworks as a flexible coatings capable of conducting Li ions, in order to tuning the properties of the electrode/electrolyte interface in the Li cell and, therefore, boosting the battery performance.

Zeolitic Imidazolate Frameworks (ZIF-8) and carboxylate-based MOFs (MIL) have been growth on Si and Cu surfaces from solution through fast and facile routes. The functionalization of Si-based surfaces with ZIF-8 coating through cyclic processes based on sequential one-pot protocol from a MeOH or EtOH solution, allowed to understand how the surface chemistry and the solvent control the film nucleation. The growth rate increases with the polarity of the solvent, and, therefore, thicker ZIF-8 films were obtained; on amorphous Si, Si and quartz surface, from MeOH solutions with respect to films grown from EtOH solutions. Similarly, surfaces, like Si and a-Si characterized by a lower silanol density and a lower amount of oxygen favour the imidazole deprotonation, resulting more reactive towards ZIF-8 functionalization. A simple SOP synthesis route at room temperature; without surface pre-functionalization and without using additive, was also used to grow MOFs films on Cu electrodes for the first time. The high basicity of Cu substrate due to the presence of native copper oxide on its surface induced fast heterogenous nucleation which leads to a thick ZIF-8 (2-4  $\mu\text{m}$  in thickness) film. ZIF-8 / Cu electrodes were therefore developed and assembled in lithium ion cells. The  $\text{Li}^+$  doped ZIF-8 systems, obtained through dipping into ethanol/water solution of lithium acetate, allowed to test the effects of Lithium acetate presence in the ZIF-8 matrix on the electrochemical activity of Cu/ZIF-8 electrode. Results suggest that the acetate group inside ZIF-8@ $\text{Li}^+$  takes part to  $\text{LiPF}_6$  decomposition and SEI formation, influencing the electrochemical activity of ZIF-8 film. Galvanostatic characterization and cyclic voltammetry proved that Cu/ZIF-8 electrodes show an intrinsic, in part reversible, electrochemical activity. In particular, the high porosity and the large surface area of ZIF-8 guarantee a suitable permeability of the electrolyte in term of charge ionic transfer but do not contribute to a capacity variation. For this reason, Cu/ZIF-8 thin films can be considered promising coating to protect anodes like metallic lithium and silicon



ensuring the electrolyte diffusion, the electronic insulation and a flexible hybrid matrix suitable to bear the expansion and the contraction of the anode material due to lithiation delithiation processes.

In addition, host-guest systems consisting of ZIF-8 matrix and dopants like I<sub>2</sub> and TCNQ, were obtained through in situ during the synthesis and ex situ post- synthesis. It has been proved that the insertion of I<sub>2</sub> into ZIF-8 cavities, guarantees a greater amount of trapped I<sub>2</sub> with respect to TCNQ, determining the change of the electrical resistivity from  $2.0 \times 10^9 \Omega$ , detected for not-doped ZIF-8, to  $4.3 \times 10^8 \Omega$ . So doing, it was possible to modulate the electrical resistivity of ZIF-8 by inserting electron acceptor and donor molecules achieving a responsive coating promising for electrochemical devices.

Three different synthetic strategy, based on the direct growth of amino functionalized MIL frameworks on Si surface from dimethyl-formamide solution, were developed to obtain coatings of iron-based MIL with different thickness and crystallinity. In particular, the presence of acetic acid as additive, influences the deprotonation of the 2-amino terephthalic acid used as organic linkers, determining low growth rate. Using this approach, isolated octahedral crystals of NH<sub>2</sub>-MIL-101 were obtained after 4h; whereas without using acetic acid a denser, but poorly crystalline coverage consisting of hexagonal crystals NH<sub>2</sub>-MIL-88 embedded in a net of tiny NH<sub>2</sub>-MIL-101 grains was achieved after 8h. A novel synthetic method based on the direct growth of MIL on a self-assembled monolayer of 4-vinylbenzoic acid was used to increase the growth rate of MIL on Si without compromising the film crystallinity. A thin homogenous layer of tiny NH<sub>2</sub>-MIL-88 crystals embedded in iron oxides was obtained after only 4 dipping hours. In addition, a novel two-step synthetic strategy was developed to grow Fe-based NH<sub>2</sub>-MIL-101 composite films on Cu foils at low temperature (80°C). An amorphous iron oxides/hydroxydes layer deposited via sol-gel on a Cu electrode was used to provide, the Fe<sup>3+</sup> centers needed for the MOF growth. A  $\alpha$ -FeOOH/NH<sub>2</sub>-MIL-101 composite film was therefore grown through using an ethanol solution containing the organic building block only (2-aminoterephthalic acid). The proposed synthetic approach is fast, makes use of mild conditions and so it is a convenient protocol to develop hybrid metal oxide/MOF films. EIS measurements showed that, despite the poor conductivity of the MOF, resulting in a high ESR value, both iron oxides/hydroxydes and  $\alpha$ -FeOOH/NH<sub>2</sub>-MIL-101 have similar circuit parameters. In particular, both systems behave like non-ideal capacitors with a value of charge transfer resistance of about 1100  $\Omega$ , which is lower than the Cu benchmark. Despite the insulating character of NH<sub>2</sub>-

MIL-101,  $\alpha$ -FeOOH/NH<sub>2</sub>-MIL-101's unique impedance behaviour makes it a promising electrode capable of combining the structural and chemico-physical MOF properties with the typical electrochemical characteristics of iron hydroxide materials.

One of the strenght points of this work is the novel Si anode characterized by a peculiar structure and obtained through non-thermal, solvent-free and low-cost synthesis based on ICP chemical vapour deposition. In particular, highly pure, crystalline and mono-disperse Si-NPs of size exceeding 150 nm with unique octahedral shape that is defined by the <111> planes that are by far the most stable Si lattice surfaces, were obtained. This specific configuration allows to bear the lithiation stress avoiding cracking or capacity fade and guarantying an excellent reversible cycling ability despite the large size proposed with respect to the examples of nanostructured-Si reported in literature. Indeed, intrinsic Si-NPs show a first discharge capacity of 3522 mAhg<sup>-1</sup>, acting as a quasi-ideal anode. In addition, the versatility of ICP-CVD allowed to modulate the chemical composition of Si-NPs carrying out P and B-doped octahedral Si nanoparticles. B-doped Si-NPs activate more efficiently compared to P-doped the electrochemical Li<sup>+</sup> alloying guarantying high cycling reversibility. Hybrid core-shell structures were obtained through the surface functionalization of octahedral Si-NPs with ZIF-8 frameworks. By optimizing the synthetic condition, using methanol as solvents and carrying out 10 SOP cycles, it was possible to further increase the surface area of Si-NPs and to envelop them into a flexible porous matrix in order to stabilize the ellectrode/electrolite interface which is a key point to develop advanced negative electrodes.

# ACKNOWLEDGMENTS

This thesis work has been partially supported by the CHALLENGE project. (HORIZON 2020-NMBP-720827, <http://www.h2020challenge.eu/>). CHALLENGE is a research and innovation action founded by the European Union's Horizon 2020 programme.

In addition, the thesis work has been permitted by the project “Piano della Ricerca d’Ateneo 2016-2018” - University of Catania.

# Curriculum, publications and conferences

## Curriculum vitae

### Personal information

Last name *Monforte*

First name *Francesca*

Nationality *Italian*

Date of birth *13/02/1987*

### Education

**2005:** Scientific High School (94/100) Liceo Scientifico G. Verga Adrano (CT), Italy.

**2011:** Bachelor's Degrees in Chemistry (103/110) at University of Catania, Italy. Thesis: "Molecular aggregation of the complexes of Zn (II) derived from Schiff bases: molecular branched nanostructures"; Supervisor: Prof. S. Di Bella.

**2013:** Master's Degrees in Chemistry of Materials (110/110 cum lode) at University of Catania, Italy. Thesis: "Induction of chirality from complexes of Zn (II) derived from Schiff bases of hetero porphyrin aggregates"; Supervisor: Prof. S. Di Bella.

**2015:** Scholarship holder (grant formation) European funded project: ENERGETIC – "Technologist expert in circuits, systems and networks for

photovoltaic high efficiency” at Consiglio Nazionale delle Ricerche (CNR), Distretto Tecnologico Micro e Nano Sistemi S. c. a. r. l, (CT), Italy.

**2019:** Ph.D. in Material Science and Nanotechnology at University of Catania, Italy. Thesis: “Plasma synthesis of silicon nanoparticles and their functionalization with metal organic frameworks as anode materials for lithium ion battery”; Tutor: Prof. G. G. Condorelli and Dr. A. La Magna; Supervisor: Dr. G. Mannino, Coordinator: Prof.ssa M.G.Grimaldi.

### **List of Papers on the PhD Topics:**

1. Francesca Monforte, Giovanni Mannino, Alessandra Alberti, Emanuele Smecca, Markus Italia, Alessandro Motta, Cristina Tudisco and Guglielmo G. Condorelli, “*Heterogeneous Growth of Continuous ZIF-8 Film on Low-Temperature Amorphous Silicon*”, *Applied Surface Science*, **2019**, 473, 182-189.
2. Francesca Monforte, Mario Urso, Alessandra Alberti, Emanuele Smecca, Salvo Mirabella, Giovanni Mannino and Guglielmo G. Condorelli, “*A new synthetic route for the growth of  $\alpha$ -FeOOH/NH<sub>2</sub>-MIL-101 film on copper foils for high surface area electrodes*”, *ACS Omega*, **2019**, 4, 18495-18501.
3. Francesca Monforte, Mario Falsaperna, Anna Lucia Pellegrino, Corrado Bongiorno, Alessandro Motta, Giovanni Mannino and Guglielmo G. Condorelli, “*Direct growth on Si (100) of isolated octahedral MIL-101(Fe) crystals for the separation of aromatic vapours*” *JPPC*, **2019**, 123, 28836-28845.
4. Francesca Monforte, Mario Falsaperna, Anna Lucia Pellegrino, Giovanni Mannino and Guglielmo G. Condorelli, “*Synthetic strategies to control the heterogenous nucleation of Fe-based MOFs on Si(100)*”, manuscript to be submitted.
5. Giovanni Mannino, Francesca Monforte, Sergio Brutti, Alessandra Alberti, Corrado Bongiorno and Guglielmo Guido Condorelli, “*Large Octahedral Si nanoparticles as high-capacity anode materials for lithium ion battery*”, manuscript to be submitted

### **List of other Publications:**

1. Augusto Marcelli, Bruno Spataro, Giovanni Castorina, Wei Xu, Stefano Sarti, Francesca Monforte, Giannantonio Cibin, G., “*Materials and Breakdown Phenomena: Heterogenous Molybdenum Metallic Films*”. *Condensed Matter*; **2017**, 2, 18.
2. Giovanni Castorina, Augusto Marcelli, Francesca Monforte, Stefano Sarti, Bruno Spataro. “*An Analytical Model for Evaluation of the Properties of Metallic Coatings in RF Structures*”. *Condensed Matter*; **2016**, 1, 12.

### **Collaborations:**

- Prof. Sergio Brutti, Dipartimento di Chimica, Università di Roma “La Sapienza”.
- Dr. Alessandro Motta, Dipartimento di Chimica, Università di Roma “La Sapienza”.
- Prof. Salvo Mirabella and Dr. Mario Urso, Dipartimento di Fisica ed Astronomia, Università degli Studi di Catania.
- Prof. ssa Graziella Malandrino and Dr. Anna Lucia Pellegrino, Dipartimento di Scienze Chimiche, Università degli Studi di Catania.
- Dr. Alessandra Alberti, IMM-CNR, Istituto per la Microelettronica e Microsistemi, Catania.
- Dr. Salvatore Lombardo and Dr. Stefania Privitera, IMM-CNR, Istituto per la Microelettronica e Microsistemi, Catania.
- Dr. Salvatore Petralia, STMicroelectronics, Catania.
- Dr. Augusto Marcelli, Dr. Bruno Spataro, Dr. Giovanni Castorina, INFN-LNF, Roma.

## Conferences:

1. Francesca Monforte, Mario Falsaperna, Anna Lucia Pellegrino, Corrado Bongiorno, Alessandro Motta, Giovanni Mannino and Guglielmo G. Condorelli; “*Synthesis of Fe-based Metal Organic Frameworks films on Si for gas sensing*”, Symposium D, E-MRS 2019 FALL MEETING, 16-19 September, Warsaw University of Technology-Poland. *Oral Presentation*.
2. Francesca Monforte, Giovanni Mannino, Sergio Brutti and Guglielmo Guido Condorelli; “*Direct growth of ZIF8 films on Cu foils from solution for lithium ion battery*”, Materials and devices for renewable energy, FisMat 2019, 30 September-4 October, University of Catania. *Oral presentation*.
3. Francesca Monforte, Giovanni Mannino, Alessandra Alberti, Emanuele Smecca, Markus Italia, Alessandro Motta, Cristina Tudisco and Guglielmo G. Condorelli, “*Nucleation and growth of ZIF8 and MIL frameworks on Si-based Substrates and Copper foils*”, Invited Contribution to the AIV XXIV Conference, May 7-10, 2019, Giardini-Naxos, Italy.
4. Francesca Monforte, Giovanni Mannino, Alessandra Alberti, Alessandro Motta, Cristina Tudisco and Guglielmo G. Condorelli, “*Growth and Post-synthetic modification of ZIF thin films*”, Materials.it 2018, October 22-26, Bologna, Italy. *Oral presentation*.
5. Francesca Monforte, Giovanni Mannino, Alessandra Alberti, Emanuele Smecca, Alessandro Motta, Cristina Tudisco and Guglielmo G. Condorelli, “*Nucleation and growth of ZIF8 thin films on Si-based substrates*”, International School of Materials for Sustainable Development and Energy, 1<sup>st</sup> Course, Materials for Energy and Sustainability, July 6-13, 2018, Erice, Italy. *Poster Session*.
6. Rachela G. Milazzo, Stefania S.M. Privitera, Silvia Scalese, Francesca Monforte, Guglielmo G. Condorelli and Salvatore Lombardo, “*IrO<sub>x</sub> nanoparticles deposition on Ni foam electrodes by galvanic displacement for catalytic applications*”, 235th ECS Meeting, May 26-30, 2019, Dallas, TX. *Co-author*.

7. Rachela G. Milazzo, Stefania S.M. Privitera, Silvia Scalese, Francesca Monforte, Guglielmo G. Condorelli and Salvatore Lombardo, “*IrO<sub>x</sub> nanoparticles deposition on Ni foam electrodes by galvanic displacement for catalytic applications*”, AIV XXIV Conference, May 7-10, 2019, Giardini-Naxos, Italy. *Co-author*.
8. Anna L. Pellegrino, Cristina Tudisco, Francesca Monforte, Guglielmo G. Condorelli, Paolo Cortelletti, Adolfo Speghini and Graziella Malandrino, “*MLD approach for hybrid metalorganic-inorganic systems: NiO thin films functionalized with a luminescent Eu complex monolayer*”, Symposium S, E-MRS 2018 Spring Meeting, June 18-22, Strasbourg, France. *Co-author*.
9. Rachela G. Milazzo, Stefania S.M. Privitera, Francesca Monforte, Silvia Scalese, Guglielmo G. Condorelli and Salvatore Lombardo, “*IrO<sub>2</sub> functionalized Nickel foam electrodes for efficient energy conversion devices*”, WODIM 2018 - 20th Workshop on Dielectrics in Microelectronics, June 10-14, Berlin, Germany. *Co-author*.
10. Rosa Ruggeri, Francesca Monforte, Gabriele Fisichella, Filippo Giannazzo, Giovanni Mannino; “*Isolated highly oriented phosphorus doped Si-NPs*”. Conference NanoSEA 2016, July 3– 8, Giardini Naxos (ME), Italy. *Co-author*
11. Sofia Gaiaschi, Rosa Ruggeri, Francesca Monforte, Simon Richard, Patrick Chapon; “*Glow Discharge Optical Emission Spectrometry and Differential Interferometry Profiling for Thickness Determination of SiO<sub>x</sub>N<sub>y</sub> Layers*”. Conference E-MRS 2016 Spring Meeting, May 2 - 6, Lille, France. *Co-author*

#### **Workshop and International School:**

- Italian-Israeli Cooperation Workshop on “*Materials and Technologies for Industrial Innovation*”, Scuola Superiore di Catania, October 16-17, 2018, Catania, Italy.
- Participations at International School of Materials for Sustainable Development and Energy, 1<sup>st</sup> Course, Materials for Energy and Sustainability, July 6-13, 2018, Erice, Italy.



**Co-tutor activities:**

Co-TUTOR with Prof. Guglielmo G. Condorelli for Bachelor's Degrees in industrial Chemistry:

- “*Sintesi e trattamenti Post-crescita di Film di ZIF-8*”, Alessi Rosario Marco, May-October 2018.
- “*Sintesi di Film di Metal Organic Frameworks (MOFs) drogati*”: Cavallaro Flavio, October 2018- April 2019.

Co-TUTOR with Prof. Guglielmo G. Condorelli for Master's Degrees in Material Chemistry:

- “*Crescita di Metal Organic Frameworks (MOF) a base di Fe su superfici di Si (100) per gas sensing*”, Falsaperna Mario, November 2018-November 2019.
- “*Crescita di Metal Organic Frameworks a base di Fe, Zn e Mn su superfici di Pt per gas sensing*”, Collaboration with StMicroelectronic, Crispi Simona, May 2019-Now.